NOVEL CLASS OF CHRONIC AND IMPLANTABLE WIRELESS OPTOFLUIDIC (wOF) NEURAL DEVICES FOR *IN VIVO* DRUG DELIVERY AND OPTOGENETICS IN FREELY MOVING ANIMALS

by

RAZA QAZI

B.Tech, National Institute of Technology, Srinagar, 2014
M.S, University of Colorado Boulder, 2017

A thesis submitted to the
Faculty of the Graduate School of the
University of Colorado in partial fulfillment
of the requirement for the degree of
Doctor of Philosophy
Department of Electrical, Computer, and Energy Engineering
2019

This thesis entitled:

Novel Class of Chronic and Implantable Wireless Optofluidic (wOF) Neural Devices for In Vivo Drug Delivery and Optogenetics in Freely Moving Animals

written by Raza Qazi

has been approved for the Department of Electrical, Computer, and Energy Engineering

Approved by:

_____	_____
Dr. Jae-Woong Jeong	Dr. Frank Barnes

_____	_____	_____
Dr. Jianliang Xiao	Dr. Kimberly Newman	Dr. Hanh-Phuc Le

Date: _____

The final copy of this thesis has been examined by the signatories, and we find that both the content and the form meet acceptable presentation standards of scholarly work in the above-mentioned discipline.

ABSTRACT

Raza Qazi (Ph.D., Electrical Engineering)

Novel Class of Chronic and Implantable Wireless Optofluidic (wOF) Neural Devices for *In Vivo* Drug Delivery and Optogenetics in Freely Moving Animals

Thesis directed by Professor Jae-Woong Jeong and Prof. Frank Barnes

Chronic in-vivo studies through multimodal modulation of neurons in the deep brain can render pivotal insights not only in identifying their roles for a specific activity, but also to decipher their contribution in various neurodegenerative diseases. To prevent askew effects, probes were implanted to directly reach the target sites and the spatiotemporal resolution was further improved by targeting key neural circuits using optogenetics and pharmacology. Multimodal optofluidic probes allow integrated access to the target region without the need for multiple surgeries thus reducing tissue damage as well as simplifying combinatorial stimulations. Conventional tools have relied on rigid metal cannulas and silica optical fibers, but they cause adverse tissue inflammation due to their large probe sizes, rigid materials and associated tethers which severely limit their chronic integration. However, minimally invasive, mechanically compliant and untethered probes are shown to significantly limit tissue scarring in freely moving animals as shown in recent advances in soft optofluidic probes controlled by wireless head mounts, however, they didn't last long primarily due to exhaustion of the drugs and power. Moreover, they were limited to the brain due to their bulky head mounts with limited range, directionality, and selectivity. Here we introduce two wireless optofluidic (wOF) neural devices each solving unique challenges faced by previous state-of-the-art devices and commercial pumps. Firstly, is the Lego wOF device which enables: 1) uninterrupted drug supply using replaceable "Lego" drug cartridges and 2) an easy-to-use smartphone app that allows long wireless range (~100m), isotropic wireless access, no Line of Sight (LOS) handicap, Over The Air (OTA) updates, high target specificity and scalable closed

loop systems within a large group as well as intuitive control through an easy to use app on any commercial handheld smartphone. Second is the fully implantable wOF device which enables: 1) both central and peripheral stimulation in any space critical location inside the body (92% smaller and 88% lighter than previous systems), and 2) battery-free operation using a soft, stretchable energy harvester that can conformally adhere to any curvilinear surface inside the body. Successful in-vivo studies in mice demonstrate their innate capability for programmable and chronic wireless pharmacology and optogenetics.

ACKNOWLEDGMENTS

"Indeed, God is with the patient." – Quran 2:153,

is among my favorite quotes that have reverberated within me repeatedly throughout my graduate studies and that I would keep reminding myself whenever I faced surmounting challenges. Remembering them even momentarily, gave me immense comfort and strength through those long dark nights of Boulder as I juggled between an intense curriculum of 13 graduate credit courses and my seemingly hopeless research wishing each day that my neural devices would finally break their 8-month long streak of continuous failures when being tested in live animals. Though overall there are innumerable people I am indebted to, who have helped me every now and then in various aspects of my graduate studies both in Kashmir, US and South Korea, due to limited space, I would specifically like to highlight few of them.

First of all, I would like to offer my sincerest gratitude to my research advisor Prof. Jae-Woong Jeong who guided me since my master's program all the way to the end of my doctorate degree. His continuous support, positive critiques, sincere advice, and invaluable knowledge has helped me grow to become the person I am today. I am very thankful for his kind patience and his willingness for open and honest confrontations that helped me become a better person and understand a little more of myself. I am forever grateful to the academic, mentorship and growth opportunities he offered me throughout my research degree (both US and South Korea) without which I wouldn't have come this far.

Also, my sincerest regards to Prof. Frank Barnes, who from the beginning of my graduate studies always had his doors open for me not just to advise about my research but even for a random friendly chat which would sometimes last for hours. There were countless times that he guided me while I made some tough decisions and would always listen keenly to all my concerns. I consider him to be among the most valuable and respectful mentors I have ever met in his life.

I would also like to thank my defense committee – Prof. Jianliang Xiao, Prof. Hanh-Phuc Lee and Prof. Kimberly Newman for offering me critical advice to improve upon my research while also being very supportive of my decisions along the way.

This work would be incomplete without the work from my colleagues, co-authors, and collaborators. I would like to thank our collaborators in Prof. Rogers group at Northwestern University who helped design the antenna for the implantable wOF device and to members in the Prof. Bruchas group at Washington University who helped with in vivo animal studies especially Adrian Gomez and Daniel Castro without whom this research would be incomplete. Also, I am grateful to Prof. Jianliang Xiao and Zhanan Zou at CU Boulder for helping in the mechanical analysis of the Lego interface and to Dr. Joo Yong Sim for helping with pressure simulations.

I am also thankful to my colleagues at Jeong group who helped me throughout my research and many of whom I had the opportunity to learn from as their mentor. Firstly, Yanyu and Frederick who helped with developing the smartphone app and kept tweaking it over the years. Also, I am grateful to Jonas and Muhammad who assisted me in fabricating a plethora of microfluidic channels and Avery who assisted in etching heater as well as some CAD work and coding. Also, am thankful to Choongyeon, Sanghyuk, and Juhyun who helped me with a lot while in Korea. I am thankful to the amazing people in our department as well, especially Adam Sadoff and Nicole who helped me a lot while transitioning my research abroad in Korea. A special thanks to my friend Jae Hur who helped me adjust to the new culture in Korea and was always up for a warm cup of coffee and an interesting chat.

Finally, I would like to thank my family including my parents – Qazi Imtiaz Rasool and Anjum Ara as well as my brothers, Qazi Inaam and Qazi Zaid, all of whom were good listeners and keen advisors on all major decisions I have made throughout my life. Their belief in me through all the decisions that I've made kept me becoming stronger and wiser. Needless to say, everything I am now, would've been impossible without their support. I would like to especially

thank the kind support I received from my grandparents – Qazi Ghulam Rasool, Muhammad Amin Sufi and Misra Begum whose consistent advice and prayers kept me moving forward against all the odds. No word would do justice to the indebted gratitude I feel for my lovely grandmother Misra Begum who raised me up ever since I was 40 days old and her continuous love, support, and belief in me never faded even once for the past 28 years. Also, I am glad to have a lovely family of Ajaz and Ruhi Siraj nearby Boulder who were very kind to invite me every now and then and it felt like a second home away from home I also feel blessed to have known, over the years, very creative and passionate individuals Lang, Rishabh and Tom together with whom, I have learnt a lot about non-academic matters of business and life. Lastly, I feel particularly thankful and blessed to have amazingly great friends Waseem Var, Aqeel Kirmani, and Basit Ishaq whose constant prayers, support and advice kept me going against all odds throughout the years.

CONTENTS

TABLES

FIGURES

1 Introduction

Interfacing with the brain tissue with maximum accuracy and minimal invasiveness has been one of the biggest challenges of this decade. Techniques for neural stimulation and subsequent acquisition of feedback signals provide information on brain functionality which is critical to understand for the scientific community. The brain is being studied in many different facets and researchers are consistently trying to come up with technologies that interact with the brain tissue more reliably and efficiently with high spatiotemporal control and resolution.

1.1 The Brain - The need for complexity and the pursuit for simplicity

The brain is considered the single most important organ in the human body, yet it is the least understood part of the body. The reason simply being that the current tools and technology available to neuroscientists today are a lot simpler and primitive to explore and dissect quadrillions of interlocked synaptic neural pathways within a convoluted mesh of about 100 billion neurons[1]. Not only it controls and monitors all the bodily functions[2], [3], movements[4] and other basic processes such as respiration[5], heart rate[6], digestion[7], excretion[8], hormone release[9], [10] etc. , it also plays key role in decision making[11], [12], learning and memory[13], perception[14] awareness[15] and cognition[16], mood swings[17], rapid response to stimuli[18], [19], stress[20] and disease[21] and speed control of various physiological events[22], [23]. At the macro scale, its primarily role is to keep the body in homeostasis (balanced state arising from negative feedback closed-loop control) such that we can make normal decisions and interact with the environment, but at the micro-scale, it is required to communicate and monitor every small micro-process in each of the 27.2 trillion cells within the body either directly or indirectly (**Fig. 1.1**). To continuously interact with such complex tasks all the time requires a highly complex processing

organ. There is no way a simply structured organ can handle this stupendous task to control everything happening both inside the body as well as sensing from the external environment.

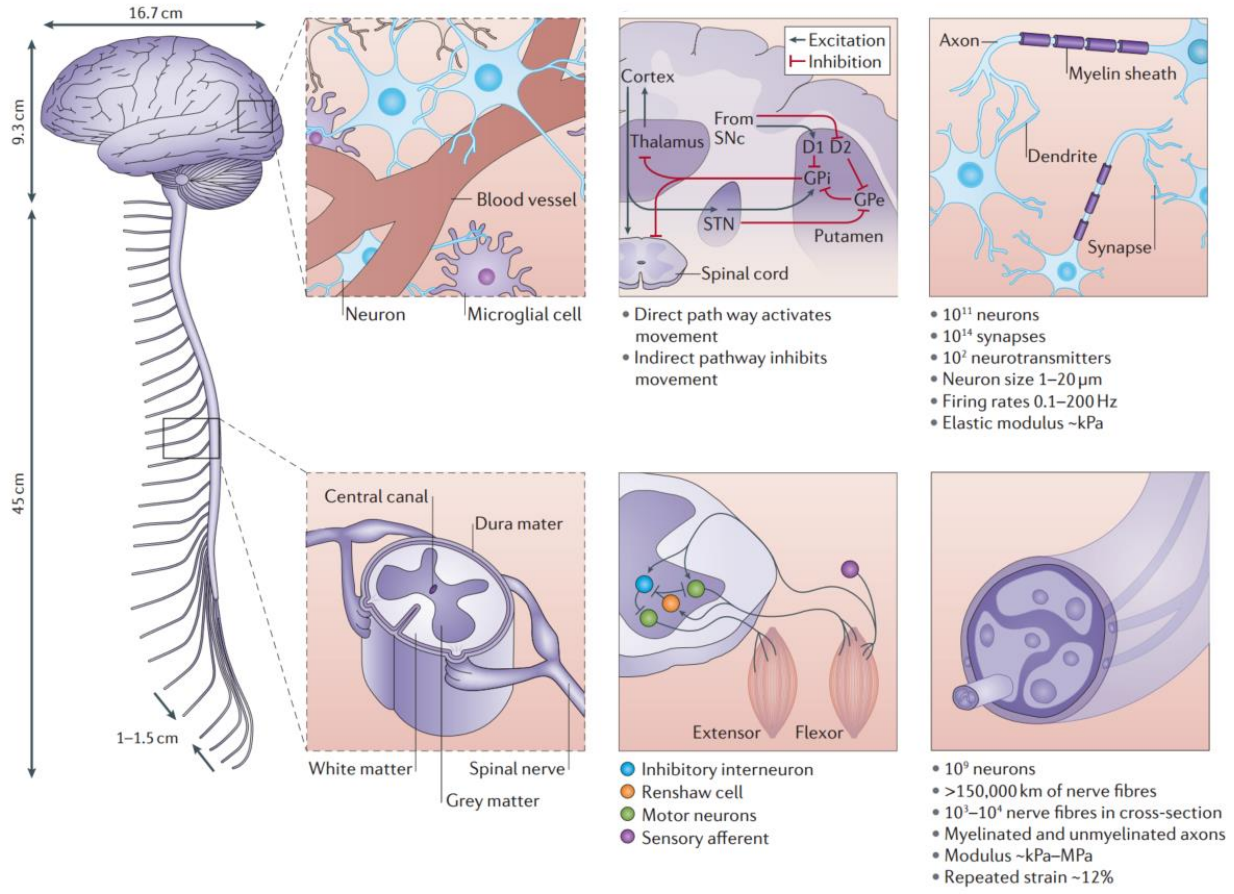

Figure 1.1 – The primary human brain network, structures, and processes.*[24]*

On the other hand, scientists have been trying to decipher this complex organ by trying to dissect its unit blocks i.e. neurons to understand its processes and functioning, primarily for three main reasons: a) to enhance knowledge about the brain, b) to improve diagnosis and therapeutics for various neurodegenerative diseases, and lastly c) to help implement the futuristic brain-machine interfaces (BMI) that can communicate directly with external computers or artificial neural networks that can mimic the optimized brain networks. However, this task has been nothing but immensely challenging. The best way to dissect is at the cellular level, where researchers can

control a specific target cell and understand the pattern of a signal flowing through it and its response to distinct stimuli. However, the inability to create micrometer-sized device structures and biological techniques to interact distinctively at the cellular scale over long periods of time without initiating adverse immune response severely limited their advances. Over the past several decades, researchers have used advances in genetics, engineering and material science to fabricate new tools which can penetrate deep inside the brain and help dissect the functionality at both tissue and cellular levels (**Fig. 1.2**).

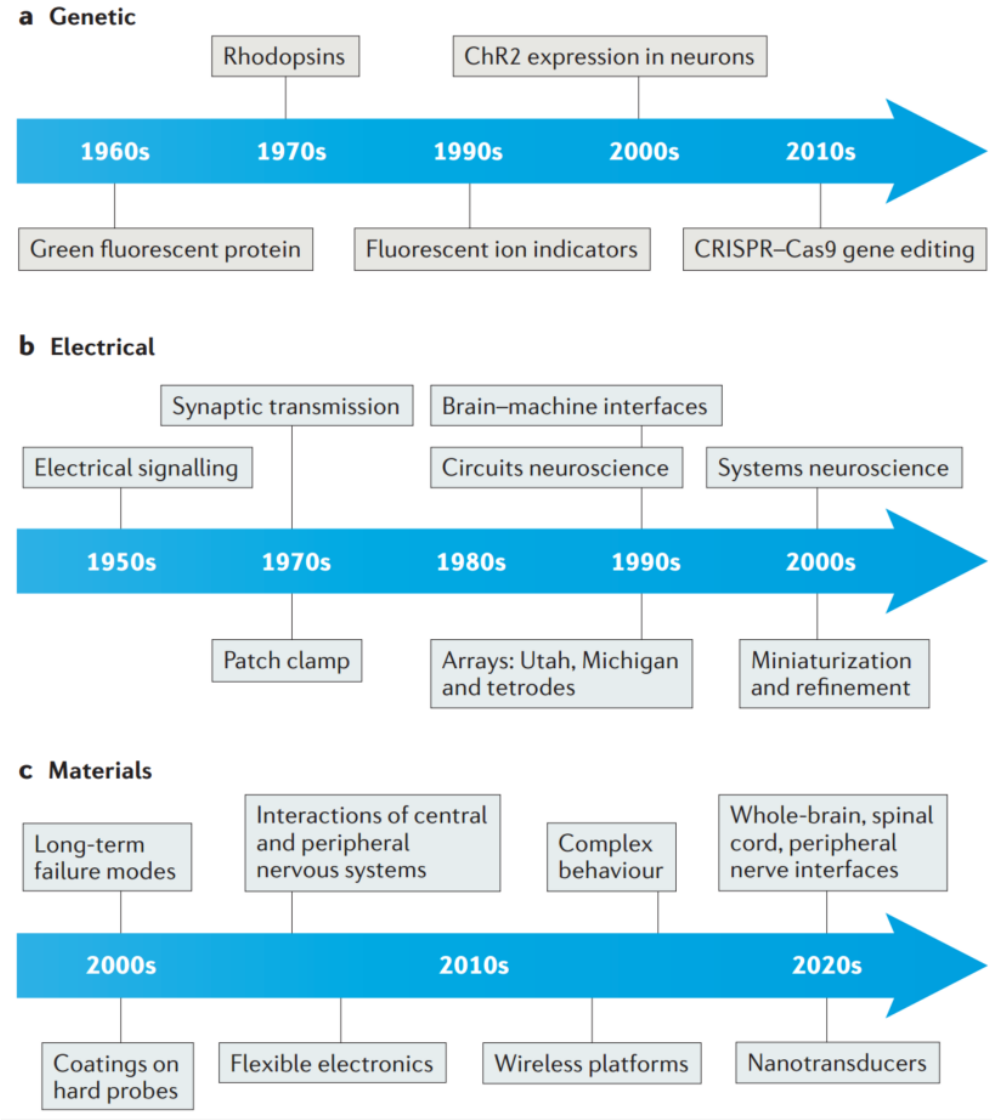

Figure 1.2 – A brief history of advances in neural circuit exploration techniques over the past decades.*[24]*

1.2 Techniques used for neural stimulation

Though there are several non-invasive sensing methods that are being clinically used (at present) which help understand brain behavior like magnetic resonance imaging (fMRI), functional MRI (fMRI) and computerized tomography (CT) Scan, however, to offer controlled millisecond stimulation deep inside the brain at cellular level and to be able to match the natural speed of neural spike patterns in the brain is very hard to achieve (**Fig. 1.3**). Hence to decipher the underlying mechanisms in the neurobiological systems and dissect various neural diseases, scientists have tried exploring the cells using a variety of biologically engineered techniques like electrical[25]–[29], chemical, optical[30], magnetic[31], genetic[32], infrared[33]–[35] and ultrasound[36]–[38] stimulations. Though many unique non-invasive approaches have been explored, we will focus on the three most popular invasive techniques that are most widely used today to access deep brain tissues at the cellular level - electrical, optogenetic and chemical stimulation which are initiated through electric fields, photostimulation and pharmacological deliveries respectively.

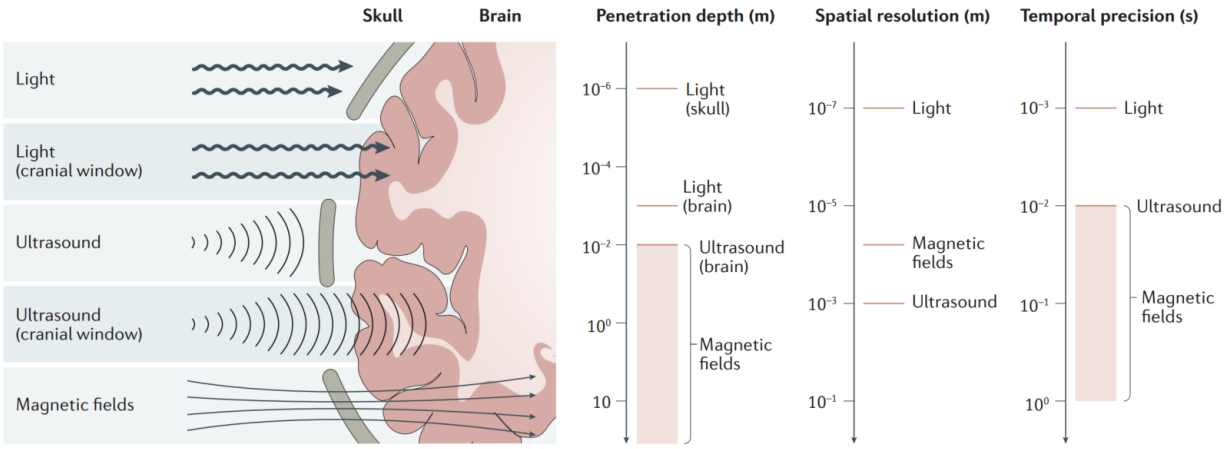

Figure 1.3 – Various non-invasive techniques to probe the brain. *[24]*

From the earliest experiments of Benjamin Franklin in 1757 where he uses current flow to treat paralytic seizures [39] to the latest electric field localization methods to increase spatial resolution for stimulation in deep brain, the electric stimulation techniques have been around for the longest period and are still used clinically for diagnostic and therapeutic applications such as Deep Brain Stimulation (DBS) using metal electrode to mitigate tremors and epileptic seizures. However, one critical drawback is their lack of spatial resolution which is a critical factor to locally dissect the neural system. An electric stimulation evoked near a neuron can travel easily across all its interconnected vicinities thus reducing the reliability of data collected using this stimulation technique. On the other hand, chemical stimulations can have a similar effect of non-localization effect. However, when used in the form a special technique called DREADD (Designer Receptors Exclusively Activated by Designer Drugs)[40], we can achieve very high spatial control in neural stimulation, thus highly localizing the effect of our study to a very few target cells and hence increasing the reliability of such studies. Moreover, the recent development of a novel technique enabled neuroscientists to achieve even better spatiotemporal resolution through photostimulation of genetically modified target cells, also known as Optogenetics[30], [41]–[44]. By genetically transfecting specific target neurons in the brain with light-sensitive proteins which are expressed in their cell membranes, upon photon exposure at distinct wavelengths, only these modified cells would be stimulated or inhibited with millisecond resolution[30]. If Channelrhodopsin-2 (ChR2) opsins were expressed and blue light (~470 nm) was used, it would stimulate the neuron while as all neurons without the protein would be completely unaffected. On the other hand, expressing proteins like Halorhodopsins when stimulated with orange light (~589 nm) can inhibit the target neuron while all neighboring neurons are functioning properly. This cellular control and inhibition of neurons are what makes optogenetics among the most promising tools at present to help dissect the complex brain circuity and disorders.

1.2.1 Micrometer-sized LEDs (μ-LEDs) for chronic optogenetics

Figure 1.4 illustrates the desired features of a neural probe system for chronic *in vivo* optogenetics. First of all, ideally, neural probe systems need a miniaturized light source. A tiny light source allows its seamless integration onto the shank of a neural probe, enabling direct light source interface with neural tissue. It can help not only reduce tissue damage and inflammation response due to its small dimensions but also achieve more power efficient optogenetic excitation by being right next to the target neural circuits, eliminating optical power loss associated with coupling waveguides of external light sources in the conventional waveguide-based method. Furthermore, the small size facilitates discrete, spatial targeting of a specific neuron or neural circuit for more precise, targeted optical manipulation. It can be easily extended to have multiple light sources with the same or distinct emission wavelengths on a single probe. This scalability is another beneficial attribute of a miniature light source that allows highly versatile optogenetic controls. Secondly, biocompatible probe-tissue integration should be achieved for the chronic neural interface. Key factors required for chronic biocompatibility are a miniaturized neural probe for minimal tissue damage, the mechanical property of the probe that matches with that of neural tissue, and material biocompatibility that causes a negligible immune response. For these reasons, ultrathin, soft and flexible biocompatible polymeric platforms are considered to be an ideal solution to minimize the adverse tissue response over long periods of time. To enable chronic *in vivo* functionality while maintaining flexibility, these probes must be encapsulated with a polymer with negligible water permeability (such as SU- 8 and Parylene C) to provide a critical hermetic barrier against surrounding biofluids for several months [45], [46]. Lastly, implantable optogenetic systems should provide wireless interfaces to allow tether-free neural circuit controls to guarantee the naturalistic behavior of animals. This can be realized by implementing miniaturized standalone wireless systems using widely available wireless techniques such as infrared (IR) and radiofrequency (RF) remote controls.

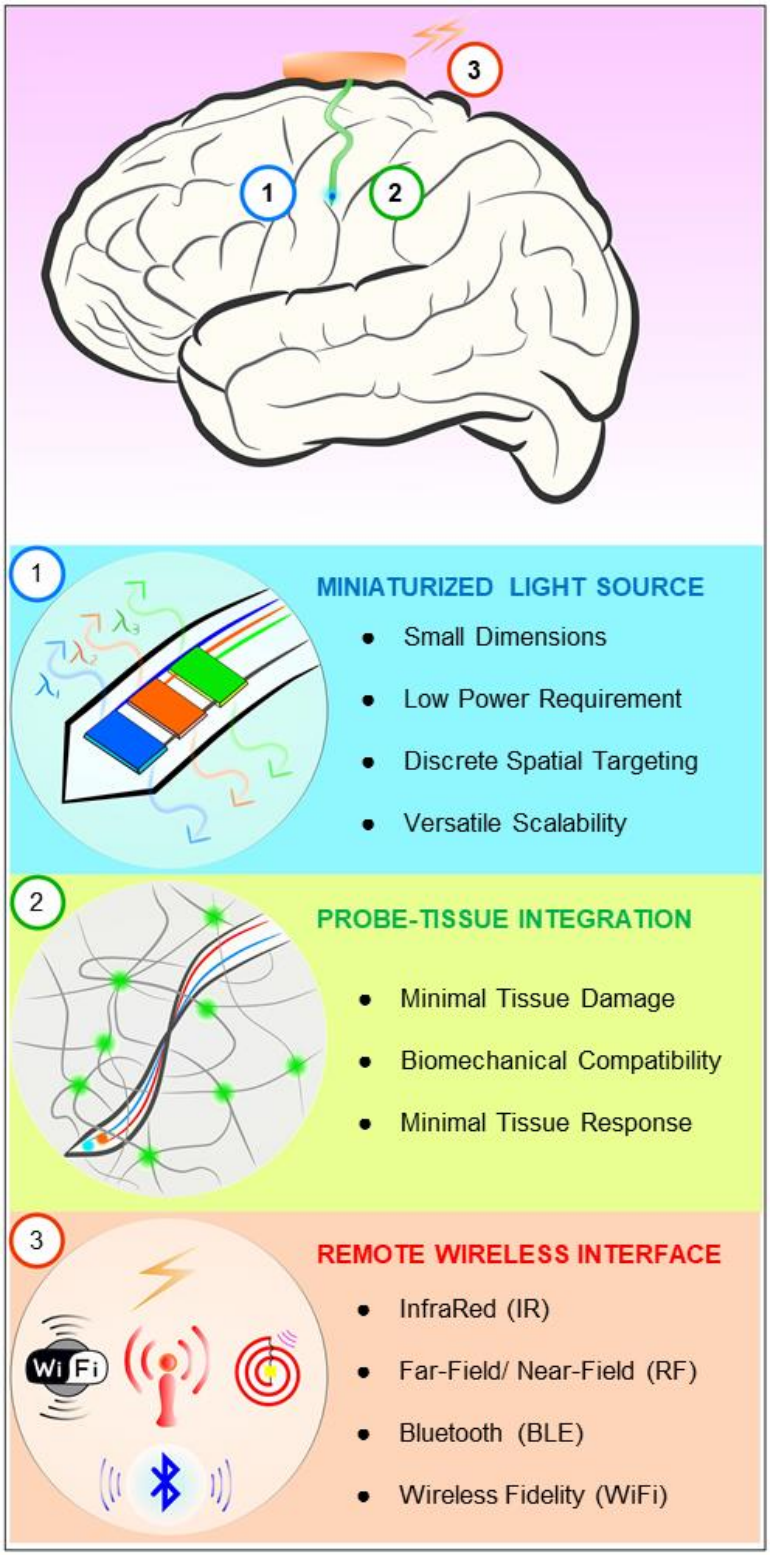

Figure 1.4 – An ideal neural probe for chronic optogenetics. *[47]*

A μ-ILED is a core enabling element that facilitates the realization of all of the above three requirements. The μ-ILEDs have dimensions smaller than 100 μm × 100 μm with the thickness of only several microns, require very low electrical input power (1–1.5 mW) for optical output intensity needed for optogenetic excitation (1 mW/mm2)[45], and provide various color options (e.g., blue, orange, etc.) [48] as well as thermally safe operation within tissue (temperature increase of the surrounding tissue: only ∼0.1◦C when operating a μ-ILED with 10 ms pulse width at 20 Hz, which produces a peak optical output power of 17.7 mW/mm^2 at an electrical input power of 8.65 mW)[45]. This favorable tiny optoelectronic component can be easily integrated with ultrathin, flexible polymeric platforms by transfer printing [49], therefore permitting minimally invasive, chronically biocompatible integration with neural tissue for *in vivo* optogenetics. For small scale integration of μ-ILEDs on flexible substrates, the polymer stamp-based transfer printing technique is favorable. Although sequential, it allows for simple and easy transfer of off-the-shelf or custom-fabricated μ-ILEDs without requiring expensive equipment and special processes, which is in contrast to wafer-level transfer using conventional laser lift-off (LLO) techniques [50]. LLO can allow single-step, mass transfer of custom-fabricated μ-ILEDs to other substrates, but require special thermal considerations, equipment setups, as well as careful layout design to ensure high yield and reliability for large scale transfer. Moreover, μ-ILEDs ease wireless operation due to its low operation current density requirement [> 44 times smaller than required current density for laser coupled waveguides for optogenetic stimulation [51]], which can be easily supplied through wireless power transfer or small batteries. In comparison to laser diodes, μ-ILEDs generally operate on lower voltages and currents [2.7 V, 0.5 mA for μ-ILEDs[52] vs. > 3 V, > 22 mA for laser diode [51]], where they demonstrate relatively higher power efficiencies and lower heat generation. Their efficiency can be further improved by limiting operational currents without affecting their capability to generate sufficient optical output power to achieve optogenetic excitation, unlike laser diodes whose threshold currents lie above tens of milliamps, making them relatively inefficient for low power wireless systems.

1.3 Optofluidic Neural Probes

Since high spatiotemporal dissection of neural circuitry can be achieved through optogenetic and chemo genetic techniques, combining both into a single platform can provide neuroscientists with a great tool that can allow multimodal dissection of same localized neural circuits without additional surgeries.

1.3.1 Motivation

Chronic in-vivo studies involving dynamically modulated, multimodal control of a distinct neuronal cell type in the deep brain tissue can render pivotal insights not only in identifying their roles for a specific physiological, cognitive or behavioral activity, but also to decipher their contribution in various enigmatic neurodegenerative diseases. To increase efficacy of stimulation and to prevent any askew effects on neighboring neural circuits, neural probes were implanted inside the volumetric brain to reach the target site thus localizing the effect and the spatiotemporal resolution was further improved by targeting key neural circuits for viral expression of light-sensitive opsins[30], [53], [54] for optogenetics and controlling volume[55], flow rates[56] and miniaturizing outlets for pharmacology. Multimodal optofluidic probes allow integrated access to the target region without the need for multiple surgeries thus reducing brain tissue damage as well as enabling hassle-free combinatorial stimulations. To improve chronic biocompatibility of these implants, they must be minimally invasive[57], [58] to limit tissue scarring and mechanically compliant[59]–[62] to reduce deleterious effects of tissue micromotions as well as achieve minimal inflammation, neuronal loss and glial scarring which otherwise can adversely affect the functionality of the implant.

1.3.2 Previously reported Optofluidic tools

Recent advances towards chronic drug delivery in the deep brain involved miniaturization (~200 μm diameter) of thermally drawn polymer based [63], [64] (E ~ 2.3 GPa) and stainless steel based [65] (~200 GPa) multifunctional probes, but the mechanical mismatch with the soft brain tissue (~ few kPa) and their requirement for multiple external bulky[63], [64] or wirelessly activated[65] tethered sources and fixtures for multimodal modulations limited their chronic biocompatible nature and versatility for animal mobility respectively for real-time *in vivo* experiments. To acquire chronic and reliable data from *in vivo* studies, a new wireless class of completely standalone and lightweight (0.22 – 0.186 g) systems [52], [66], [67] was created based on ultrathin (80 μm thick) and soft (E ~ 1 MPa) optofluidic probes, so as not to affect the behavior in freely moving animals[68] which was made possible through advances in material science[49], [69] integrating with wireless technologies[70]–[72]. Although chronic optogenetic operation can be enabled by rechargeable batteries[52], [66] or wireless power transfer[67], one of the major challenges for chronic wireless standalone optofluidic systems is the need to continuously replenish its limited drug supply. Also, previously reported wireless techniques were handicapped due to their limited range, directionality as well as their limited scalability for target selectivity within a large group.

1.4 Novel Class of Wireless Optofluidic Devices (wOF)

Here we introduce two classes of novel wOF neural devices that solve a set of unique problems for untethered optofluidic studies in freely moving animals.

1.4.1 The Lego Optofluidic device (chronic drug supply)

This unique first-of-its-kind device provides – i) repeated long term drug supply through its “replaceable Lego drug cartridge” technology ii) biocompatible deep brain multimodal access due

to the minimal invasiveness of its mechanically soft optofluidic probes and iii) easy-to-use smartphone app-controlled wireless Bluetooth Low Energy (BLE) system that allows long wireless range (~100m), isotropic wireless access, no Line of Sight (LOS) handicap, Over The Air (OTA) updates, high target specificity and scalable closed loop systems within a large group as well as intuitive control through an easy to use app on any commercial handheld smartphone. The critical need for chronic drug delivery in a standalone wireless optofluidic neural implant is achieved by repeated hermetic Lego assembly and disassembly processes (optimized by characterizing the forces to find the minimum force required to achieve hermetic sealing) between a replaceable drug cartridge and an optofluidic probe that needs to be surgically implanted only once. Successful in-vivo studies in mice demonstrate their innate capability for programmable and chronic wireless pharmacology and optogenetics.

The interdisciplinary nature of the work is clearly reflected in three significant accomplishments:

1. The invention of completely self-contained, wireless optofluidic neural device platform with replaceable drug cartridges, which is capable of long-term, unlimited and concurrent fluid delivery and photostimulation in the deep brain tissue of freely behaving animals. The results allow for combinatorial “chronic” *in vivo* pharmacological and optogenetic approaches with a high degree of spatial resolution and limited disruption to sensitive neural tissues.
2. Development of a user-friendly smartphone Bluetooth-based wireless control module. The result allows for scalable and highly selective behavioral experiments, both in choosing a specific animal within a large group as well as configuring stimulation modalities and/or parameters within each animal through an ‘easy-to-use’ smartphone app.
3. Demonstration of *in vivo* applications of this technology for wireless pharmacology and optogenetics in freely moving animals in complex environmental contexts. The results reveal proof-of-principle findings in neuroscience and create many opportunities for future work involving *in vivo* optopharmacology, wireless optogenetics and related behavioral sciences.

The results open up many opportunities for basic research in biological sciences especially within the neuroscience community, with promising potential pathways to translation into clinically relevant technologies.

1.4.2 The Fully Implantable Optofluidic system (Applicable to any part of the body)

This device offers a miniaturized ultrathin, soft wireless optofluidic system with stretchable radiofrequency (RF) antenna for wireless power transfer. This not only eliminates the need for large batteries making the device 92% smaller and 88% lighter when compared to latest wireless optofluidic systems but also enables the device to be used conformally in various space critical locations of the body. To ensure its functionality, the sensitivity of output characteristics to transmitted RF power were analyzed – optical intensity for μ-ILEDs and temperature profile for thermal drug actuator. Also, temporal profiles for drug release and antenna gain for energy harvesting were studied. Furthermore, the effect of mechanical deformation (20%) of the soft stretchable antenna on the output characteristics was analyzed through Finite Element Analysis (FEA) to ensure reliable operation even during conformal integration to curvilinear tissue surfaces. Lastly, the device functionality and implantable nature were tested in model mice and live mice respectively.

1.5 Outline

In this dissertation, the two main classes of wireless optofluidic systems (wOF) are discussed in detail, each of which helps solve a critical issue faced by neuroscientists during *in vivo* optogenetic and pharmacological studies in freely moving animals.

1.5.1 Chapter 1

Chapter 1 highlights the background for this research and the development of previously tools and techniques explored by neuroscientists to study the brain.

1.5.2 Chapter 2

In Chapter 2, the Lego optofluidic device is introduced. It exploits advances in materials science, device engineering, wireless systems, and mechanical/thermal/fluidic designs and analysis to develop a class of soft, optofluidic neural device with replaceable drug cartridges that enables wireless chronic drug supply and optical manipulation in deep brain tissue of freely behaving animals. Our ‘plug-n-play’ replaceable Lego-like drug cartridge offers an unlimited repetition of untethered drug deliveries to the target region of the brain, overcoming the critical limitations of current wireless drug delivery technologies for ‘chronic’ *in vivo* pharmacology. Combined with a soft, ultrathin neural probe integrating microfluidic channels with microscale-scale light-emitting diodes, the standalone neural device enables co-localization of fluids and photons at precisely the same cells for *in vivo* dissection of neural circuitry. Bluetooth wireless control of drug delivery and photostimulation enables intractable neuroscience experiments in freely behaving animals. The smartphone-controlled Bluetooth module allows versatile and highly selective control as well as scalable closed-loop manipulation of specific target animals within a large group. This technology is a significant, qualitative advance over current cannula-based and other wireless approaches because it enables simple control of fluid delivery and photostimulation, accessible to nearly any biologist, with smartphone-based wireless, untethered functionality suitable for use in any environment.

1.5.3 Chapter 3

In Chapter 3, the fully implantable, battery-free optofluidic device with stretchable radiofrequency (RF) antenna is detailed. This device remotely harnesses wireless energy (Noh et al., 2018) to power its multimodal outputs (light and fluids). The exclusion of battery not only minimizes the device bulk (220mg; 125 mm^3) but also facilitates its integration within various space critical peripheries inside the body. The fully implantable, battery-less optofluidic system comprises of a micropump and microscale inorganic light emitting diodes (μ-ILEDs) integrated with soft, flexible optofluidic channels for drug and light delivery respectively and a stretchable RF antenna which harvests power through capacitive coupling. The serpentine dimensions of antenna traces are optimized for both flexibility to conformally accommodate on any curvilinear surface inside the body as well as selectivity to allow independently controlled, non-overlapping resonant channels (1.8GHz for drug; 2.9GHz for light). The device worked reliably irrespective of angular or mechanical variations (~20% strain). Its proof-of-concept experiment in mice highlights its unique potential for *in vivo* opto-pharmacology. The number of antenna channels is scalable, thus opening novel avenues for conducting versatile, multimodal opto-pharmacological experiments in freely moving animals.

1.5.4 Chapter 4

In Chapter 4, we mention all the associated fabrication, assembly and programming steps required to reproduce these wireless optofluidic devices.

1.5.5 Chapter 5

In Chapter 5, we discuss possible future directions and challenges to advance this technology further.

1.6 Declarations

- Parts of this thesis have been published in the following journal articles:

    - **Raza Qazi**, Choong Yeon Kim, Sanghyuk Byun, and Jae-Woong Jeong. "Microscale Inorganic LED based Wireless Neural Systems for Chronic *In Vivo* Optogenetics." Frontiers in Neuroscience 12, 764 (2018).
      (related to Chapter 1)

    - **Raza Qazi*, Adrian M. Gomez***, D.C. Castro, Z. Zou, J.Y. Sim, Y. Xiong, J. Abdo, C.Y. Kim, A. Anderson, F. Lohner, S.-H. Byun, B.C. Lee, K.-I. Jang, J. Xiao, M.R. Bruchas and J.-W. Jeong. “Chronic, Smartphone-Enabled Wireless In-Vivo Neuropharmacology and Optogenetics”, Nature Biomedical Engineering (2019). (***In Press***)
      (related to Chapter 2 and 4)

    - **Kyung Nim Noh*, Sung Il Park*, Raza Qazi***, Zhanan Zou, Aaron D. Mickle, Jose G. Grajales-Reyes, Kyung-In Jang, Robert W. Gereau IV, Jianliang Xiao, John A. Rogers* and Jae-Woong Jeong "Miniaturized, battery-free optofluidic systems with potential for wireless pharmacology and optogenetics", Small (2017). Featured on Front Cover.
      (related to Chapter 3 and 4)

      (* = Co-first Authors)

- All animal studies were approved by the Animal Care and Use Committee of Washington University and conformed to US National Institutes of Health guidelines.

1.7 References

[1] E. R. Kandel *et al.*, *Principles of neural science*, vol. 4. McGraw-hill New York, 2000.

[2] G. J. Morton, D. E. Cummings, D. G. Baskin, G. S. Barsh, and M. W. Schwartz, “Central nervous system control of food intake and body weight,” *Nature*, vol. 443, no. 7109, pp. 289–295, Sep. 2006.

[3] J. C. Brüning *et al.*, “Role of Brain Insulin Receptor in Control of Body Weight and Reproduction,” *Science*, vol. 289, no. 5487, pp. 2122–2125, Sep. 2000.

[4] M. A. Goodale and A. D. Milner, “Separate visual pathways for perception and action,” *Trends in Neurosciences*, vol. 15, no. 1, pp. 20–25, Jan. 1992.

[5] J. A. Neubauer, A. Simone, and N. H. Edelman, “Role of brain lactic acidosis in hypoxic depression of respiration,” *Journal of Applied Physiology*, vol. 65, no. 3, pp. 1324–1331, Sep. 1988.

[6] H. D. Critchley, P. Rotshtein, Y. Nagai, J. O’Doherty, C. J. Mathias, and R. J. Dolan, “Activity in the human brain predicting differential heart rate responses to emotional facial expressions,” *NeuroImage*, vol. 24, no. 3, pp. 751–762, Feb. 2005.

[7] E. A. Mayer, “Gut feelings: the emerging biology of gut–brain communication,” *Nature Reviews Neuroscience*, vol. 12, no. 8, pp. 453–466, Aug. 2011.

[8] R. Bastos, W. Abra˜o Saad, J. Vanderlei Menani, A. Renzi, J. Nogueira Silveira, and L. A. de Arruda Camargo, “Role of adrenergic pathways of the medial preoptic area in ANGII-induced water intake and renal excretion in rats,” *Brain Research*, vol. 636, no. 1, pp. 81–86, Feb. 1994.

[9] L. M. Garcia-Segura, J. A. Chowen, and F. Naftolin, “Endocrine Glia: Roles of Glial Cells in the Brain Actions of Steroid and Thyroid Hormones and in the Regulation of Hormone Secretion,” *Frontiers in Neuroendocrinology*, vol. 17, no. 2, pp. 180–211, Apr. 1996.

[10] R. I. Weiner and W. F. Ganong, “Role of brain monoamines and histamine in regulation of anterior pituitary secretion.,” *Physiological Reviews*, vol. 58, no. 4, pp. 905–976, Oct. 1978.

[11] B. D. Martino, D. Kumaran, B. Seymour, and R. J. Dolan, “Frames, Biases, and Rational Decision-Making in the Human Brain,” *Science*, vol. 313, no. 5787, pp. 684–687, Aug. 2006.

[12] G. Bush *et al.*, “Dorsal anterior cingulate cortex: A role in reward-based decision making,” *PNAS*, vol. 99, no. 1, pp. 523–528, Jan. 2002.

[13] K. Yamada, M. Mizuno, and T. Nabeshima, “Role for brain-derived neurotrophic factor in learning and memory,” *Life Sciences*, vol. 70, no. 7, pp. 735–744, Jan. 2002.

[14] T. Allison, A. Puce, and G. McCarthy, “Social perception from visual cues: role of the STS region,” *Trends in Cognitive Sciences*, vol. 4, no. 7, pp. 267–278, Jul. 2000.

[15] R. E. Clark and L. R. Squire, “Classical Conditioning and Brain Systems: The Role of Awareness,” *Science*, vol. 280, no. 5360, pp. 77–81, Apr. 1998.

[16] R. Adolphs, “Social cognition and the human brain,” *Trends in Cognitive Sciences*, vol. 3, no. 12, pp. 469–479, Dec. 1999.

[17] K. Hashimoto, E. Shimizu, and M. Iyo, “Critical role of brain-derived neurotrophic factor in mood disorders,” *Brain Research Reviews*, vol. 45, no. 2, pp. 104–114, May 2004.

[18] I. Liberzon *et al.*, “Brain activation in PTSD in response to trauma-related stimuli,” *Biological Psychiatry*, vol. 45, no. 7, pp. 817–826, Apr. 1999.

[19] S. Feldman, N. Conforti, and J. Weidenfeld, “Limbic pathways and hypothalamic neurotransmitters mediating adrenocortical responses to neural stimuli,” *Neuroscience & Biobehavioral Reviews*, vol. 19, no. 2, pp. 235–240, Jun. 1995.

[20] B. S. McEwen and P. J. Gianaros, “Central role of the brain in stress and adaptation: Links to socioeconomic status, health, and disease,” *Annals of the New York Academy of Sciences*, vol. 1186, no. 1, pp. 190–222, 2010.

[21] C. Zuccato and E. Cattaneo, “Role of brain-derived neurotrophic factor in Huntington’s disease,” *Progress in Neurobiology*, vol. 81, no. 5, pp. 294–330, Apr. 2007.
[22] Pei Chin Tang, “Brain stem control of respiratory depth and rate in the cat ,2,” *Respiration Physiology*, vol. 3, no. 3, pp. 349–366, Dec. 1967.
[23] D. P. Brooks, L. Share, and J. T. Crofton, “Role of Brain Prostaglandins in the Control of Vasopressin Secretion in the Conscious Rat,” *Endocrinology*, vol. 118, no. 4, pp. 1716–1722, Apr. 1986.
[24] R. Chen, A. Canales, and P. Anikeeva, “Neural recording and modulation technologies,” *Nature Reviews Materials*, vol. 2, no. 2, p. 16093, Feb. 2017.
[25] J. M. Kerns, A. J. Fakhouri, H. P. Weinrib, and J. A. Freeman, “Electrical stimulation of nerve regeneration in the rat: The early effects evaluated by a vibrating probe and electron microscopy,” *Neuroscience*, vol. 40, no. 1, pp. 93–107, Jan. 1991.
[26] M. S. Humayun, E. de Juan, G. Dagnelie, R. J. Greenberg, R. H. Propst, and D. H. Phillips, “Visual Perception Elicited by Electrical Stimulation of Retina in Blind Humans,” *Arch Ophthalmol*, vol. 114, no. 1, pp. 40–46, Jan. 1996.
[27] S. C. Núñez, A. S. Garcez, S. S. Suzuki, and M. S. Ribeiro, “Management of Mouth Opening in Patients with Temporomandibular Disorders through Low-Level Laser Therapy and Transcutaneous Electrical Neural Stimulation,” *Photomedicine and Laser Surgery*, vol. 24, no. 1, pp. 45–49, Feb. 2006.
[28] P. D. MacLean and J. R. Delgado, “Electrical and chemical stimulation of frontotemporal portion of limbic system in the waking animal,” *Electroencephalography and Clinical Neurophysiology*, vol. 5, no. 1, pp. 91–100, Feb. 1953.
[29] T. L. Rose and L. S. Robblee, “Electrical stimulation with Pt electrodes. VIII. Electrochemically safe charge injection limits with 0.2 ms pulses (neuronal application),” *IEEE Transactions on Biomedical Engineering*, vol. 37, no. 11, pp. 1118–1120, Nov. 1990.
[30] E. S. Boyden, F. Zhang, E. Bamberg, G. Nagel, and K. Deisseroth, “Millisecond-timescale, genetically targeted optical control of neural activity,” *Nature Neuroscience*, vol. 8, no. 9, p. nn1525, Aug. 2005.
[31] R. Guduru *et al.*, “Magnetoelectric ‘spin’ on stimulating the brain,” *Nanomedicine*, vol. 10, no. 13, pp. 2051–2061, May 2015.
[32] R. Chen, G. Romero, M. G. Christiansen, A. Mohr, and P. Anikeeva, “Wireless magnetothermal deep brain stimulation,” *Science*, vol. 347, no. 6229, pp. 1477–1480, Mar. 2015.
[33] K. Eom *et al.*, “Enhanced Infrared Neural Stimulation using Localized Surface Plasmon Resonance of Gold Nanorods,” *Small*, vol. 10, no. 19, pp. 3853–3857, 2014.
[34] J. D. Wells, C. Kao, E. D. Jansen, P. E. Konrad, and A. Mahadevan-Jansen, “Application of infrared light for in vivo neural stimulation,” *JBO*, vol. 10, no. 6, p. 064003, Nov. 2005.
[35] M. Chernov and A. W. Roe, “Infrared neural stimulation: a new stimulation tool for central nervous system applications,” *NPh*, vol. 1, no. 1, p. 011011, Aug. 2014.
[36] “Transcranial focused ultrasound modulates the activity of primary somatosensory cortex in humans | Nature Neuroscience.” [Online]. Available: https://www.nature.com/articles/nn.3620. [Accessed: 13-Apr-2018].
[37] L. R. Gavrilov, E. M. Tsirulnikov, and I. ab I. Davies, “Application of focused ultrasound for the stimulation of neural structures,” *Ultrasound in Medicine and Biology*, vol. 22, no. 2, pp. 179–192, Jan. 1996.
[38] M. D. Menz, Ö. Oralkan, P. T. Khuri-Yakub, and S. A. Baccus, “Precise Neural Stimulation in the Retina Using Focused Ultrasound,” *J. Neurosci.*, vol. 33, no. 10, pp. 4550–4560, Mar. 2013.
[39] B. Franklin, “An Account of the Effects of Electricity in Paralytic Cases. In a Letter to John Pringle, M. D. F. R. S. from Benjamin Franklin, Esq; F. R. S.,” *Philosophical Transactions (1683-1775)*, vol. 50, pp. 481–483, 1757.

[40] B. L. Roth, “DREADDs for Neuroscientists,” *Neuron*, vol. 89, no. 4, pp. 683–694, Feb. 2016.
[41] J. G. Bernstein and E. S. Boyden, “Optogenetic tools for analyzing the neural circuits of behavior,” *Trends in Cognitive Sciences*, vol. 15, no. 12, pp. 592–600, Dec. 2011.
[42] J. G. Bernstein, P. A. Garrity, and E. S. Boyden, “Optogenetics and thermogenetics: technologies for controlling the activity of targeted cells within intact neural circuits,” *Current Opinion in Neurobiology*, vol. 22, no. 1, pp. 61–71, Feb. 2012.
[43] A. Guru, R. J. Post, Y.-Y. Ho, and M. R. Warden, “Making Sense of Optogenetics,” *Int J Neuropsychopharmacol*, vol. 18, no. 11, Oct. 2015.
[44] L. Grosenick, J. H. Marshel, and K. Deisseroth, “Closed-Loop and Activity-Guided Optogenetic Control,” *Neuron*, vol. 86, no. 1, pp. 106–139, Apr. 2015.
[45] T. Kim *et al.*, “Injectable, Cellular-Scale Optoelectronics with Applications for Wireless Optogenetics,” *Science*, vol. 340, no. 6129, pp. 211–216, Apr. 2013.
[46] G. Shin *et al.*, “Flexible Near-Field Wireless Optoelectronics as Subdermal Implants for Broad Applications in Optogenetics,” *Neuron*, vol. 93, no. 3, pp. 509-521.e3, Feb. 2017.
[47] R. Qazi, C. Y. Kim, S.-H. Byun, and J.-W. Jeong, “Microscale Inorganic LED Based Wireless Neural Systems for Chronic in vivo Optogenetics,” *Front. Neurosci.*, vol. 12, 2018.
[48] S. I. Park *et al.*, “Stretchable multichannel antennas in soft wireless optoelectronic implants for optogenetics,” *Proceedings of the National Academy of Sciences*, p. 201611769, 2016.
[49] J. G. McCall *et al.*, “Fabrication and application of flexible, multimodal light-emitting devices for wireless optogenetics,” *Nature Protocols*, vol. 8, no. 12, pp. 2413–2428, Nov. 2013.
[50] R. Delmdahl, R. Pätzel, and J. Brune, “Large-Area Laser-Lift-Off Processing in Microelectronics,” *Physics Procedia*, vol. 41, pp. 241–248, Jan. 2013.
[51] M. Schwaerzle, O. Paul, and P. Ruther, “Compact silicon-based optrode with integrated laser diode chips, SU-8 waveguides and platinum electrodes for optogenetic applications,” *J. Micromech. Microeng.*, vol. 27, no. 6, p. 065004, 2017.
[52] J.-W. Jeong *et al.*, “Wireless Optofluidic Systems for Programmable In Vivo Pharmacology and Optogenetics,” *Cell*, vol. 162, no. 3, pp. 662–674, Jul. 2015.
[53] F. Zhang, A. M. Aravanis, A. Adamantidis, L. de Lecea, and K. Deisseroth, “Circuit-breakers: optical technologies for probing neural signals and systems,” *Nature Reviews Neuroscience*, vol. 8, no. 8, p. nrn2192, Aug. 2007.
[54] K. M. Tye and K. Deisseroth, “Optogenetic investigation of neural circuits underlying brain disease in animal models,” *Nature Reviews Neuroscience*, vol. 13, no. 4, p. nrn3171, Mar. 2012.
[55] M. A. Parada, M. Puig de Parada, and B. G. Hoebel, “A new triple-channel swivel for fluid delivery in the range of intracranial (10 nl) and intravenous (100 µl) self-administration volumes and also suitable for microdialysis,” *Journal of Neuroscience Methods*, vol. 54, no. 1, pp. 1–8, Sep. 1994.
[56] H. J. Lee *et al.*, “A new thin silicon microneedle with an embedded microchannel for deep brain drug infusion,” *Sensors and Actuators B: Chemical*, vol. 209, pp. 413–422, Mar. 2015.
[57] Zhang Wenguang, Ma Yakun, and Li Zhengwei, “Experimental evaluation of neural probe’s insertion induced injury based on digital image correlation method,” *Medical Physics*, vol. 43, no. 1, pp. 505–512, Jan. 2016.
[58] T. D. Y. Kozai *et al.*, “Ultrasmall implantable composite microelectrodes with bioactive surfaces for chronic neural interfaces,” *Nat Mater*, vol. 11, no. 12, pp. 1065–1073, Dec. 2012.
[59] A. Sridharan, J. K. Nguyen, J. R. Capadona, and J. Muthuswamy, “Compliant intracortical implants reduce strains and strain rates in brain tissue in vivo,” *J. Neural Eng.*, vol. 12, no. 3, p. 036002, 2015.

[60] J. K. Nguyen *et al.*, “Mechanically-compliant intracortical implants reduce the neuroinflammatory response,” *J. Neural Eng.*, vol. 11, no. 5, p. 056014, 2014.
[61] G. Lind, C. E. Linsmeier, and J. Schouenborg, “The density difference between tissue and neural probes is a key factor for glial scarring,” *Scientific Reports*, vol. 3, p. 2942, Oct. 2013.
[62] J.-W. Jeong, G. Shin, S. I. Park, K. J. Yu, L. Xu, and J. A. Rogers, “Soft Materials in Neuroengineering for Hard Problems in Neuroscience,” *Neuron*, vol. 86, no. 1, pp. 175–186, Apr. 2015.
[63] A. Canales *et al.*, “Multifunctional fibers for simultaneous optical, electrical and chemical interrogation of neural circuits *in vivo*,” *Nature Biotechnology*, vol. 33, no. 3, pp. 277–284, Mar. 2015.
[64] S. Park *et al.*, “One-step optogenetics with multifunctional flexible polymer fibers,” *Nature Neuroscience*, vol. 20, no. 4, pp. 612–619, Apr. 2017.
[65] C. Dagdeviren *et al.*, “Miniaturized neural system for chronic, local intracerebral drug delivery,” *Science Translational Medicine*, vol. 10, no. 425, p. eaan2742, Jan. 2018.
[66] J. G. McCall *et al.*, “Preparation and implementation of optofluidic neural probes for in vivo wireless pharmacology and optogenetics,” *Nat. Protocols*, vol. 12, no. 2, pp. 219–237, Feb. 2017.
[67] K. N. Noh *et al.*, “Miniaturized, Battery-Free Optofluidic Systems with Potential for Wireless Pharmacology and Optogenetics,” *Small*, vol. 14, no. 4, p. 1702479, Jan. 2018.
[68] B. A. Copits, M. Y. Pullen, and R. W. Gereau, “Spotlight on pain: optogenetic approaches for interrogating somatosensory circuits,” *Pain*, vol. 157, no. 11, pp. 2424–2433, Nov. 2016.
[69] T. Kim *et al.*, “Injectable, cellular-scale optoelectronics with applications for wireless optogenetics,” *Science*, vol. 340, no. 6129, pp. 211–216, Apr. 2013.
[70] S. I. Park *et al.*, “Soft, stretchable, fully implantable miniaturized optoelectronic systems for wireless optogenetics,” *Nature Biotechnology*, vol. 33, no. 12, pp. 1280–1286, Nov. 2015.
[71] K. L. Montgomery *et al.*, “Wirelessly powered, fully internal optogenetics for brain, spinal and peripheral circuits in mice,” *Nature Methods*, vol. 12, no. 10, pp. 969–974, Aug. 2015.
[72] G. Shin *et al.*, “Flexible Near-Field Wireless Optoelectronics as Subdermal Implants for Broad Applications in Optogenetics,” *Neuron*, vol. 93, no. 3, pp. 509-521.e3, Feb. 2017.

2 Chronic, Smartphone Controlled Lego Optofluidic Device

Chronic wireless *in vivo* pharmacology and optogenetics can provide innovative approaches for decoding neural circuitry as well as opening therapeutic strategies for brain disorders. However, current neural interface platforms are limited by their inability for prolonged delivery of multiple distinct drugs, bulky and customized control systems with limited target selectivity, and lack of multi-functionality, thereby restricting advanced experimental settings and long-term studies in awake, behaving animals. Here we present a smartphone-controlled, soft optofluidic neural implant with replaceable Lego™-like drug cartridges that can replenish drug supply for multiple, chronic pharmacological studies. This class of wireless devices provides chronic, minimally invasive, programmable versatility for sustained wireless drug delivery and photostimulation with spatiotemporal resolution for selective manipulation of brain circuits. These standalone wireless devices exhibit potential for uncovering the basis for neuropsychiatric diseases as well as for translational studies due to their capability to deliver both drugs and photo-pharmacology into the brain repeatedly over long periods of time.

2.1 Introduction

In vivo pharmacological manipulation of brain circuits remain one of the most extensively used and important methods for large scale dissection of brain circuit function. Local *in vivo* pharmacology can render pivotal insights not only to identify roles of distinct cell types for a specific physiological, cognitive or behavioral activity; but also, to decipher and treat various neurodegenerative diseases. In addition, local infusion of drugs over time into brain structures offers a reliable, high throughput means for developing and testing neuropharmacological compounds that can impact brain function. Recent efforts in cell-type selective control of neural circuits with optogenetics have uncovered more specificity in the identification of translationally viable brain targets. Combinatorial use of pharmacology and optogenetics can provide specific and versatile control of neuronal populations and cells[1]–[3], opening opportunities for neuroscience and clinical medicine; however, combining local pharmacology and optogenetics with spatiotemporal control using wireless methods has proven to be an arduous undertaking.

Conventionally, drug infusions use implanted metal cannulas connected to an external fluid pumping system to locally deliver pharmacological agents. However, chronic regional drug delivery and its advanced applications combined with optogenetics are significantly limited due to the use of these rigid cannulas, which can cause prolonged brain tissue damage and inflammation, and also their tethered operation restricts the animals' natural movement[4], [5]. For these reasons, there has been an unmet need for combining advances in materials engineering, microfluidics, optoelectronics, and wireless control to pharmacologically and optically engage neuronal function in freely moving animals alongside a chronic, stable biocompatible platform. Recent research and development have permitted miniaturized, flexible multifunctional fibers integrating fluidic channels and optical waveguides to mitigate neural tissue damage as well as to realize the full potential of combined optogenetics and pharmacology[6], [7]. However, these fibers still require tethered operation due to the need for multiple connections with external

hardware for each modality, thus not only causing angular stress but also hindering real-time *in vivo* manipulation of freely moving animals in their natural environments.

To enable non-tethered neuromodulation, researchers have developed standalone neural implants using various wireless technologies (e.g. infrared (IR)[8]–[11] or radiofrequency (RF)[12]–[24]), however these wireless technologies are limited due to their short operation range, Line-of-Sight (LoS) handicaps, susceptibility to orientations and angle, requirement of special and/or bulky electronic systems, as well as limited target selectivity within a large group of animals. Additionally, current wireless platforms limit researchers in their ability to conduct multi-animal testing with a different experimental treatment for each animal in a single behavioral session. More importantly, achieving chronic *in vivo* pharmacology in awake, behaving animals is hindered by challenges to provide repeated drug delivery over an extensive timeframe using a standalone wireless neural implant[8], [9], [14].

Here we introduce smartphone-controlled, wireless soft “Lego” optofluidic neural implants to enable “chronic” *in vivo* neuropharmacology together with optogenetic control schemes. This self-contained platform overcomes the key limitations of current state-of-the-art technologies by integrating: 1) Lego^{TM}-like replaceable drug cartridges that can replenish drug supply with simple plug-and-play, 2) an ultrathin and soft multimodal probe that can independently deliver four distinct drugs and two different wavelengths of light to targeted areas of the deep brain, and 3) a smartphone-controlled, Bluetooth Low Energy (BLE) wireless module that features long-range coverage (10–100 m), omnidirectional access, no LoS handicap, the capability for specific target selectivity, and scalable closed-loop control features. This user-friendly, the chronically stable design enables long-term neural circuit studies by allowing for repeated, intact, pharmacological and optogenetic access to the same region with only one surgery. Our studies presented here demonstrate the innate capabilities of these Lego^{TM}-like optofluidic devices for chronic wireless *in vivo* pharmacology and optogenetics.

2.2 Design Structure and Working Principle

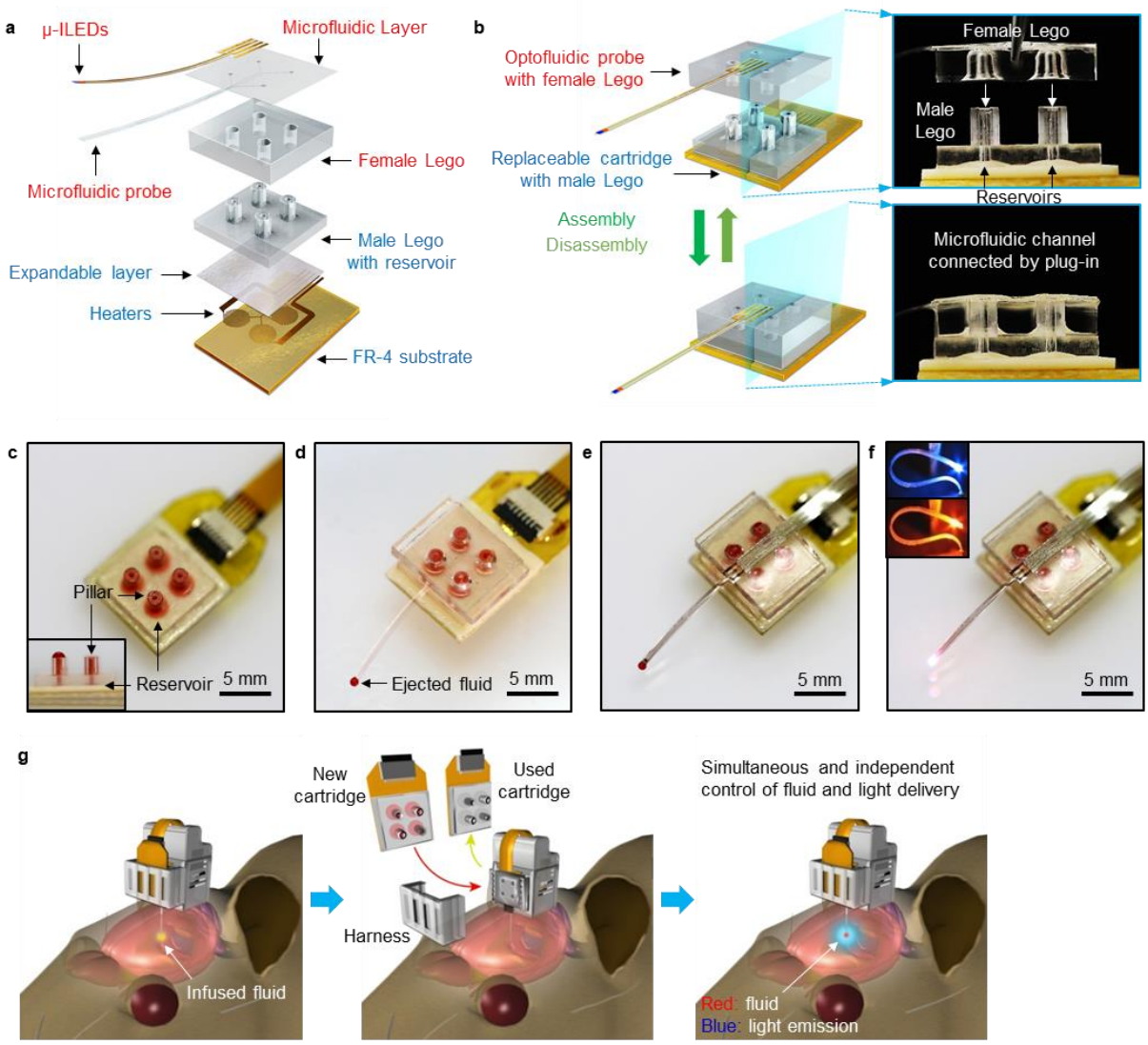

Figure 2.10 – Design and operation principles of soft optofluidic probe system with replaceable Lego drug cartridges. (a) *Exploded view schematic diagram of a Lego optofluidic neural probe system, consisting of μ-ILEDs, a soft microfluidic probe with a female Lego adapter, a male Lego integrated with four drug reservoirs, a thermally expandable layer, and micro-heaters as thermally actuated pumps.* ***(b)*** *Concept of Lego microfluidic assembly and disassembly between a female Lego optofluidic probe and a male Lego replaceable drug cartridge that can provide long-term, repeated drug delivery (left) and their respective cross-sectional optical images highlighting the 'plug-in' interaction at the Lego interface (right).* ***(c–f)*** *Optical images that illustrate device assembly.* ***(c)*** *A male Lego replaceable cartridge loaded with red fluid. The inset shows a side view of the replaceable cartridge after activating one of its chambers with a smartphone, showing ejected fluid at the tip of a male Lego pillar.* ***(d)*** *A female Lego microfluidic probe plugged into the male Lego replaceable cartridge for microfluidic assembly.* ***(e)*** *An optofluidic probe system consisting of a microfluidic probe integrated with μ-ILEDs for simultaneous fluid delivery and photostimulation.* ***(f)*** *An optofluidic probe system demonstrating its capability for simultaneous and independent control of blue and orange μ-ILEDs. The insets highlight the flexible nature of the optofluidic probe that can provide selective, independent control of μ-ILEDs.* ***(g)*** *Schematic illustration of a concept of*

chronic wireless pharmacology and optogenetics using an optofluidic device with replaceable drug cartridges. After delivering fluids (left), the used drug cartridge can be replaced with a new one via Lego disassembly and assembly (middle) for repeated fluid delivery (right). This replaceable cartridge enables chronic delivery of distinct or same fluid. Integrated with an optofluidic probe, the device offers simultaneous and independent control of fluid and light delivery for long-term neural intervention (right).

In **Figure 2.1a–b,** we present schematic diagrams and optical micrographs of the optofluidic probe system highlighting the "Lego™"-based replaceable drug cartridge architecture. This cartridge-based approach allows the unlimited on-demand supply of drug without the need for repeated disruptive surgeries or replacement of the entire neural implant. The various components of the Lego optofluidic system (**Fig. 2.1a**) can be grouped into two parts – a) the replaceable male Lego drug cartridge (blue, for chronic drug delivery) and b) the ultrathin, soft female Lego optofluidic probe (red, for chronic deep brain access). The male Lego drug cartridge consists of four individual fluid reservoirs (0.5 µL) each connected to a male Lego pillar (1.3 mm outer diameter (OD), 0.45 mm inner diameter (ID), 1.7 mm tall) and thermally-actuated pumps, which can push fluid out from the reservoirs via thermal expansion of the polymer composite layer (2:1 mixture of polydimethylsiloxane (PDMS) and expandable microspheres (Expancel 031 DU 40, AkzoNobel)) through Joule heating of micro-heaters. The reservoir uses cyclic olefin polymer (COP, Zeonor 1420R) as a structural material due to its low water vapor permeability (0.028 g·mm/m^2/day) and its inner walls have 7 µm-thick conformally coated Parylene C film (0.083 g·mm/m^2/day) to further minimize drug evaporation[25]. The female Lego optofluidic probe integrates a female Lego adapter (1.5 mm-thick PDMS layer with four 1.15 mm ID holes) connected to four separate microfluidic channels (each with 10 µm × 10 µm cross-section) of a microfluidic probe (50 µm-thick PDMS) with an optical layer composed of two independently controlled micro-scale inorganic light-emitting diodes (µ-ILEDs; blue (470 nm, TR2227, Cree Inc.) and orange (589 nm, TCE10-589, Three-Five Materials)) and thin metal interconnects (5 nm/250 nm of Cr/Au) on a 6 µm-thick polyethylene terephthalate (PET) film. The µ-ILEDs help in achieving chronic optogenetics[26] while as the Lego microfluidic assembly of the replaceable cartridges

enables repeated, chronic drug delivery. The male Lego component of the cartridge is plugged into the female Lego structure of the microfluidic probes such that each of the four vertical fluidic channels are self-aligned and connected to allow robust drug delivery through the microfluidic channels (**Fig. 2.1b**). Unlike prior wireless optofluidic devices where the lifespan of the device was limited to only 2 weeks post-surgery due to evaporation issues[8], [14], the detachable nature of the current device establishes long-term cartridge storage (-20°C) until right before an *in vivo* behavioral experiment. Illustration in **Figure 2.1c–f** presents plug-and-play operation of the optofluidic device. Upon activation of a thermally-actuated pump, the male Lego cartridge pushes the fluid out of a reservoir through its pillars (**Fig. 2.1c**). When assembled with a female Lego microfluidic (**Fig. 2.1d**) or an optofluidic probe (**Fig. 2.1e**), the same operation delivers fluid through the Lego interface into ultrathin, soft microfluidic channels. Integration of μ-ILEDs on the Lego optofluidic probe makes the device highly versatile, allowing multimodal access to targeted brain circuits (**Fig. 2.1e–f**). The ultrathin, soft and flexible probe (13-18 N/m in bending stiffness[8]) together with the conceptualization of replaceable drug cartridges facilitates minimally invasive and minimally disruptive chronic operation in awake, behaving animals. This design minimizes neural tissue damage with its biomechanical compatibility and offers a simple way to replenish drug supply on demand.

Figure 2.1g illustrates the concept of device operation with replaceable drug cartridges for chronic wireless *in vivo* pharmacology and optogenetics. After delivering fluid to the target site in the brain, the drug supply can be easily renewed by simply “plugging out” the male Lego cartridge from the implanted female Lego optofluidic probe and “plugging in” a new one (**Fig. 2.1g**, middle). The harness that securely holds the cartridge provides additional means to guarantee robust microfluidic assembly between the optofluidic probe part and the drug cartridges. With this replaceable cartridge concept, the drug reservoirs can be replaced as often as needed, while the soft implanted probe stays intact to provide independent or simultaneous delivery of multiple,

distinct drugs and different wavelengths of light (blue or orange) to the same brain region of interest (**Fig. 2.2**). This design makes the optofluidic probes reusable for unlimited, repeated drug delivery, and also minimizes brain tissue damage that would otherwise be worsened by multiple, disruptive surgeries required for implanting new devices.

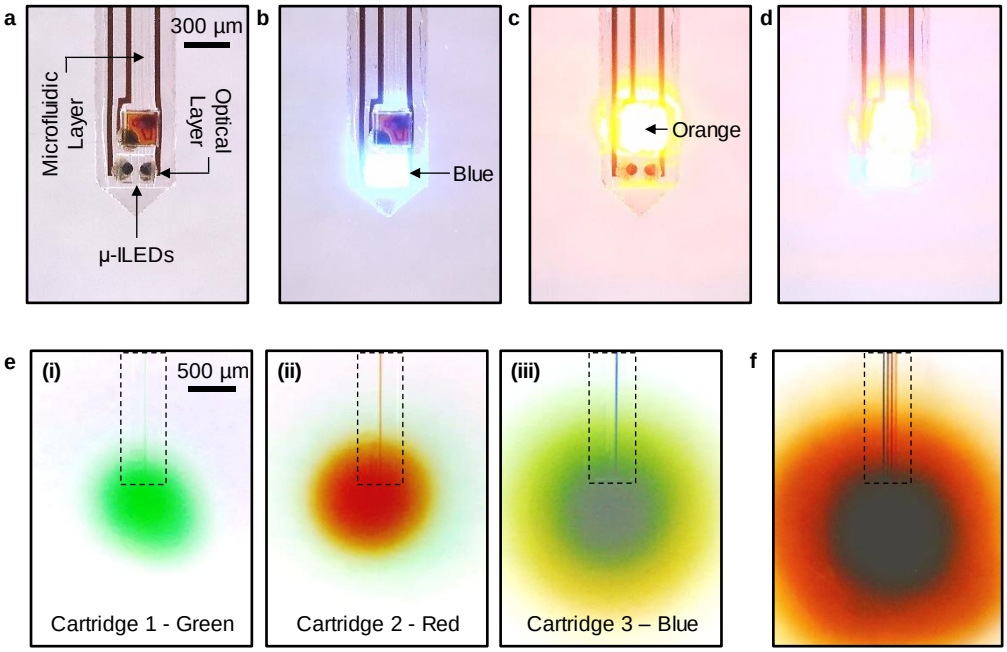

Figure 2.2 – Independently controlled multimodal output channels. (a-d) *Optical micrographs of an optofluidic probe highlighting independent and simultaneous control of blue and orange µ-ILEDs.* ***(a)*** *Micrographic image of an optofluidic probe showing its architecture.* ***(b–d)*** *Micrographs showing independent control of blue (470 nm) and orange (589 nm) µ-ILEDs (**b** and **c**, respectively) as well as their simultaneous triggering.* ***(e-f)*** *Optical images demonstrating delivery of fluid (aqueous solution with different color dyes) into brain phantom tissue (0.6% agarose gel) through microfluidic channels.* ***(e)*** *Sequential multiple fluid deliveries through the same microfluidic channel by using different replaceable drug cartridges (i.e. delivery of green, red, and blue delivery from cartridge 1, 2, and 3, respectively).* ***(f)*** *Separate delivery of multiple distinct fluids through four individual microfluidic channels.*

Additionally, its construction allows delivery of two or more distinct drugs simultaneously or with a high-precision temporal control (**Fig. 2.3**) for a customized, combinatorial *in vivo* pharmacology approach. **Figure 2.4a** shows the cross-sectional schematic diagram of a fully self-contained, wireless Lego optofluidic system, highlighting the four key components – (i) a male Lego replaceable drug cartridge, (ii) a female Lego optofluidic probe, (iii) a Bluetooth wireless control module, and (iv) two rechargeable lithium polymer batteries (**Fig. 2.4–2.5**). The

standalone wireless system assembled into a 3D printed case is small (1260 mm^3) and lightweight (~2 g; **Fig. 2.4b**), therefore does not obstruct animals' natural movement and behavior (**Fig. 2.6a** and **Fig. 2.7**). The proof-of-principle experiment with a brain phantom (0.6% agarose gel) and multiple fluid releases into solution (water) proves that the wireless Lego optofluidic system can make reliable, multiple deliveries of distinct or the same fluid with a simple replacement of drug cartridges (**Fig. 2.6b**). This attribute combined with programmability for fluid and LED control support the notion that the wireless Lego optofluidic system is useful for chronic, versatile neuroscience studies in freely behaving animals.

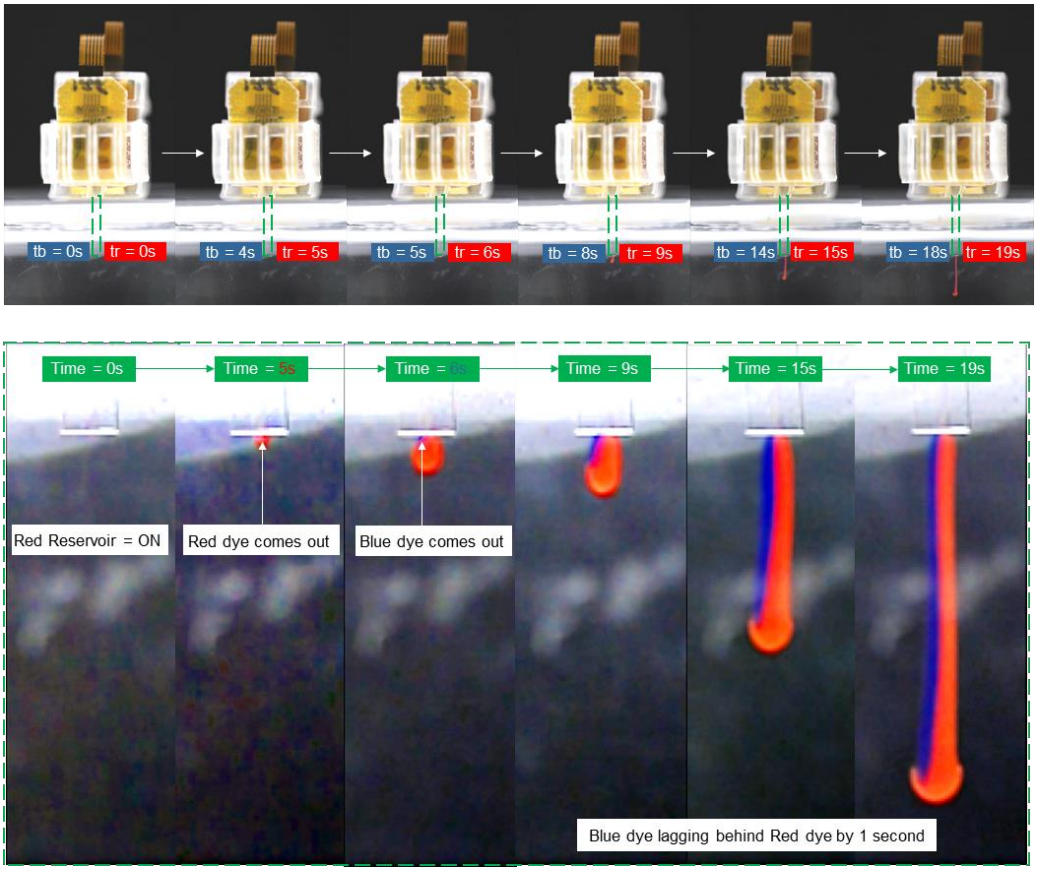

Figure 2.3 – Highly precise and customizable temporal control for simultaneous release of two distinct fluids with a pre-programmed delay. *A set of time-sequential optical images of the Lego device (and their corresponding zoomed snapshots below) during fluid delivery, highlighting controlled temporal delivery of two distinct dyes – red and blue dyes with one-second delay in between. The temporal delay can be easily altered from zero to hours through wireless reprogramming, while the sequence can be customized between four distinct fluids in a single cartridge.*

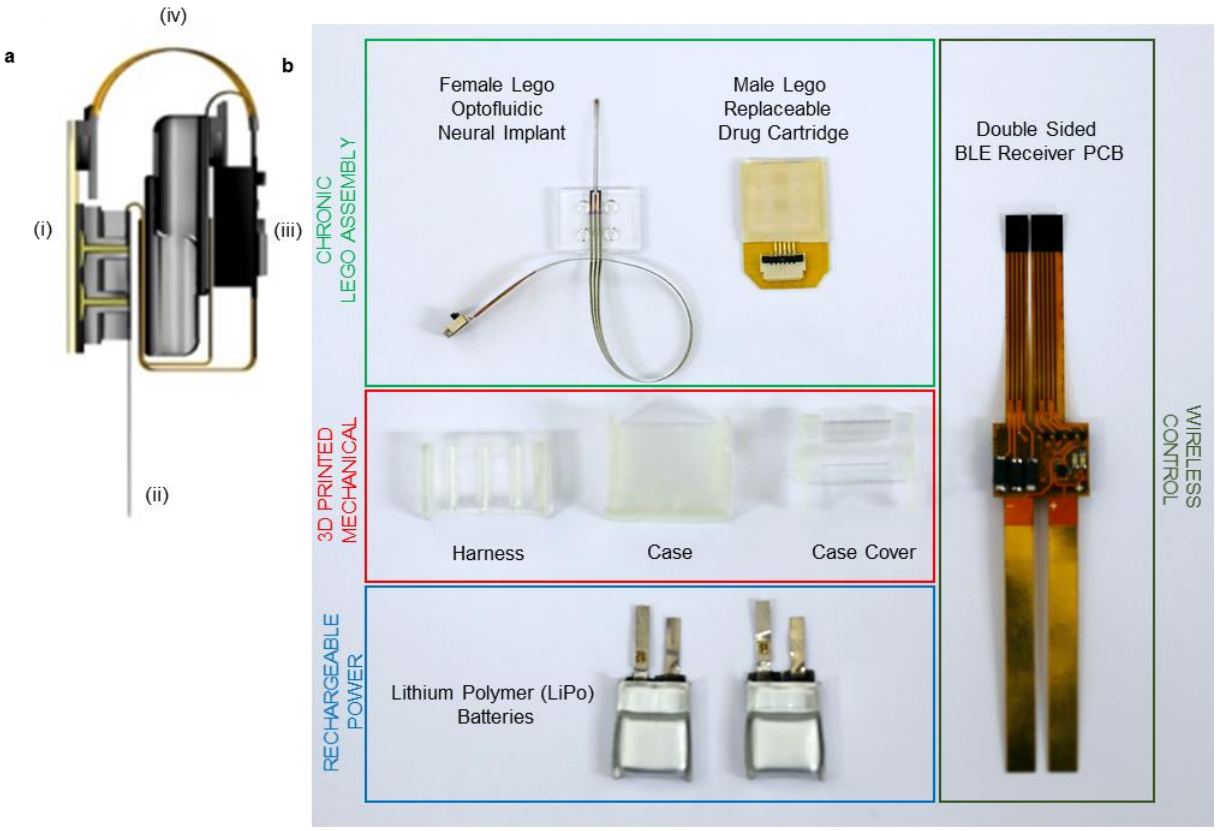

c

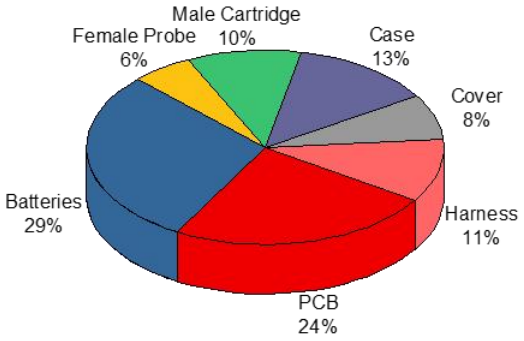

Part	Weight (g)
PCB	0.484
Batteries (x2)	0.590
Female Lego Optofluidic Implant	0.112
Male Lego Drug Cartridge	0.208
Case	0.260
Cover	0.153
Harness	0.213
Total	**2.020**

Figure 2.4 – Construct of a wireless Lego optofluidic system. (a) *A cross-sectional view of a Lego optofluidic system assembled with (i) a replaceable drug cartridge, (ii) ultrathin, soft optofluidic probe, (iii) Bluetooth wireless control module, and (iv) two rechargeable lithium polymer batteries. (i) Optical image of a freely moving mouse implanted with a wireless Lego optofluidic system.* ***(b)*** *An optical image showing various components of the system – that is, a female Lego optofluidic probe, a male Lego replaceable drug cartridge, two lithium polymer batteries, a wireless BLE module, a 3D printed device case, a harness that helps secure robust assembly of a male Lego drug cartridge with the female Lego, and a case cover to enclose the case opening from the top.* ***(c)*** *A table showing the weight breakdown of a wireless Lego optofluidic system (total weight 2.02 g).*

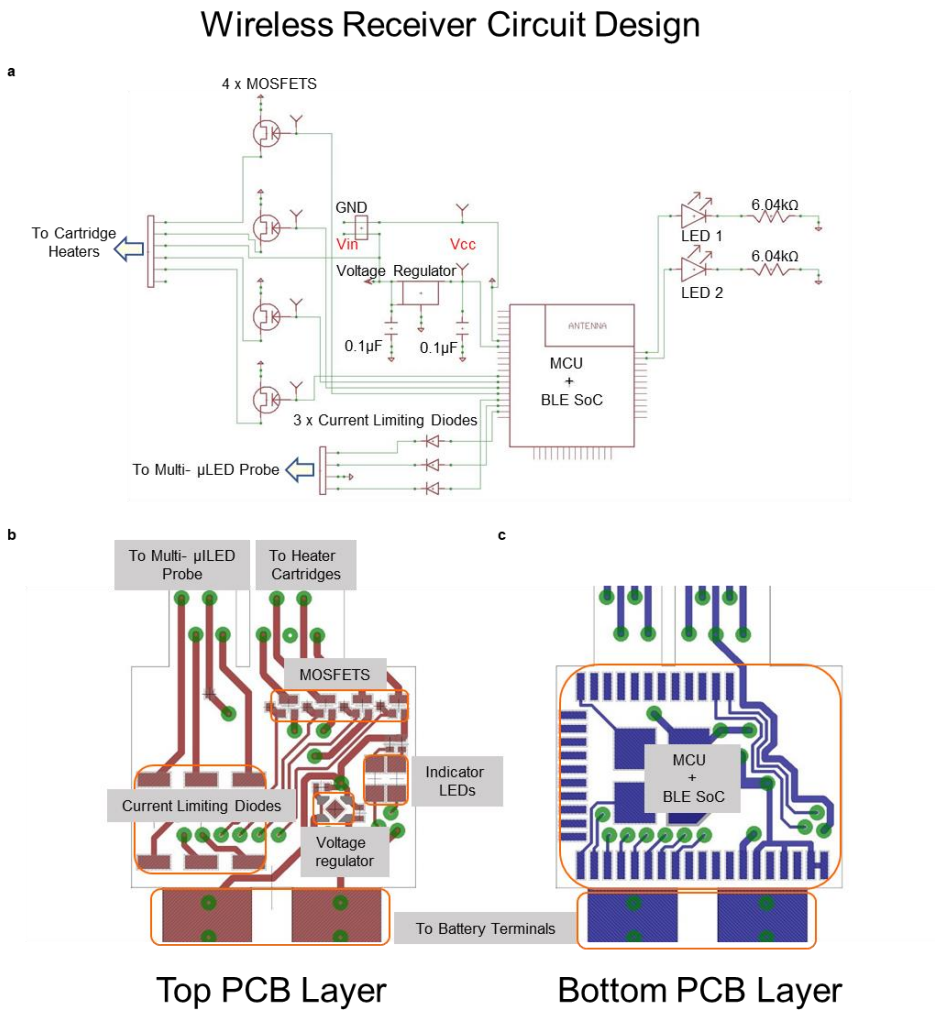

Figure 2.5 – Wireless receiver circuit design. (a) *A circuit diagram of a wireless BLE control module that controls Lego optofluidic systems.* ***(b–c)*** *PCB layout design of the diagram in* ***(a)****.* ***(b)*** *and* ***(c)*** *shows the top and bottom side of the PCB layout, respectively.*

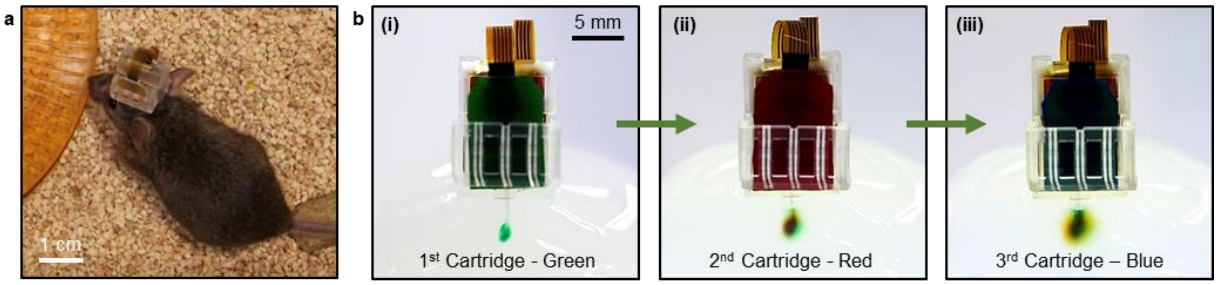

Figure 2.6 – Repeated fluid delivery demonstration using replaceable cartridges. (a) *Optical image of a freely moving mouse implanted with a wireless Lego optofluidic system.* ***(b)*** *A series of optical images showing multiple sequential wireless fluid delivery in a brain tissue phantom (0.6% agarose gel) using three different replaceable drug cartridges with green* ***(i)****, red* ***(ii)****, and blue* ***(iii)*** *dye aqueous solution.*

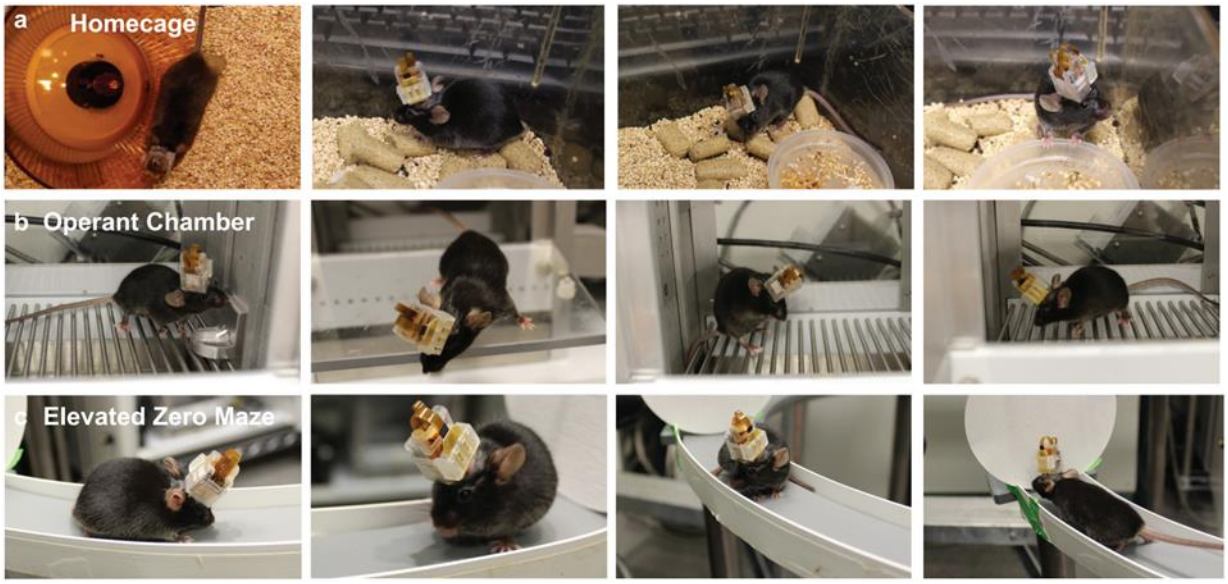

Figure 2.7 – Representative images of mice with optofluidic implants in various behavioral apparatuses highlighting "no effect" on animal's behavior due to the head mounted device. *Images of mice 2 weeks after device implantation within the* ***(a)*** *home cage (top row),* ***(b)*** *an operant conditioning chamber (middle row), and* ***(c)*** *an elevated zero maze (bottom row).*

2.3 Device Characterization and Analysis

2.3.1 Thermal Characteristics

The optofluidic system uses thermally actuated pumps for drug delivery. To study the spatiotemporal distribution of heat during drug actuation process, thermal imaging through an infrared camera (U5856A TrueIR Thermal Imager, Keysight Technologies) was performed at 8 frames per second at 320 × 240-pixel resolution with commercial software (TrueIR Analysis & Reporting Tool, Keysight). At 10 cm focal distance, the microheater (resistance ~125 Ω) was placed on a flat surface and actuated wirelessly through the custom BLE PCB after powering it with two serially connected power lithium polymer batteries.

Figure 2.8a illustrates the operational principle of the fluidic pumping. Upon receiving an activation signal (at t = 0 s) from the wireless transmitter (i.e. smartphone), an electrical current begins to flow through a heater (resistance ~125 Ω) resulting in a localized temperature increase

by Joule heating until the current stops after t = 20 s (**Fig. 2.8b**). When the temperature rises above the threshold of ~82°C[8], it leads to irreversible volume expansion of the polymer composite layer, thereby pumping out fluid from the reservoir through the hermetically sealed Lego interface into the microfluidic probe for ejection.

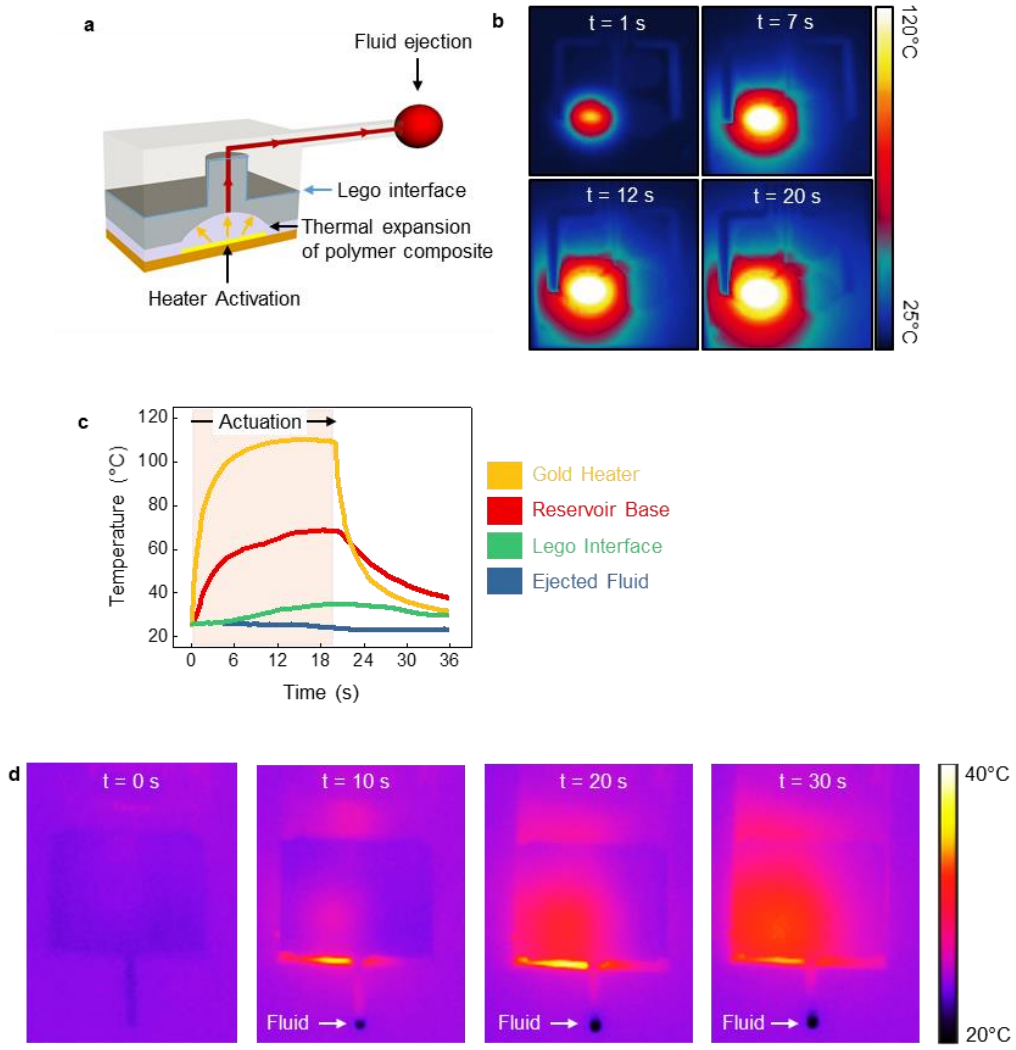

Figure 2.8 – Thermal Characteristics of the Lego Optofluidic Device. ***(a)*** *Schematic diagram illustrating the mechanism of fluid delivery using a thermally actuated pump. Joule heating of a micro-heater leads to thermal expansion of an expandable polymer composite into the fluid reservoir, thereby pushing out the fluid through a microfluidic probe.* ***(b)*** *Time sequence of infrared images of a heater showing the temperature rise and thermal spread as the activation command is sent from a smartphone at t = 0 s.* ***(c)*** *Temporal variation of the temperature at various parts of the device after a thermal pump is actuated at t = 0 s.* ***(d)*** *A series of spatiotemporal IR thermal images showing temperature change and distribution during fluid delivery.*

The temperature of the ejected fluid is almost close to room temperature, while as the temperature experienced by the drugs in the reservoir is close to 60°C (**Fig. 2.8c**), hence ensuring its safe and reliable operation for *in vivo* animal studies. **Figure 2.8d** highlights the spatiotemporal spread of heat at the Lego Interface as well as that of the ejected fluid until 10 s after the actuation process (20 s long) ends. As is evident, the temperature seen is spatially limited as well as rapidly decreases close to normal levels after the actuation process stops.

2.3.2 Fluidic and Micropump Characteristics

The fluid flow rate was measured using the same method used in our previous work[8]. To measure the flow rate in the microchannel, fluorescent polystyrene microbeads (2 μm, Ex/ Em: 505/ 515 nm, F-8827, Thermo Fisher Scientific) were used as a trace particle. Prior to the tracer injection, the microbead solution was diluted with distilled water in the ratio of 100:1 followed by sonication for 5 minutes to prevent aggregation of bead particles. An inverted optical microscope (Leica) equipped with a digital high-speed camera (Phantom v7.3, Vision Research), a 20X objective and a wide-field fluorescence light source (X-Cite 120Q, Excelitas Technologies) was used to record the video of fluid flow. The recorded video was analyzed by using PIV (particle image velocimetry) to calculate the displacement of microbeads and their velocity between each frame. PIV was implemented by using Matlab (Mathworks) after modification of open source code (PIVMat, http://www.fast.u-psud.fr/pivmat/). The volumetric flow rate was calculated by multiplying the cross-sectional area (10 μm × 10 μm) with the average speed of flow. Based on this measured result, delivered volume over time was calculated.

The thermally actuated pump starts to eject fluid from the tip at ~4.5 s and delivers ~93% of the total infused volume in about 12 s (**Fig. 2.9a–b**). The device shows minimal variability in the delivered fluid volume (~0.47 ± 0.02 μL) between different reservoirs of the same cartridge

as well as between different cartridges (**Fig. 2.9c**). This reliable, uniform delivery of fluid volume is facilitated by the harness, which robustly joins the Lego interfaces between the microfluidic channels and the cartridge. During actuation, the temperature of fluid in the reservoirs stays below ~60°C and decays rapidly (within ~0.02 s at the maximum flow rate of 0.87 m/s) to the ambient temperature around the implanted probe as it comes out through the long (10 mm) and narrow microfluidic channel (cross-section of 10 µm × 10 µm), therefore ensuring thermal compatibility with many pharmacological agents and biological tissue (**Fig. 2.8c**).

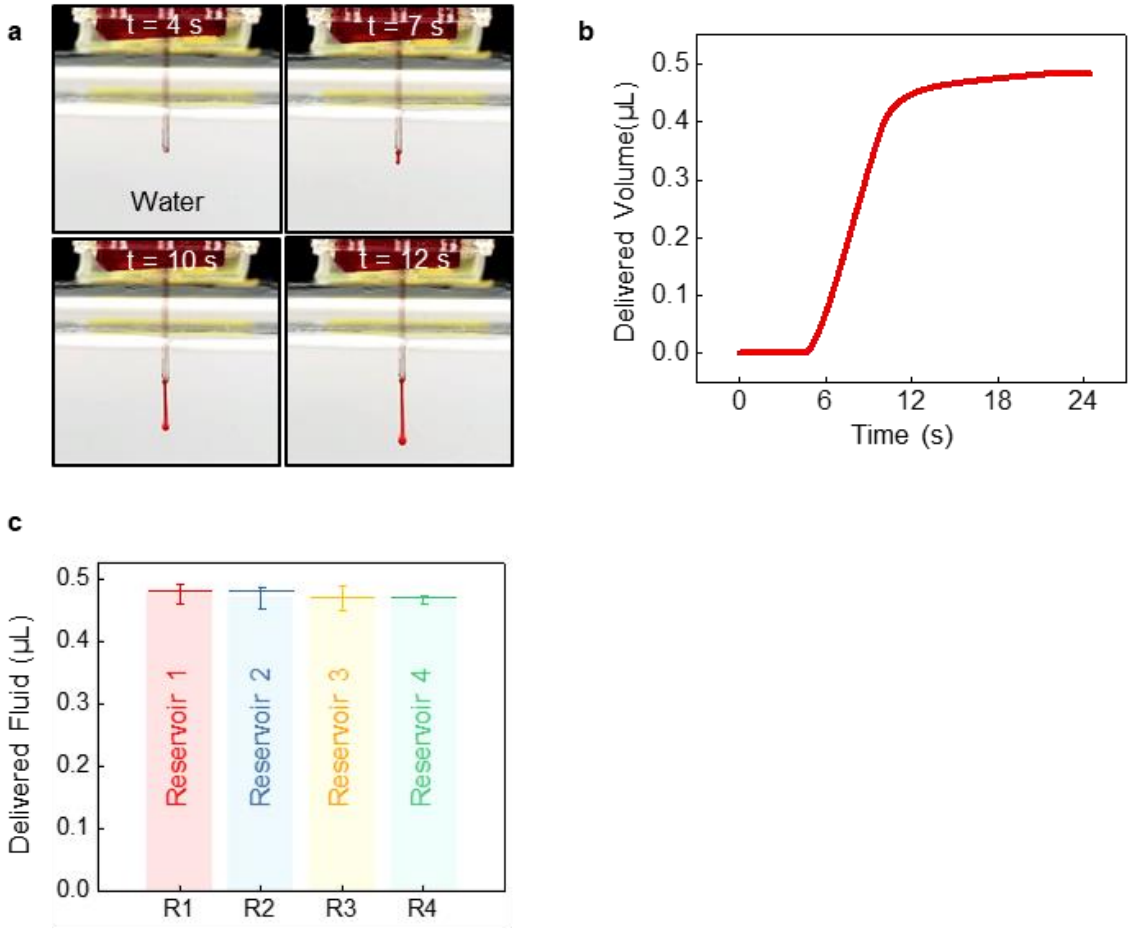

Figure 2.9 – Fluidic Characteristics of the Lego optofluidic device. (a) *Time sequence of optical images showing fluid ejection from an optofluidic probe in water as the activation command is sent from a smartphone at t = 0 s.* ***(b)*** *Delivered fluid volume as a function of time after actuation of a pump at t = 0 s.* ***(c)*** *Variability in delivered fluid volume from each of four reservoirs in representative replaceable cartridges. Data shows the average delivered volume of 0.47 µL with a standard deviation of 0.02 µL.*

2.3.3 Pressure Analysis near the Optofluidic Probe Tip during *In Vivo* Drug Delivery

It is also important for an actuation system to provide moderate fluid pressure during fluid delivery to prevent unwanted neural tissue damage by the infused fluid. To analyze the spatiotemporal distribution of pressure and stress during drug delivery near the target brain tissue, Finite Element Analysis (FEA) was carried out to simulate the fluid flow and mechanical stress built up around the brain tissue (COMSOL Multiphysics version 4.2, COMSOL Inc.). The fluid flow was assumed to be laminar with the experimentally measured flow rate (**Fig. 2.9b**) and to have fluid properties of a density of 1000 kg/m^3 and a dynamic viscosity of 0.89 Pa·ms. Brain tissue was modeled as a poroelastic material with a Young's modulus of 3156 Pa, Poisson ratio of 0.35, porosity of 0.3, and compressibility of 0.35[27]. The PDMS microfluidic probe layer was assumed to be a linear elastic material with a Young's modulus of 1 MPa, and Poisson ratio of 0.49. For simplicity, we used a two-dimensional cross-sectional model for the brain tissue and fluid flow interaction. The resulting mechanical stress near the target brain tissue was extracted by von Mises stress to display a scalar value of stress from the Cauchy stress tensor (**Fig. 2.10a–b**). Finite element analysis (FEA) simulation shown in **Fig. 2.10a–b** highlights the spatiotemporal characteristics of the mechanical stress developed during fluid delivery near the microfluidic outlet embedded in brain tissue. The results reveal that even the peak stress developed in tissue during fluid delivery is extremely low (peak stress of 0.77 kPa at t = 8.2 s, which is equivalent to 77 nN force for a 10 µm × 10 µm microfluidic outlet), verifying its negligible influence on brain tissue surrounding the infusion site. While it is possible that fluid delivery itself may modulate neural activity (e.g., activation of mechano-receptors), the extremely low pressure exerted from our devices (0.77 kPa), combined with no discernable effects of inert vehicle injections on behavior, suggest that is unlikely the case, at least within the brain sites tested during *in vivo* studies.

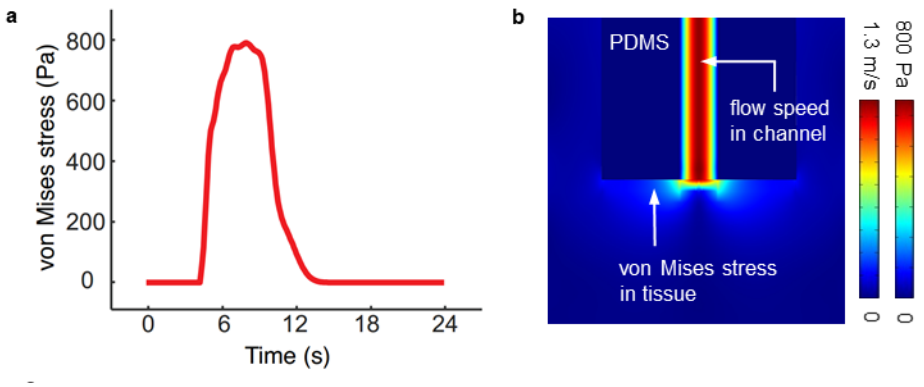

Figure 2.10 – Pressure Characterization at the optofluidic probe tip during fluid delivery. (a) *FEA result showing temporal variation of fluid pressure against brain tissue at the probe-tissue interface during fluid delivery.* ***(b)*** *FEA modeling of fluid pressure distribution at the probe-tissue interface at the maximum flow rate during fluid delivery. Maximum pressure applied to the tissue is only about 800 Pa, ensuring negligible influence of fluid ejection on the tissue.*

2.3.4 Force characterization for Lego Assembly and Disassembly Processes

Mechanical characterization of the Lego assembly and disassembly processes was carried out using Instron Mechanical Testing System. To align the structures before testing, the female Lego was first glued on top of a glass slide (75 mm × 25 mm), which was fixed to the bottom of the loading clamps of the mechanical testing machine. The male Lego (each pillar with OD = 1.3 mm) was then assembled into the female Lego, and liquid thermal glue (Mini Hot Melt Glue Gun, CCbetter) was applied on top of the assembly (opposite surface to the male Lego pillars). The upper loading clamp of the machine was driven down, attaching it to the liquid thermal glue, which cools down and solidifies within 15 min. This method helped align the male Lego part with female PDMS part without developing any mismatch between assembling and disassembling (due to a possible spatial misalignment error). For each sample, tests were carried out thrice and the loading forces were recorded with respect to insertion lengths. Various force profiles were analyzed as various female Lego parameters were varied. Four different insertion lengths (1 mm, 1.2 mm, 1.4 mm, 1.6 mm), four different diameter values of the female PDMS holes (1.00 mm,

1.15 mm, 1.20 mm, 1.25 mm), and two different PDMS base to curing agent ratios (5:1, 10:1) were used for characterization of Lego assembly and disassembly forces.

The principle strain at the Lego interface and the maximum force for both assembling and disassembling processes of the male and the female Lego with respect to four different inserting lengths and speeds was investigated (**Fig. 2.11 a-d).** It was found that the maximum forces required during an assembly and disassembly process increase when 1) the ratio of PDMS elastomer to curing agent decreases, 2) the female Lego diameter (ID) decreases, or 3) inserting length increases, as shown in **Fig. 2.11c.**

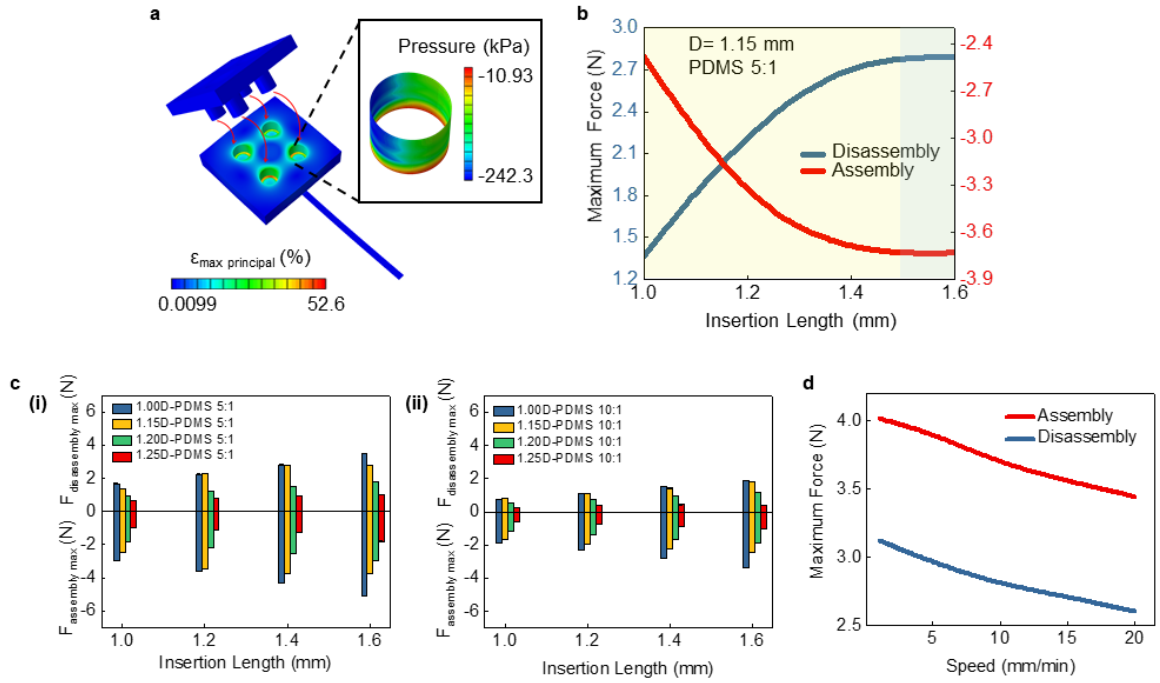

Figure 2.11 – Pressure and maximum force analysis at the Lego interface. (a) *FEA simulation of Lego assembly that shows the maximum principal strain experienced on the inner walls of the female Lego structure by the plug-in of a male Lego replaceable cartridge. The inset shows mechanical pressure generated at the Lego interface due to the assembly.* ***(b)*** *The maximum forces required for assembly and disassembly of the Lego parts as a function of Lego insertion length for the PDMS female Lego (elastomer: curing agent = 5:1) with a diameter of 1.15 mm and the COP-based male Lego with a pillar diameter of 1.3 mm.* ***(c)*** *Effect of female Lego material property on the maximum assembly and disassembly force. Maximum assembly/disassembly force variation as a function of the insertion length (1–1.6 mm) of Male Lego into the female Lego (diameter D in mm) for Lego assembly with PDMS female pad compositions (elastomer: curing agent ratio) of (i) 5:1 and (ii) 10:1. Note that the increase in D as well as the PDMS mixing ratio substantially decreases the maximum force required for assembly. Also, the maximum force is always greater in the assembly process than the disassembly process for the same insertion displacement.*

The detailed force profiles with varying parameters (**Fig. 2.12**) indicate that the absolute value of assembling force increases until the desired inserting length (female Lego thickness) is reached.

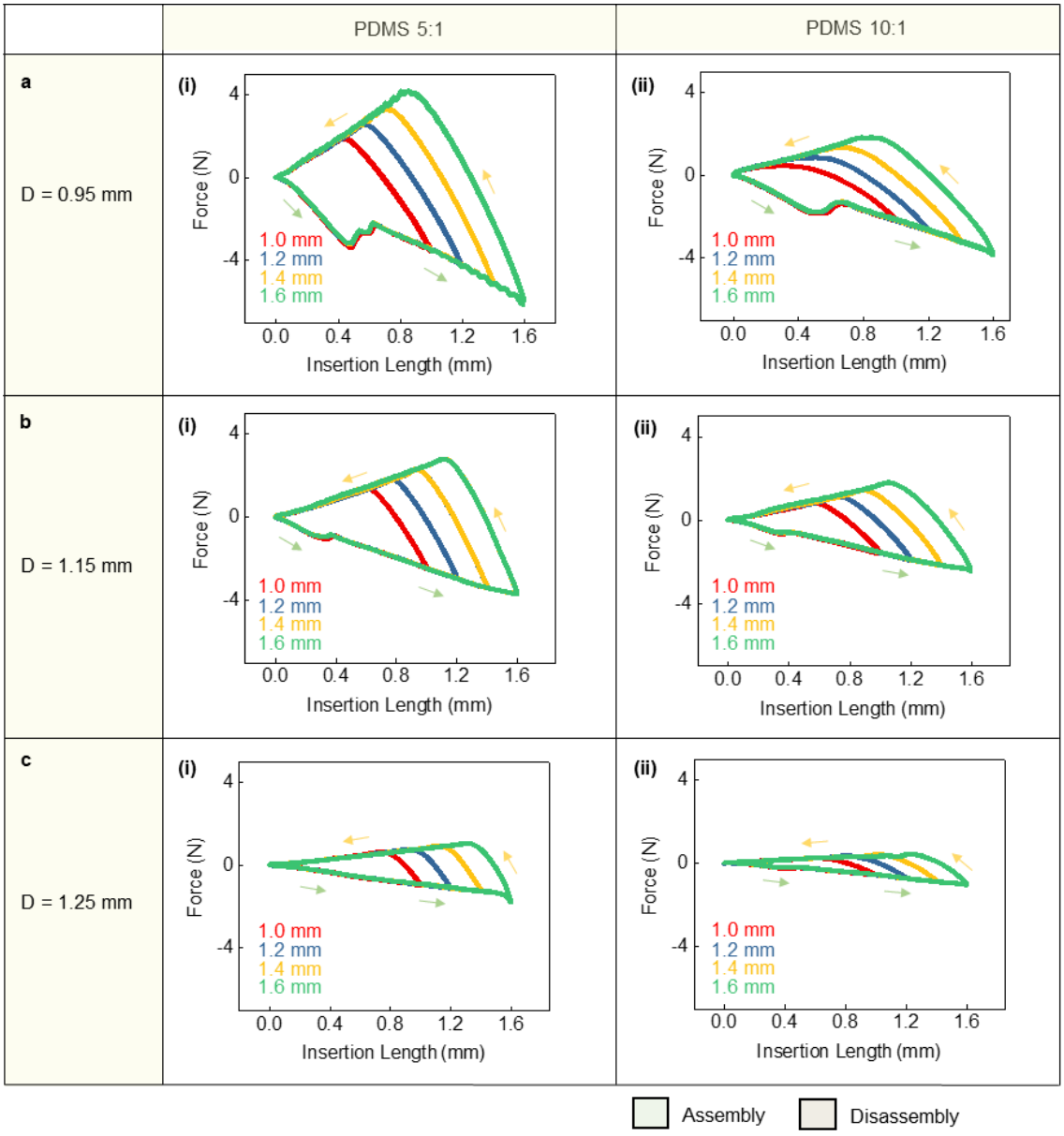

Figure 2.12 – Assembly/disassembly force vs Insertion length profiles, demonstrating the interaction between the male Lego and the female Lego as parameters such as female Lego diameter (D) and PDMS elastomer-curing agent mixing ratio are varied. *Each of the six graphs show four different plots, each of which represents the maximum thickness of the female Lego (t) that is inserted in the male Lego (1.7 mm pillar length and 1.3 mm diameter) – 1mm (red), 1.2mm (blue), 1.4mm (yellow) and 1.6mm (green). Note that the peak disassembly force occurs at an insertion length proportional to the total female Lego thickness (t). Increasing the PDMS elastomer- curing agent mixing ratio from 5:1 to 10:1 also reduces the peak assembly and disassembly forces.*

An assembly and disassembly process can be described as a counterclockwise cycle from the origin in **Fig. 2.12** where the negative sign of force corresponds to the pressing force of the male Lego against the female Lego, and the positive sign of force is the pulling force of the male Lego from the female Lego. The assembling force initiates as a static friction and a compression, then its further increase triggers the sliding of the male Lego inside the female Lego holes. At the point when the applied force overcomes the static friction, it leads to a sudden relative motion between surfaces resulting in a 'notch' shape of the assembling force profile. Note that the female Lego is mechanically much softer than the male Lego, so the elastic deformation of the female Lego cannot be excluded and thus a certain amount of elastic energy is also stored in the female Lego. During the disassembly process (after an assembly), the elastic deformation energy (due to assembly) first decreases but then increases further due to the force from the pulling effect of the male Lego acting on inner walls of the female Lego holes, while the assembled structure is still in static friction. This force eventually reaches a limit (which corresponds to the peak disassembling force) after which the male Lego begins to slide out from the female Lego holes. Further pulling of the male Lego results in the decline of the disassembling force due to the reduced contact interface between the male Lego and the female Lego holes until the dissembling force drops to zero.

The male Lego pillars (COP) in the drug cartridge are designed to have a slightly larger diameter than the female Lego holes (PDMS) in the probe part (male Lego OD: 1.3 mm vs. female Lego ID: 1.15 mm). Because the modulus of the male Lego pillars (2.6 GPa) is much larger than the modulus of the elastomeric female structure (~1 MPa), when press-fitted, the female structure experiences large deformation (maximum strain of 52.6%) and exerts radial pressure (~242 kPa) that tightly locks the Lego assembly for hermetic sealing (**Fig. 2.11a**). The dimensions of male and female Lego structures are determined by systematic parametric studies to enable robust Lego assembly (**Fig. 2.11–12**). In our experiments, the maximum force required for Lego

assembly and disassembly increases by increasing the insertion length (saturating to peak values at an insertion length ~1.5 mm, **Fig. 2.11b**), decreasing female Lego diameters, and decreasing PDMS elastomer/curing agent ratio. Our Lego design with optimized parameters (i.e., female Lego: hole ID = 1.15 mm, hole height = 1.5 mm, PDMS elastomer: curing agent = 5:1; male Lego: pillar OD = 1.3 mm, pillar height = 1.7 mm) ensures that the required force for Lego operation is neither too high (inconvenient for *in vivo* experiments) nor too low (poor hermeticity of Lego assembly).

2.3.5 Pressure and Leakage Characterization at the Lego Interface

Optimized design of the Lego structures is critically important for robust microfluidic assembly and leakage-free operation. Mechanical analysis of fluidic leaking between the male Lego drug cartridge and the female Lego optofluidic probe was performed using 3D FEA software (Abaqus, Dassault Systemes) by simulating the mechanical interaction pressure developed between the assembled Lego parts and a simplified estimation of fluidic flow pressure at the Lego interface. Eight-node, 3D hexahedron elements (C3D8R) were used to model the soft female Lego (E = 2 MPa; each hole with ID = 1.15 mm) and the rigid male Lego (E = 3 GPa; each pillar with OD = 1.3 mm). Then the deformation and strain distribution in the female component of the Lego assembly was calculated, in order to estimate the critical leaking pressure at the Lego interface according to Liu, et al.[28]. Based on our measured data for fluid velocity, we analytically estimated the fluidic pressure developed at the Lego interface during fluid delivery and quantitatively compared this fluidic pressure with the critical leaking pressure to evaluate fluid leaking through the Lego interface. At chosen design parameters, it guaranteed secure hermetic sealing at the Lego interface such that the maximum fluid pressure developed at the Lego interface (0.38 kPa) is far below the critical leaking pressure (4270 kPa), thus allowing leakage-free fluid delivery (**Fig. 2.13**).

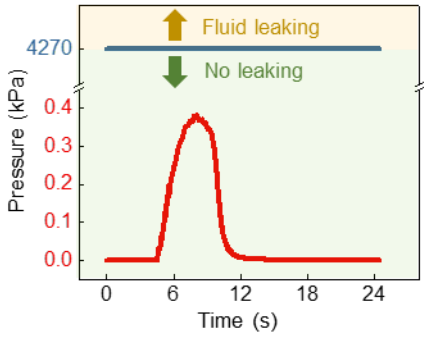

Figure 2.13 – Comparison of the critical pressure required for fluid leakage through the assembled Lego structure and the pressure generated at the reservoir outlet during fluid delivery. *The maximum fluid pressure (0.38 kPa) generated at the Lego interface is significantly smaller than the critical pressure for fluid leakage (4270 kPa), indicating robust, leakage-free Lego microfluidic assembly.*

2.3.6 Pressure estimation for the microfluidic channel at the Lego interface during drug actuation

Assume the fluid velocity and pressure respectively are v_1 and P_1 at the outlet of the reservoir; v_2 and P_2 at the microfluidic outlet, as shown in **Fig. 2.14** below. Since the liquid at the outlet is open to outside, it can be assumed that $P_2 = 0$ to simplify the analysis. According to the Bernoulli equation and ignoring the influence of gravity,

$$P_1 + \frac{\rho v_1^2}{2} = P_2 + \frac{\rho v_2^2}{2} \tag{2.1}$$

where ρ is the density of the fluid. Since the diameter of the microfluidic channel is much smaller than that of the outlet of the reservoir, the pressure in the reservoir can be obtained as,

$$P_1 = \frac{\rho v_2^2}{2} . \tag{2.2}$$

The velocity at the outlet is known from the experimental data, thus the pressure at the outlet of the reservoir can be estimated.

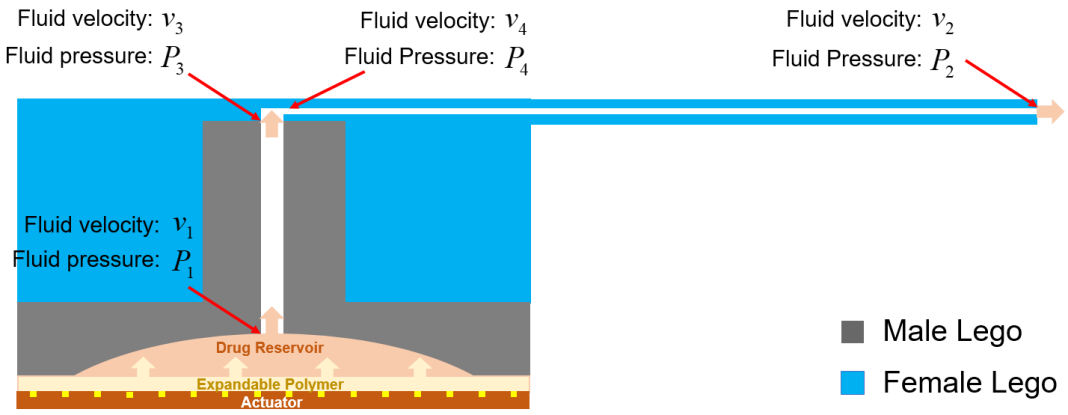

Figure 2.14 – Descriptive image of Lego interface for fluid leakage analysis.

To estimate the possibility of fluid leaking in the Lego assembly, the pressure P_3 (pressure at the Lego interface right after the outlet (0.45mm ID) of the male pillar) and P_4 (pressure right after Lego interface at the inlet (10 μm × 10 μm) of the microfluidic channel) were analyzed. Since the flow volumes at the two different cross-sections remain the same,

$$Q = A_3 v_3 = A_4 v_4 , \tag{2.3}$$

And the velocity at the input of the microfluidic channel right after Lego interface is

$$v_4 = \frac{A_3 v_3}{A_4} \tag{2.4}$$

where A_3 and A_4 are the cross-section areas of the fluidic channels in the male Lego drug cartridge and female Lego probe, respectively.

As the fluidic channel dimensions inside the male Lego pillar is constant, $v_1 = v_3$ and $P_1 = P_3$. Since $A_3 > A_4$ and $v_4 > v_3$, then $P_4 < P_3$ according to the Bernoulli equation and hence $P_4 < P_1$. Thus, the pressure at the input of mithe crofluidic channel right after the Lego interface is lower than that in the reservoir.

The experimental fluid velocity at the outlet (v_2) vs. time is shown below in **Fig. 2.15**.

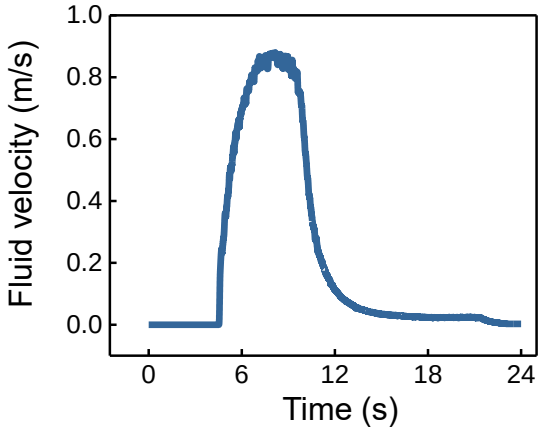

Figure 2.15 – *Fluid flow velocity over time at the optofluidic probe outlet*

According to equation (2.1), the Pressure at the outlet of the reservoir ($P_3 = P_1$) over time can be obtained as shown in **Fig. 2.16**.

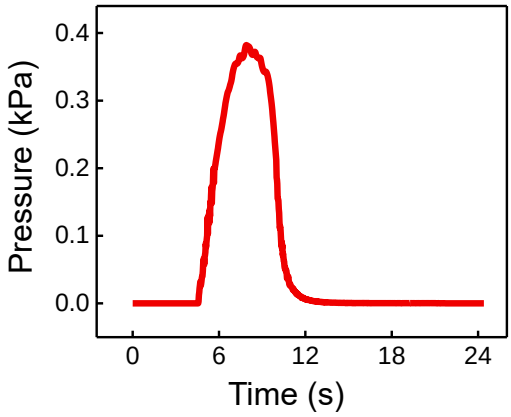

Figure 2.16 – *Pressure developed at Lego interface (P3) during fluid delivery*

Critical leaking pressure:

According to Liu et. al[28], the critical pressure of fluid leaking for such a Lego interface is,

$$\frac{P_c}{u} = \frac{A}{1-\varepsilon}\left(\frac{l}{h}\right) + \frac{B\varepsilon}{1-\varepsilon}\left(\frac{l}{h}\right)^2 \tag{2.5}$$

where P_c is the critical pressure of fluid leaking; u is the shear modulus of 5:1 PDMS; l is the depth of the female Lego hole; *h* is the radius of the male pillar; ε is the normal strain at the female/male interface; *A = 3* and *B = 2.9* are experimental constants[28].

The strain at the interface was calculated by Finite element analysis (FEA) as shown in **Fig. 2.17**

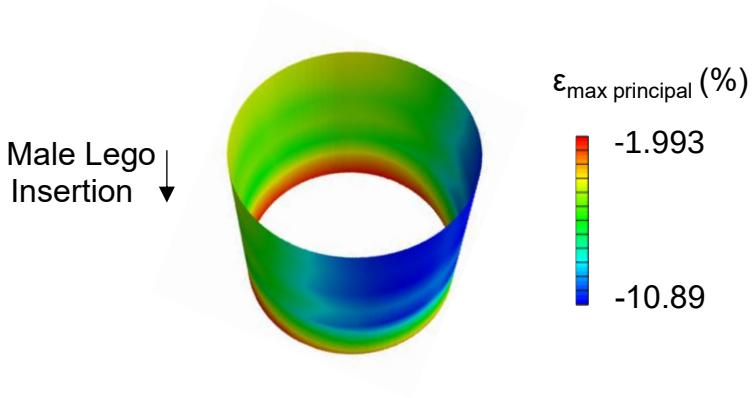

Figure 2.17 – *Maximum strain profile at the Lego Interface in assembled form*

According to the FEA result,

$$-10.89\,\% < \varepsilon < -1.993\,\%$$

Thus, the critical leaking pressure is within the range of

$$4.27\,MPa < P_C < 5.66\,MPa$$

Thus, according to **Fig. 2.16**, the largest pressure developed during fluid delivery at the Lego interface is about 0.38 kPa, which is much smaller than the critical leaking pressure

($P_3 \ll P_c$). Also, the pressure right after the Lego interface is even lower based on our analysis. Hence, we can conclude that the Lego assembly can offer robust hermetic sealing and prevent fluid leakage.

Though the current microfluidic system is capable to deliver sub-microliter volumetric fluids over a distance of several centimeters reliably, it should be noted however that to use this device in large animals, appropriate calculation adjustments need to be analyzed to appropriately design the microfluidic actuation needs such as volume, flow rate, and microfluidic channel length.

2.3.7 Analysis during Ambient Fluctuations in Temperature and Pressure

In order to verify that normal temperature and pressure do not induce unwanted injection, we engineered special caged setups where we bidirectionally modulated both temperature (10 to 40°C) and pressure (970 to 1050mbar) to simulate various ambient conditions. We found that that there was no unwanted drug release (from probe tip of the assembled device) or unwanted expansion of the actuating polymer (from the cartridge micropump) by such fluctuations (**Fig. 2.18**). Therefore, we reached the conclusion that ambient environmental disturbances do not affect the behavior of the device. Overall, the device works reliably such that it delivers desired fluids only when the micro-pumps are activated. Hence it was concluded that changes in the ambient temperature and pressure fluctuations in the environment do not affect the reliable functionality of the device.

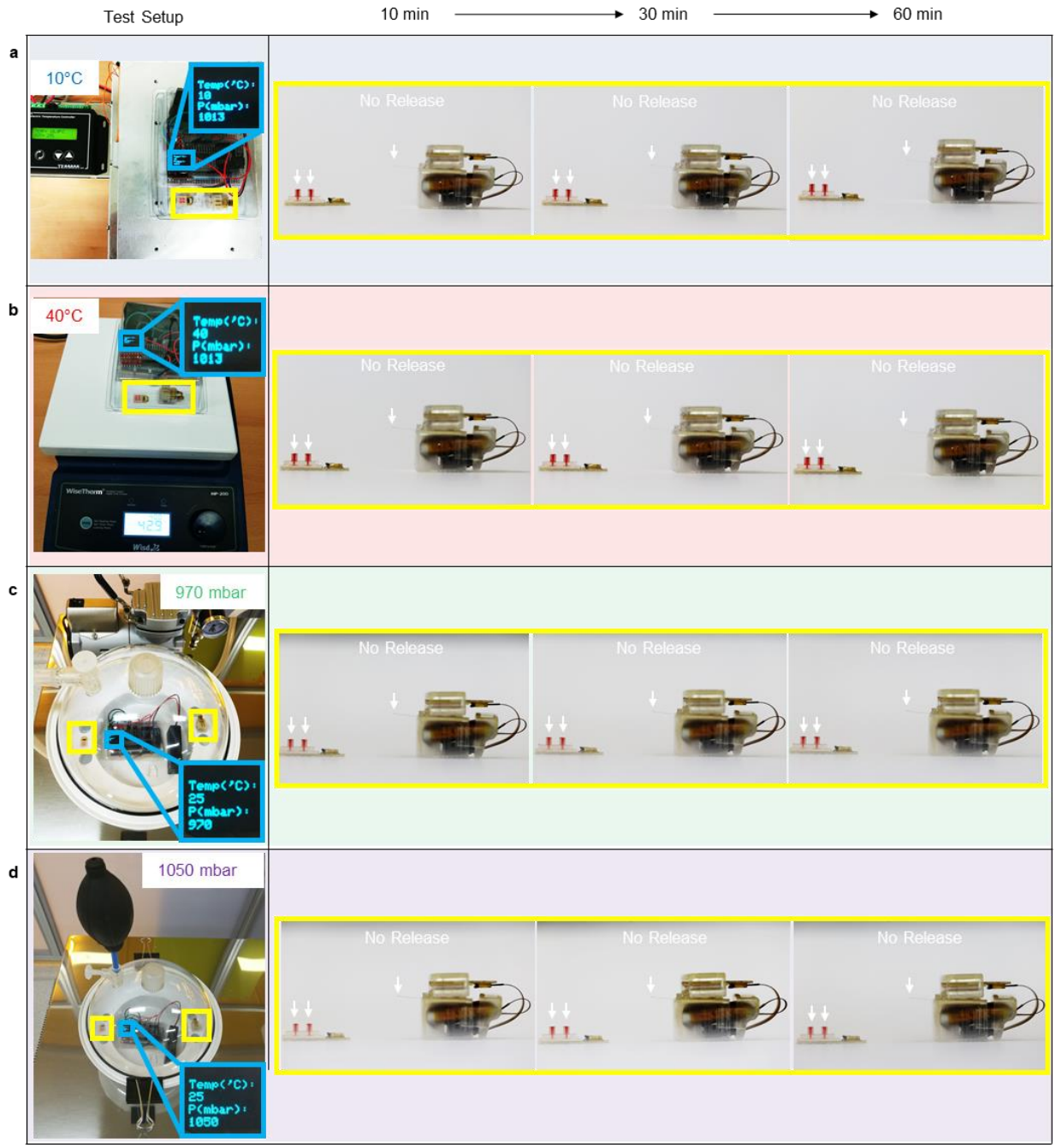

Figure 2.18 – Effect of ambient temperature and pressure fluctuations on the device. *A series of optical images shows that no unwanted fluid ejection is induced by varied ambient environmental conditions: (a) at 10°C under 1013 mbar pressure, (b) at 40°C under 1013 mbar pressure, (c) at 25°C under 970 mbar pressure and (d) at 25°C under 1050 mbar pressure.*

2.3.8 Injection and Suction Analysis during Lego Assembly and Disassembly Processes

To directly determine the possibility of unwanted injection due to Lego assembly, we examined Lego assembly of a color-filled dye cartridge and took timestamp photographs of the probe tip (**Fig. 2.19a (i)**) showing no unwanted injection at normal assembling speeds of 0.5mm/s (~3s required to hermetically cover the Lego interaction length of 1.5mm between male Lego pillars and female lego holes). This was further validated by assembling a color dye while the probe was implanted into the mouse brain. No dye was detectable in the brains of mice sacrificed immediately after the Lego was inserted (**Fig. 2.19a (ii)**), further corroborating that there is no injection after insertion of the Lego device.

For unwanted suction during cartridge disassembly, we placed the probe tip in saline water (to simulate CSF) and found that at normal disassembly speeds of 3 mm/s (it is faster because the cartridge pops off quickly), due to decrease in pressure inside the channels there was a very minute amount of fluid imbibed at the tip momentarily. However, upon plugging in a new cartridge (to replenish drugs) or a blocker (to protect exposed channels in between experiments), the imbibed fluid was pushed back from the microfluidic channels (**Fig. 2.19b**). Through repeated experiments, we found that an insignificant amount of fluid is sucked up and this fluid did not travel all the way up to the microfluidic channel.

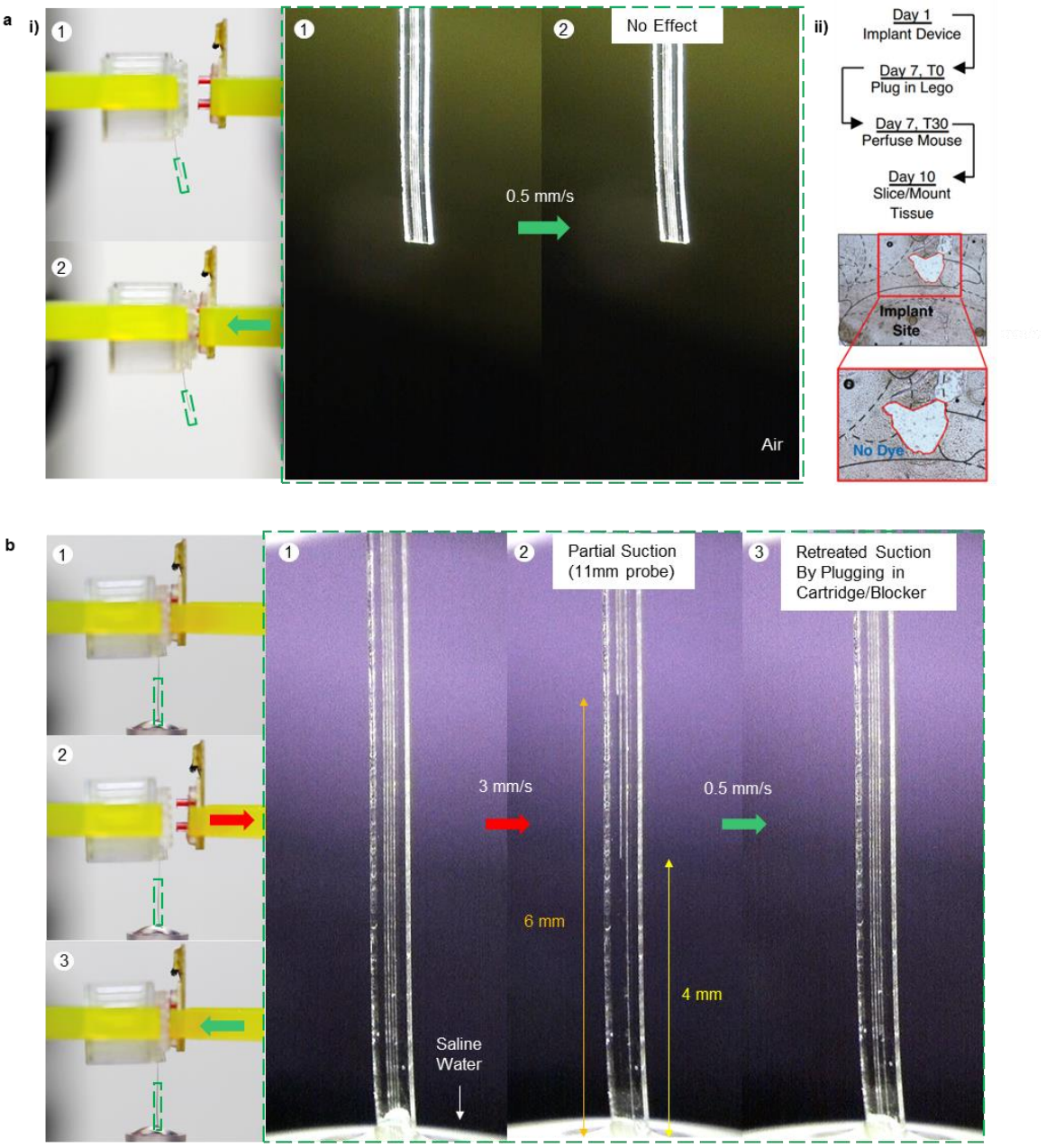

Figure 2.19 – Testing for unwanted fluid injection or suction during assembly and disassembly process of the Lego cartridges. (a) *A Lego assembly of a red dye-filled cartridge simulated at normal assembling speeds of 0.5 mm/s in (i) air and (ii) brain tissue in vivo, showing no unwanted fluid injection from the microfluidic probe tip.* ***(b)*** *A Lego disassembly of a red dye-filled cartridge at normal disassembly speeds of 3 mm/s while the microfluidic probe tip is inside saline water (simulating Cerebrospinal fluid), showing minute, non-uniform suction of fluid at the tip due to a momentary decrease in pressure inside the channel. However, upon plugging in a new cartridge (to replenish drugs) or a blocker (to protect exposed channels in between experiments), the imbibed fluid is pushed back from the microfluidic channels.*

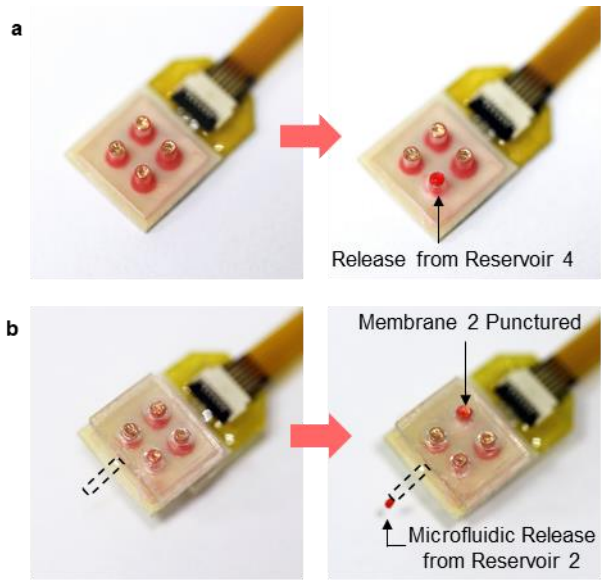

Figure 2.20 – Sealing of Lego drug cartridges with copper membranes to prevent unwanted fluid evaporation and injection. (a) *A Lego drug cartridge hermetically sealed with transfer-printed 3 µm-thick copper membranes (left). Upon actuation, this thin membrane is ruptured by fluid pressure for fluid delivery (right).* ***(b)*** *A Lego drug cartridge assembled with a microfluidic probe before (left) and after actuation (right). Fluid is ejected from the microfluidic probe outlet through the punctured copper membrane.*

Even though the imbibed fluid never travels all the way up to the microfluidic channels as validated through repeated studies, as a safety measure, the cartridge can be hermetically sealed by transfer-printed copper membranes, which can be ruptured to allow fluid delivery during pump actuation (**Fig. 2.20**). With this modification, the device will be completely free from any concern of unwanted injection or suction.

2.3.9 Wireless Control and Characteristics

Wireless manipulation of Lego optofluidic systems is enabled through smartphone control using Bluetooth Low Energy (BLE) technology. **Figure 2.21a** shows a conceptual illustration of smartphone control (master) of a target mouse implanted with a Lego optofluidic device (target) within the BLE ecosystem, offering easy wireless access, accurate target selectivity and programmable output multi-modality (i.e. drug delivery and/or photostimulation).

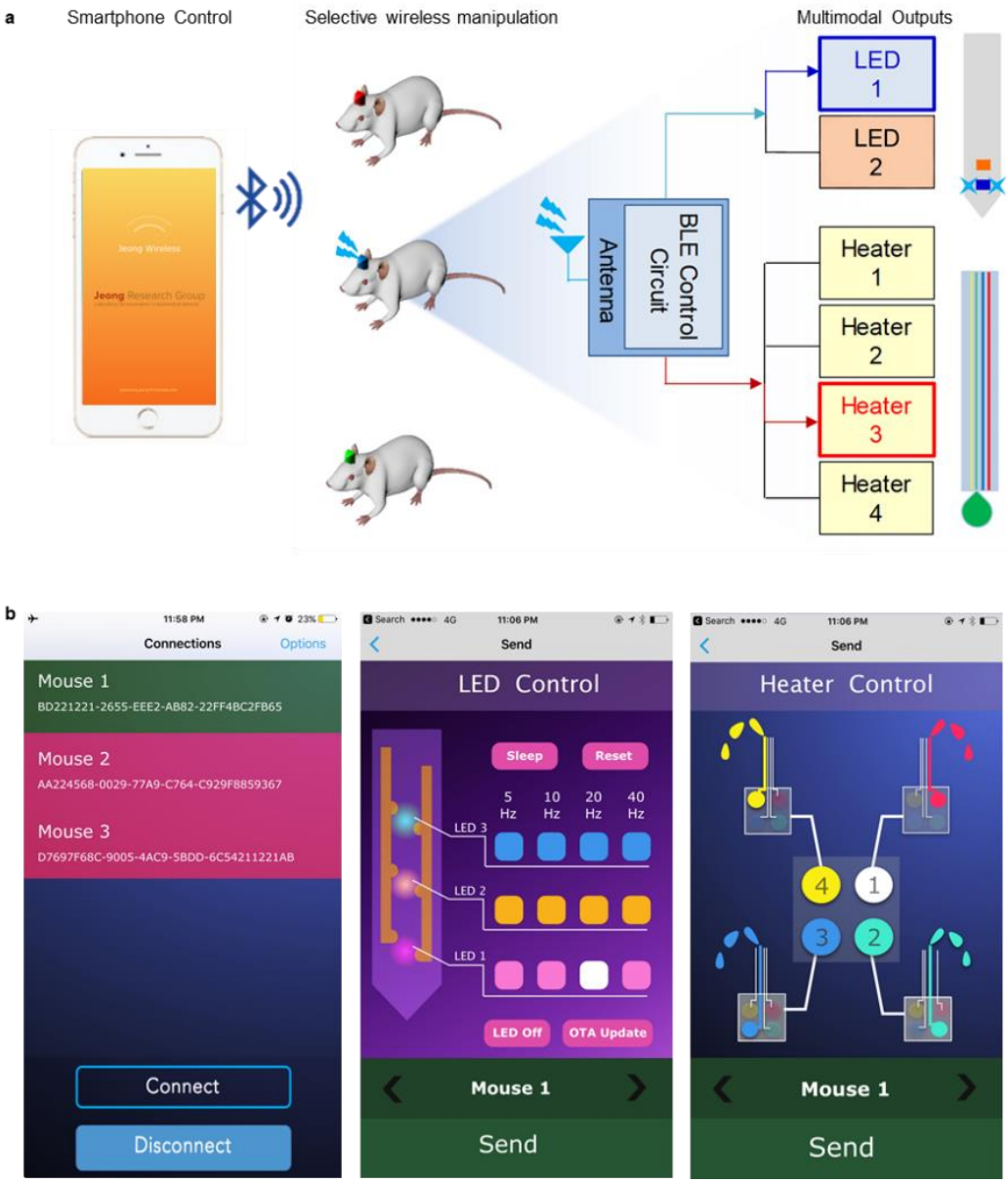

***Figure 2.21 – Smartphone control of wireless Lego optofluidic neural implants**. **(a)** A schematic illustration of a smartphone Bluetooth control of a specific mouse in a group of multiple mice implanted with wireless optofluidic devices. Bluetooth enables simultaneous and/or independent manipulation of specific outputs (i.e. single or multiple LEDs and/or one of the heaters) for photostimulation and/or drug delivery. **(b)** Screen captures of the smartphone app – (left) the mouse selection panel displaying a selected mouse (Mouse 1) among the list of available mice in the vicinity of the smartphone, (middle) the LED control panel with command 'LED 1 at 20Hz' selected (default pulse width: 10 ms), (right) the heater control panel with 'Heater 1' selected for drug delivery from the reservoir 1. Note that two commands can be sent separately or simultaneously. Also, different frequencies can be set for each LED in simultaneous operation mode.*

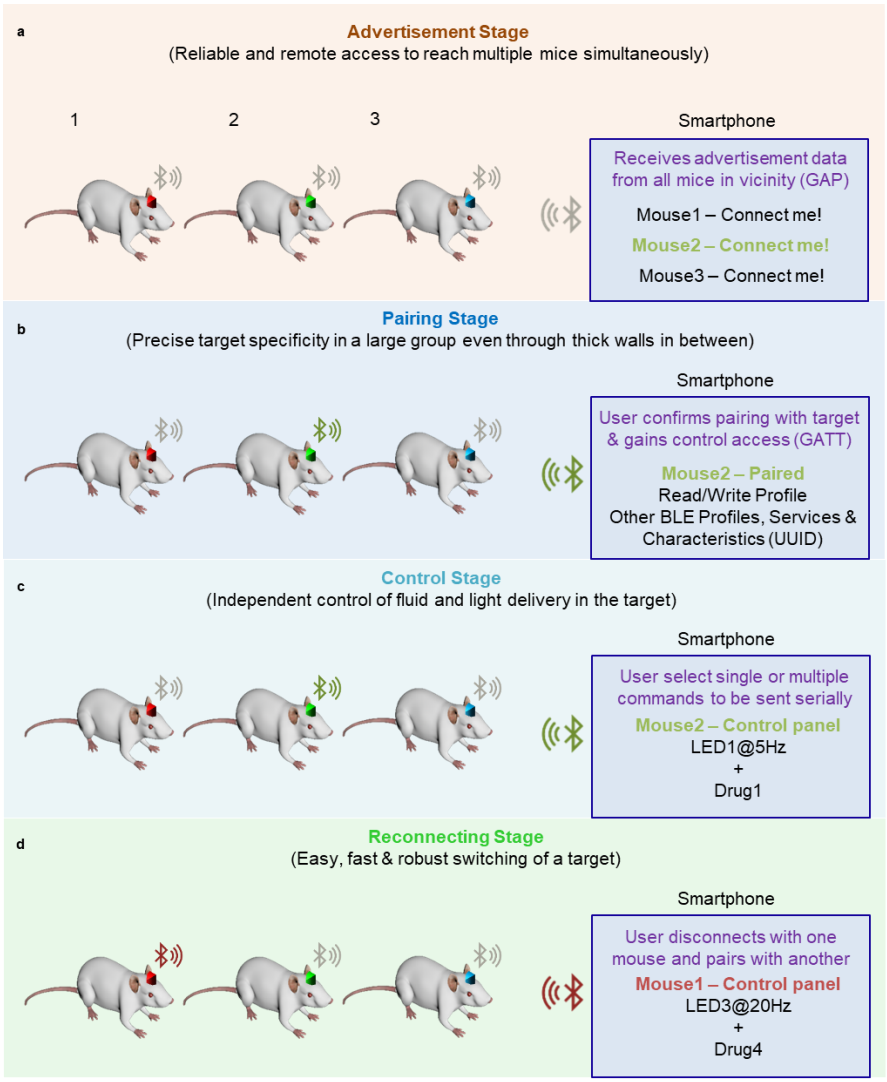

Figure 2.22 – Schematic illustration of selective Bluetooth paring concept for smartphone control of wireless Lego optofluidic systems. (a) *Advertisement stage: all mice (red, green, blue) start advertising their information in their vicinity and the advertisement packets are collected by the smartphone (displayed on the smartphone application) and this information is controlled by Generic Access Profile (GAP) part of the Bluetooth Protocol Stack (helps determine the generic advertisement process). Each mouse can be programmed to have a unique advertisement name and that helps select a specific mouse in a large group with 100% accuracy.* ***(b)*** *Paring stage: the user selects the target mouse (green here) on the smartphone application and presses the "Connect" button (see Fig. 3b). The smartphone pairs with the selected mouse and gets access to communicate with the device. The paired mouse stops advertising and goes into connection mode, while the other mice (red and blue) keep advertising. After pairing, the user gets access to the various services and characteristics (each with a specific 16-bit universally unique identifier-UUID) of the connected mouse (green) including Read/Write profiles that are governed by Generic Attribute Profile (GATT) of the Bluetooth Protocol Stack.* ***(c)*** *Control stage: the user is able to control all multimodal outputs of the connected mouse (green) either independently (select one command before pressing "Send" button) or simultaneously (select multiple commands before pressing "Send") through the LED and Heater Control Panels (Fig. 3b).* ***(d)*** *Reconnecting stage: after being done with controlling the paired mouse (green), it can be either disconnected from the smartphone (it again goes into advertising mode) or put to Ultra Low Power (ULP) sleep mode. We can then reconnect to a different mouse (red) by pairing with it, by following the same communication and control procedure (steps (a) to (d)).*

A custom smartphone app (**Fig. 2.21b**) facilitates user-friendly control of a target device by allowing easy long-range access to a specific device among many available devices in the vicinity (10 - 100 m)[29] via Bluetooth pairing between a smartphone and the target device (detailed illustration of pairing process shown in **Fig. 2.22** and for the firmware see **Appendices**). Through the smartphone app, the user can determine operating conditions of LEDs and heaters (e.g. selection of blue and/or orange LEDs, LED modulation frequency, targeted heater number, etc.) for independent or simultaneous control of photostimulation and drug delivery (**Fig. 2.2**).

Although BLE itself is not a new type of wireless technology, its integration with neural devices enables a whole host of possible wireless *in vivo* neuroscience experiments that have been inefficient and hard to be achieved through tethered and other wireless approaches. BLE wireless controls have several compelling advantages for neuroscience experiments over other wireless technologies such as infrared (IR)[8]–[11] and radio frequency (RF)[12]–[24]. Unlike IR or other RF systems, BLE provides orientation-independent wireless control, thus guaranteeing reliable omnidirectional activation of a target device as proved with model rats at various angular orientations (**Fig. 2.23**). This feature ensures the stable operation of wireless devices in freely moving animals.

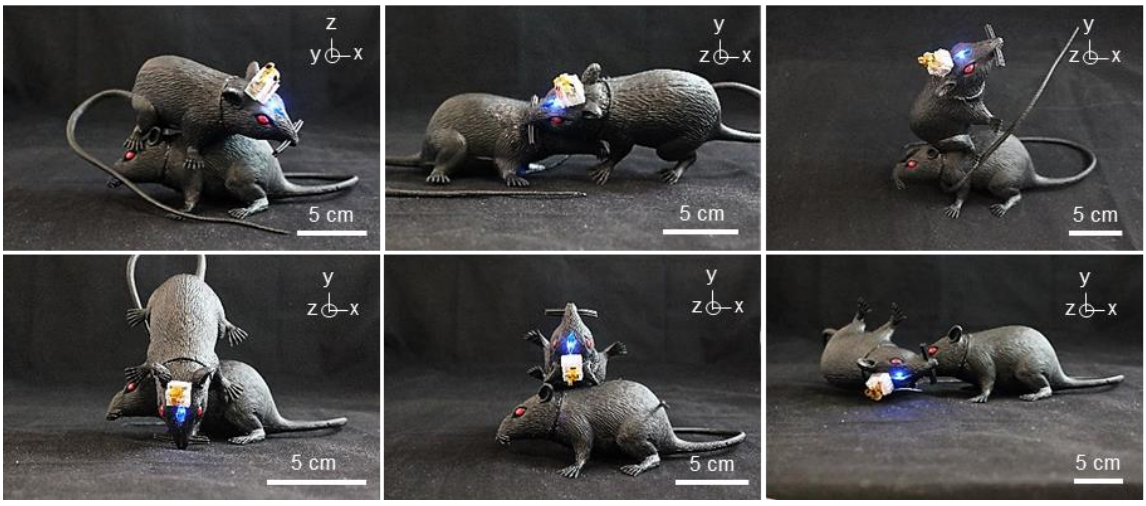

Figure 2.23 – Model rats with implanted Lego optofluidic systems showing Bluetooth capability for omnidirectional control.

Bluetooth also allows a secure wireless binding (pairing) between a smartphone and a selected wireless device for direct control of a target with 100% accuracy even in a crowded group of animals (**Fig. 2.24a**). This opens up new opportunities for complex social behavior experiments. In addition, unlike IR systems where obstacles can completely incapacitate the wireless control, BLE offers high penetration power of signals through even walls without affecting the precision of wireless communication as demonstrated by the through-door control of a wireless device (**Fig. 2.24b**). Moreover, it provides a large range of wireless operation (up to ~100 m)[29] without any LoS handicap (**Fig. 2.24c**). Other powerful features of the BLE include over the air (OTA) programmability that allows the user to wirelessly reprogram the BLE chip to enable easier adjustment of device operation parameters for various applications including *in vivo* pharmacology with high-precision temporal control of multiple fluid deliveries (**Fig. 2.3**) and closed-loop control for advanced behavior experiments as demonstrated in our real-time place preference control experiment. The latter exploits a BLE wireless transmitter (SimbleeCOM protocol[30]) communicating with a camera tracking system for automated conditional controls, which can be easily switched to the direct smartphone control mode depending on applications (**Fig. 2.24d**). The closed-loop protocol can be further extended to enable complex social behavior experiments where the behavior of one animal affects the stimulation parameters of other animals (via positive or negative feedback loops) in the vicinity (**Fig. 2.25**). Another feature of the BLE closed-loop communication is that it allows the user to check the status of the wireless operation. In other words, the wireless control can be not only authenticated through “success” or “fail” toasts for the confirmation of the desired operations but also tracked through the saved timestamp readings on the smartphone app (**Fig. 2.26**). This function helps to ensure successful wireless operation and avoid visual cues through indicator LEDs on the device during behavioral studies, which can sometimes affect animals’ behavior. All these incorporated device attributes make BLE a useful and highly functional option for wireless neural implants.

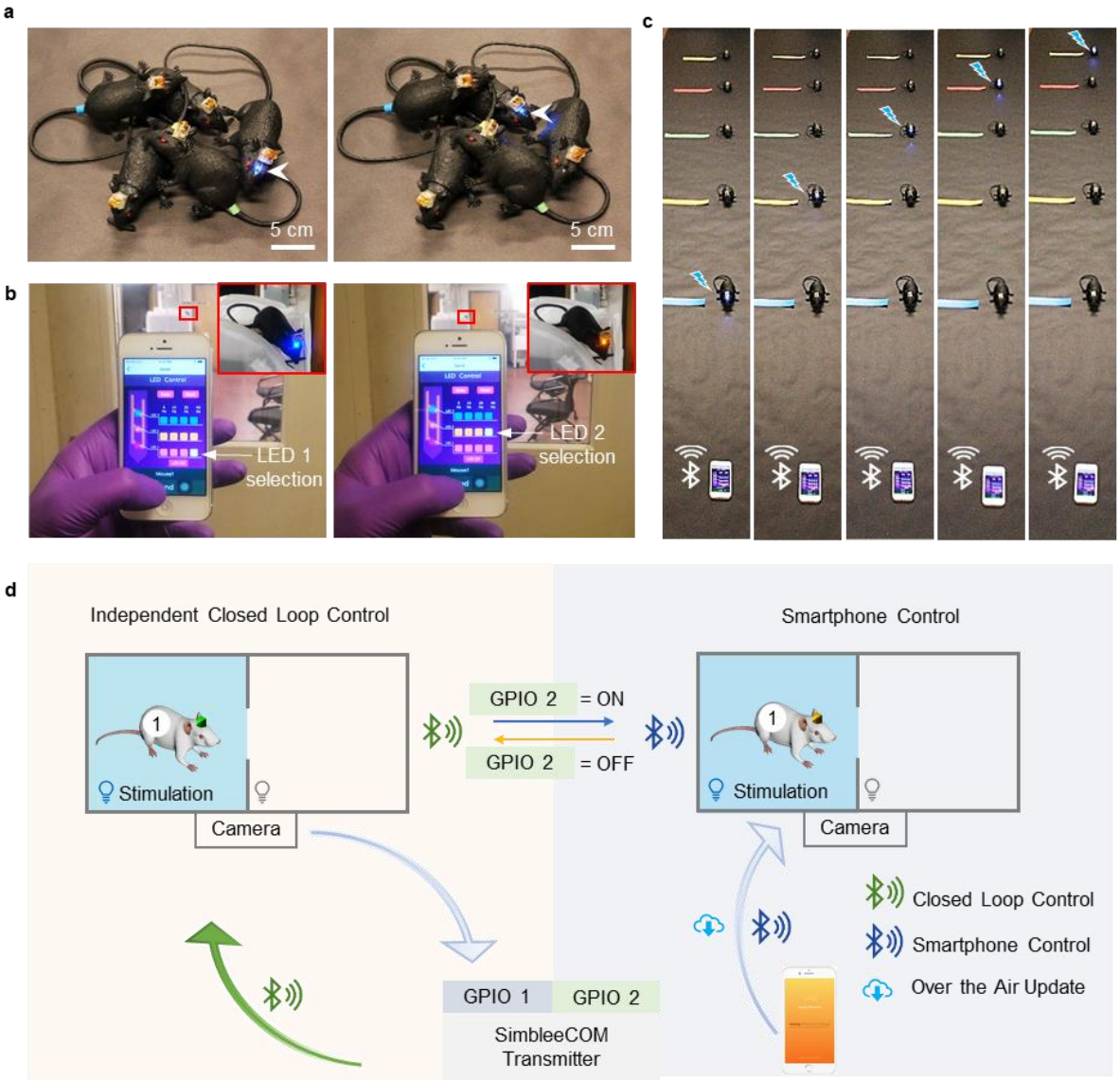

Figure 2.24 – Wireless, long-range selective control and closed loop networks. ***(a)*** *Optical images demonstrating Bluetooth selective control capability that can target a specific animal in a group of multiple animals implanted with wireless devices. Moreover, the target animal can be switched easily with a simple button press on the smartphone app.* ***(b)*** *Demonstration of through-wall control of a Bluetooth wireless device – LED 1 (blue μ-ILED, left) and LED2 (orange μ-ILED, right) blinking at 40Hz. Insets show the zoomed-in pictures of the controlled model rat.* ***(c)*** *Optical images highlighting selective control capability of the Bluetooth wireless system implanted in a group of model rats, overcoming the Line of Sight handicap as well as the limited coverage present in other contemporary wireless technologies such as infrared and radio frequency. Each horizontal color line represents a 1 m equivalent separation between the smartphone and each model rat.* ***(d)*** *Closed loop control for a typical place preference experiment, which can be versatilely switched between self-triggered, automated closed-loop control (left) and direct smartphone control (right) modes by simply switching the voltage on a GPIO (General Purpose Input/Output) pin of the SimbleeCOM transmitter.*

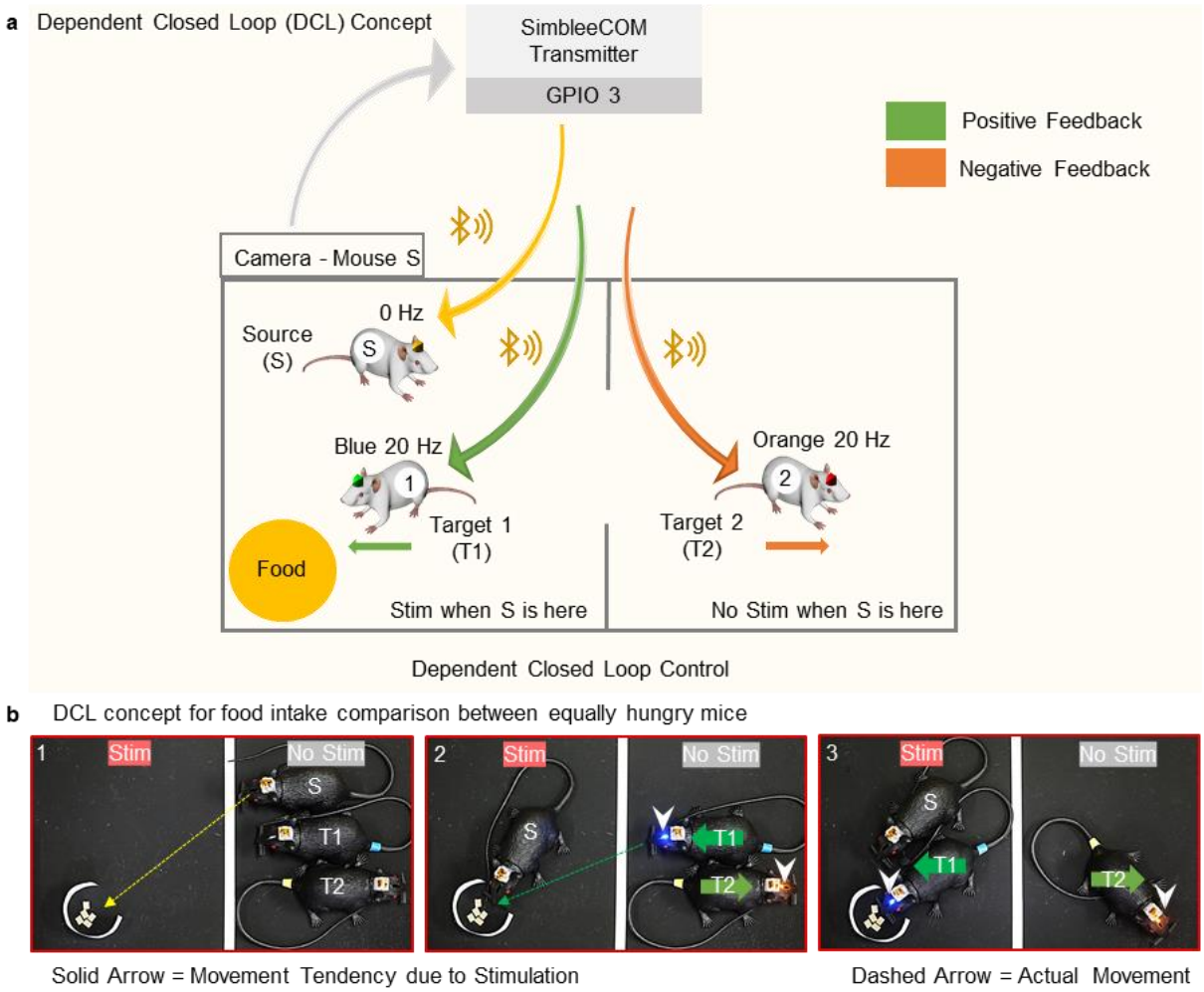

Figure 2.25 – A conceptual schematic diagram demonstrating a wireless BLE dependent closed-loop ecosystem for a social food preference behavioral setup – (a) *Concept of Dependent Closed Loop and* ***(b)*** *its illustration using model rats: This is an extension of a simple closed loop concept, where the behavior of one animal (Mouse S) can affect the stimulation profiles for other mice (Mouse T1, T2) in the same or different vicinities or environmental parameters. Because of the programmable nature of Lego optofluidic systems, the same commands sent out wirelessly by the SimbleeCOM transmitter (after receiving an interrupt from the camera based on the location of Mouse S) can be perceived as different stimulation profiles. Hence, multiple feedback loops can be implemented easily with programmable features where stimulation of different target animals (Mouse T1, T2) is dependent on the behavior of a source animal (Mouse S), thus creating multitude of positive (Mouse T1) and negative feedback loops (Mouse T2) within a complex and large behavioral animal setup. This mode is also switchable with user mode where each animal can be reprogrammed (through OTA update) before putting it back into a dependent closed loop state.*

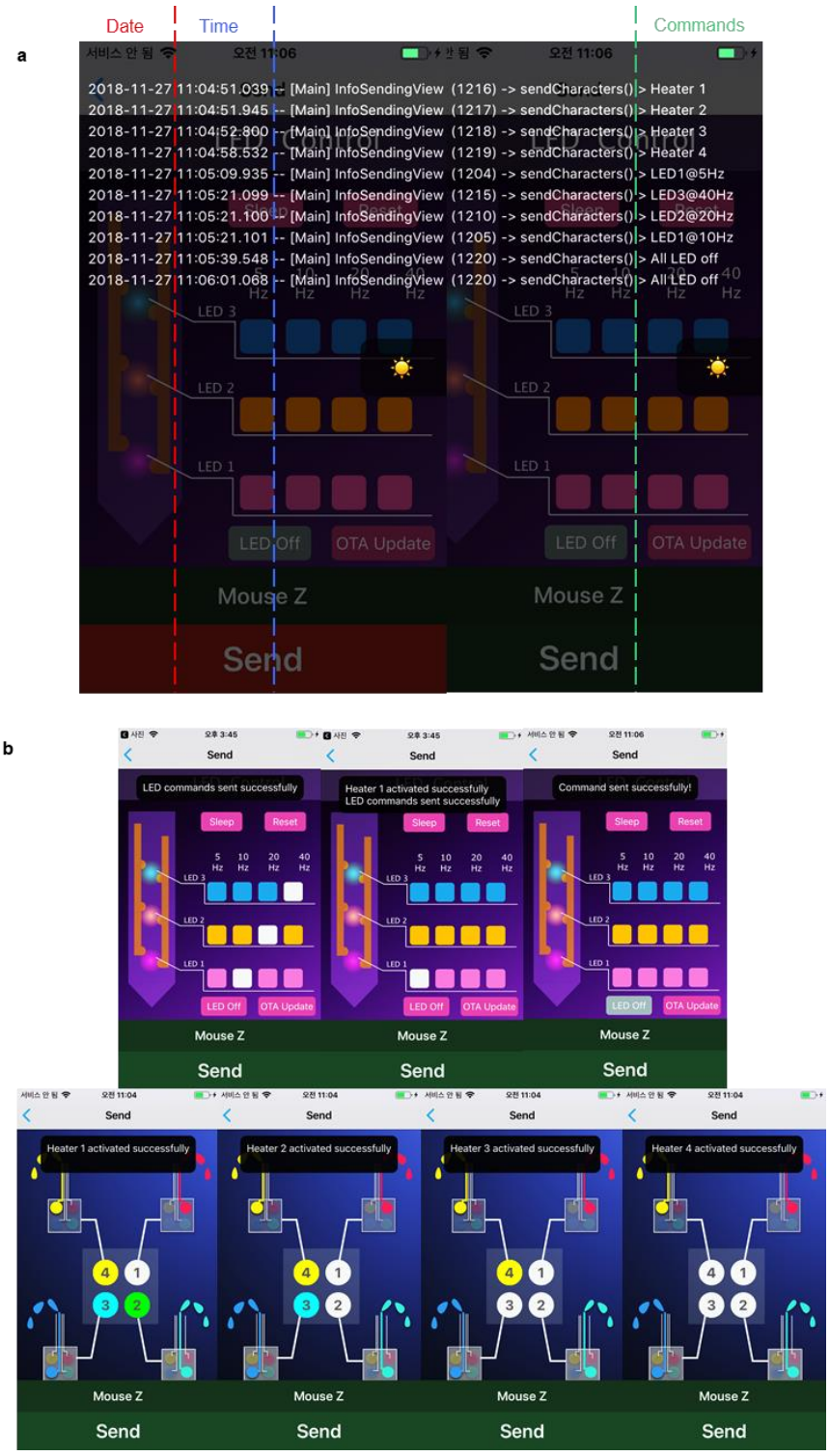

Figure 2.26 – Tracking and validation features in the smartphone app through Bluetooth communication. (a) *A snapshot of the app displaying the timestamps (with millisecond resolution) of the wireless operation.* ***(b)*** *A series of snapshots of the app showing "Success" confirmation toasts whenever a command successfully triggers the device. These features can allow device operation without any concerns regarding visual cues, especially for photosensitive experiments, that may arise due to indicator LEDs on the wireless module.*

The BLE transmission tests were conducted to check the isotropic penetration power of wireless signals through different material types of varying thicknesses – wood, plastic and glass. It was found that materials with a thickness up to ~10 cm had no significant effect on the transmission and reliability of the wireless signal packets as shown in **Table 2.1**, highlighting the obstacle invariability in Bluetooth technology compared to other wireless techniques like IR and RF. A 2.4 GHz antenna connected to a RF spectrum analyzer was placed inside a custom built enclosed metal box which was open only on one side. The BLE receiver module was programmed to be in advertising mode transmitting advertisement packets every 300 ms (+4 dB transmission power). The open side of the metal box was covered by materials of varying thicknesses (24 mm, 48 mm, 76 mm, 96 mm) and the resulting received power of packets sent at 2.403 GHz channel were measured at two specific distances from the receiving antenna (0.5 m and 1 m) and the results showed insignificant loss in signal power. Successful functional tests were also conducted from outside closed rooms (**Fig. 2.24b**) and concrete walls.

TABLE 2.1 BLUETOOTH SIGNAL PENETRATION TESTS THROUGH DIFFERENT OBSTACLES

Penetration Power	**Power (dB) through Wood**		**Power (dB) through Plastic**		**Power (dB) through Glass**	
Thickness (mm)	**D = 0.5 m**	**D = 1 m**	**D = 0.5 m**	**D = 1 m**	**D = 0.5 m**	**D = 1 m**
24	-27 to -32	-33 to -35	-27 to -31	-31 to -35	-29 to -33	-35 to -43
48	-27 to -32	-33 to -35	-27 to -31	-31 to -35	-29 to -33	-35 to -43
72	-27 to -32	-33 to -35	-27 to -31	-31 to -35	-29 to -33	-35 to -43
96	-27 to -32	-33 to -35	-27 to -31	-31 to -35	-29 to -33	-35 to -43
GOOD (> - 70 dB)		**WEAK (- 70 dB to - 90 dB)**			**BAD (< - 90 dB)**	

t = thickness of material, and D = distance of BLE SoC from receiver antenna connected to RF spectrum analyzer. The signal integrity stays within a reliable range as shown[31].

2.4 *In Vivo* Functional Validation in Freely-moving Mice

2.4.1 Chronic, wireless drug delivery with precise temporal control produces repeatable behavioral changes in mice

We first aimed to establish chronic reusability over previous wireless and standalone optofluidic platforms[8], [14] by expanding on the 'use-n-throw' nature of the device. Whereas, the previous platform allowed for a one-time heater activation for drug release, our goal was to utilize the Lego components to allow for multiple activations of drug release across an extended timeframe enabling more chronic applications of this optofluidic platform. Previous work has shown that these types of microfluidic probes have reduced immunoreactive glial responses, in comparison to conventional cannulas; however, it is not known whether the immunoreactive glial response changes over time with chronic implantation of these microfluidic probes. In order to determine the immunoreactive glial responses from chronic, deep brain implantation of these microfluidic probes, we examined astrocytic glial fibrillary acidic protein (GFAP) activity and ionized-binding molecule 1 (Iba1) microglial immunostaining at multiple time points after device implantation (**Fig. 2.27a–d**). We observed reductions in both GFAP (39%) and Iba1 (35%) immunostaining around the implant site as soon as two weeks after implantation (compared to one-week post-surgery expression). This reduction in GFAP (44%) and Iba1 (80%) was even more dramatic 4 weeks after implantation. Moreover, the Lego optofluidic probe (which can deliver four independent drugs and two wavelengths of light) displace less tissue area (one-third) than a 400 μm-diameter conventional metal cannula. This is not to mention that the metal cannula (E = 200 GPa for stainless steel) has large mechanical mismatch with soft neural tissue (on the order of kPa for brain tissue), prone to cause more tissue damage and inflammatory response compared to soft polymeric probes (1 MPa for PDMS). These results suggest that these microfluidic probes are suitable for long-term implantation and elicit minimal and transient glial response over time.

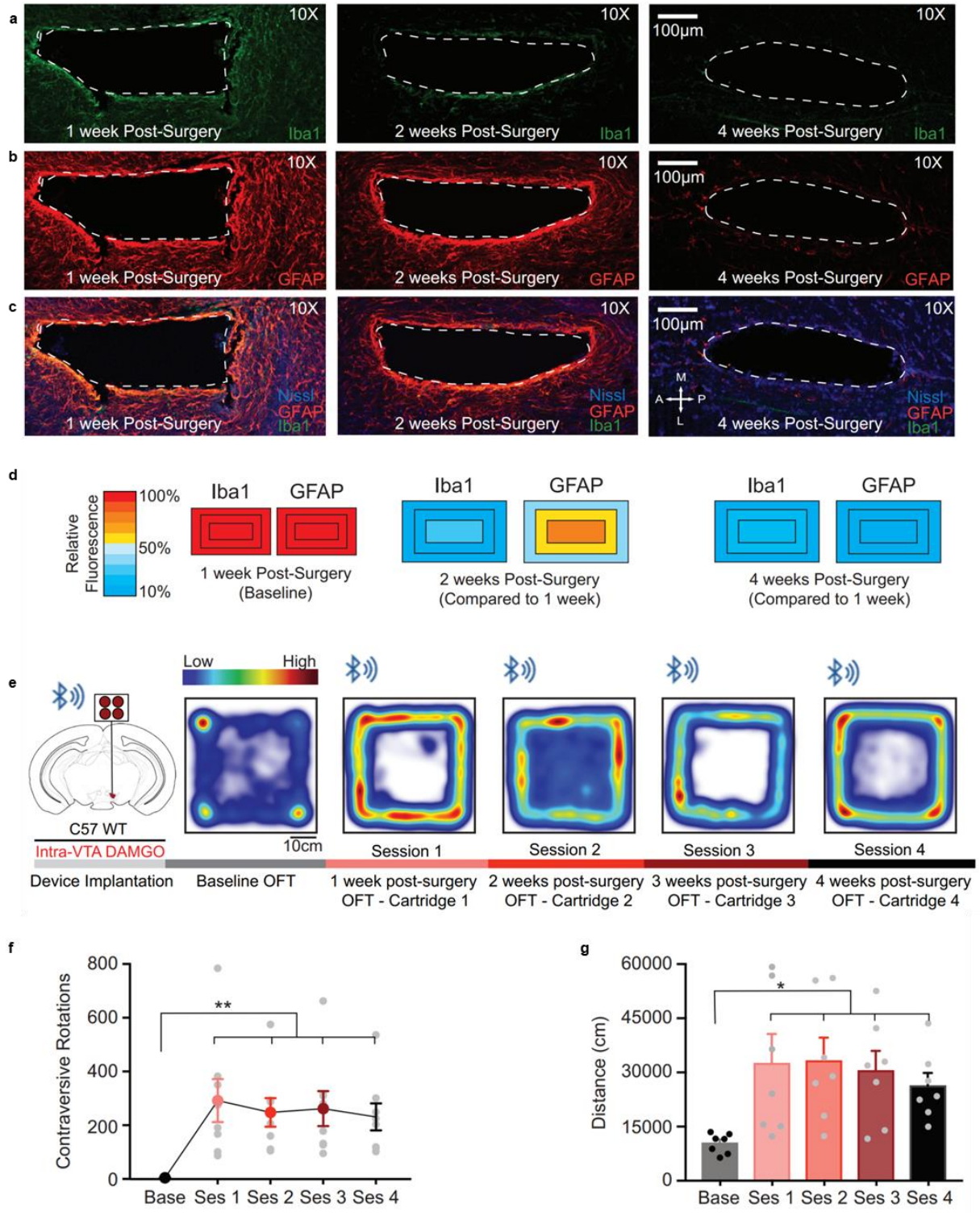

Figure 2.27 – Chronic, wireless drug delivery produces repeatable behavioral changes in mice. *Wireless delivery of multiple DAMGO infusions into the Ventral Tegmental Area produces consistent, repeatable increases in stereotypical rotational behavior.* ***(a–d)*** *Representative fluorescence images (10X) of 30 µm horizontal striatal slices depicting immunohistochemical lesion staining for activated microglia (**a,***

*Iba1, green), astrocytes (**b,** GFAP, red), and overlaid with Nissl bodies (**c,** blue) after 1 week (left column), 2 weeks (middle column), and 4 weeks (right column) of implant surgery. All histological and confocal settings were kept consistent across groups. Scale bar = 100 μm. **(d)** Immune responses were quantified by comparing 1-week post-surgery immunoreactivity (baseline) of Iba1 and GFAP to immunoreactivity 2 weeks and 4 weeks post-surgery. Mean fluorescence was quantified within increasing rectangles surrounding the implant site using FIJI, and expressed as percent changes (1-week baseline = 100%). Immune responses dramatically decreased over the 2 (~50%) and 4 (>50%) week timepoints compared to 1-week post-surgery immediately surrounding the implant site. **(e)** Calendar outlining timeline for device implantation and subsequent, repeated open-field (OFT) testing (60 min sessions), with respective representative heat maps of locomotion after Bluetooth, wireless intra-VTA DAMGO release. **(f)** Contraversive rotations and **(g)** overall locomotion after within-subject, counter-balanced experiments following Bluetooth, wireless intra-VTA infusion of vehicle (baseline), and DAMGO (1 week, 2 weeks, 3 weeks, 4 weeks post-surgery) (n = 7, repeated One-Way ANOVA, *p<0.05, **p<0.01; F(4,35) = 4.181 for contraversive rotations, F(4,30) = 2.916 for locomotion). Data represented as mean ± SEM.*

To demonstrate the feasibility of chronic, repeated delivery of localized pharmacological agents, we implanted microfluidic devices unilaterally into the ventral tegmental area (VTA) of wild-type mice (C57Bl6). Previous studies have shown that activation of μ-opioid peptide receptors (MOPRs) within the VTA cause a pronounced, rapid increase in locomotion as well as a dramatic increase in stereotypical contraversive (from the site of drug delivery) rotational behavior[32], [33], making this an ideal demo behavior for repeated pharmacological challenge *in vivo*. We then wirelessly delivered the selective MOPR peptide agonist, DAMGO ([D-Ala2 , N-MePhe4 , Glyol]-enkephalin, 500 pmol, 0.5 μL total volume, Tocris), into the VTA of wild-type mice performing an open-field task (OFT) across multiple timepoints post-surgery (1 week, 2 weeks, 3 weeks, and 4 weeks after device implantation) (**Fig. 2.27e**). We found that intra-VTA DAMGO significantly increased the number contraversive rotations (**Fig. 2.27f**), as well as the distance, traveled (**Fig. 2.27g**) (locomotor activity) in comparison to baseline measurements. Additionally, DAMGO-induced increases in rotations and locomotor behavior were consistently maintained at all measurable timepoints (**Fig. 2.27f-g**) for up to at least 4 weeks post-implantation. Though tested for only four weeks, the replaceable nature of these devices could allow for long term chronic pharmacological delivery for the duration of the animal's lifetime (>6 months). It should be noted that activation of only 1 reservoir was sufficient to produce DAMGO-mediated behavioral effects and that we used the same microfluidic channel by activating the same location reservoir in a new cartridge throughout the behavioral paradigm. This result strongly suggests that the

microfluidic channels remain unobstructed over long term use or after repeated use. However, it is also feasible to use a separate cartridge filled with saline and activate the same microfluidic channel to flush the channel from the previous use/drug.

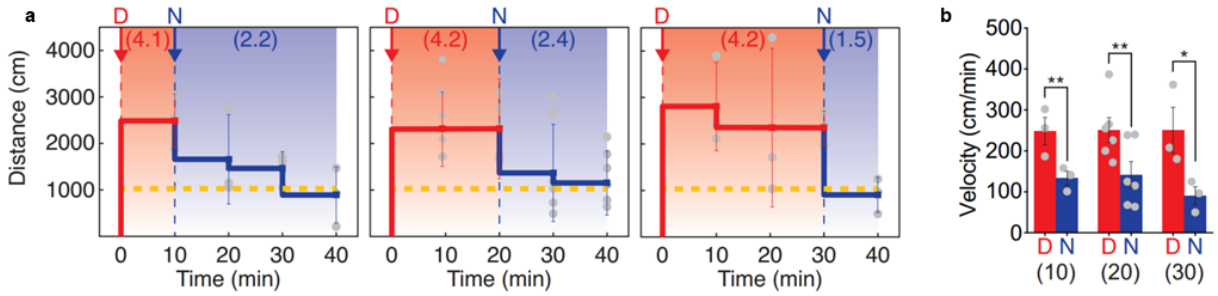

Figure 2.28 – Highly precise in vivo temporal sequencing of multiple drugs. (a) *Bidirectional behavioral modulation through multidrug infusions in VTA within the same animal cohort (n = 6) using the same devices that were wirelessly re-programmed with precise temporal delays. DAMGO infusions (red arrow) robustly increased locomotor activity (distance, cm) and velocity (cm/s, values in red parentheses) compared to vehicle-injected mice (dashed yellow line, values derived from* ***Fig. 2.27f-g****). Naloxone infusions occurred 10 (left), 20 (center) or 30 (right) minutes after DAMGO in the same mice across different test days (counterbalanced). Naloxone blocked DAMGO enhanced locomotion and velocity (values in blue parentheses).* ***(b)*** *A comparative bar graph highlighting the relative decrease in average velocity (cm/minute) when naloxone is released 10, 20 and 30 min after releasing DAMGO (n = 6, repeated One Way ANOVA, *p<0.05, **p<0.01; F(1,9) = 41.18).*

To further highlight the wirelessly reprogrammable, temporally controlled capabilities for multiplexed drug deliveries within the same behavioral session, we infused intra-VTA DAMGO, followed by an intra-VTA infusion of the non-selective, competitive opioid antagonist naloxone ((5α)-4,5-Epoxy-3,14-dihydro-17-(2-propenyl)morphinan-6-one hydrochloride) at various timepoints (10, 20, 30 min after DAMGO) (**Fig. 2.28a**). We demonstrate that naloxone reverses the DAMGO-induced increases in locomotion in a time-specific manner (**Fig. 2.28a**), thereby demonstrating multi-drug release within the same brain region during a single behavioral task. Notably, DAMGO-increased locomotion remained significantly high until the delivery of Naloxone (**Fig. 2.28b**). This same animal could feasibly be controlled via multiple drug deliveries over an extended timeframe through replaceable drug cartridges and wirelessly re-programmed time delays, thus highlighting its precise temporal control for multiplexed drug delivery. Taken

together, these proof-of-principle experiments demonstrate that these optofluidic devices are suitable for chronic, repeated delivery of agents with precise temporal control within the deep brain of awake-behaving animals.

2.4.2 Wireless, selective control of drug delivery within a group of simultaneously behaving mice

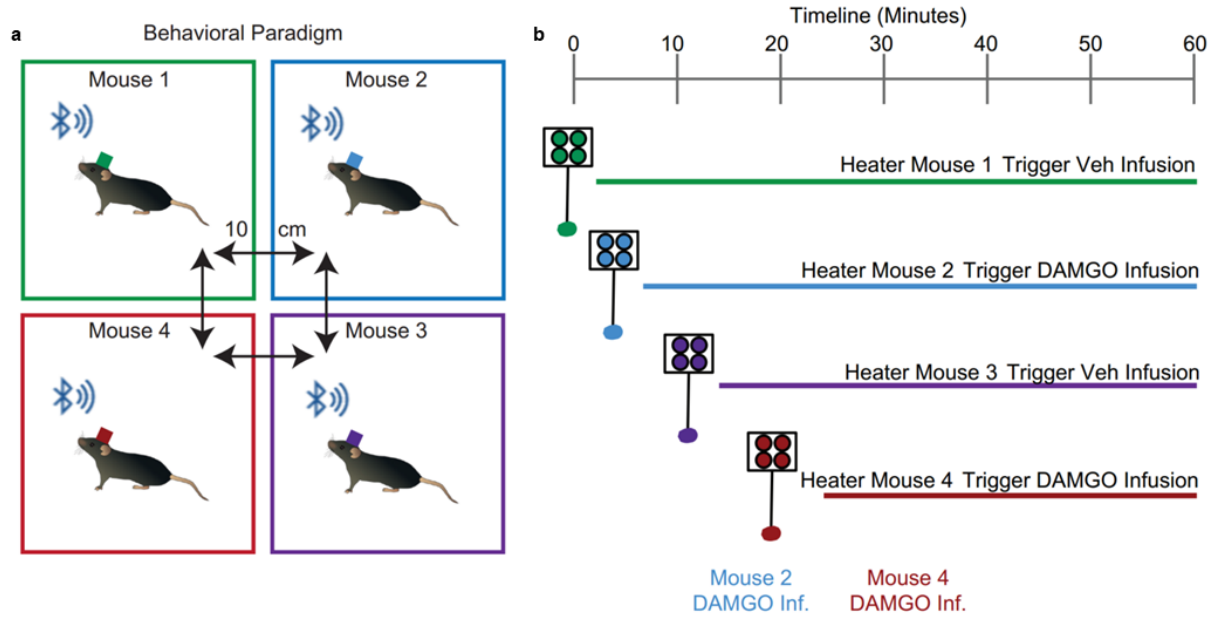

Figure 2.29 – Wireless, selective control of drug delivery within a group of simultaneously behaving mice. *Individual, selective control of wireless-mediated intra-VTA infusion of DAMGO increases stereotypical locomotor behavior within a group of mice.* ***(a)*** *Behavioral paradigm depicting color-coded mice behaving simultaneously in separate, neighboring (10 cm) arenas* ***(b)*** *Timeline depicting separate Bluetooth, wireless heater activations of intra-VTA vehicle (Veh) or DAMGO release within multiple mice during the same 60 min OFT test.*

Another drawback of the prior wireless optofluidic device platforms[8], [14] was the inability to efficiently activate a specific mouse selectively in a group of multiple mice within a compact laboratory behavioral space. This limited the investigator to run one animal in a behavioral assay in an area well-separated from other animals. This is true for most wireless platforms[8]–[24], as requirements for the specific receiver antenna design and unique transmitter setups severely limit the combinatorial scalability and selectivity to efficiently run multiple behavioral experiments within

a confined space that consist of different treatment groups with same or distinct stimulation parameters.

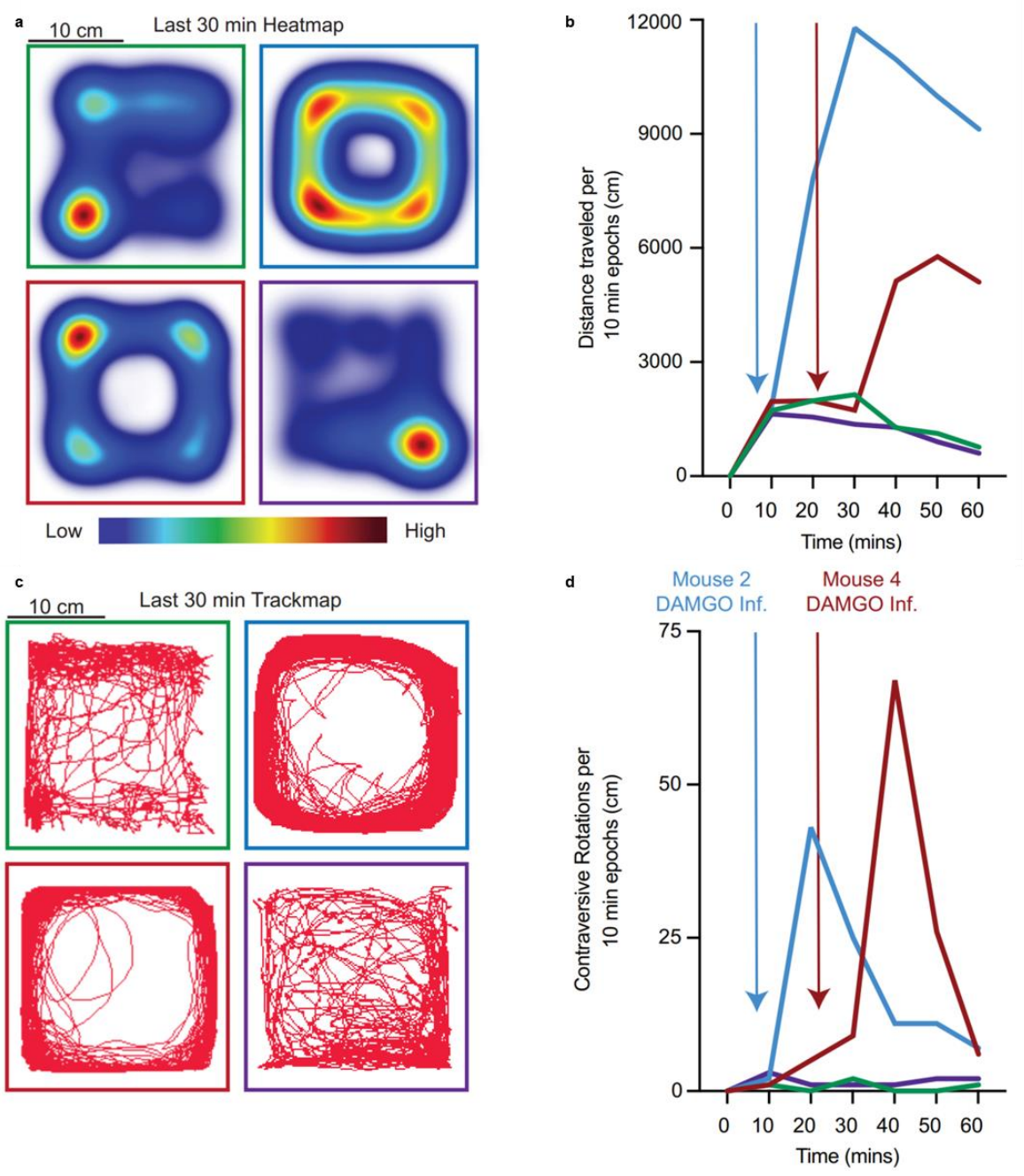

Figure 2.30 – Selective animal behavior control and analysis. (a) *Representative heatmaps depicting locomotion from the last 30 mins of the OFT session corresponding to the panel in* ***Fig. 2.29b****.* ***(c)*** *Representative traces depicting locomotion from the last 30 mins of the OFT session corresponding to the panel in* ***Fig. 2.29b****.* ***(b)*** *Locomotion and* ***(d)*** *contraversive rotations during within-session 10-min epochs after separate heater activations of intra-VTA vehicle (Veh) or DAMGO release with colors corresponding to mice in panel b (n = 4). Data represented as within-session total during 10 min time epochs.*

To determine the capability of individual selective control within a group of mice, we implanted wildtype mice (C57/Bl6) with optofluidic devices into the VTA. During the test day, we filled two of the cartridges with vehicle (saline), and the other cartridges with DAMGO. We then placed each animal within an open field arena that was spaced 10 cm from the other open field arenas for a 60 min open field test (**Fig. 2.29a**). After the start of the session, we wirelessly delivered either vehicle or DAMGO at different timepoints within the 60 min test session (**Fig. 2.29b**). We found that wireless activation of intra-VTA DAMGO at different timepoints within the same session rapidly increased both contraversive rotations and distance traveled, in comparison to mice that received wireless activation of intra-VTA vehicle (**Fig. 2.30a–d**). Additionally, in utilizing a smartphone-based app for selective control, there was a negligible temporal lag in the feasibility of switching reservoir activations between individual mice. This also was a clear indication that Bluetooth signal interference did not impact the behavior of surrounding mice. These data demonstrate the multiplexed capability of these optofluidic devices for dynamic, selective control of pharmacological manipulations in several individual mice concurrently within a behavioral paradigm.

2.4.3 Incorporation of wireless photostimulation and wireless pharmacology in awake, behaving mice

We next sought to demonstrate the *in vivo* capabilities of this optofluidic platform by extending the above drug delivery capabilities to incorporate concomitant optogenetics and pharmacology. We chose to demonstrate this multiplexed functionality in a real-time place preference assay. This close-loop behavioral method is now heavily utilized in behavioral neuroscience to assess the valence of a brain circuit within a neutral context[34]. It has been previously reported that photostimulation of lateral hypothalamic (LH) GABAergic terminals that originate from the bed nucleus of the stria terminalis (BNST) promotes reward-like behaviors[35]. Using this model, we

tested whether selective activation of the *Vgat*$^{BNST-LH}$ pathway would produce a specific preference within a neutral context using a real-time place test assay (RTPT). In a RTPT, animals have access to two identical chambers and receive photostimulation upon entering one chamber, but not the other (counterbalanced across animals). Here, we employed a closed-loop BLE network (SimbleeCOM protocol), which can be synchronized with an animal tracking camera system whereby the animal's behavior conditionally triggers activation of the μ-ILED. The SimbleeCOM transmitter was placed outside the chamber and based on the nature of received interrupts (depending on the position of the mouse) from the camera tracking system (Noldus Ethovision), it wirelessly manipulated the device (μ-ILED stimulation) in the animal by sending out pre-configured commands. Preference and avoidance data are then calculated as time spent in the photostimulation-paired chamber, expressed as a percentage of total time[36], [37]. To stimulate this pathway, we first injected a Cre-dependent Channelrhodopsin-2 viral construct (AAV5-DIO-EF1α-ChR2-eYFP) unilaterally into the BNST of *vGAT*-Cre mice and positioned optofluidic devices in the LH to allow for photostimulation of GABAergic projections (**Fig. 2.31a–b**).

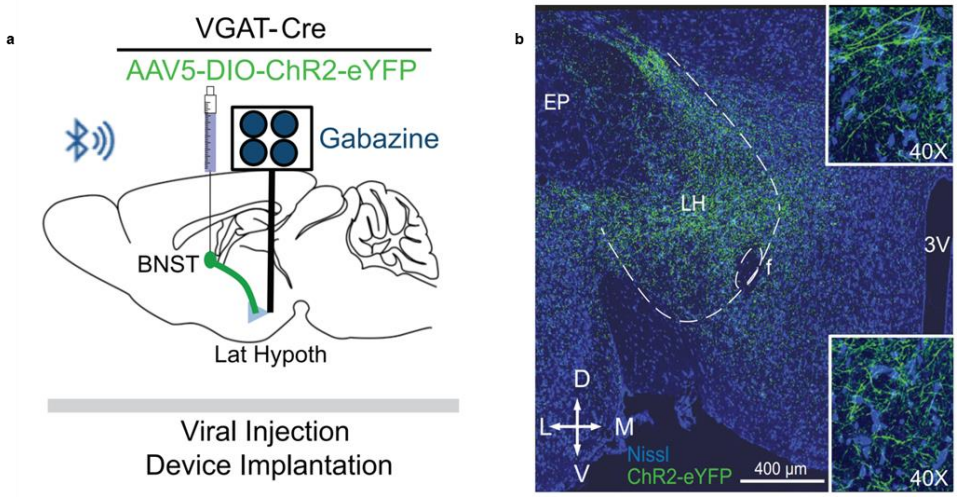

Figure 2.31 – Incorporation of wireless photostimulation and wireless pharmacology in awake, behaving mice. *Wireless activation of GABAzine blocks VGATBNST-LH photostimulation-mediated real-time place preference.* ***(a)*** *Schematic diagram for ChR2 virus injection into the bed nucleus of the stria terminalis (BNST) and optofluidic device implantation into the lateral hypothalamus (LH).* ***(b)*** *Coronal images (40X) of ChR2-eYFP terminal expression in the LH following viral injection in VGAT-Cre animals. Images show Nissl (blue) and ChR2-eYFP (green). EP; entopeduncular nucleus, LH; lateral hypothalamus, f; fornix, 3V; third ventricle.*

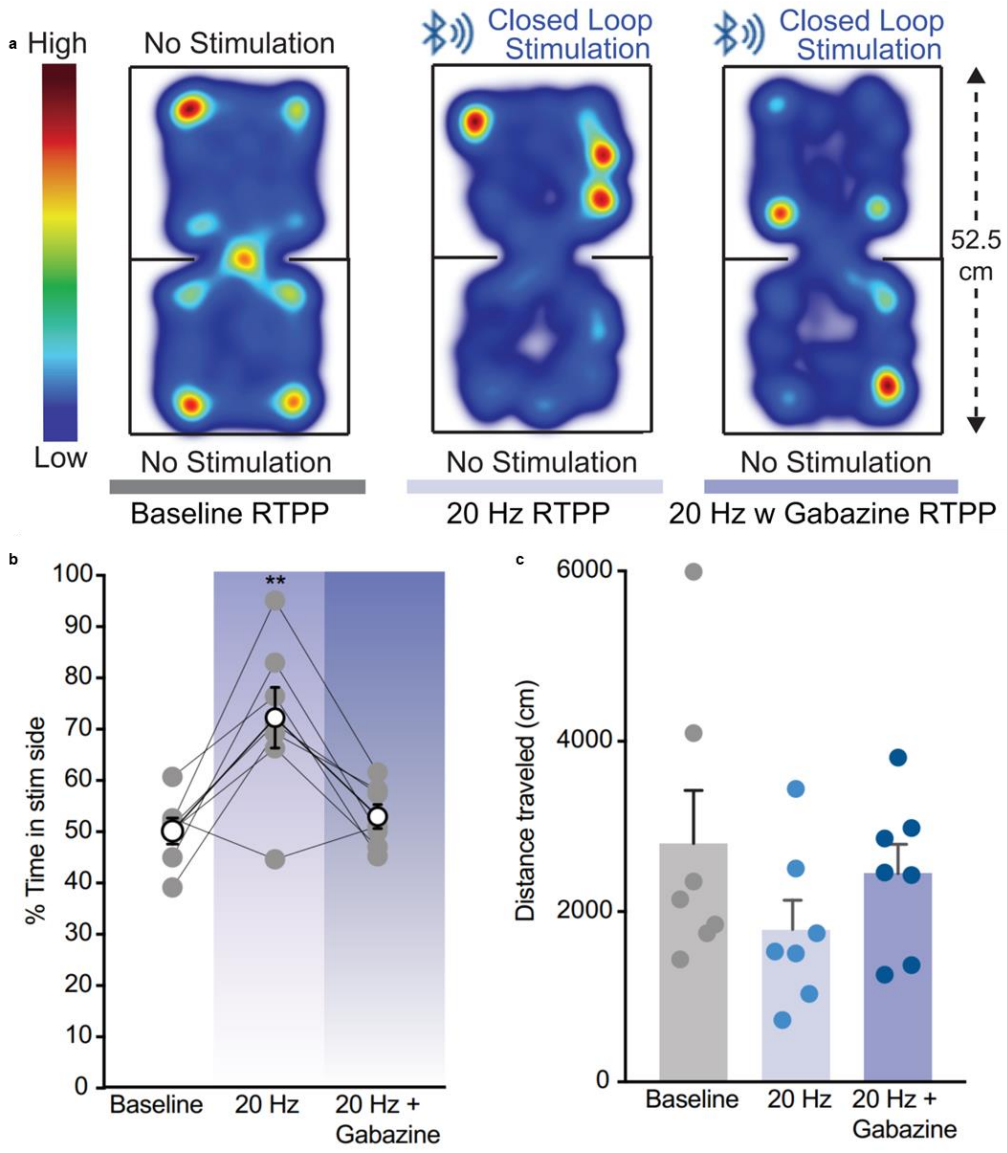

Figure 2.32 – Closed loop in vivo photostimulation and drug delivery in mice. ***(a)*** *Subsequent panels depict 20 min RTPP sessions with corresponding, representative heat maps of locomotion during baseline, 20 Hz photostimulation, and 20 Hz photostimulation with GABAzine sessions.* ***(b)*** *Photostimulation of BNST-LHGABAergic terminals (473 nm, 20 Hz, 10 ms pulse width) expressing ChR2 drives a real-time place preference, as measured by % time spent in stimulation side, and is blocked by pre-session infusion of GABAzine.* ***(c)*** *Total locomotion was not different across all session of RTPP testing. All data represented as mean ± SEM (n = 6 One-Way ANOVA, **p<0.01; F(6,12) = 9.702).*

We then tested animals for 3 consecutive days consisting first of a 20 min baseline session with no stimulation. This was then followed by a 20 min, 20 Hz session where animals received photostimulation (20 Hz, 10 ms pulse width, 470 nm wavelength) upon entering the photostimulation-paired side. Lastly, the animals received micro-infusions of Gabazine ($GABA_A$

receptor antagonist) into the LH prior to undergoing the real-time place testing session. In accordance with the previous findings[31] we found that *vGAT*-Cre mice expressing ChR2 exhibited a robust preference for the photostimulation-paired chamber in comparison to their baseline measurements (**Fig. 2.32a**). However, upon wireless pharmacological delivery of Gabazine (10 µM, 0.5 µL total volume, Tocris) into the LH prior to the real-time place preference assay, the preference for the photostimulation-paired chamber was completely blocked and decreased the preference scores to reflect those seen within the baseline test session (**Fig. 2.32b**). Additionally, we found no effect of 20 Hz photostimulation nor with Gabazine + 20 Hz photostimulation on locomotor activity, compared to baselines, during the real-place preference test sessions (**Fig. 2.32c**). These data demonstrate the parallel incorporation of smartphone, wireless control of µ-ILED photostimulation of neural circuits in combination with pharmacological delivery in freely moving mice.

2.5 Discussion

Here we describe the development of a combinatorial wireless device platform for *in vivo* neuropharmacology and optogenetics that is a self-contained multifunctional system capable of chronic, selective control within freely moving animals. These thin, flexible neural probes allow researchers long-term, biocompatible optofluidic access to neural tissue deep inside the brain as well as chronic drug supply with temporal control through its replaceable Lego drug cartridges. The platform provides scalable output modalities with programmable wireless control where an 'easy-to-use' smartphone app transforms any commercial smartphone into a long range and isotropic wireless transmitter possessing wireless re-programmability as well as precise selectivity within large animal cohorts. This provides a significant advancement from the existing embodiments of fluidic neural interfaces[6]–[8], [14], [38]–[40] (**Table 2.2**).

TABLE 2.2. COMPARISON OF VARIOUS STATE-OF-THE-ART DEVICES FOR FLUIDIC NEURAL INTERFACES [6]–[8], [14], [41]

Property	**Chronic Lego Optofluidics** (This Work)	**Implantable Optofluidics**[6] (Noh *et al.*, 2018)	**Programmable Optofluidics**[1] (Jeong *et al.*, 2015)	**MiNDS**[9] (Dagdeviren *et al.*, 2018)	**Multifunctional Fibers**[7,8] (Park *et al.*, 2017, Canales *et al.*, 2015)
Standalone System?	**Yes**	Yes	Yes	No (Tethered electronics with wireless drug delivery pumps)	No
Operation	**Bluetooth Wireless** (Omnidirectional control) 10 m - 100 m	RF Wireless (Angular dependency) ~10 cm	Infrared Wireless (Directional control) ~2 m	Bulky & Heavy Commercial Wireless Pumps <3 m	Tethered
Modalities	**Optical & Fluidic** (Independent control of multiple light wavelengths)	Optical & Fluidic (Single Light Wavelength)	Optical & Fluidic (Single Light Wavelength)	Electrical & Fluidic (No Photostimulation)	Optical, Fluidic & Electrical (Single Light Wavelength)
# of Drug Deliveries (maximum)	**Unlimited (Standalone replaceable cartridges)**	1	4	Limited (Refillable pumps until batteries last)	Unlimited (External tethered sources)
# of Independent Drug Channels	**4 (Deliver to the same target location)**	1	4 (Deliver to the same target location)	1	2 (Deliver to the same target location)
Time constraint of experiment after surgical implantation	**None | Chronic (Drug cartridges plugged in anytime; rechargeable batteries)**	Within 2 weeks (Drug evaporation)	Within 2 weeks (Drug evaporation)	<4 weeks (Battery lifespan/ Disposable)	None (Tethered)
Mechanical Property of the Probe	**Soft, flexible Modulus ~ 1 MPa Stiffness: 13-18 N/m Thickness = 80µm**	Soft, flexible Modulus ~ 1 MPa Stiffness: 13-18 N/m Thickness = 80µm	Soft, flexible Modulus ~ 1 MPa Stiffness: 13-18 N/m Thickness = 80µm	Rigid Modulus ~ 200 GPa Thickness = 200 µm	Flexible Stiffness~107-149 N/m Thickness = 400 -700 µm
Remote controller	**Smartphone**	Bulky RF hardware and antenna	Custom-built IR transmitter	Commercial iPrecio hardware	Tethered external hardware
Multiple Independently controllable animals within a Large Group	**Yes (Scalable, > 10)**	No, Limited (All devices receiving RF signals will be activated)	No, Limited (All devices within same LoS will be activated)	No	N/A
Scalable Target/Output Selectivity within a Large Congested Group	**Yes, 100% accuracy (Software based wireless pairing)**	No (All devices receiving RF signals will be activated)	No (Manual pointing within close proximity)	No	No (Limited feasibility due to External Tethering)
Line of Sight/ Obstacle Handicap	**No**	Yes	Yes	No	N/A
Wireless Re-Programmability	**Yes (Over the Air Update)**	No	No	No	N/A
Programmable/ Scalable Closed Loop Networks	**Yes (Wirelessly reconfigurable)**	No	No	No	N/A

Wireless/ Standalone Tethered/ External Connections

2.5.1 Summary of Unique Device Capabilities

The unique features and capabilities of the Lego optofluidic device, as outlined below, can open up novel opportunities to conduct a whole new avenue of chronic multimodal *in vivo* neuroscience experiments. Overall, our new device clearly establishes its distinct footmark by offering unique "plug-n-play" replaceable drug cartridges for chronic wireless *in vivo* pharmacology, highly precise temporal control for delivery of multiple, distinct drugs, multi-wavelength photostimulation for versatile optogenetics, and a superior Bluetooth wireless platform that offers powerful, yet easy-to-use control features for neuroscientists, overcoming limitations of conventional tethered tools as well as other types of wireless modules. The main key features of our Lego optofluidic devices that make it stand out among contemporary technologies are summarized below:

1. The Lego optofluidic devices possess the ability to repeatedly deliver pharmacological agents and/or viral vectors wirelessly in freely moving animals. This is enabled through unique 'plug-n-play' type replaceable "Lego" drug cartridges, which is optimized for reliable, robust assembly/disassembly through engineered material mechanics and form factors (requiring minimum force for assembly while allowing hermetic seal). This feature allows the wireless standalone device to achieve chronic wireless *in vivo* pharmacology with potential for chronic wireless optopharmacology.
2. It furthermore allows **highly precise and customizable temporal control** for simultaneous or pre-programmed delayed release of multiple, distinct drugs, thus enabling versatile, combinatorial chronic pharmacology in freely behaving animals. We now demonstrate this feature in a new experiment (Fig. 4h-i). The different temporal profiles can be easily set up through Over The Air (OTA) wireless re-programming, which is a feature provided by the Bluetooth module we have incorporated into our design, thus providing scientists with an ease-of-use option for remotely setting customized temporal

control profiles for distinct experiments. This was demonstrated through two unique experiments, one table top (to highlight precise temporal resolution) and another *in vivo* (to demonstrate wirelessly reprogrammable delay for multiple drug deliveries over several days in multiple animals):

a. We demonstrated this capability by delivering two different fluids into the water with a one second delay (Supplementary Fig. 3, Supplementary Video 1). Sub-second resolution control of fluid is possible, but we used one-second delay to noticeably separate the ejected dyes in water for a visual demonstration. This delay can easily be set to zero to allow simultaneous delivery of two similar or different drugs (for unique combinatorial dynamics).

b. Using this temporal control capability, we could successfully conduct the suggested *in vivo* experiment using drugs with opposing effects to control behavior in a bidirectional manner within the same animal. Due to the fact that drugs take time to reflect their effect *in vivo*, we increased this temporal delay to 10, 20, and 30 minutes – delivering the selective opioid antagonist drug (Naloxone), 10, 20 and 30 minutes after releasing the selective Mu-opioid agonist drug (DAMGO). Through this *in vivo* experiment (Fig. 4h-i), we demonstrate that we can temporally release DAMGO to increase locomotion (in adherence with Fig. 4f-g); and then we can reverse DAMGO-induced locomotion via delivery of the receptor antagonist Naloxone in a temporally-defined manner. Notably, DAMGO-increased locomotion remains high until the delivery of Naloxone, regardless of whether the Naloxone is administered 10, 20, or 30 minutes after DAMGO.

3. The different temporal profiles can be easily set up through Over The Air (OTA) wireless re-programming, which is a feature provided by the Bluetooth module we have incorporated into our design, thus providing neuroscientists with an ease-of-use option for remotely setting customized temporal control profiles for distinct experiments thus limiting

any effect of human intervention on the natural behavior of freely moving subjects. In summary, we have demonstrated an additional unique feature of our optofluidic device for chronic, wireless temporal control of multiple, distinct fluids, which is substantial advancement over conventional cannula-based approach.

4. Integration of **independently controlled, multi-wavelength µ-ILEDs** at the tip of microfluidic channels allows programmable and multi-modal photo-switching of distinct opsins or chemical compounds within the same local region of tissue, thus opening up opportunities for advanced *in vivo* optogenetics, pharmacology as well as optopharmacology in a chronic yet stable manner.
5. **Uniqueness with Bluetooth:** Bluetooth itself is not new, but the integration of Bluetooth technology with neural devices enables a whole new set of wireless behavior neuroscience experiments that have been inefficient and hard to be achieved through tethered and other wireless approaches:
6. Integration of a Bluetooth wireless module **enables user-friendly smartphone control**, eliminating complex, bulky and expensive tools that are hard to be controlled by non-engineers, and easy to use in typical animal testing environments.
    a. Bluetooth facilitates **scalable, dynamic selective control** that allows to efficiently run multiple behavioral experiments with same or distinct stimulation profiles within a limited laboratory space, thus improving data throughput and efficiency over time. All customizations for distinct animals can be dynamically changed without even closing the smartphone App, thus minimizing external hardware setups, manual effort, and temporal lag to switch between animals. These are hard to achieve if implemented through Infrared or RF based techniques due to line-of-sight handicap and complicated transmitter setups.

b. Bluetooth allows an **omnidirectional and long range of operation** (up to 100 m), which also enables wireless control from outside the behavioral room, thus completely removing potential for observational effects on experimental session.
c. Moreover, **easy-to-set-up wireless closed loop controls** further widen opportunities for complex behavior experiments such as social interaction studies.
d. The **wirelessly re-programmable** nature allows neuroscientists to reprogram multimodal stimulation profiles on-the-fly, including timed delays and sequencing for combinatorial multidrug deliveries and/or multiwavelength photostimulation patterns, thus significantly improving flexibility and versatility of experiments.

7. **Advantages over a state-of-the-art commercial pump (more detailed review in the next section)**: The Lego optofluidic device provides a significant advance over the state-of-the-art commercially available wireless pumps (SMP-300, iPrecio) by allowing multidrug release without affecting animal's natural behavior within a single behavior session and easy switching of drugs through replaceable Lego cartridges for versatile chronic studies, unlike the commercial pump, which can deliver only a single drug within a behavioral session and requires cumbersome process of cleaning a reservoir before replacing an original drug with a different type. Furthermore, our device is smaller and lighter (ours: 1260mm3;2g vs SMP-300: 2678 mm3; 3.3g), thus allowing implantation in freely moving animals as small as mice. Even with a smaller form factor compared to the smallest commercial alternative, the device also allows simultaneous and independent neural manipulation with four distinct drugs and photostimulation with two unique wavelengths, providing an ultra-compact multimodal, multifunctional solution. Thus, by integrating rechargeable batteries and replaceable cartridges, our device enables truly chronic optofluidic studies, unlike disposable commercial alternative which cannot be used once the battery is exhausted (1-6 weeks depending on usage).

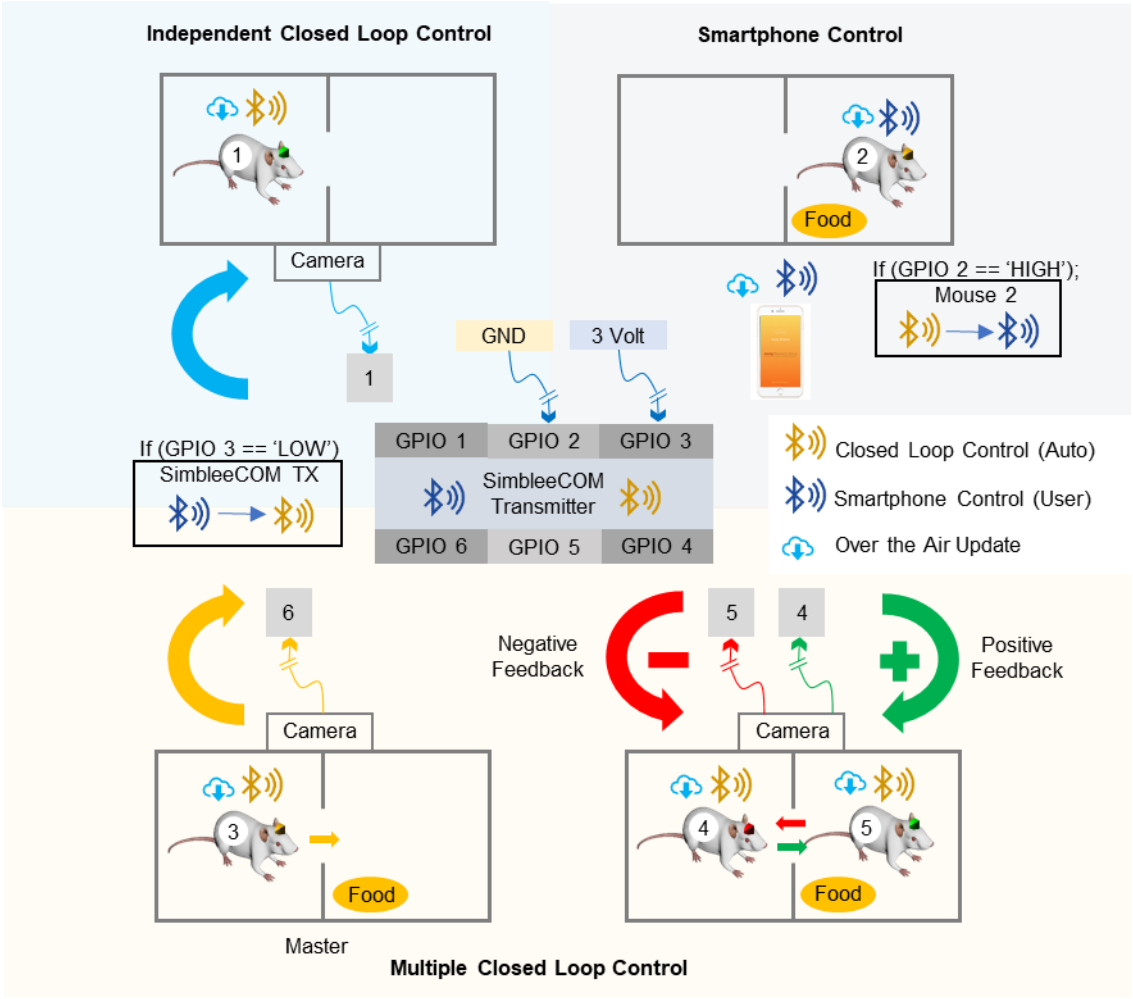

Figure 2.33 – Programmable, customizable, scalable wireless ecosystem for chronic optofluidic studies in freely moving animals.

Overall, integration of Bluetooth as the wireless ecosystem truly leverages the versatile, multimodal and chronic capabilities of the Lego optofluidic device through a commercially available smartphone with user-friendly interfaces.

2.5.2 Comparison with State-of-the-Art Commercial Pumps

The Lego optofluidic device has its own set of distinct abilities and features, which can open new opportunities in neuroscience research. It must be noted that we are comparing our device with a state-of-the-art commercial pump, SMP-300 (iPrecio), which is not readily available in the

market yet, unlike its predecessor SMP-200 (iPrecio), which is larger and bulkier than SMP-300 and thus not suitable for use in mice:

1. **Size:** The smallest commercial microfluidic wireless pump SMP-300 (to-be-released; 2678 mm3; 3.3g), with the ability to deliver only a single drug, is still bulkier and larger than our wireless optofluidic device (1260mm3; 2g) and not suitable for use in mice.
2. **Additional Appendages:** The SMP-300 weights and size mentioned above does not include the non-removable, 50 mm long titanium antenna as well as the associated catheter tubing, which delivers the drug from the implanted device location to the target region (e.g.: the brain), which is usually located at a far location from the device. Also, the device bulk is implanted subcutaneously inside the body; such a bulky, rigid device with associated tethers implanted inside the body can lead to unnecessary tissue displacement, undue stress, and irritation in freely moving animals.
3. **Disposability:** The SMP series are disposable in nature and thus cannot be reused once batteries are exhausted (even if reservoirs can be refilled) and hence are non-chronic in their utility. For SMP-300, depending on the programmed flow rate, the device will need to be disposed within 1-8 weeks after implantation. On the other hand, the Lego optofluidic device has the ability to replenish both drugs and power indefinitely though rechargeable batteries and replaceable drug cartridges.
4. **Multimodality:** The SMP-300 can only deliver a single drug within a behavioral session. On the other hand, the Lego optofluidic device can deliver up to four unique drugs and two wavelengths of light simultaneously or independently, thus assuring promising applications in chronic opto-pharmacological studies in the future.
5. **Wirelessly Re-programmable Precise Temporal Control:** Due to its multimodal features and wirelessly (pre/re)-programmable capabilities, specific drug and/or light stimulations can be programmed to be delivered at a specific sequence at specific parts of the day. This highly

precise and wirelessly customizable temporal sequencing can be extremely useful to conduct nocturnal studies where the researcher need not be in the lab, thus improving the throughput of such multimodal *in vivo* stimulations. Delayed delivery with multiple flow rate profiles is possible in SMP-300 but only for single type of drug and no optogenetic ability. However, it is static in nature i.e once set and implanted, the profiles cannot be modified.

6. **Drug Switching:** The SMP-300 requires a cumbersome technique to clean the reservoir to replenish it with a new drug while as the Lego optofluidic device, we can easily switch reservoir activations or even swap cartridges a lot faster and easier, thus reducing time lag to conduct *in vivo* studies involving multiple distinct drug deliveries.
7. **Power Efficiency:** The SMP-300 can never be turned off and hence leads to power wastage (and hence unnecessary shortening of device lifetime) when not being used. On the other hand, the Lego Optofluidic Device can not only be put into the sleep mode for power saving but also be easily recharged without additional surgery.
8. **Wireless capability:** The SMP-300 has been tested to work only within <1m distance. That makes it equivalent to InfraRed based systems. Moreover, they cannot be wirelessly controlled in real time to deliver drugs but can only be pre-programmed before implantation. Once implanted, they use wireless communication only to communicate information related to the battery life and reservoir leftover volumes to the computer software. On the other hand, the unique Bluetooth abilities of the Lego optofluidic device allows it to be actuated remotely in real time from at least 10m away in an omnidirectional fashion. The SMP-300 is further incapable for reprogramming once implanted *in vivo*, unlike Lego optofluidic device which can be wirelessly reprogrammed indefinitely on-the-fly. On top of this, the highly selective control and scalable closed-loop control features allow easy-to-set-up operations for the neuroscience community.

In **Table 2.3** we have objectively compared the advantages and disadvantages of Lego optofluidic device and commercial wireless pumps in our discussion.

TABLE 2.3 COMPARISON WITH STATE-OF-THE-ART WIRELESS DRUG DELIVERY DEVICES

Property/Device	*Lego optofluidic device (This work)*	*SMP-200, iPrecio*	*SMP-300, iPrecio*
# of distinct drugs that can be delivered	4 per cartridge	1	1
# of wavelengths for photostimulation	2	0	0
Battery Rechargeability	Yes	No (Battery lasts < 6 months)	No (Battery lasts < 7 weeks)
Drug Replenishing Method	Replaceable cartridges	Refillable reservoir	Refillable reservoir
Implantation	Head-mounted	Fully-implantable	Fully-implantable
Device volume	1260 mm^3	7207 mm^3	2678 mm^3
Device Weight	2 g	7.9 g	3.3 g
Animal use	Mice or larger	Rats or larger	Mice or larger
Additional connections	No (100% standalone)	Yes (50mm long antenna, tubing and probe)	Yes (50mm long antenna, tubing and probe)
Drug Reservoir capacity	0.5 µL x 4 (2 µL) (can be replenished by replacing cartridges)	900 µL	130 µL
Flow Rate Control	No	Yes	Yes
Re-programmability after Implantation	Yes	No	No
Wireless Range	10-100 m	Not wireless	<1m
Wireless Selectivity	Yes	No	No
Smartphone Control	Yes	No	No

As we can see, each technology has its own set of distinct capabilities, making each one more suitable for different type of applications (green color highlighting the best option for a particular feature). The Lego optofluidic device offers unique capabilities such as smaller footprint (1260mm^3; 2g) more suitable for mice, multimodal drug and light deliveries, wirelessly reprogrammable temporal sequencing, efficient multidrug switching through plug-N-play cartridge replacement, indefinite power recharging, long wireless range (>10 m), wireless selectivity and easy-to-setup closed loop control. It also does not require any additional tethers like wire antenna and tubing required in a state-of-the-art commercial pump (SMP-300, iPrecio). However, it is

limited by small reservoir volumes, inability to control flow rates and its head-mounted design. Based on these features, the Lego optofluidic device would be more suitable for neuroscience research applications, which require chronic delivery of both drug and light for dissection of neural circuitry as well as highly localized, multiplexed delivery of multiple, distinct drugs for advanced pharmacological studies.

On the other hand, commercial pumps can withhold a larger volume of drug, offer precise flow rate control, and allow drug deliveries for several weeks through periodic refilling of a reservoir. However, even a state-of-the-art commercial pump (SMP-300) is still bulkier (2678 mm^3; 3.3g) and requires additional tubing to transport drugs to the brain from its implanted remote location in the body, thus more suitable for use in rats or larger animals. In addition, commercial pumps can only deliver a single drug within a behavioral session, requires a cumbersome process to switch drugs, and unable to support multimodal operation. These attributes make them more appropriate for studies that involve delivering large amounts of a single drug over long periods of time with precise flow control. Moreover, its fully implantable nature ensures potential translation for various clinical applications.

In summary, we believe that both Lego optofluidic device and commercial technologies can offer invaluable solutions to the neuroscience community in a complementary way as stated above. However, it is evident that Lego Optofluidic Device not only can be used for pharmacological studies but optogenetic and optopharmacological studies as well.

2.5.3 Comparison with Conventional and Contemporary Devices

Current features of the Lego device platform have the ability to minimize the stress imposed on the surrounding brain tissue normally associated with conventional rigid drug delivery cannulas and also the behavioral stress imposed on the animal associated with tethering[4], [5]. The

miniature and mechanically compliant nature of the optofluidic probes improve its chronic *in vivo* integration by reducing glial response and tissue inflammation that occur during surgical implantation as well as due to micro-motions within surrounding soft neural tissues post-surgery. In contrast, the rigidity in conventional metal cannulas causes lesions and deleterious tissue inflammation that can subsequently lead to cannula clogging after repeated use. For *in vivo* studies, this adverse effect is further reduced in freely moving animals by untethering soft optofluidic probes through integration with a wireless platform. This allows for minimal disruption to the natural state of the animal as well as un-interrupting access during ongoing behavior when employing multiple infusions of a drug compound during a behavioral session. This wireless capability also enables researchers to trigger untethered animals from outside the behavioral room (up to ~10m through indoor walls, **Fig. 2.24b**), or in a pre-programmed manner while they are within a natural environment. Even after improving their mechanical compliance, tethered drug delivery systems[6], [7], [40] still promote either angular stress and higher risk of tissue inflammation on freely moving animals (if tethered throughout session), or dictate that the infusion has to take place prior to the experiment (if untethered during session). For an *in vivo* session, the latter means that the animal has to be typically removed from their current, ongoing behavioral environment, thus limiting the real-time manipulation of particular cellular targets with multiple infusions.

Finally, to clarify the advantages of our wireless Lego optofluidic device through direct comparison with a tethered metal cannula, we summarized the main points below:

1. The large, bulky and rigid nature of cannulas and silica fibers with associated tethers cause significant tissue damage and adverse glial response when compared to soft, ultra-compact optofluidic probes due to their mechanical mismatch with soft neural tissue, as has been consistently shown in previous studies (Jeong et al., 2015; Kim et al., 2013).

2. For multiplexed studies in optogenetics and pharmacology, the cannula-based platform requires separate external tether for each drug or light, which will likely restrict the natural movement of freely behaving animal.
3. Even for pharmacology experiments alone, the procedure for infusing mice can be very stressful (e.g., scruffing the mouse), effectively altering the psychological and psychological state of the animal. Given that the purpose of *in vivo* studies is to better clarify how neural systems underlie behavior, it is significant that every effort is made to reduce stress burdens upon the animals being tested.
4. For pharmacological and optogenetic studies, the relatively bulky dimensions of an implanted cannula and an optical fiber make it very difficult to achieve spatial accuracy as multiple tethers try to access the same local region. In fact, the field largely avoids doing dual local pharmacological-optogenetic studies for this reason. The reality is, they aren't convenient or easy to use and have substantial limitations including massive tissue displacement, and a high degree of variability. The multimodal optofluidic platform here allows for a less invasive multiplexed dissection of the same local region thus minimizing behavioral variability that may occur by switching animals or tether setups.
5. The tethered metal cannulas require interruption with an animal to switch drugs when required. By contrast, the Lego device can deliver the same or up to four distinct drugs without any human-animal intervention.
6. Our optofluidic probes integrate four separate fluidic channels within dimensions smaller than the conventional cannula. This feature allows infusion of four distinct fluids to the same target region of tissue.
7. Moreover, this optofluidic platform can wirelessly deliver multiple, distinct drugs and light with two distinct wavelengths independently and/or simultaneously without impeding the natural movement of freely moving animal.

2.5.4 Unique Capability for Long Term Drug Delivery

Another key feature of the Lego optofluidic devices is their capacity for chronic wireless drug delivery to the same target region of the brain. In the previous systems[8], [14], to deliver pharmacological compounds more than once, an integrated drug reservoir with four individual chambers was used to deliver four similar or different drugs allowing multiplexity within the same localized region. But this severely limited such devices for chronic studies, as they were completely unusable after all chambers were activated due to the irreversible expansion of the thermally expandable polymer actuators. By implementing a detachable 'plug-n-play' Lego interface (**Fig. 2.1b**), the Lego device allows for repeated, unlimited and chronic pharmacological manipulation within an untethered freely moving animal, demonstrating a substantial improvement over the previous optofluidic remote-delivery systems[8], [14]. This feature was highlighted by recurring intra-VTA DAMGO unilateral infusions (**Fig. 2.27**) in live mice where we observed consistent, repeated increases in stereotypical locomotion up to at least a month after implantation of the optofluidic device. The head-mounted non-removable part of the implant is robust enough to last several months (>6 months) with the addition of Metabond (see Methods), and therefore, in principle, can allow for *in vivo* pharmacology for an extended timeframe. Furthermore, we repeatedly delivered pharmacological agents using different drug cartridges through the same microfluidic channel (same heater activation), thus suggesting that the microfluidic channels do not become blocked or clogged over time after repeated use. The cartridge replaceability provides the option to change or refill drug compounds (**Fig. 2.34–2.35**) within the same or different behavioral session, and also overcomes the evaporation issue present in previous wireless devices[8], [14]; where limited non-chronic drug sources must be delivered within two weeks after surgical implantation thus significantly shortening their experimental timeline.

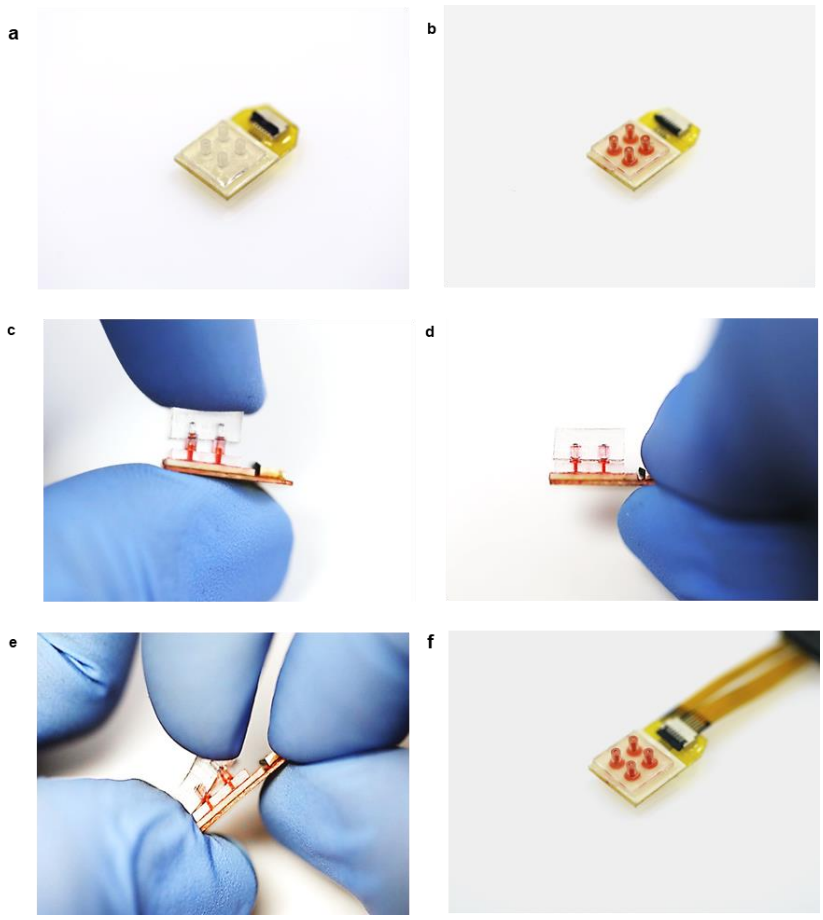

Figure 2.34 – Loading and storage of replaceable drug cartridges before an experiment. (a) *Prepare a drug cartridge.* ***(b)*** *Load a drug.* ***(c)*** *Plug a Parylene C coated PDMS cover to prevent evaporation of drug.* ***(d)*** *Store the plugged cartridge in a freezer for future experiments.* ***(e)*** *Remove the cover when the cartridge is needed for an experiment.* ***(f)*** *Connect the cartridge to the circuit after checking the drug quantity in the cartridge. In case of some evaporation, refill the pillars with the fresh drug until it is filled optimally.*

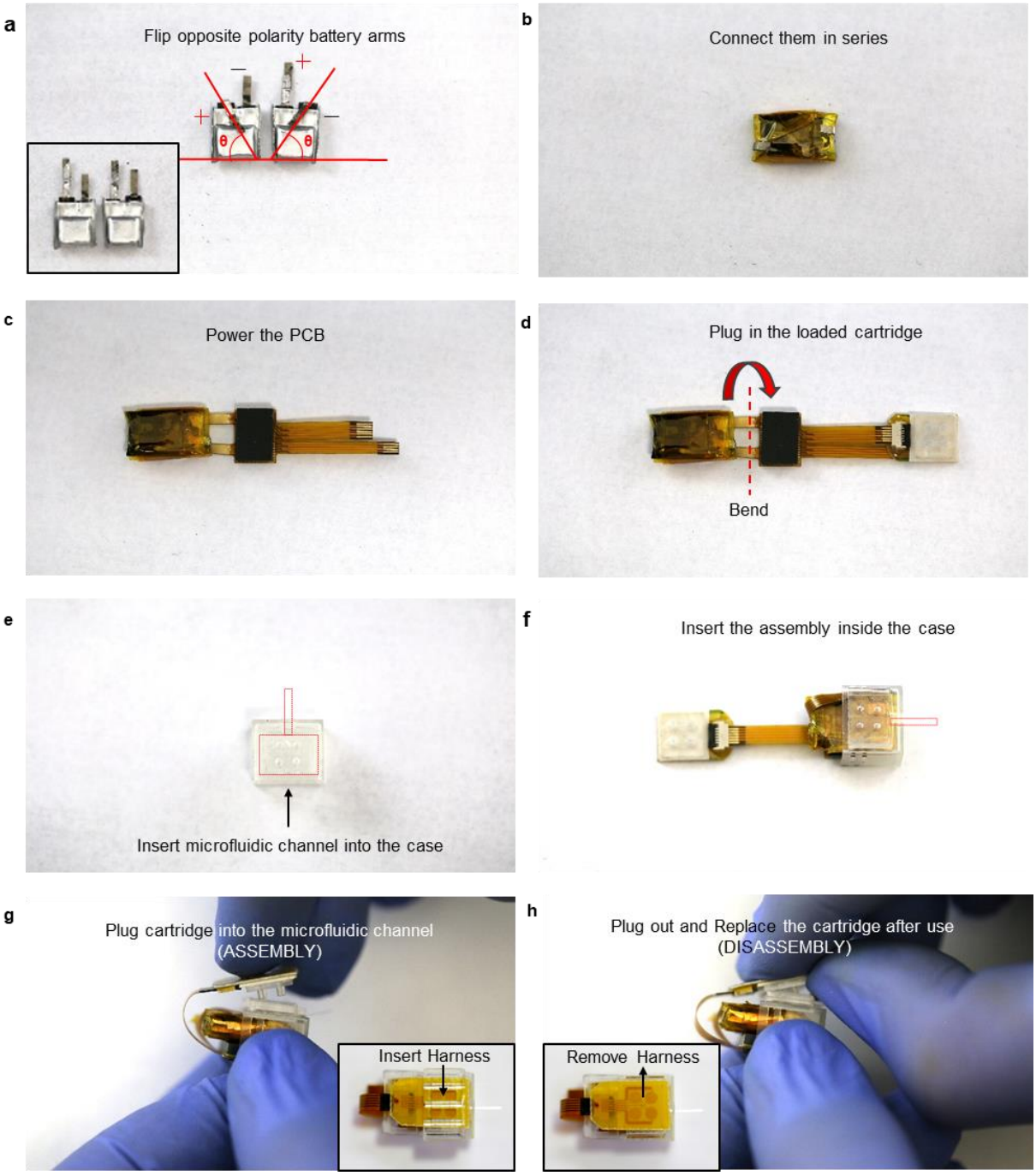

Figure 2.35 – Assembly procedure of a wireless Lego microfluidic system with a replaceable cartridge. (a) *Connect two lithium polymer batteries in series after bending the opposite polarity flaps.* ***(b)*** *Sandwich them together using a polyimide tape.* ***(c)*** *Connect the power terminals of the wireless BLE PCB to the appropriate terminals of the battery set.* ***(d)*** *Connect the loaded male Lego replaceable drug cartridge to the heater cable of the wireless BLE PCB.* ***(e)*** *Slide the female Lego (connected to microfluidic channels) into the 3-D printed case slot which holds it securely at the place.* ***(f)*** *Insert the electronics into the case body.* ***(g)*** *Bend the heater cable to plug the male Lego replaceable drug cartridge into the female Lego microfluidic probe system. The inset shows bolstering of the mechanical assembly by plugging a harness on the case front by holding the Lego assembly together.* ***(h)*** *After use, remove the harness and the replaceable male Lego drug cartridge from the female Lego microfluidic probe system. The inset shows the*

*front view of Lego optofluidic device after removing the harness. For complete disassembly of the Lego device, after step **(h)**, follow all steps **(a–f)** in reverse order. For partial disassembly (replacing drug cartridge only) of the Lego device, after step **(h)**, swap the old male Lego replaceable cartridge from the BLE PCB heater cable with a new one, while the device configuration is as shown in **(f)**. Then follow step **(g)** to complete the assembly step by plugging the new male Lego replaceable drug cartridge into the female Lego microfluidic probe system and finally clipping the harness on the assembly.*

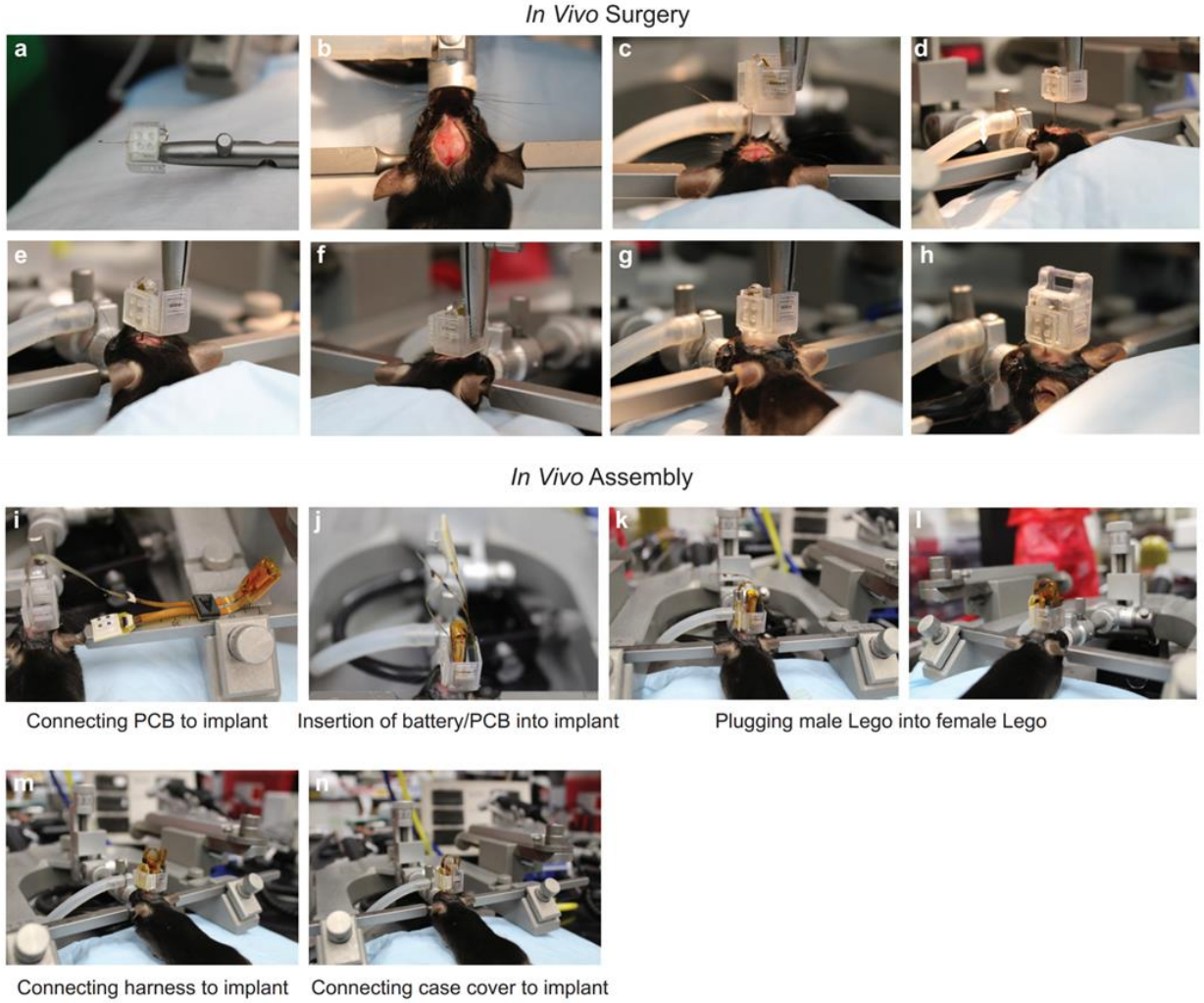

Figure 2.36 – Representative images of surgical procedures for implanting the optofluidic device and in vivo assembly of the optofluidic device. *Images displaying steps for implanting the optofluidic device consisting of: **(a)** attaching the device with female Lego and blocker to a standard stereotaxic arm; **(b)** creating an opening for skull access and drilling a small hole for device needle insertion; **(c–f)** insertion of device needle into the brain; **(g)** application of Metabond for adhering the device to the skull; and **(h)** covering the optofluidic connection with the case cover. Images displaying the steps for in vivo assembly of the optofluidic device consisting of: **(i)** connecting the PCB to the device; **(j)** folding the battery and PCB together to insert into the optofluidic case; **(k–l)** folding and plugging the male lego into the female lego (microfluidic channels); **(m)** insertion of the harness over the male lego portion of the assembled device; and **(n)** assembly of the case cover to the assembled optofluidic cartridge.*

In addition, its ability for precisely controlled temporal delivery of two or more similar or distinct drugs within a single experimental session opens avenues for versatile, combinatorial chronic pharmacology in freely moving animals. Such chronic and combinatorial, yet localized pharmacological intervention of neural circuits with precise temporal control is rare and enables researchers to test compounds in pre-clinical phases through long-term repeated *in vivo* drug deliveries at the same target location. This is an improvement over other non-localized pharmacological methods such as oral delivery, topical application or intravenous injections which can be slow-acting and may also lead to off-target exposure or rejection through the blood-brain barrier, thus adversely affecting their selectivity, efficiency, and reliability. Through a single surgical step (**Fig. 2.36**), this miniaturized device can provide high spatiotemporal and multi-modal access of a target neural circuit in a series of experimental testing. This ability to deliver viral vectors and pharmacological agents as well as light locally over long epochs of time can also allow for chronic optopharmacological studies in the future. In turn, the full capability of this device platform could decrease the need for experimental subjects as well as the experimental timelines. The ability to chronically administer drugs to a highly localized region in a non-tethered nature offered by this platform could also have future implications in boosting advancements in repeatable targeted chemotherapeutics.

2.5.5 Unique Smartphone Controlled Wireless Applications

One of the main advantages of this wireless Lego device is its ability to transform any commercially available smartphone into a custom wireless transmitter with long omnidirectional range (up to ~100 m) through an easy-to-use and readily available smartphone app. This eliminates not only the need for special transmitter electronic systems and/or bulky control equipments[8]–[24], including special resonant cavities[17], [24] or special antenna cages[16], [20]; but also the requirement in modifying behavioral apparatuses to conform with wireless

integration. Therefore, this smartphone-based wireless platform allows a researcher to simply test the animal in any of their existing behavioral paradigms. Moreover, simple presses on the readily usable app and easily customizable smartphone control parameters (**Fig. 2.21b**) enable smooth and 'on-the-fly' rapid transitions between optical and pharmacological modalities. Another advantage of the Lego optofluidic platform is the ability to selectively control specific mice during a single behavioral session within a limited, confined space (**Fig. 2.29 - 2.30**). One limiting feature of many recent wireless techniques involving optogenetic or pharmacological control[8]–[17], [21], [23], [24] is their inability for versatile selectivity (for both animal selection and configuring its multimodal output) that is scalable, although some of such systems can allow for selectivity to a certain degree by modifying their hardware or transmitter setups. This is further limited by the wireless equipment size and laboratory spaces, which can hinder their configurability for versatile and 'on-the-fly' selection of target animals and/or output modes (light or drugs) with variability in stimulation parameters. By harnessing software intelligence integrated within its hardware, the Lego device overcomes such limitations by allowing not only accurate specificity of animal selection within a large congested group but also scalability and programmability of multimodal outputs within each selected animal. This allows researchers to trigger each animal in a large group using its own distinct stimulation modes and parameters without modifying receiver hardware or requiring special transmitters and setups. This can also overcome the singular paradigm nature of behavioral experiments within limited laboratory spaces. Running multiple animals within the same congested behavioral cage can help increase data generation and research efficiency without significant modification of a laboratory environment. The ability to test multiple mice during a behavioral session is critical for productivity, high throughput, and behavioral consistency (i.e. timing of day, room temperature, etc.). Other key advantages of the Bluetooth platform include wireless re-programmability which can allow researchers to change stimulation parameters 'on-the-fly'. Moreover, the system offers not only 'easy-to-setup' and scalable closed loop systems, enabling social experiments with dependent feedback-based

triggering, but also obstacle invariability, permitting researchers to initiate actions from outside the behavioral room, using a simple smartphone graphical user interface (GUI).

2.5.6 Device Manufacturability

The device materials and design are devised to be rapidly reproduced in most engineering labs with access to basic tools. Many of the components of the device are either readily available (electronic components, rechargeable batteries, connectors, etc.), 3D printable (case, case covers, harness, male Lego, etc.) or can be fabricated with simple soft lithography in a standard fabrication laboratory (Lego optofluidic probe). Researchers with basic training can easily fabricate and assemble a multitude of optofluidic probes within a few days.

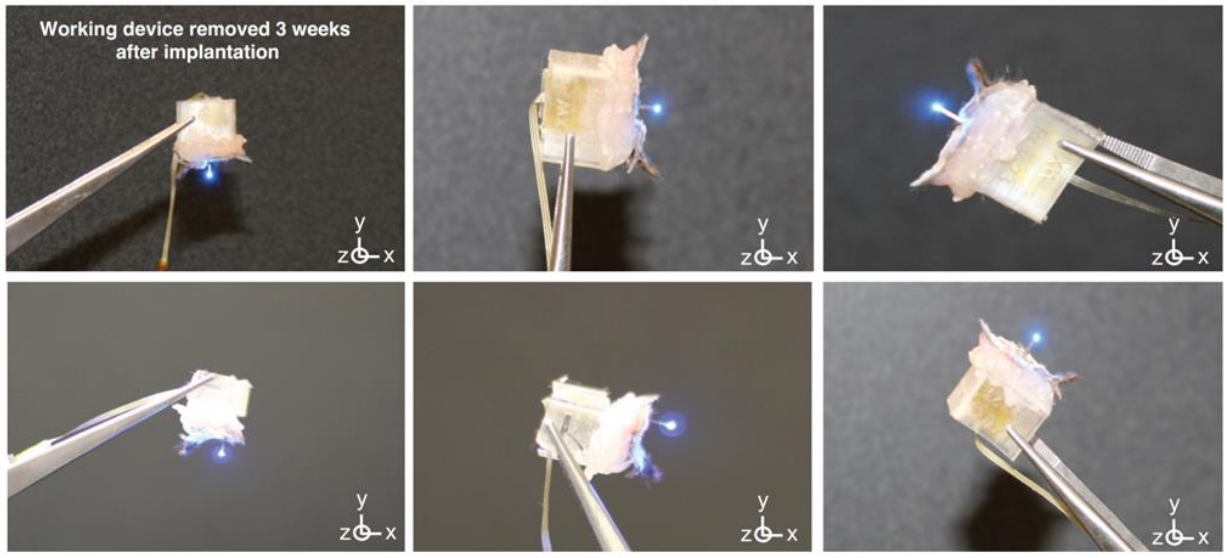

Figure 2.37 – Device removed from an animal 3 weeks post-implantation showing its robust functionality in various angular orientations.

The economical overheads can be further reduced by reusing these devices (**Fig. 2.37**) by finding a technique to cleanly eliminate dental cement/adhesive used to attach the optofluidic device platform to the skull, without damaging the devices. Moreover, the stackable nature of this probe architecture[12] allows versatile functional scalability by integrating multimodal components

such as pressure, temperature and chemical sensors as well as recording electrodes. Such attributes can reduce costs and time to prepare and allow for more complex neuroscience experiments.

2.5.7 Future Work

Although we vouch for the specific advantages of our device over other available methodologies, we agree that there are several limitations of the device which can be further improved upon. This sub-section highlights the device caveats and drawbacks of the Lego platform at its current stage:

1. First of all, its inability to dynamically control flow rate and volume for drug delivery limits studies requiring variable infusion rate with variable doses, which is possible to be achieved through tethered cannula systems or commercial micropumps. This feature was excluded at the expense of its miniaturized overall footprint to offer an ultracompact solution for wireless chronic optofluidics. Although in our discussion, we provide certain ways in which this limitation can be mitigated to some extent, those solutions are not on par with commercial alternatives.
2. Drug loading into the plastic drug reservoirs requires oxygen plasma or ozone treatment to make the reservoirs hydrophilic to facilitate fluid loading.
3. The current wireless module design requires time-consuming assembly and disassembly process for battery recharging, thus requiring further optimization to provide a time-efficient technique and more user-friendly design (such as swappable magnetic connectors) for neuroscientists.

Integration of advanced materials and efforts for optimized engineering design can help to unleash the full potential of this device by further improvements and fully recognizing its current

limitations. Currently, the inability to easily modify the volume of fluid delivery as well as the infusion rate hinders the real-time customization of fluid control, limiting some applications. However, we can deliver the same type of fluid to the target neural circuit multiple times to compensate for the required dose deliveries. Alternatively, the dose amount and flow rate can be controlled at some degree by modifying the reservoirs and microfluidic channel dimensions in a similar design architecture or can be fully overcome by integrating micro-stepper motors or micromachined linear actuators for refined fluid control. The current thermal actuation technique also requires the drugs to be thermally stable and compatible with the reservoir temperatures (~60°C) during the very brief heater activation. The concern associated with high-temperature actuation can be dramatically mitigated by replacing the current expandable polymer composite with thermally responsive hydrogel, which can be engineered to have its activation temperature as low as 32°C[42], [43]. The use of hydrogel, which is intrinsically hydrophilic, in drug reservoirs can also facilitate loading drugs into cartridge reservoirs, thus eliminating the need for oxygen plasma or ozone tools for hydrophilic treatment, which is not readily accessible to neuroscientists. Additionally, although mice tolerate these head-mounted devices well, the device can be potentially damaged or detached from the head by very active movements or social defeat interactions. This also limits their ability to access various space-critical locations within the peripheral nervous system unlike fully implantable devices where an entire system can be implanted under the skin[14]–[16]. Besides, the current head-mounted wireless module design requires somewhat cumbersome assembly and disassembly process for battery recharging (**Supplementary Fig. 2.35**), although it can be further optimized to some extent by using magnetic plug-n-play connectors for quick swapping of fully charged batteries to save time and effort. All these issues associated with the head-mounted design can be possibly resolved by creating miniaturized, wireless neural systems that could be chronically embedded in tissue. Combinatorial integration of custom-fabricated or unpackaged Bluetooth and IC chips, wireless energy harvester, and drug reservoirs refillable with a syringe needle from outside the skin has

the potential to create such systems. Specifically, this fully implantable device could be achieved by encapsulating the entire system with soft, biocompatible waterproof structures[44]. Moreover, integration of Bluetooth-based neural devices with the Internet networks (e.g. Wireless Fidelity (WiFi)) can open avenues for simultaneous, large scale triggering of remote animals in a highly programmed throughput manner. These large networks can also allow for simultaneous selective control of multiple animals each with a different command (treatment) in the same behavioral space, thus aggrandizing experimental throughput and efficiency by multitudes, enabling quick and reliable acquisition of big data and hence enable faster experimental timelines. Integrating such platforms with the Internet can help transfer a magnitude of data by exploiting the high throughput capabilities of WiFi as well. Utilizing the processing power and software tools in smartphones along with programmable capabilities of BLE modules, experiments can also be programmed to deliver drugs or trigger photostimulation during a specific time of day and thus dramatically reducing the experimental burden for circadian-sensitive experiments. This will allow neuroscientists to run automated, pre-defined, programmable and high throughput animal studies without always being present in their laboratories.

2.5.8 Conclusions

Here, we present a wireless Lego optofluidic platform that provides technology for chronic behavioral studies involving *in vivo* pharmacology and optogenetics. This approach allows researchers the ability to selectively control single or multiple animals within a congested vicinity with an easy to use Bluetooth smartphone app. The potential of these devices will be greatly enhanced as the field of *in vivo* photopharmacology advances[45]–[47], where photosensitive compounds can modify protein activity upon exposure to certain wavelengths of light. This platform enables compound control using optofluidics in a variety of experimental settings and allows for naturalistic animal behaviors and chronic *in vivo* studies.

2.6 References

[1] A. C. Felix-Ortiz, A. Beyeler, C. Seo, C. A. Leppla, C. P. Wildes, and K. M. Tye, “BLA to vHPC Inputs Modulate Anxiety-Related Behaviors,” *Neuron*, vol. 79, no. 4, pp. 658–664, Aug. 2013.

[2] J. H. Jennings *et al.*, “Distinct extended amygdala circuits for divergent motivational states,” *Nature*, vol. 496, no. 7444, pp. 224–228, Apr. 2013.

[3] R. H. Kramer, A. Mourot, and H. Adesnik, “Optogenetic pharmacology for control of native neuronal signaling proteins,” *Nat Neurosci*, vol. 16, no. 7, pp. 816–823, Jul. 2013.

[4] J. G. McCall and J.-W. Jeong, “Minimally invasive probes for programmed microfluidic delivery of molecules in vivo,” *Current Opinion in Pharmacology*, vol. 36, pp. 78–85, Oct. 2017.

[5] J. Y. Sim, M. P. Haney, S. I. Park, J. G. McCall, and J.-W. Jeong, “Microfluidic neural probes: in vivo tools for advancing neuroscience,” *Lab Chip*, vol. 17, no. 8, pp. 1406–1435, Apr. 2017.

[6] S. Park *et al.*, “One-step optogenetics with multifunctional flexible polymer fibers,” *Nature Neuroscience*, vol. 20, no. 4, pp. 612–619, Apr. 2017.

[7] A. Canales *et al.*, “Multifunctional fibers for simultaneous optical, electrical and chemical interrogation of neural circuits *in vivo*,” *Nature Biotechnology*, vol. 33, no. 3, pp. 277–284, Mar. 2015.

[8] J.-W. Jeong *et al.*, “Wireless Optofluidic Systems for Programmable In Vivo Pharmacology and Optogenetics,” *Cell*, vol. 162, no. 3, pp. 662–674, Jul. 2015.

[9] J. G. McCall *et al.*, “Preparation and implementation of optofluidic neural probes for in vivo wireless pharmacology and optogenetics,” *Nat. Protocols*, vol. 12, no. 2, pp. 219–237, Feb. 2017.

[10] M. Hashimoto, A. Hata, T. Miyata, and H. Hirase, “Programmable wireless light-emitting diode stimulator for chronic stimulation of optogenetic molecules in freely moving mice,” *NPh, NEUROW*, vol. 1, no. 1, p. 011002, May 2014.

[11] Y. Iwai, S. Honda, H. Ozeki, M. Hashimoto, and H. Hirase, “A simple head-mountable LED device for chronic stimulation of optogenetic molecules in freely moving mice,” *Neuroscience Research*, vol. 70, no. 1, pp. 124–127, May 2011.

[12] T. Kim *et al.*, “Injectable, cellular-scale optoelectronics with applications for wireless optogenetics,” *Science*, vol. 340, no. 6129, pp. 211–216, Apr. 2013.

[13] J. G. McCall *et al.*, “Fabrication and application of flexible, multimodal light-emitting devices for wireless optogenetics,” *Nature Protocols*, vol. 8, no. 12, pp. 2413–2428, Nov. 2013.

[14] K. N. Noh *et al.*, “Miniaturized, Battery-Free Optofluidic Systems with Potential for Wireless Pharmacology and Optogenetics,” *Small*, vol. 14, no. 4, p. 1702479, Jan. 2018.

[15] S. I. Park *et al.*, “Soft, stretchable, fully implantable miniaturized optoelectronic systems for wireless optogenetics,” *Nature Biotechnology*, vol. 33, no. 12, pp. 1280–1286, Nov. 2015.

[16] G. Shin *et al.*, “Flexible Near-Field Wireless Optoelectronics as Subdermal Implants for Broad Applications in Optogenetics,” *Neuron*, vol. 93, no. 3, pp. 509-521.e3, Feb. 2017.

[17] K. L. Montgomery *et al.*, “Wirelessly powered, fully internal optogenetics for brain, spinal and peripheral circuits in mice,” *Nature Methods*, vol. 12, no. 10, pp. 969–974, Aug. 2015.

[18] M. Alam, X. Chen, and E. Fernandez, “A low-cost multichannel wireless neural stimulation system for freely roaming animals,” *J. Neural Eng.*, vol. 10, no. 6, p. 066010, 2013.

[19] T. Ativanichayaphong, J. W. He, C. E. Hagains, Y. B. Peng, and J.-C. Chiao, “A combined wireless neural stimulating and recording system for study of pain processing,” *Journal of Neuroscience Methods*, vol. 170, no. 1, pp. 25–34, May 2008.

[20] C.-W. Chang and J.-C. Chiou, “A Wireless and Batteryless Microsystem with Implantable Grid Electrode/3-Dimensional Probe Array for ECoG and Extracellular Neural Recording in Rats,” *Sensors*, vol. 13, no. 4, pp. 4624–4639, Apr. 2013.
[21] S. I. Park *et al.*, “Ultraminiaturized photovoltaic and radio frequency powered optoelectronic systems for wireless optogenetics,” *Journal of Neural Engineering*, vol. 12, no. 5, p. 056002, Oct. 2015.
[22] R. C. Pinnell, J. Dempster, and J. Pratt, “Miniature wireless recording and stimulation system for rodent behavioural testing,” *Journal of Neural Engineering*, vol. 12, no. 6, p. 066015, Dec. 2015.
[23] C. T. Wentz, J. G. Bernstein, P. Monahan, A. Guerra, A. Rodriguez, and E. S. Boyden, “A wirelessly powered and controlled device for optical neural control of freely-behaving animals,” *Journal of Neural Engineering*, vol. 8, no. 4, p. 046021, Aug. 2011.
[24] A. J. Yeh, J. S. Ho, Y. Tanabe, E. Neofytou, R. E. Beygui, and A. S. Y. Poon, “Wirelessly powering miniature implants for optogenetic stimulation,” *Applied Physics Letters*, vol. 103, no. 16, p. 163701, 2013.
[25] L. K. Massey, *Permeability Properties of Plastics and Elastomers, 2nd Ed.: A Guide to Packaging and Barrier Materials*. William Andrew, 2003.
[26] R. Qazi, C. Y. Kim, S.-H. Byun, and J.-W. Jeong, “Microscale Inorganic LED Based Wireless Neural Systems for Chronic in vivo Optogenetics,” *Front. Neurosci.*, vol. 12, 2018.
[27] A. Mehrabian and Y. Abousleiman, “General solutions to poroviscoelastic model of hydrocephalic human brain tissue,” *Journal of Theoretical Biology*, vol. 291, pp. 105–118, Dec. 2011.
[28] Q. Liu, Z. Wang, Y. Lou, and Z. Suo, “Elastic leak of a seal,” *Extreme Mechanics Letters*, vol. 1, pp. 54–61, Dec. 2014.
[29] R. Frank, W. Bronzi, G. Castignani, and T. Engel, “Bluetooth Low Energy: An alternative technology for VANET applications,” in *2014 11th Annual Conference on Wireless On-demand Network Systems and Services (WONS)*, 2014, pp. 104–107.
[30] RF Digital Corp., “Getting Started with SimbleeCOM v1.0.” Simblee Corporation, 2015.
[31] T. Kessler, “How to check Bluetooth connection strength in OS X,” *CNET*, 2013.
[32] F. Jenck, M. Bozarth, and R. A. Wise, “Contraversive circling induced by ventral tegmental microinjections of moderate doses of morphine and [D-Pen2, D-Pen5]enkephalin.,” *Brain Res*, vol. 450, no. 1–2, pp. 382–386, May 1988.
[33] D. P. Devine and R. A. Wise, “Self-administration of morphine, DAMGO, and DPDPE into the ventral tegmental area of rats,” *J. Neurosci.*, vol. 14, no. 4, pp. 1978–1984, Apr. 1994.
[34] P. Namburi, R. Al-Hasani, G. G. Calhoon, M. R. Bruchas, and K. M. Tye, “Architectural Representation of Valence in the Limbic System,” *Neuropsychopharmacology*, vol. 41, no. 7, pp. 1697–1715, Jun. 2016.
[35] J. H. Jennings, G. Rizzi, A. M. Stamatakis, R. L. Ung, and G. D. Stuber, “The Inhibitory Circuit Architecture of the Lateral Hypothalamus Orchestrates Feeding,” *Science*, vol. 341, no. 6153, pp. 1517–1521, Sep. 2013.
[36] R. Al-Hasani *et al.*, “Distinct Subpopulations of Nucleus Accumbens Dynorphin Neurons Drive Aversion and Reward,” *Neuron*, vol. 87, no. 5, pp. 1063–1077, Sep. 2015.
[37] J. G. McCall *et al.*, “CRH Engagement of the Locus Coeruleus Noradrenergic System Mediates Stress-Induced Anxiety,” *Neuron*, vol. 87, no. 3, pp. 605–620, Aug. 2015.
[38] C. Dagdeviren *et al.*, “Miniaturized neural system for chronic, local intracerebral drug delivery,” *Science Translational Medicine*, vol. 10, no. 425, p. eaan2742, Jan. 2018.
[39] S. Spieth, A. Schumacher, C. Kallenbach, S. Messner, and R. Zengerle, “The NeuroMedicator—a micropump integrated with silicon microprobes for drug delivery in neural research,” *J. Micromech. Microeng.*, vol. 22, no. 6, p. 065020, 2012.
[40] I. R. Minev *et al.*, “Electronic dura mater for long-term multimodal neural interfaces,” *Science*, vol. 347, no. 6218, pp. 159–163, Jan. 2015.

[41] C. Dagdeviren *et al.*, “Miniaturized neural system for chronic, local intracerebral drug delivery,” *Science Translational Medicine*, vol. 10, no. 425, p. eaan2742, Jan. 2018.
[42] Y. Qiu and K. Park, “Environment-sensitive hydrogels for drug delivery,” *Advanced Drug Delivery Reviews*, vol. 53, no. 3, pp. 321–339, Dec. 2001.
[43] K.-I. Jang *et al.*, “Soft network composite materials with deterministic and bio-inspired designs,” *Nature Communications*, vol. 6, p. 6566, Mar. 2015.
[44] Y. Liu *et al.*, “Epidermal mechano-acoustic sensing electronics for cardiovascular diagnostics and human-machine interfaces,” *Science Advances*, vol. 2, no. 11, p. e1601185, Nov. 2016.
[45] M. R. Banghart and B. L. Sabatini, “Photoactivatable Neuropeptides for Spatiotemporally Precise Delivery of Opioids in Neural Tissue,” *Neuron*, vol. 73, no. 2, pp. 249–259, Jan. 2012.
[46] I. Tochitsky *et al.*, “Restoring visual function to blind mice with a photoswitch that exploits electrophysiological remodeling of retinal ganglion cells,” *Neuron*, vol. 81, no. 4, pp. 800–813, Feb. 2014.
[47] S. Banala *et al.*, “Photoactivatable drugs for nicotinic optopharmacology,” *Nature Methods*, vol. 15, no. 5, pp. 347–350, May 2018.

3 Fully Implantable, Battery-Free Optofluidic Device

3.1 Introduction

Multimodal neural intervention in the form of optofluidic devices allows neuroscientists to achieve minimally invasive and uninterrupted versatile access to the convoluted neuronal synapses deep inside the tissue surface. This enables enhanced dissection of complex biological interconnections through highly selective and temporally precise techniques such as combinatorial approaches in optogenetics[1], [2] and pharmacology[3]. Both these biological tools have been extensively used in the neuroscience field with a proven record to help decipher various neural circuits [4], [5], decision-making processes [6], neurodegenerative diseases[7] as well as for many other applications [8]–[10].

Various techniques have been used to approach combinatorial photostimulation and drug delivery as highlighted in **Fig. 3.1**, which also summarizes the various limitations of previous approaches. Conventional tethered and rigid tools have used optical fibers (16 GPa) and metal cannulas (200 GPa) to modulate deep lying tissues within bodies of freely moving animals. Apart from being mechanically mismatched causing tissue lesions and deleterious tissue inflammation response near the implanted site, the multiple connections required for each modularity can also cause behavioral distress in the animal thus affecting the reliability of data gathered through such *in vivo* studies. The implant size, rigidity, and related tethered issues were partly solved through the fabrication of soft integrated optofluidic probes connected to external head mounted systems[ref]. Although providing a standalone and highly compact solution for integrated optofluidic stimulation, they still come with their own caveats.

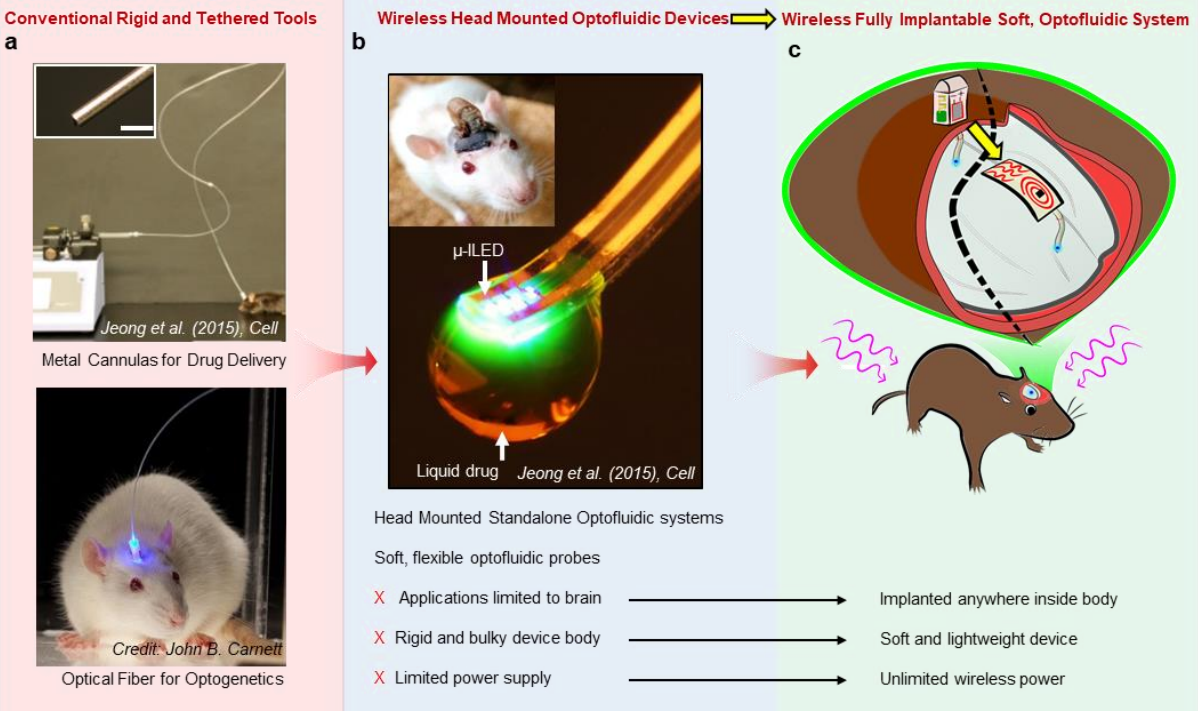

Figure 3.1 – Comparison of various techniques used for combinatorial optogenetics and pharmacology in freely moving animals. (a) *Conventional tools,* ***(b)*** *Wireless head mounted devices (including the Lego device discussed in Chapter 2) and* ***(c)*** *the Fully implantable optofluidic device.*

Most of the device bulk in head mounted wireless devices is mounted outside the body, hence its applications are limited only to horizontal surfaces of the body such as the head of animals (or brain). Secondly, the large and relatively heavier mounted structures, primarily due to the bulky lithium batteries, increase the weight of the device and may cause undue stress in smaller animal rodents such as mice. Moreover, the limited power of their storage cells requires recurring periods of recharging, thus interrupting the natural state of the animal periodically and hindering their applications for continuously prolonged *in vivo* studies. Lastly, the rigid and bulky batteries, as well as the mounted device structure, doesn't conform to the curvilinear body surfaces, an essential feature for chronic wearable integration, unless special glue or adhesive is used to fix it. The probe, though soft and flexible, is tethered to the rigid and static head mounted structure thus causing the development of residual mechanical stress at the intersection between

the mismatched device parts especially in case of head movements or tissue micromotions near the brain surface.

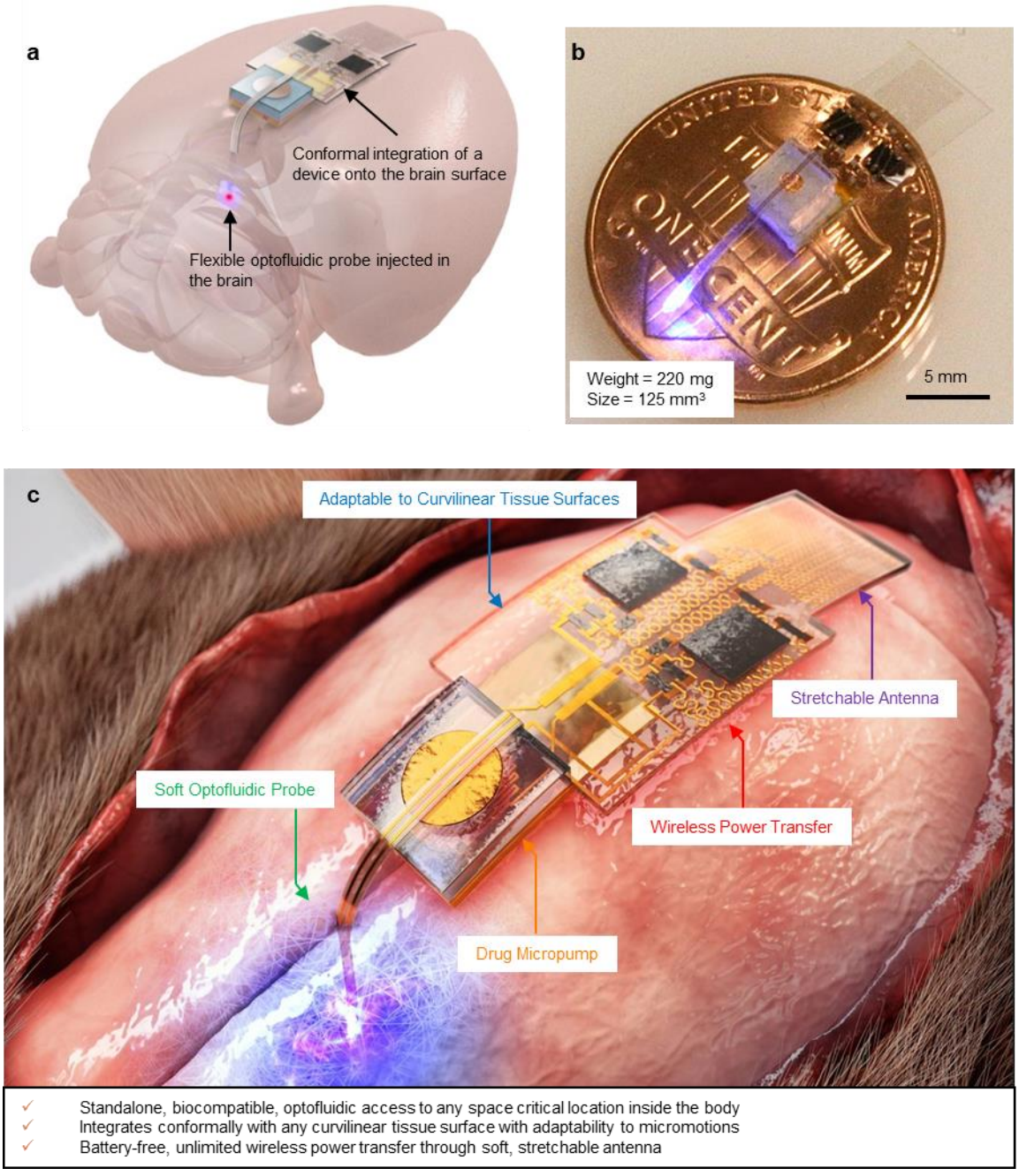

***Figure 3.2 – The fully implantable, battery-free optofluidic device**, **(a)** highlighting its soft, flexible deep tissue access and soft, flexible conformal capability and **(b)** being compared in size with a US 1 cent coin. **(c)** Rendered concept highlighting the unique capabilities of the fully implantable device.*

Here we develop a new class of ultra-miniaturized optofluidic neural devices that can be fully implanted inside the body. Its soft optofluidic probes allow minimally invasive access to the target site while as it's soft, mechanically compliant and flexible body allows its conformal bio-integration with various curvilinear tissue surfaces (**Fig. 3.2a**), thus enhancing its compatibility with soft and sensitive biological tissues inside the body. Compared to contemporary head mounted systems, as is shown from **Table 3.1**, it offers a significant advantage in terms of both size and weight (equivalent to approx. four drops of water) which allows it to fit inside various space-critical locations of the body (**Fig. 3.2b**). The primary reason that this device can achieve such a minimalistic, lightweight and soft footprint is that of exclusion of large and rigid batteries used in previous wireless optofluidic systems. **Figure 3.2c** highlights the key features of the device. By directly harnessing wireless power through the stretchable and soft antenna which harvests energy from a remote transmitter, this device does not need periodic recharging and thus need for interrupting the animal's natural behavior.

TABLE 3.1 COMPARISON OF HEAD MOUNTED VS FULLY IMPLANTABLE NEURAL DEVICES

Property/Device	**Head Mounted IR [11]**	**Chronic Lego BLE (Chapter 2)**	**Fully Implantable RF[12] (This device)**
Weight (g)	1.86	2	0.22
Size (mm^3)	1575	1260	125
Chronic Optofluidics	No	Yes	No
Fully Implantable	No	No	Yes

Moreover, the soft optofluidic probe provides minimally invasive photo-access and drug outlets to deep regions in soft biological tissues thus minimizing tissue damage and glial response compared to conventional rigid alternatives (**Fig. 3.3**). Lastly, the soft polymeric encapsulation allows the device to be flexible and conform to various curvilinear tissue surfaces inside the body. It also presents the surrounding biofluids from shorting the electrical electrodes during *in vivo* studies. Overall, due to such minimalistic design structure, uninterrupted wireless power, and mechanically compliant design, it can not only allow neuroscientists to use it in various parts of

the Central Nervous System (CNS) but any peripheral part or space critical location inside the body of freely moving animals.

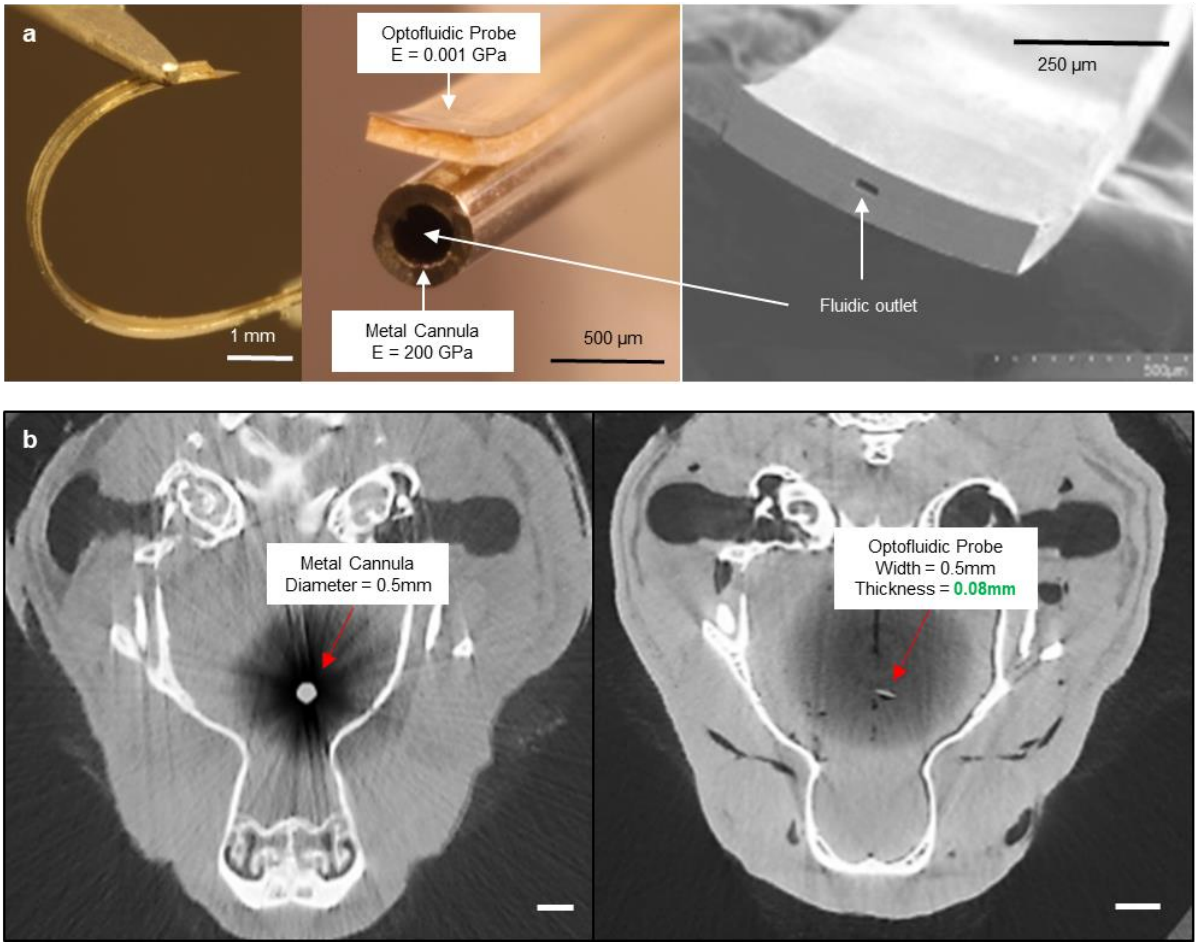

Figure 3.3 – Comparison of the soft and flexible optofluidic probe of a fully implantable device with a conventional metal cannula *through* ***(a)*** *series of optical images and* ***(b)*** *X-ray computed tomographic scans of the brain inserted with each implant showing reduced physical tissue displacement for a soft optofluidic probe which can deliver both drugs and light.*

3.2 Design Architecture and Working Principle

Figure 3.4a highlights the overall power flow diagram and as well as the exploded view of various functional layers of the implantable device.

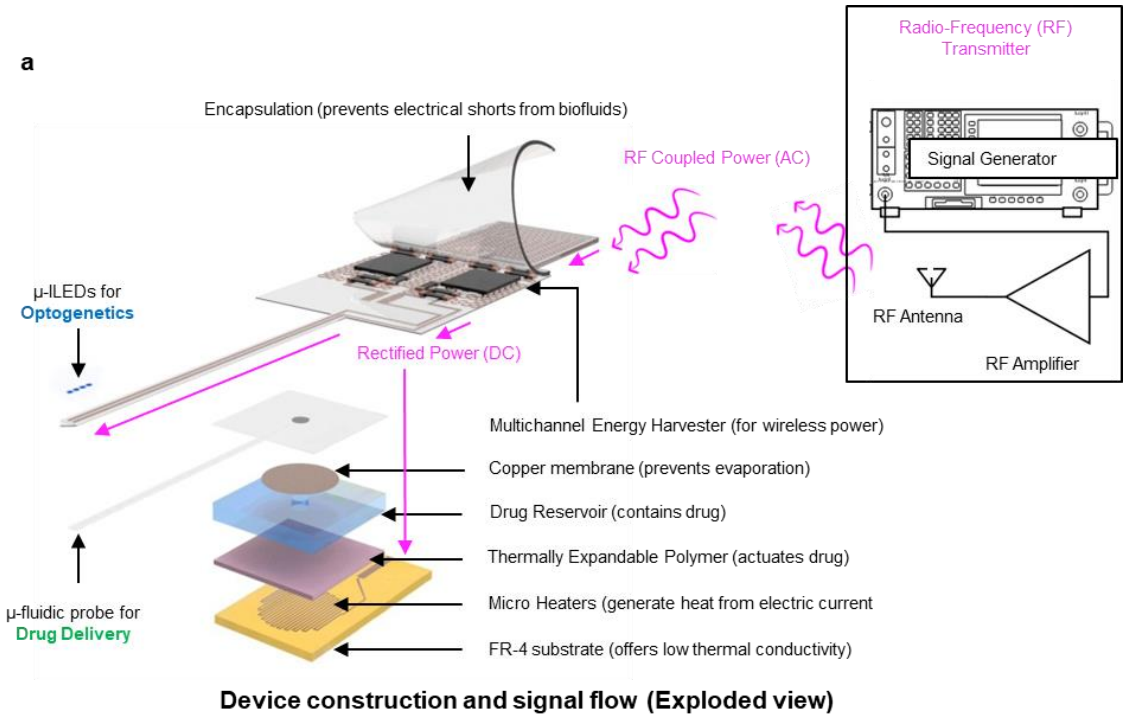

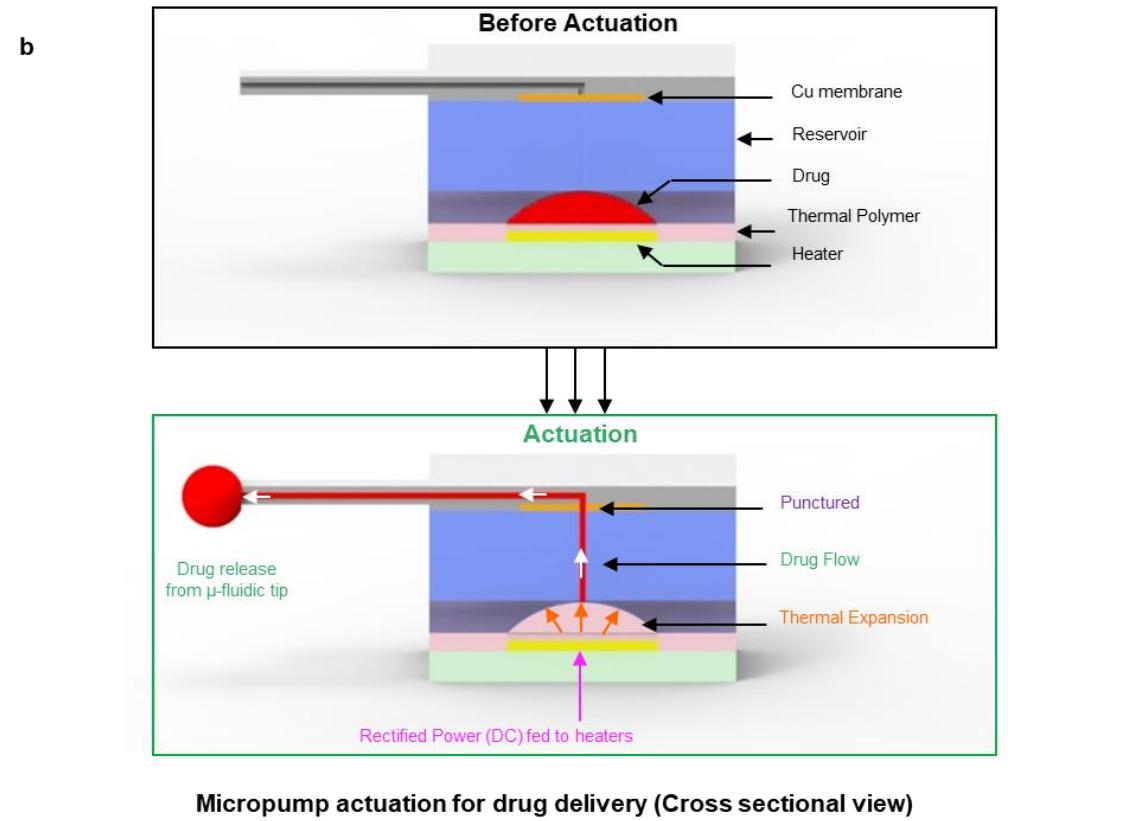

Figure 3.4 – Design and functional structure of the fully implantable device. (a) *Exploded view of various layers and associated signal flow.* ***(b)*** *Micropump actuation process.*

First, the power is generated in a remotely placed wireless transmission system which consists of a serially connected signal generator, a radio frequency (RF) amplifier, and an antenna. The wireless power is then harnessed by the soft, stretchable antenna of the implantable device and based on the frequency of transmission, the energy harvested is directed independently to either for photostimulation or drug delivery. The two major components of the implantable device are a) an optofluidic actuator and b) a power harvester. The primary role of the optofluidic actuator is to enable combinatorial photostimulation and pharmacological delivery deep inside the soft tissue while as the power harvester's function is to capture wireless RF energy and pass it along to the optofluidic actuator after rectifying it. Since the battery is excluded from the design, all power is transferred to respective outputs, processed and utilized in real time with minimum control delay, thus enabling an unlimited power supply to the untethered device inside the body.

3.2.1 Optofluidic Actuator

The optofluidic actuator consists of three main components – i) μ-ILEDs for photon delivery, ii) microfluidic channel for drug delivery and iii) micro-actuator for fluid actuation. To achieve power efficient and low power optogenetic excitation [ref] with minimal tissue displacement, it employs of four μ-ILEDs (220um x 220um x 50um, TR2227, Cree Inc.) which generate enough optical power (>1mW/mm^2 [ref] to achieve optogenetic excitation) at 470nm wavelengths. Moreover, their thin profile along with recessed oblique edges help minimize tissue displacement and subsequent damage during *in vivo* surgery in animal brains. Their scalable and easily configurable nature allows easy customization for a wide variety of multiwavelength optogenetic stimulations. The wireless power after rectification is directly fed to these μ-ILEDs which enables them to blink at a frequency proportional to the transmitter frequency. On the other hand, the 500 μm wide microfluidic probe offers ultra-soft (1 MPa), ultra-thin (50 μm thick) and biocompatible fluidic

access by allowing drugs through a 10 μm x 10 μm cross-sectional channel for feasible drug delivery from the micro-actuator.

The micropump is the key component that drives drug actuation upon receiving power from the wireless harvester before drugs are passed to the microfluidic channel. At its bottom layer, it consists of a thermally insulative [value] and lightweight support material made from FR-4. This helps contain the thermal energy generated within the target area thus improving power efficiency to achieve thermal actuation. Figure 3.4b illustrates the drug actuation process. Gold heaters (300nm) deposited on top the FR-4 layer generates thermal energy through Joule heating to actuate the thermally expandable layer above them. Then the layer right above consists of thermally expandable microspheres (Expancel 031 DY, AkzoNobel) which are mixed with PDMS in the ratio of 1:2. Upon absorbing the heat, this expandable polymer extrudes into the drug reservoir (semicircular cavity with a height close to 230 μm capable to storing fluids up to 0.5uL) above it which is made of cyclo-olefin polymer (COP) material (with low water vapor permeability ($0.023\ g.mm.m^{-2}.day^{-1}$) to limit drug evaporation). This leads to upward actuation of the drugs as they move towards the thin copper membrane (3 μm). The actuated drug after puncturing the copper membrane (which also prevents drug evaporation from the top orifice), flows into the 8 mm long microfluidic probe (with 10 μm x 10 μm cross-sectional channel size) before being ejected from the polydimethylsiloxane (PDMS) based microfluidic channel orifice. PDMS based microfluidic probe offers higher mechanical compliance with soft biological tissues when compared to alternate approaches being used for constructing microfluidic channels like Parylene C (2.5 GPa) or thermally drawn fibers (2.7 GPa). Better mechanical matching helps achieve chronic biocompatible integration with soft biological tissues. Together, the μ-ILEDs and microfluidic probes form a very flexible, soft and thin (80 um) optofluidic probe (13-18 N/m) that provides minimally invasive deep tissue access for chronic studies that extend over long periods of time.

3.2.2 Stretchable Power Harvester

The flexible, thin, soft and stretchable power harvester is the key to miniaturization of the implantable device by allowing the exclusion of batteries and thus significantly reducing the footprint of the device. The power harvester consists of two main stages – the serpentine shaped stretchable antenna and the rectifying circuitry. **Figure 3.5** and **Figure 3.6** highlight the overall schematic design and components used required to construct the wireless power harvesting system. The process starts from the transmitter system which consists of a signal generator which is used to generate a specific frequency at which we will transmit the wireless power. It is then passed through an RF amplifier ($Gain_{1dB}$ = 50 dB) which amplifies the signal to the power level enough to allow its transmission through air. Finally, the RF antenna directs this power for untethered energy transmission to the remotely located implantable device inside the body.

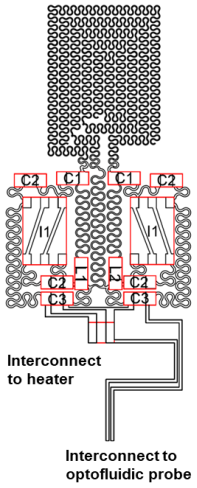

	Manufacturer	Part Number	Description
C1	Murata Electronics	GRM0335C1H1R0CA01D	1 pF Ceramic Capacitor
C2	Murata Electronics	GRM1885C1H220JA01D	22 pF Ceramic Capacitor
C3	Murata Electronics	GRM155R71C104KA88D	0.1 µF Ceramic Capacitor
L1	Taiyo Yuden	HKQ0603U2N7B-T	2.7 nH Inductor
L2	Taiyo Yuden	HKQ0603U5N0C-T	5 nH Inductor
I1	NXP Semiconductor	BAS70VV	Diode Array Schottky

Figure 3.5 – Circuit schematics and component list of the energy harvester circuit.

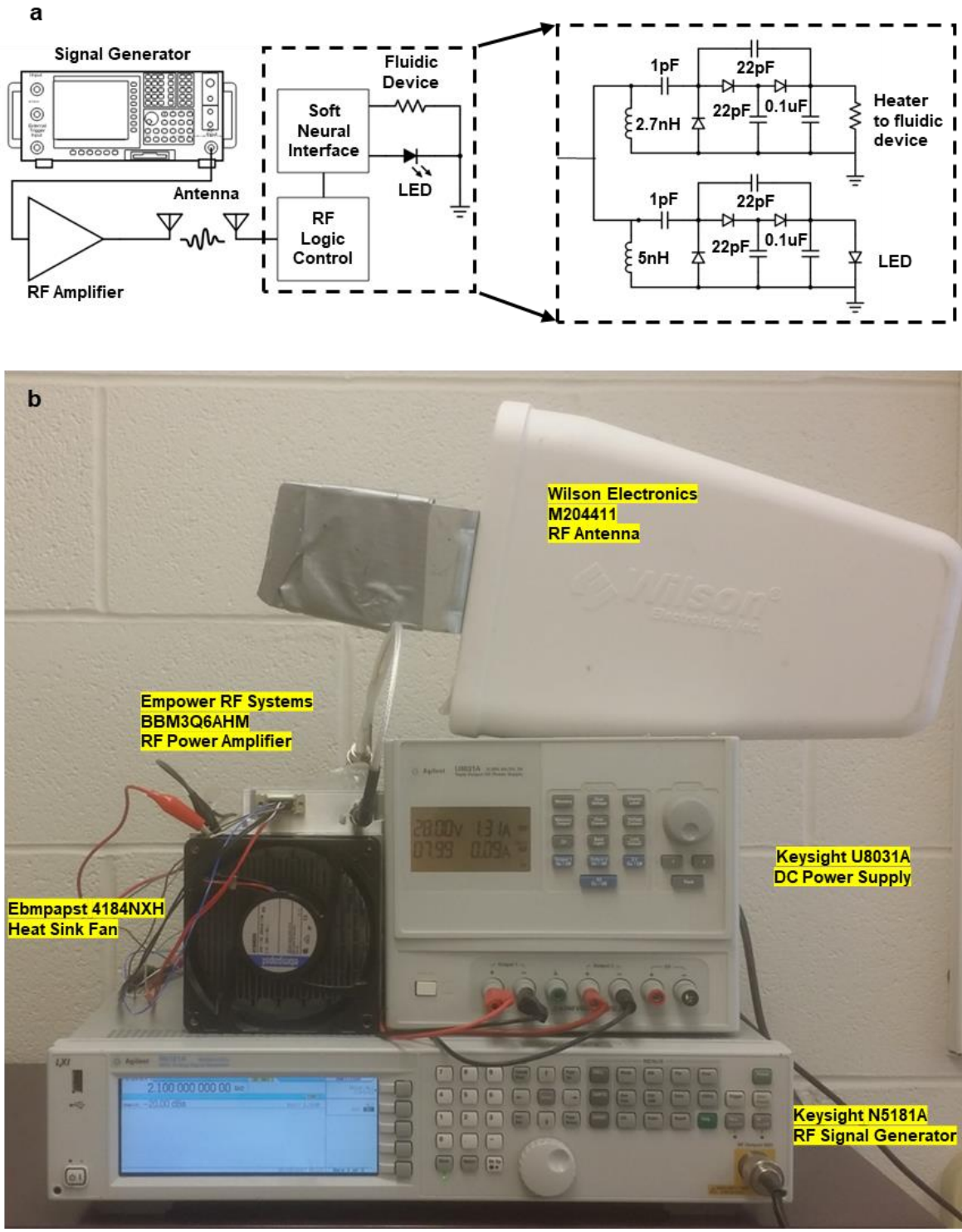

Figure 3.6 – Wireless transmitter and receiver setup. (a) *Schematics* ***(b)*** *Wireless transmitter component list.*

The ultracompact, thin and stretchable antenna consists of serpentine shaped, metal traces that harvest RF electromagnetic waves (which were generated by the RF transmitter setup discussed above) through capacitive coupling between adjacent traces (**Fig. 3.7a**). This design helps create a pair of multiple non-overlapping resonant channels in the ultrahigh frequency range (**Fig. 3.7b**). Using the ultrahigh frequency range for wireless transmission allows a reduction in antenna size and thus the overall device structure. Each of the two independent resonant channels (Channel 1 at 1.8 GHz and Channel 2 at 2.9 GHz) is capable of directing the harvested power to either the μ-ILEDs or the microactuator, thus allowing independent control of its photostimulation (**Fig. 3.7c**) and drug delivery (**Fig. 3.7d**) abilities respectively. This is enabled by having large enough bandgap between the resonant channels so as to not allow the cross-coupled power to reach the threshold to activate either output modality i.e. the μ-ILEDs or the microactuator. To achieve independent control for drug delivery (Channel 1), the reflected power (S_{11}) of Channel 2 (μ-ILEDs) is only 0.1 dB which is about 2.2% of input power. This coupled power is transmitted to μ-ILEDs also when drug actuation occurs. However, 2.2% of the minimum power to achieve drug actuation (125 mW) is only 2.75 mW which is not sufficient enough to power up the array of μ-ILEDs. On the other hand, the minimum power required to activate the array of μ-ILEDs is much lower than the power needed to actuate the drugs. The bandgap between individual resonant frequencies can be increased (by altering antenna dimensions and pitch), in case the cross-coupled power needs to be reduced for some specific output modalities. On the contrary, to achieve simultaneous drug delivery and photostimulation, the RF power can be increased enough to allow simultaneous power delivered in both channels through the cross-coupling, thus allowing promising applications in novel fields such as optopharmacology (**Fig. 3.7e**) which involves unique actuation of drug compounds using light. The average transmitted power used is kept around 2.1 W which does not exceed the safe values suggested by the Federal Communications Commission (FCC) guideline (4W equivalent Isotropically Radiated Power, FCC 15.247 [ref]) After harnessing the RF electromagnetic power, it is transferred to the rectifying

circuit components which convert this alternating current (AC) signal into pulsating Direct Current (DC) signal. Based on which resonant channel was able to capture the power, the rectified energy is then either transferred to either μ-ILEDs or the micropump accordingly.

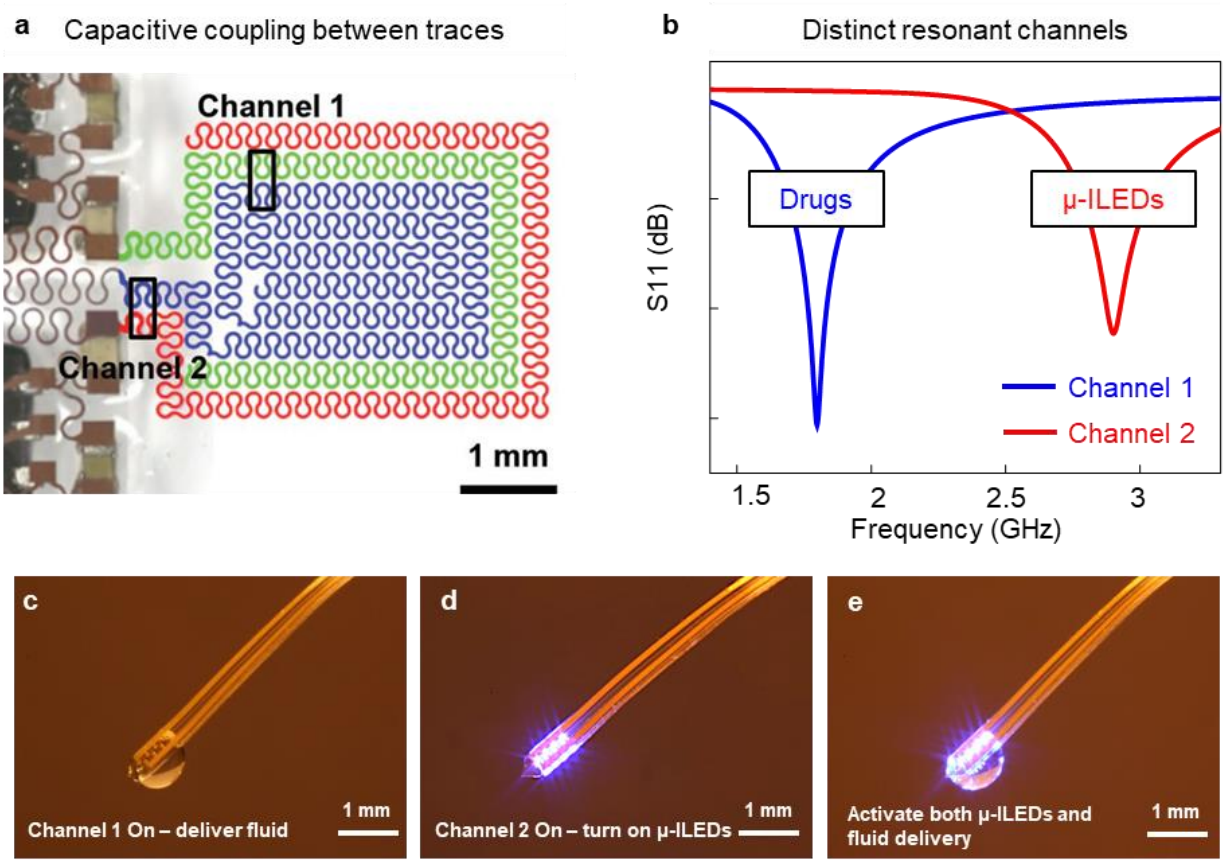

Figure 3.7 – Selective Channel Control of Multichannel Wireless Antenna. (a) *False-colored optical image of the wireless antenna highlighting the two antenna pairs forming two independent channels at distinct resonant frequencies allowing it to actuate drugs* ***(c)*** *and light* ***(d)*** *independently or both simultaneously* ***(e)****.*

Another useful feature of this serpentine antenna structure is its scalable and tunable design to easily allow a variety of customizable neuroscience experiments. The antennas can be precisely tuned at various frequencies by adjusting the spacing between adjacent traces. Decreasing the distance between the trace pair allows an increase in the capacitive effect and hence the coupling occurring between them. This leads to lowering of the operational resonant frequency of that specific pair. On the other hand, increasing the distance between the trace pair decreases the capacitive effect in the pair which also decreases the capacitive coupling between

them. This leads to an increase in the resonant operating frequency of that pair. Another interesting capability id the ease of scalability in this design. The number of resonant channels can be easily increased by increasing the number of serpentine metallic traces and engineering their pitch so create independent resonant channels (as demonstrated later in this chapter in the sub-topic called “Scalability”). This can allow for easily configurable and multiplexed neuroscience studies involving a multitude of output sensors and actuators being controlled using the same stretchable antenna without any increase in this thickness or flexibility, thus retaining its fully implantable nature.

3.3 Device Characterization and Analysis

In this section, we shall discuss the device performance and reliability for each modality. From its optical output performance to its ability for drug actuation and delivery, including the associated time lag and thermal characterization for the actuation process, the wireless performance, the thorough tests determined that the device was able to reliably work well in a variety of experimental setups.

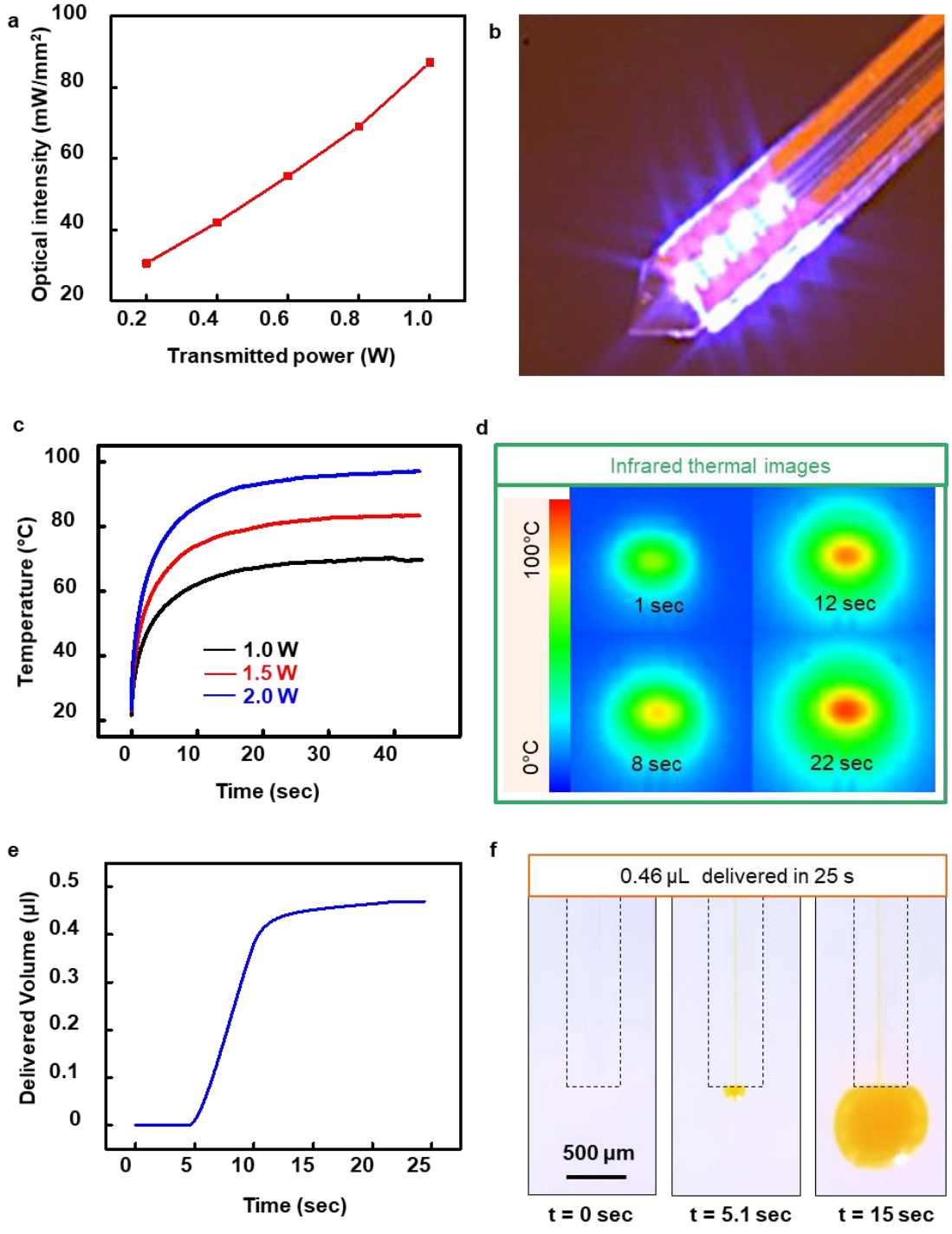

Figure 3.8 – Optical, Thermal and Fluidic Characteristics for light and drug actuation. (a-b) *Optical intensity of µ-ILEDs as a function of RF power transmitted from 10 cm away.* ***(c-d)*** *Spatiotemporal heat distribution on heater coils of the thermal actuator to reach threshold temperature of 87 °C.* ***(e-f)*** *Temporal analysis of fluid volume delivery from the microfluidic probe tip.*

3.3.1 Optical Characteristics

The optogenetic stimulation is enabled by four parallelly connected μ-ILEDs, operating at peak wavelengths of 470 nm, are soldered at the tip of the soft optofluidic probe. Each LED is attached at a pitch of about ~200 μm from an adjacent neighbor, thus spanning a total of 800 μm approximately. Upon harvesting power in Channel 2, the power is rectified to DC voltage and then directly fed to these μ-ILEDs. The optical intensity of each μ-ILED is proportional to the harvested power which is directly dependent on the power transmitted from the remotely based station (**Fig. 3.8a**). It has been found in previous studies that power of 1mW/mm^2 is sufficient enough to excite channelrhodopsin2 (ChR2) protein in the genetically altered target cells. As is evident from **Figure 3.8a**, we can easily generate an output power that is way beyond the minimum threshold. A power of 0.2W or above from 10cm away from the implanted device can easily achieve significant optical intensity (> 30mW/mm^2) to switch light-sensitive opsins. By increasing the transmitted power, we can easily increase the optical intensity in all four μ-ILEDs uniformly (**Fig. 3.8b**), thus allowing us to stimulate a relatively larger area over a span of about 0.8mm along the probe tip.

3.3.2 Spatiothermal analysis of actuation

The drug delivery is initiated through the thermal expansion of expancel microspheres embedded in a PDMS (1:10) matrix. The heat generated occurs at the gold based serpentine traces (300nm thick) sandwiched between the thermally responsive layer on the top and the thermally insulating FR-4 layer at the bottom. Since the process occurs through Joule heating, it takes a few seconds for the haters to raise the surface temperature close to the peak possible temperature (**Fig. 3.8c**) after which the temperature increase rate significantly drops and maintains the peak temperature over time. As is evident from the graphs, the heat generated is proportional to the power transmitted from the remote base station. Since the power harnessed is proportional to the

transmitted power, hence increased RF electromagnetic signal amplitude harnessed at Channel 1 corresponds to higher heat generation at the gold heater surface. Since the thermally responsive polymer requires at least 87°C to start expansion, the average transmitted power must be equal to or greater than 2W to be able to achieve that temperature range. At 2W of average transmitted power from when the wireless power transmitter is 10cm away from the implantable device, we are able to achieve about 100°C at the heater surface which is sufficient enough to achieve drug actuation. To reduce transmitter power required or to actuate micropump at lowers power levels, we need to increase the power efficiency to induce actuation. To help achieve this, using FR-4 layer as a substrate for the gold heaters assists by allowing minimal dissipation and spread of heat energy from the bottom side, thus improving efficiency for heat transfer to the polymer layer above throughout the drug actuation process (**Fig. 3.8d**) which lasts for over 20 seconds.

3.3.3 Fluidic Characterization and Testing

Upon receiving rectified power from the energy harvester circuit (2W of transmitted power when transmitter antenna is 10 cm away from the device) through Channel 1 at 1.8 GHz, the micropump begins the actuation process immediately. This is initiated by the commencement of joule heating effect which leads to the immediate rise in temperature on the heater coils, as is evident from **Fig. 3.8c**. However, the transduction from the heating energy to actual expansion of the thermally expandable layer requires some latency and that causes a time delay after actuation before the drug actually starts to flow. **Figure 3.8e** highlights the temporal characteristic of the drug delivered from the microfluidic probe tip once the device is actuated at time t = 0s. The drug starts ejecting from the tip close to t = 5s and delivers >95% of total delivered volume at around t = 15s (**Fig. 3.8f**). After that, the output flow rate is significantly reduced as the remaining drug is slowly pushed out. Overall, the total capacity of the drug being stored in the reservoir is 0.5 µL.

However, as we can see only 0.46 µL of fluid is actually ejected over a period of 25s. The residual volume of about 0.04 µL is within the tolerance limits for micropumps of such size [ref]. A part of it is contributed to the residual volume left in the reservoirs and the channels and another part due to machining tolerances while making of the reservoirs. This can be compensated by slightly increasing concentration of drugs or modification of reservoir volumes. However, it must be noted that the volume delivered is variable within a 0.02 µL tolerance while modifying any part of the design.

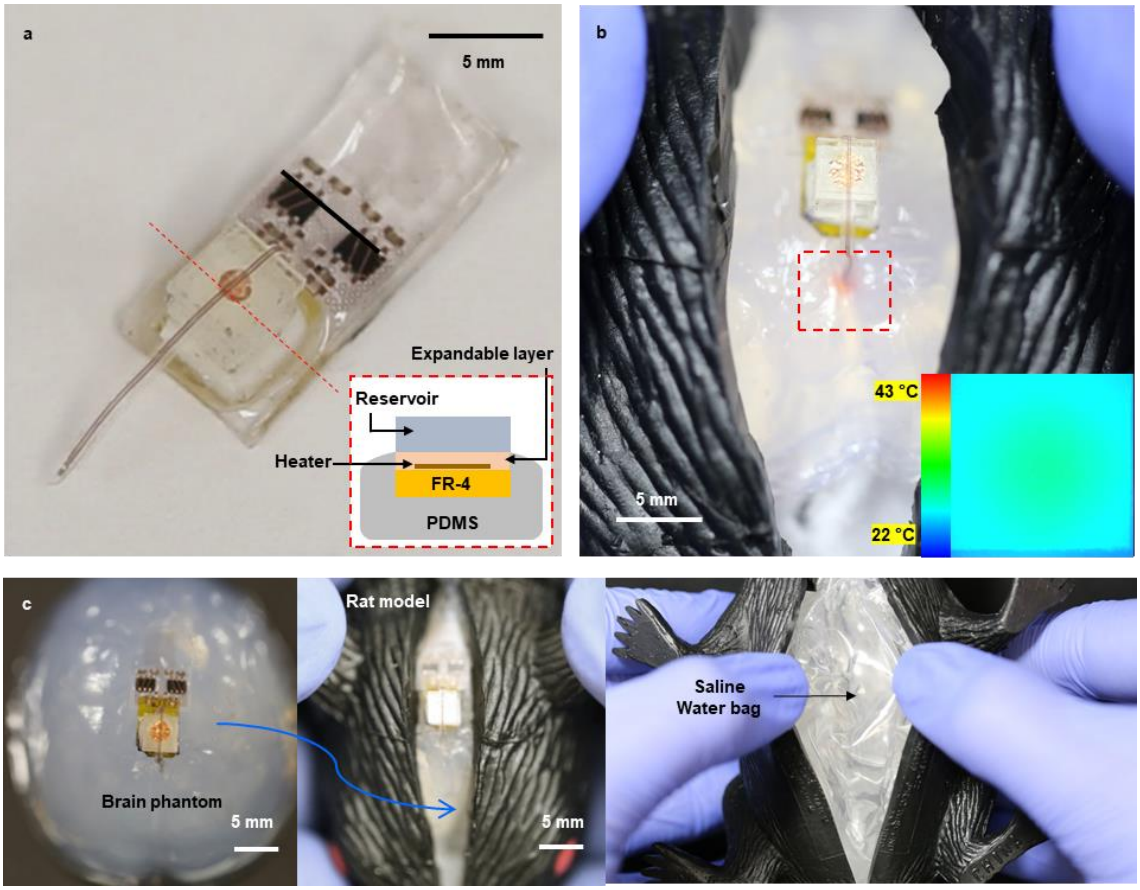

Figure 3.9 – Wireless fluid delivery using the 2mm thick PDMS encapsulated implantable device in a dummy rat. (a) *An optically projected image highlighting various functional layers (inset) for drug actuation.* ***(b)*** *Wireless delivery of red dye into the phantom brain (0.6% agarose gel) in the rat model. The red dotted box indicates the infused dye. IR image in the inset shows surface temperature of the heater's PDMS encapsulant (≈30 °C) in the ambient environment at room temperature when the heater temperature reaches ≈100 °C during fluid delivery, verifying rapid heat dissipation through the PDMS encapsulant.* ***(c)*** *Setup prepared for the experiment using agarose brain and saline water bad to simulate brain and body fluids respectively.*

Figure 3.9 highlights functional validation of the micropump drug delivery as it simulates *in vivo* operation in a model rat with an embedded phantom brain. **Figure 3.9a** highlights the cross-sectional composition of various layers that take part in the drug actuation. The 2mm thick PDMS layer at the bottom helps protect the underlying tissue from the heat generated during the drug delivery process (**Fig. 3.9b**), as can be seen infrared image taken of the bottom side of the device (= 30 °C) during drug actuation in ambient conditions (inset of **Fig. 3.9b**). The soft optofluidic probe is inserted into the phantom brain made of 0.6% agarose gel and the rat body is stuffed with a saline water bag in order to simulate the composition of biological tissue and to check if there would be any effect on the RF triggering of the drug delivery (**Fig. 3.9c**).

3.3.4 Mechanical Characterization

Understanding the mechanical dynamics of the fully -implantable optofluidic device as it lies within layers of biological tissues is very important, especially because the soft, fluidic biological environment is always in a state of micromotions. This can especially have a significant effect on the power transfer efficiency of the wireless stretchable antenna traces as the tissue deformations and associated micromotions can relatively increase or decrease the average spacing between the resonant pair traces and thus alter the resonant frequency. Since the deformations in the tissue cannot be predicted or accurately quantified to alter transmitted resonant frequencies on the fly, we must study if normal tissue disturbance has any effect on the reliable functionality of the device and if it does, how to mitigate the adverse effect. A possible strain on the stretchable antenna may significantly shift the resonant frequency and thus incapacitating the power transfer to either of the two channels. In order to verify the reliable functionality of the device and study effect of physical strain on the device, especially the soft, stretchable serpentine antenna, finite element analysis (FEA) of the antenna region was conducted.

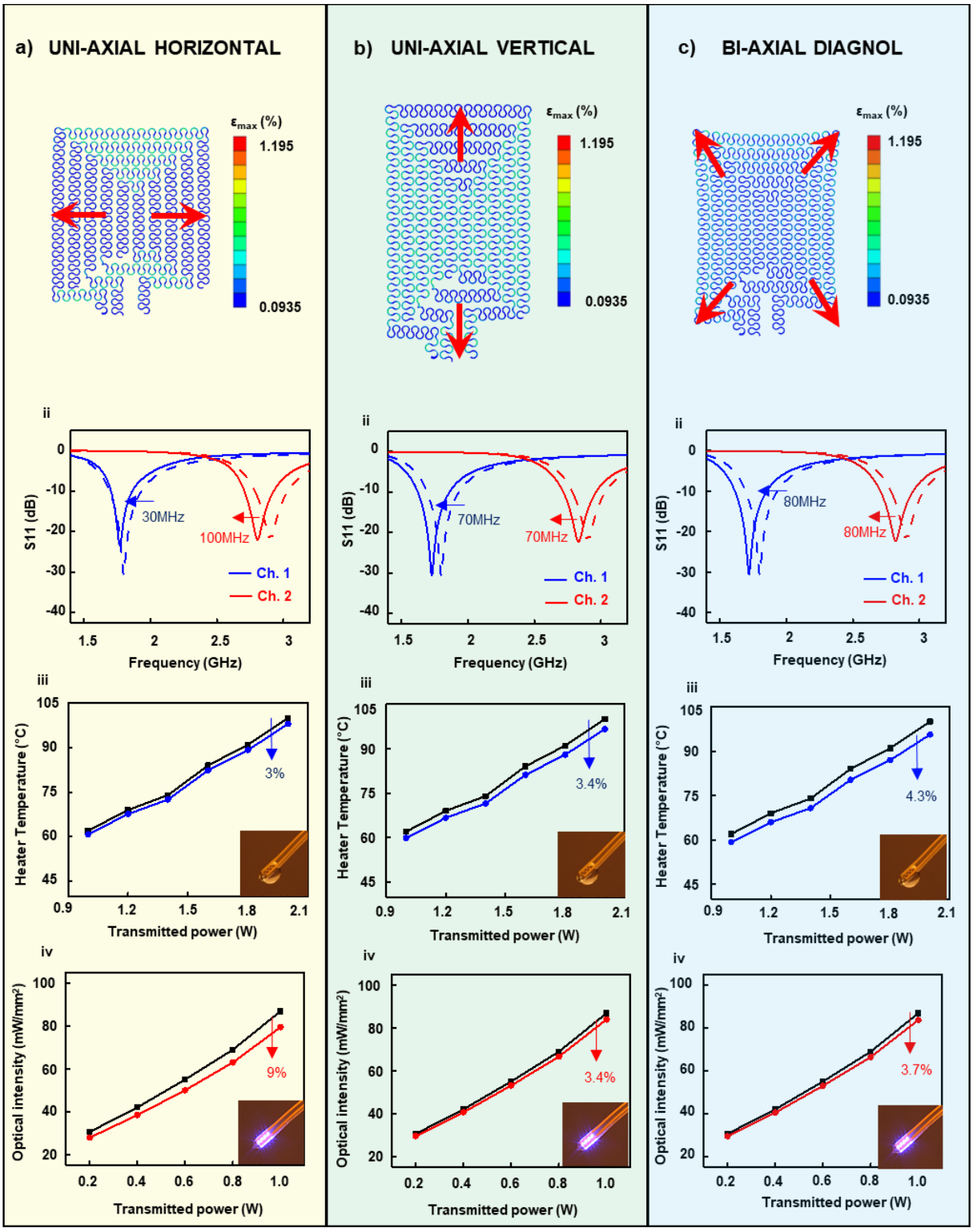

Figure 3.10 – Mechanical characterization of the stretchable antenna *and related output performance under* ***(a)*** *unidirectional horizontal,* ***(b)*** *unidirectional vertical and* ***(c)*** *biaxial diagonal strains of 20%.*

Assuming worst case strain scenarios of 20% tissue strain inside the body, we apply this strain in three distinct directions as shown in Figure 3.10. Electromechanical simulations of the antenna reveal that 20 % strain on the serpentine traces in uniaxial horizontal (**Fig. 3.10a**), uniaxial vertical (**Fig. 3.10b**) and biaxial diagonal (**Fig. 3.10c**) have very less effect on lowering of the resonant frequency and thus does not raise any major concern on the power harnessed by the device while the biological environment dynamically moves around the stretchable antenna. It was found that only ~1.195% maximum principal strain is caused in the serpentine copper traces due to 20% stretching of the antenna substrate. This ensures that the metal connections stay intact during such stress as the fracture strain for copper lies between 20% to 40%. Figure 3.10 highlights the effect of strain applied on the resonant frequency, optical output power, and micropump temperature profiles. As is evident, that both resonant frequency shifts and a decrease in output optical power (Channel 2) have a minimal effect due to the applied strain, although it slightly decreases the power efficiency at that specific frequencies. Even at 0.2 W of average transmitted power the μ-ILEDs reliably operate far beyond the threshold output optical power required for optogenetic excitation (1mW/mm^2), both before and after applying strain. On the other hand, for micropump actuation, when an average transmitted power of 2W was applied, it was enough for it to generate the threshold temperature (87 °C) through Joule heating on the metal coils which is critically needed by the thermally expandable polymer to push the fluid. However, upon applying 20% strain, we see that the temperature achieved comes very close to a threshold temperature and may incapacitate the drug actuator functionality. This can be easily mitigated by increasing average transmitted power by 5% (i.e. 2.1 W) which can assure reliable actuation of the micropump even under strain conditions. Furthermore, the strain in the antenna does not affect the bandgap between the two independent channels (because both channels are shifted by almost similar amounts), thus retaining its independent control feature of each output modality under 20% strain conditions.

3.3.5 Thermal Impact on Surrounding Biological Tissues

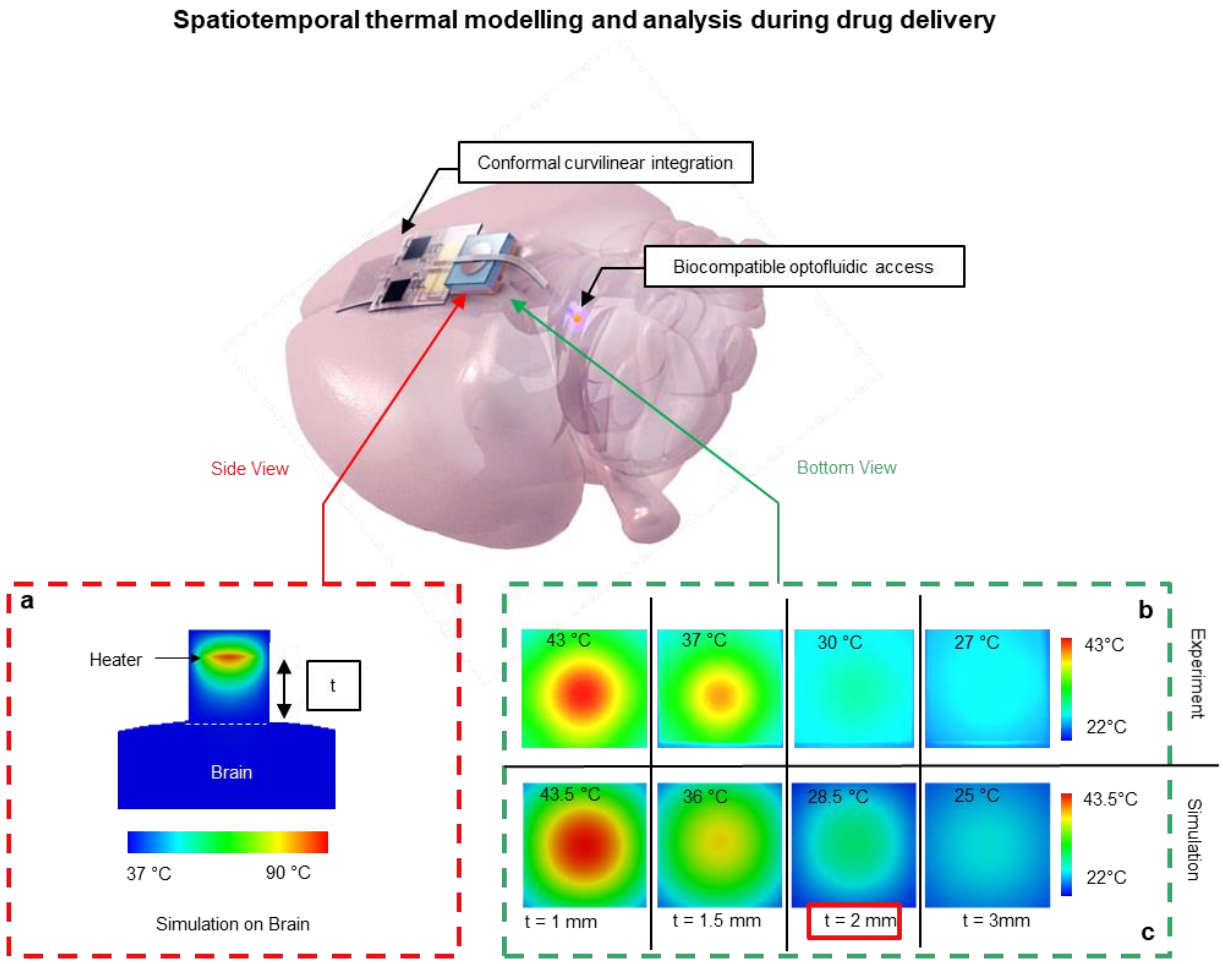

Figure 3.11 – Thermal Simulation and Characterization of the effect of the device on tissues *when placed* ***(a)*** *on biological tissues and* ***(b)*** *in ambient conditions at various PDMS encapsulation thicknesses.*

The soft, flexible nature of the implantable device allows it to conformally contact the tissue surface as shown in **Fig. 3.11**. Due to this mounting setup, it may raise concerns related to the heating effect of the underlying tissue because of the vicinity of the micropump what functions on thermal actuation. As we have seen earlier that the temperatures on the heater coils may rise up to 100 °C to generate thermal energy required to actuate the drugs and if transferred to the biological tissues can prove to be very detrimental. To avoid such a situation, we stack two distinct layers between the heater coils and the tissue. First of all, is the FR-4 material which itself acts

as a substrate for the gold metal heaters. Its low thermal conductivity limits the transfer of heat to the bottom tissue as well as restricts its spatial spread as we can see in **Fig. 3.8d**. Below it is a 2 mm thick encapsulating layer of PDMS which further limits the temperature that reaches the biological tissue as is evident from the simulation shown in **Fig. 3.11a**. As the thickness of the PDMS layer (t) is altered, the temperature seen at the bottom side of the PDMS surface during drug actuation is shown in **Fig. 3.11b** using IR camera (top) and simulations (bottom). The temperature reaching the tissue is inversely proportional to the encapsulation thickness of the soft polymeric PDMS sheath. This PDMS sheath also helps prevent electrical shorts within the device once it is surrounded by biological fluids inside the body. As shown in **Fig. 3.11b**, an encapsulation thickness which is 2 mm or more can be considered safe enough for *in vivo* operation of the device for drug delivery.

3.3.6 Directional Characteristics of Wireless Antenna

Since the freely moving animals constantly move in random directions during *in vivo* studies, it is very important to characterize the directionality of the wireless antenna and see if altering directions can affect reliable functionality of the device. **Figure 3.12** highlights the omnidirectional normalized radiation gain patterns of the soft, stretchable antenna on the implanted device in all three orthogonal directions, thus ensuring its robust behavior irrespective of direction with respect to the wireless transmitter antenna. Moreover, preliminary testing of its omnidirectional pattern to light up the array of μ-ILEDs in model rats (with agarose phantom brain and saline water bag to simulate biological tissue) irrespective of the direction or orientation of the model rat (**Fig. 3.13**). this highlights its unique potential for reliable functionality during *in vivo* studies in freely moving animals.

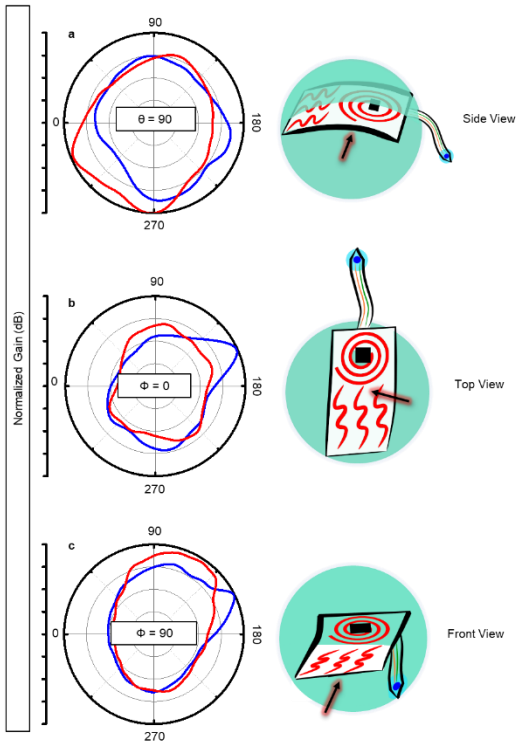

Figure 3.12 – Omnidirectional wireless characteristics of the stretchable antenna on the implantable device.

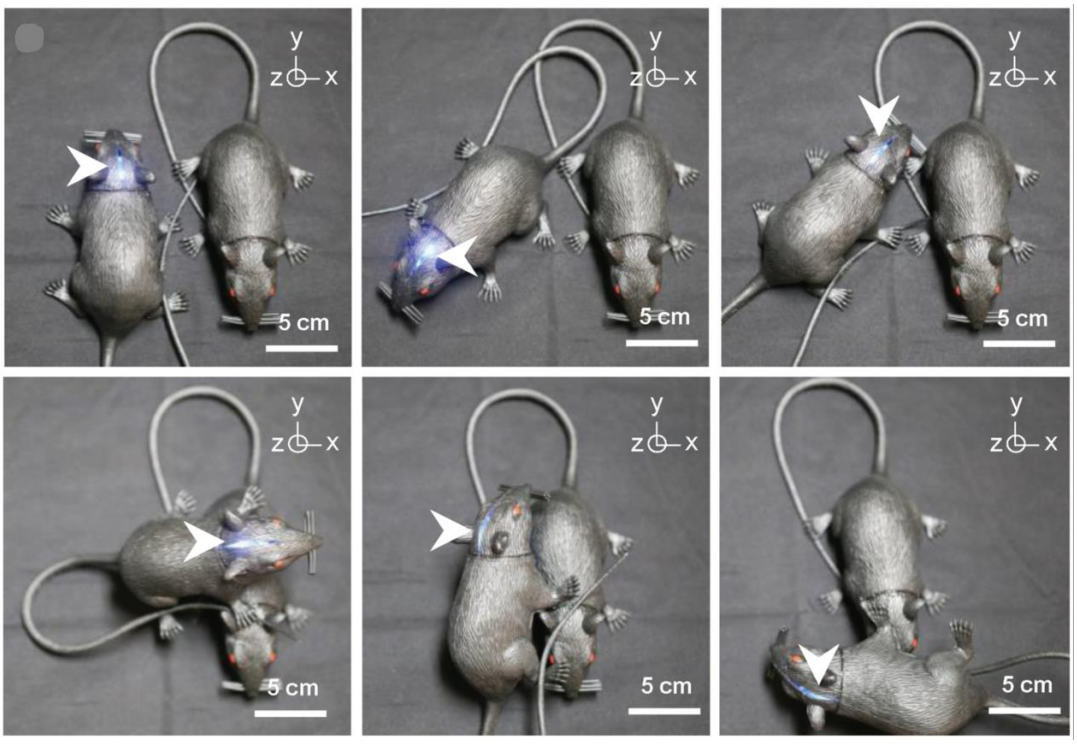

Figure 3.13 – Pictures of a model rat implanted with a wireless optofluidic system, demonstrating wireless operation at various angles.

3.3.7 Scalable Design Characteristics

One of the most important features of a device is its ability to be easily customized to suit various experimental needs. This allows the device to be optimized for a specific experimental need without any significant design change. The fully implantable optofluidic device can be easily scaled to have additional independent channels, reservoirs, drug actuators, microfluidic channels, μ-ILEDs because of its unique design structure as shown in **Fig. 3.14 - 3.15**. More antenna pairs can be easily added by to increase the number of resonant channel pairs and hence a number of independently controllable outputs (**Fig. 3.14a**). As an example, four gold heaters can also be laid side by side (in square formation) with a large reservoir containing four separate drug reservoirs that can be actuated independently (**Fig. 3.14b**). Then the microfluidic channels can be laid side by side (inset of **Fig. 3.14b**) to allow the release of each drug through a distinct microfluidic channel.

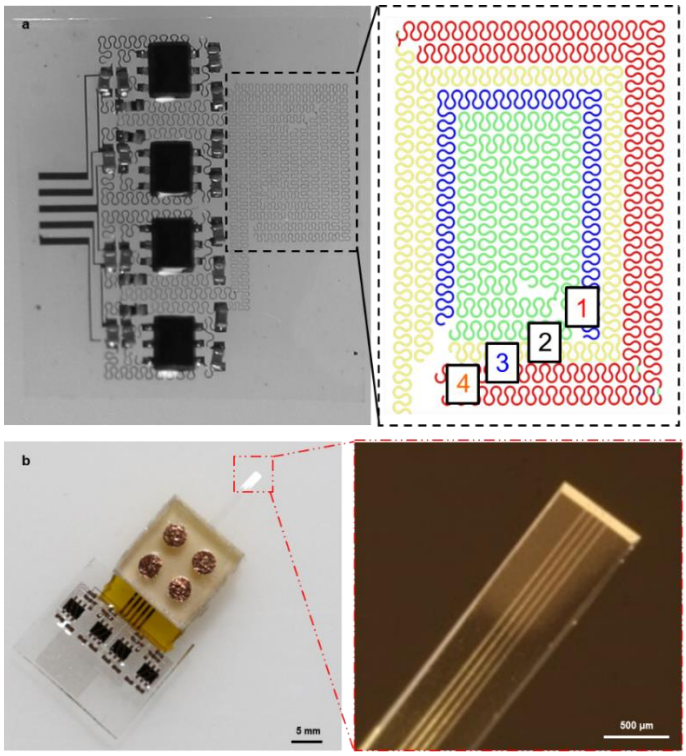

***Figure 3.14** – **Scalability of the implantable device** for **(a)** antenna **(b)** drug reservoirs and **(c)** microfluidic channels.*

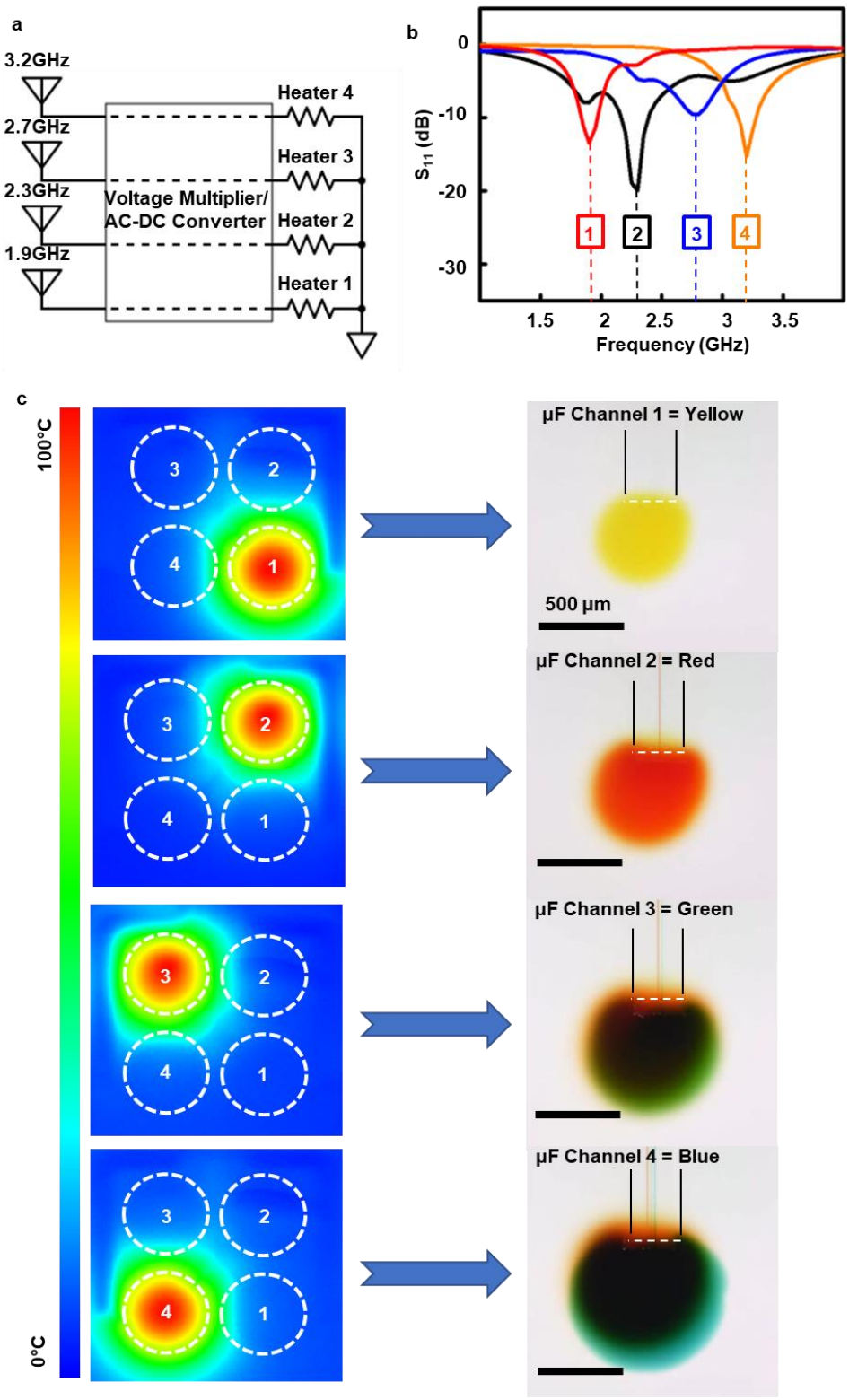

Figure 3.15 – Functional Validation of a scaled implantable device *with* ***(a)*** *four channel pairs operating at* ***(b)*** *four resonant frequencies and able to deliver* ***(c)*** *four independently controlled drug reservoirs to release distinct drug from each of the four microfluidic channels on an agarose surface.*

Figure 3.15 a-b highlights the antenna resonant frequencies chosen to allow significant bandgap between adjacent resonant pairs so that independent control of each output can be achieved. The antenna traces need to be engineered so they can have four resonant frequencies at 1.9 GHz (Heater 1), 2.3 GHz (Heater 2), 2.7 GHz (Heater 3) and 3.2 GHz (Heater 4). **Figure 3.15c** highlights the micropump actuation process and associated fluid delivery once power is transferred to the specific resonant channel. This technique can also be allowed to add additional μ-ILEDs of same or different wavelengths (without increasing the cross-sectional area of the optofluidic probe) that can be independently controlled as well. This can enable the device to potentially be used for highly localized multiplexed delivery of multimodal stimulations for neural circuit dissection or drug developmental studies.

3.4 Functional Validation through Preliminary *In Vivo* Tests

To test the fully implantable nature of the optofluidic device (**Fig. 3.16a-f**) and its functionality (**3.16g**) when implanted inside a freely moving animal (mouse), we conducted preliminary *in vivo* studies to verify its reliability in real animal experiments. To fully implant the device inside the body, the mouse was put under anesthesia and a superficial incision was made on its head under aseptic conditions. Based on desired stereotaxic coordinates, a small opening was drilled for placement of the optofluidic probe. Then the soft device was inserted under the skin, caudal to the implantation site. The soft optofluidic probe was temporarily stiffened with a biodegradable polymer (PLGA). After securing the implant, the mouse's skin was sutured, and the wound was closed for recovery. After the recovery period, the mouse was placed inside a chamber and the μ-ILED array on the implanted device was wirelessly operated (independent of the micropump), thus validating its omnidirectional functionality for *in vivo* studies.

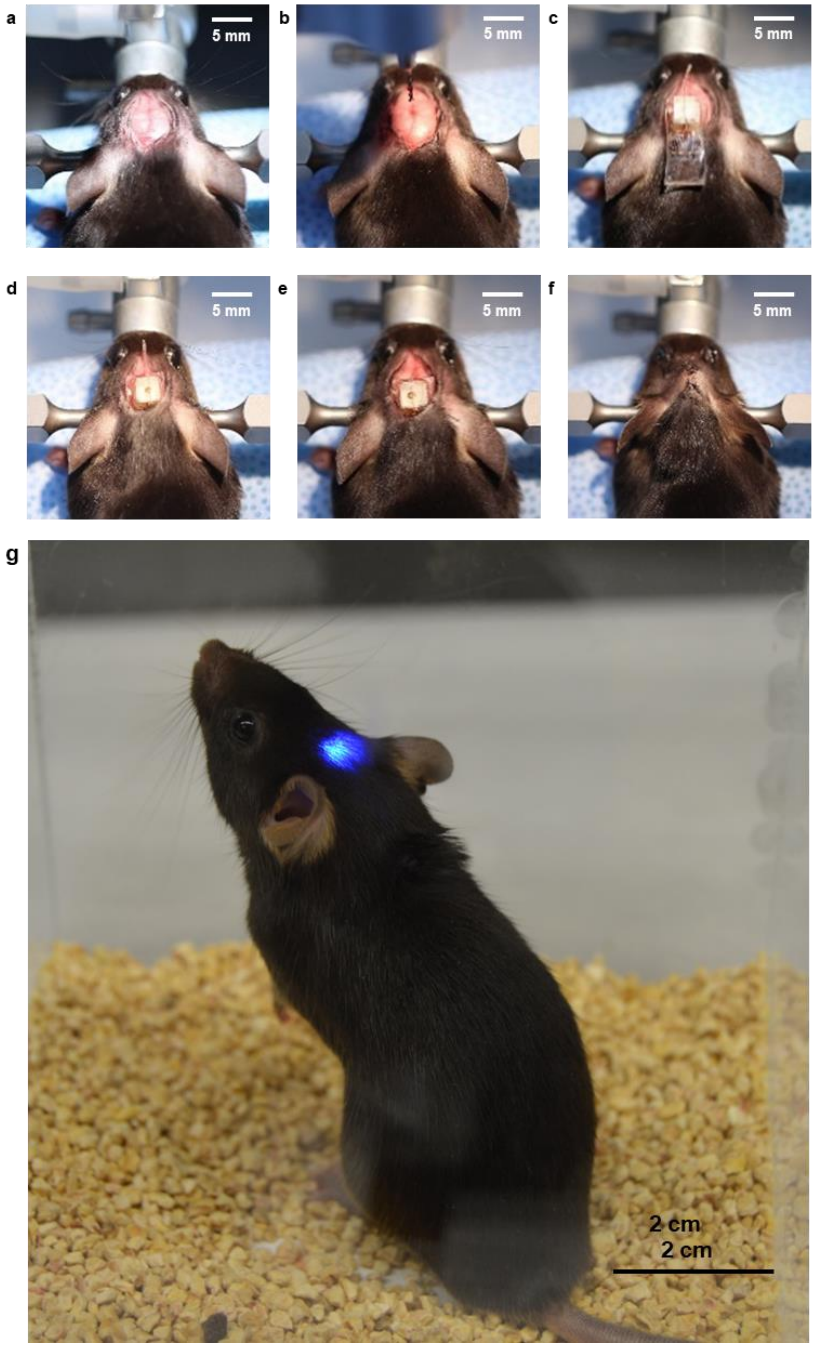

Figure 3.16 – Proposed surgical procedure for implantation of the optofluidic device in the mouse brain. (a) *The mouse's skull is exposed after a superficial midline incision is performed under aseptic conditions.* ***(b)*** *Following the identification of the desired stereotaxic coordinates for the implantation of the device, we proceed to drill a small opening for placement of the optofluidic probe.* ***(c)*** *The relative size of the implant with relation to the animal's head.* ***(d)*** *Insertion of the soft RF harvester under the skin, caudal to the implantation site.* ***(e)*** *Placement of the optofluidic probe into the brain cortex, following temporary stiffening of the implant with a biodegradable polymer (PLGA).* ***(f)*** *After securing the implant, the mouse's skin was sutured to close the wound and allow for recovery.* ***(g)*** *In vivo functional validation of the implantable device through wireless control of micro-LEDs using wireless power transfer.*

3.5 Conclusion and Future Directions

Being first of its kind as a fully implantable standalone optofluidic device, it offers a lot of advantages over contemporary technologies (Lego device included in Chapter 2).

TABLE 3.2 COMPARISON OF IMPLANTABLE OPTOFLUIDIC DEVICE WITH PREVIOUS TECHNOLOGIES

Property	**Implantable Optofluidics** (Noh *et al.*, 2018)	**Programmable Optofluidics** (Jeong *et al.*, 2015)	**MiNDS** (Dagdeviren *et al.*, 2018)	**Multifunctional Fibers** (Park *et al.*, 2017, Canales *et al.*, 2015)
Standalone System?	Yes	Yes	No (Tethered electronics with wireless drug delivery pumps)	No
Fully Implantable	Yes	No	No	No
Operation	RF Wireless ~10 cm	Infrared Wireless (Directional control) ~2 m	Bulky & Heavy Commercial Wireless Pumps <3 m	Tethered
Modalities	Optical & Fluidic	Optical & Fluidic	Electrical & Fluidic (No Photo-stimulation)	Optical, Fluidic & Electrical (Single Light Wavelength)
# of Independent Drug Channels	4	4	1	2 (Deliver to the same target location)
Mechanical Property of the Probe	Soft, flexible E ~ 1 MPa k: 13-18 N/m Thickness = 80μm	Soft, flexible E ~ 1 MPa k: 13-18 N/m Thickness = 80μm	Rigid E ~ 200 GPa k = 200 μm	Flexible E~107-149 N/m k = 400 -700 μm
Remote controller	RF hardware and antenna	Custom-built IR transmitter	Commercial iPrecio hardware	Tethered external hardware
Line of Sight/ Obstacle Handicap	Yes	Yes	No	N/A

Wireless/ Standalone

Tethered/ External Connections

Table 3.2 highlights the unique capabilities of this device with previous contemporary technologies. Compared to the device discussed in Chapter 2 (Lego optofluidic device), it lacked chronic functionality and some wireless features, however, its fully implantable nature allows its feasible integration in any space critical location inside the body. These fully implantable, battery-free, wireless optofluidic systems have enormous potential for use *in vivo* optogenetics and pharmacology with possible future applications in optopharmacology. The miniaturized geometry and soft construction of these devices enable their implantation into the brain as well as other biological tissues. A straightforward extension of the number of operation channels via an advanced impedance matching technique can offer opportunities for more versatile implementation of various functions of neural implants for complex neuroscience research and clinical applications. Such an approach will allow dissection of neural circuits in a dual fashion, using light to modulate neuronal activity via optogenetics, while allowing localized administration of pharmacological agents targeting multitude cellular pathways that mediate neuronal physiology. In addition, due to the device design and integration of μ-ILEDs with a multiple-chamber reservoir, multiple rounds of drug administration can be performed. This feature can enable analysis of dose-response relationships for a single drug, or testing the effects of several different drugs, independently, in freely moving, awake animals. This point should not be ignored as being able to repeatedly deliver drugs and manipulate neuronal activity in an animal without tethers or handling can reduce the critical experimental variables. While battery-free operation allows a virtually infinite lifetime of the implanted optofluidic device, reuse of the fluid reservoir is challenging with the current design. We envision that improved designs with refillable or replaceable reservoirs will address this issue to maximize the utility of the device. In brief, the ability to manipulate neuronal circuits using wireless optogenetics and pharmacology, together with the possibility of repeated manipulations, represents a significant technological advancement and will allow researchers to ask questions that would have not been possible using existing technologies.

3.6 References

[1] E. S. Boyden, F. Zhang, E. Bamberg, G. Nagel, and K. Deisseroth, “Millisecond-timescale, genetically targeted optical control of neural activity,” *Nature Neuroscience*, vol. 8, no. 9, p. nn1525, Aug. 2005.

[2] O. Yizhar, L. E. Fenno, T. J. Davidson, M. Mogri, and K. Deisseroth, “Optogenetics in Neural Systems,” *Neuron*, vol. 71, no. 1, pp. 9–34, Jul. 2011.

[3] R. H. Kramer, A. Mourot, and H. Adesnik, “Optogenetic pharmacology for control of native neuronal signaling proteins,” *Nature Neuroscience*, vol. 16, no. 7, pp. 816–823, Jul. 2013.

[4] J. G. Bernstein and E. S. Boyden, “Optogenetic tools for analyzing the neural circuits of behavior,” *Trends in Cognitive Sciences*, vol. 15, no. 12, pp. 592–600, Dec. 2011.

[5] J. G. Bernstein, P. A. Garrity, and E. S. Boyden, “Optogenetics and thermogenetics: technologies for controlling the activity of targeted cells within intact neural circuits,” *Current Opinion in Neurobiology*, vol. 22, no. 1, pp. 61–71, Feb. 2012.

[6] K. A. Zalocusky, C. Ramakrishnan, T. N. Lerner, T. J. Davidson, B. Knutson, and K. Deisseroth, “Nucleus accumbens D2R cells signal prior outcomes and control risky decision-making,” *Nature*, vol. 531, no. 7596, pp. 642–646, Mar. 2016.

[7] V. Gradinaru, M. Mogri, K. R. Thompson, J. M. Henderson, and K. Deisseroth, “Optical Deconstruction of Parkinsonian Neural Circuitry,” *Science*, vol. 324, no. 5925, pp. 354–359, Apr. 2009.

[8] T. Bruegmann *et al.*, “Optogenetic control of heart muscle in vitro and in vivo,” *Nat Meth*, vol. 7, no. 11, pp. 897–900, Nov. 2010.

[9] V. Busskamp, S. Picaud, J. A. Sahel, and B. Roska, “Optogenetic therapy for retinitis pigmentosa,” *Gene Ther*, vol. 19, no. 2, pp. 169–175, Feb. 2012.

[10] A. C. Felix-Ortiz, A. Burgos-Robles, N. D. Bhagat, C. A. Leppla, and K. M. Tye, “Bidirectional modulation of anxiety-related and social behaviors by amygdala projections to the medial prefrontal cortex,” *Neuroscience*, vol. 321, pp. 197–209, May 2016.

[11] J.-W. Jeong *et al.*, “Wireless Optofluidic Systems for Programmable In Vivo Pharmacology and Optogenetics,” *Cell*, vol. 162, no. 3, pp. 662–674, Jul. 2015.

[12] K. N. Noh *et al.*, “Miniaturized, Battery-Free Optofluidic Systems with Potential for Wireless Pharmacology and Optogenetics,” *Small*, vol. 14, no. 4, p. 1702479, Jan. 2018.

4 Development of Optofluidic Neural Devices for *In Vivo* Studies

4.1 Preparation of replaceable male Lego drug cartridges

The Lego drug reservoirs with four (2 × 2 array with 3.1 mm pitch) male Lego pillars (1.7 mm long, 1.3 mm OD) were machined out from a 3 mm thick block of cyclic olefin polymer (COP, Zeonor 1420R), which has low water permeability (0.028 g·mm/m^2·day). Thermal actuators for pumping drug out from reservoirs were created with Cr/Au (5 nm/250 nm) serpentine traces on an FR-4 substrate covered with a thermally expandable polymer composite on top[1]–[3]. The male Lego drug reservoirs were then attached on the thermal actuators using a double-sided adhesive (ARClear 8932EE) after aligning each of its four reservoirs to the four micro-heaters. A 7 μm-thick Parylene C was additionally coated on the inner walls of the reservoirs and pillars (PDS 2010 Labcoater 2, Speciality Coating Systems) to minimize drug evaporation further. To facilitate drug loading into the hydrophobic reservoirs, they were made temporarily hydrophilic through oxygen plasma treatment (300 mTorr/200 W/55 s/6 sccm O_2 in March Jupiter III RIE), and desired drugs were then loaded using thin blunt syringe needles (30 Gauge, 0.31 mm OD). To minimize drug evaporation from open pillar ends, the pillars were plugged by a Parylene C-coated, 3 mm-thick PDMS cover consisting of cylindrical cavities (1mm long, 1mm ID) for each pillar and kept frozen at -20°C until ready for the *in vivo* experiment – the fabrication of PDMS covers followed the same procedure as the female Lego layer.

4.2 Fabrication and assembly of the female Lego:

1. Prepare female Lego pads after casting PDMS 5:1 into the 3D printed mold and cutting them to appropriate size as detailed above.
2. Align and attach them with the bonded microfluidic layer (from the previous step) using a 25 μm thick double-sided silicone adhesive (ARClear 8932EE). Cut the adhesive from near the channel edges to ensure that it does not block the channel inlets before vertically aligning the fluidic channels of the female Lego and the microfluidic channel inlets under an optical microscope.
3. Pass deionized (DI) water through the microfluidic layer and female Lego assembly using a blunt syringe needle (18 Gauge) plugged into each female Lego hole (1.15mm ID) to ensure the functionality of all four microfluidic channels.

4.3 Fabrication of ultrathin, soft microfluidic channel structures

An ultrathin, soft array of four parallel microfluidic channels (10 μm × 10 μm × 10 mm) was fabricated through soft lithographic and manual assembly procedures, as detailed in our previous protocols[1], [2].

4.3.1 SU-8 mold preparation and soft lithography:

1. Fabricate SU-8 mold on a 3-inch silicon wafer.
2. Treat SU-8 mold and glass slides (75 mm × 50 mm × 1 mm) with chlorotrimethylsilane (Sigma Aldrich) and 5% solution (with methanol) of AEAPS (3-(2-Aminoethylamino) Propylmethyldimethoxysilane, Sigma-Aldrich) respectively. This will ensure easy release of casted PDMS from both SU-8 mold and the glass surface later.

3. Cast PDMS (10:1) between the treated mold and glass slides. Clamp them together using a clamper on all four edges for the uniform force.
4. Cure the assembly for 55 min in the oven at 70oC (partially cured) and remove the casted structure along with the glass slide from the mold.
5. Punching and bonding microfluidic layers:
6. Punch through the alignment marks for each of the four microfluidic channel inlets using a 0.5 mm inner diameter (ID) puncher (Harris uni-core) under an optical microscope.
7. Using oxygen plasma treatment (March RIE II: 45 W/ 50 s/ 6 sccm O2), covalently bond the microfluidic casting with a thin PDMS layer (10:1). This step encloses the molded channel patterns into microfluidic channels and also covers one end of the through hole (punched in the previous step) for each microfluidic channel inlet.

4.4 Fabrication of optical layer with integrated µ-ILEDs

The optical probe layer was prepared using a similar process presented in our previous studies[1], [4], [5].

4.4.1 Preparation of the support substrate:

1. Spincoat PDMS (10:1) at 3000 rpm/ 600 rpm/ 30 s on a large glass slide (75 mm × 50 mm).
2. Cure at 70 °C for at least 70 min. This layer will help adhere to the ultra-thin optical layer substrate conformally flat on the surface throughout the fabrication process.

4.4.2 Preparation of the optical layer:

1. Place an ultra-thin 6 μm thick polyethylene terephthalate (PET) film conformally on the PDMS support layer (fabricated in the previous step).
2. Laser cut the film into a large array of probe needles with dimensions of 10 mm × 0.5 mm in the probe area (penetrating support) and 5 mm × 1.58 mm in the basal area (connection part).
3. Deposit Chromium (Cr, 5 nm) and Gold (Au, 250 nm) on the surface using an e-beam evaporator.
4. Clean the surface with acetone, then iso-propyl alcohol (IPA) followed by deionized (DI) water and dehydrate the sample at 110 °C for 120 s.
5. Spincoat positive photoresist on the samples (AZ4210P, IMI Micromaterials) at 3000 rpm/ 1000 rpm/ 30 s to etch deposited metal layers into electrode structures through photolithography.
6. Soft-bake at 110 °C for 90 s.
7. Expose UV light (80 mJ/ cm2) on the photoresist using a Mask Aligner (Karl Suss, MJB series) after aligning electrode structures in the patterned chromium-glass mask within the laser cut pattern (from the earlier step) for each optical probe.
8. Develop the photoresist by immersing the sample in a diluted AZ400K developing solution (1:3 with water, AZ4000 developer, IMI Micromaterials) for ~ 60 s (+10 s increments if under-developed).
9. Etch the metal electrodes by immersing in conc. gold etchant (Gold Etch TFA, Transene) for 60s (+10 s increments if under-etched) followed by 5s (+2 s increments if under-etched) in conc. Chromium etchant (CE-200, HTA Enterprises).
10. Peel off individual optical probe substrates slowly from the surface using a sharp tweezer and mount them carefully on a PDMS (10:1) coated glass slide to prepare them for LED bonding in the next step.

4.4.3 μ-ILEDs and connector assembly:

1. Attach two μ-ILEDs — blue (470 nm, TR2227, Cree Inc.) and orange (589 nm, TCE10-589, Three-Five Materials) to their respective electrodes by transferring them using a tweezer after applying a special conductive silver epoxy (Cat. No. 8331, MG Chemicals) on the exposed electrode contacts.
2. Cure the assembly at 65^{o}C for at least 45 min. Test the optical functionality before proceeding to the next step.
3. Thermally bond a thin anisotropic conductive film (ACF, HST-9805-210, Elform) with the 3 distinct electrodes (2 positives for blue and orange with a common ground) of the optical layer by manually pressing (> 30 kg/cm^2) them under a temperature of ~180 °C for at least 40 s. The flexibility in the ACF cable allows acute bends in the optical connection to achieve compact assembly inside the device case.
4. Fabricate an array of copper electrodes (10 mm × 0.25 mm × 0.036 mm each) deposited on a polyimide (PI) substrate (10 mm × 5 mm × 100 μm). This ACF PCB layer acts as a mediation layer between ACF cable and the flexible custom printed circuit board (PCB).
5. Thermally bond the other side of ACF on one side of the copper array (from the previous step) using the same parameters as earlier.
6. Cover the other end of the copper array with a 0.5 mm thin PDMS (10:1) pad before mounting these structures (Optical Probe + ACF cable + ACF PCB) on a glass slide to prepare them for Parylene C coating in the next step.

4.4.4 Encapsulation and Electrical Connection:

1. Coat the optical layer with 7 μm thick Parylene C using PDS 2010 Labcoater 2 (Speciality Coating Systems). This helps insulate the exposed electrodes from tissue fluid during *in vivo* experiments.
2. Remove the thin PDMS covers from the copper electrode array.
3. Solder a 4-pin FPC connector (FH34S-4S-0.5SH(50), Hirose Connector) on the uncoated/exposed side of the copper electrode array by soldering it using a solder paste (SPE-0012, Zephyrtronics). Soldering the connector allows robust electrical connection to optical layer inside the mechanical casing during random free behavior of moving mice.
4. Test each individual μ-ILED independently for functionality (uniform and consistent illumination) by supplying a 2.7 V – 3 V power supply from a DC power generator (GPC-30300, Instek).

4.5 Preparation of a female Lego optofluidic probe

The three distinct layers of the ultrathin, soft female Lego optofluidic probes – the female Lego layer, the microfluidic probe layer, and the optical probe layer, were fabricated through soft lithographic and photo-lithographic techniques. For the female Lego, a mold (70 mm × 45 mm) consisting of a 3 × 5 array of female Lego structures was printed in a 3D printer (Objet30, Stratasys). Degassed 5:1 PDMS (base: curing agent) was cast into the mold followed by pressing and clamping with a polycarbonate (PC) sheet supported by a glass slide (75 mm × 50 mm). After curing at 70°C in the oven (for about 70 min), the PC sheet and the glass support were delaminated, and the 3 × 5 female Lego array was removed from the mold surface. The 1.5 mm thick array was then cut into individual female Legos (10 mm × 7.5 mm) along the alignment marks under an optical microscope (OM4713, Omano). Before reusing the mold, it was washed with isopropyl alcohol (IPA) and let dry at room temperature (~1 day) or oven (70°C for ~1 hour) before pouring PDMS again. A puncher (1.2 mm ID, Harris uni-core) was used to cut clean through-holes (1.15 mm) in the female Lego layer. The microfluidic probe layer, consisting of four

parallel ultrathin, soft microfluidic channels (10 μm × 10 μm × 10 mm), was fabricated through soft lithography using 10:1 PDMS as outlined in our previous work[1], [2]. The channel inlets of the microfluidic layer were aligned and connected to the female Lego holes using a double-sided silicone adhesive (ARClear 8932EE) under a stereo microscope. The microfluidic connections through the female Lego holes were then manually tested by pushing deionized (DI) water through a blunt syringe needle (18 Gauge) plugged into the female Lego hole (1.15mm ID). The optical probe layer was prepared using a similar process presented in our previous studies[1], [4], [5] as discussed above. After creating metal electrodes (5 nm/250 nm of Cr/Au) on a 6μm thick PET film, two μ-ILEDs – blue (470 nm, TR2227, Cree Inc.) and orange (589 nm, TCE10-589, Three-Five Materials) were attached to their respective electrodes using a silver epoxy (Cat. No. 8331, MG Chemicals). An anisotropic conductive film was bonded to the optical probe. The optical probes were then coated with 7 μm thick Parylene C using PDS 2010 Labcoater 2 (Specialty Coating Systems) to insulate the μ-ILEDs and metal electrodes from the biofluid for *in vivo* experiment. After confirming the functionality of both microfluidic (with female Lego) and optical layers, the two layers were attached together using double-sided silicone adhesive (ARClear 8932EE) to form the female Lego optofluidic probe (**Fig. 1a–b**). Further fabrication details can be found in the Supplementary Information.

4.6 Preparation of female Lego optofluidic probes for *in vivo* chronic optofluidic experiments

4.6.1 Integrating optical and microfluidic layers:

1. Test the functionality of both microfluidic (with female Lego) and optical layers before proceeding to the assembly step – water flow and optical power testing for microfluidic and optical layers respectively.

2. Place the microfluidic layer on a glass slide assembly such that the female Lego holes face downwards, while as the microfluidic probe is in same horizontal plane as other side of the female Lego.
3. Adhere a 25μm thin double-sided adhesive (ARClear 8932EE) on top of the microfluidic layer. Be careful while removing the top cover as it may rip the channel if not done carefully. Also, make sure that the adhesive is not blocking the microfluidic outlets at the probe tip. The adhesive used is silicone based and is hence biocompatible with the brain tissue.
4. Align and attach the optical layer on top of the microfluidic setup under the optical microscope to form the female Lego optofluidic probe.

4.6.2 Attaching Temporary Injection Support:

1. Prepare the layout for the support needle array in a CAD software (AutoDesk) with the following parameters – a 0.5 mm wide × 10 mm long probe (tissue insertion part) connected to a 5 mm wide × 1 mm long base (adhesion support part).
2. Laser cut (40 μm beam width) support structures to assist tissue penetration from a 25 mm × 25 mm × 38 μm stainless steel AISI 316 annealed sheet (FE240240, Goodfellow) placed on a flat paper support substrate (absorbs heat).
3. Remove cut needles from the paper substrate slowly. Clean their surfaces with damp cotton pads (wet with IPA) to remove any support paper or impurities, before letting it dry at room temperature.
4. Align and attach it on top of the ultra-flexible optofluidic probe (on optical layer side) under the optical microscope using silk fibroin[1]. This will provide temporary injection support during an *in vivo* surgery.

5. Test each optofluidic probe one more time for impermeability to biofluids and robust functionality by placing them in water for several hours to ensure that there was no puncture in the Parylene C coating during testing and assembly procedures.

4.7 3D printing of mechanical structures:

1. Model all the transparent mechanical structures – case (to contain the electronics), case cover (to help contain the electronics) and the harness (to press fit on the Lego assembly), which contain and support all constituents of the standalone Lego device, in commercial CAD software (SolidWorks Corp.).
2. Prepare the 3D printer (Ember 3D, Autodesk) by renewing its photocurable resin (PR-48 Clear, CPSpolymers) and cleaning its tray, if required.
3. Calibrate its build head to appropriate depth inside the resin by allowing it to free fall on the liquid surface and lock the assembly tight.
4. Setup Ember3D printer with the following parameters – 405 nm LED, 5W power, first layer (30 s exposure), burn-in layer (20 s exposure) and model layer (10 s exposure). The times may vary depending on the quality of UV light source and PDMS window in resin tray. Please calibrate it accordingly.
5. Initiate the printing process. Putting multiple samples per run can allow for rapid prototyping through Digital Light Processing Stereolithography (DLP SLA) in the 3D printer since all horizontal layers in all samples are exposed simultaneously thus reducing overall printing time.
6. Wash components in IPA and water to clean off remaining resin before letting them dry at room temperature.

4.8 Mounting Optofluidic Probe to 3D printed Casing:

1. Apply some clear epoxy (5-min epoxy, Devcon) on the inner walls of the ridges on the 3D printed plastic casing to hold female Lego in place. Apply epoxy in moderation, else excess

epoxy will squeeze out and may soil the exposed female Lego holes. This provides robust stability to the probe during repeated Lego assembly and disassembly processes during *in vivo* optofluidic experiments.

2. Mount and align the soft optofluidic probe assembly (with temporary rigid support) on the plastic casing (90^{o} with case edge along its central axis) under an optical microscope. Make sure the probe is perpendicular in both coordinates (horizontal and vertical). The edges of the female Lego slide into the epoxied side ridges as its probe part comes out from the hole at the bottom edge of the casing.
3. After aligning the straight optofluidic probe assembly coming out through the probe hole, apply some epoxy near the probe hole as well to fix it perpendicular to the casing, which helps securely hold it in place during surgery.

4.9 Protecting Exposed Lego Holes before an experiment:

1. Using similar 3D printer settings as before, print a blocker piece with 4 pillars (in a 2 × 2 array with 3.1 mm pitch, 1.3 mm dia and 1.7 mm long).
2. Plug it inside the exposed female Lego holes to avoid contamination with particles during surgery or storage periods throughout the long term *in vivo* studies.

4.10 Experimental subjects

Adult (25–35 g) male C57BL/6J and *vGAT*::IRES-Cre backcrossed to C57BL/6J mice were group-housed, given access to food pellets and water *ad libitum* and maintained on a 12 h:12 h light:dark cycle (lights on at 7:00 AM). All animals were kept in a sound-attenuated, isolated holding facility in the lab, 1 week prior to surgery, post-surgery and throughout the duration of the behavioral assays to minimize stress. All procedures were approved by the Animal Care and Use Committee of Washington University and conformed to US National Institutes of Health guidelines.

4.11 Stereotaxic Surgery

After the mice were acclimatized to the holding facility for seven to nine days, they were anaesthetized in an induction chamber (4% Isolflurane) and placed in a stereotaxic frame (Kopf Instruments, Model 1900) where they were maintained at 1-2% isoflurane. For the inflammation assays, mice were implanted with the microfluidic device into the dorsal striatum (stereotaxic coordinates from bregma (mm): anterior-posterior (AP): +1.10, medial-lateral (ML): +/−1.50, dorsal-ventral (DV): −4.00). For the DAMGO-mediated locomotor assays, mice were implanted with the microfluidic device above the VTA (stereotaxic coordinates from bregma (mm): AP: −3.10, ML: +/−0.50, DV: −4.25). For the optofluidics experiment, a craniotomy was performed and VGAT-Cre mice were injected with 0.4 µL of AAV5-EF1a-DIO-ChR2(H134)-eYFP (WUSTL Hope Center Viral Core) unilaterally into the BNST (stereotaxic coordinates from bregma (mm): AP: 0.14, ML:+/−0.90, DV: −4.75). Five weeks later, mice were then implanted with the optofluidic device adjacent to the LH (stereotaxic coordinates from bregma: −1.55 AP, +/−1.50 ML, −5.00 mm DV). A standard electrode holder (KOPF 1770) was adapted to implant the microfluidic and optofluidic devices. The implants were secured and affixed with dental cement (C&B Metabond® Adhesive Luting Cement, Parkell). All mice were allowed to recover for 5 days prior to behavioral testing. Post-surgery, all mice received subcutaneous injections of buprenorphine hydrochloride (0.05 mg/kg, Reckitt Benckiser Healthcare Ltd., USA) for pain management, and of ampicillin (50 mg/kg, Sage Pharmaceuticals, USA) to prevent infection at the implantation site.

4.12 Immunohistochemistry

Immunohistochemistry was performed as previously described by our previous studies[1], [5], [6]. In brief, mice were intracardially perfused with 4% paraformaldehyde, and then brains were sectioned (30 microns) and placed in 1X PB until immunostaining. Free-floating sections were washed in 1X PBS for 3 x 10 min intervals. Sections were then placed in blocking buffer (0.5%

Triton X-100 and 5% natural goat serum in 1X PBS) for 1 hr at room temperature. After blocking buffer, sections were placed in primary antibody (see below) overnight at room temperature. After 3 x 10 min 1X PBS washes, sections were incubated in secondary antibody (see below) for 2 hrs at room temperature, followed by subsequent washes (3 X 10 min in 1X PBS). Subsequently, sections were incubated in NeuroTrace (435/455 blue fluorescent Nissl stain, Life Technologies) for 1 hr, followed by 3 x 10 min 1XPBS and 3 x 10 min 1XPB washes. After immunostaining, sections were mounted and coverslipped with Vectashield Hard set mounting medium (Vector Laboratories) and imaged on a Leica TCS SPE confocal microscope.

Antibody	Species	Dilution	Source
GFAP	Guinea Pig	1:500	Synaptic Systems
Iba1	Rabbit	1:300	Wako Chemicals
Alexa Fluor 488 anti-rabbit IgG	Goat	1:1000	Invitrogen
Alexa Fluor 546 anti-guinea pig IgG	Goat	1:1000	Invitrogen
Neurotrace 435/455	N/A	1:400	Life Technologies

4.13 Behavioral Assays

4.13.1 Open Field Test

OFT testing was performed as described in Bruchas et. al[5], [7] in a sound-attenuated room maintained at 23ºC. Lighting was measured and stabilized at 2000 lux and performed in the afternoon between 13:00–16:00 hrs. The open field was a 50 x 50 cm square enclosure and was cleaned with 70% ethanol between testing trials. For testing, C57Bl6 mice (microfluidic devices were implanted in the VTA as described, n = 7/group) were placed in the center of the open field and allowed to roam freely for 60 mins. Movements were video recorded and analyzed using Ethovision. The center was defined as a square comprised of 50% of the total area of the OFT.

4.13.2 Contraversive Rotation and Locomotor Testing Assay

C57Bl6 mice with microfluidic devices implanted above the VTA were placed in the center of the same arena used for the OFT and allowed to roam freely for 60 mins. Wireless infusion of vehicle, DAMGO (500 pmol, 0.5 µL total volume, Tocris), or naloxone hydrochloride (500ng / 0.5 µL, Tocris) was initiated and movements were video recorded and analyzed using Ethovision. Rotations were defined as full 360º revolutions in the path of movement.

4.13.3 Real-Time Place Preference

VGAT-Cre$^{BNST\text{-}LH:ChR2}$ animals were placed in a custom-made unbiased, balanced two-compartment conditioning apparatus (52.5 × 25.5 × 25.5 cm) as described previously[8], [9]. On Day 1 Mice were allowed to freely roam the entire apparatus for 20 min baseline testing. Entry into one compartment triggered photostimulation (10 ms light pulses at 20 Hz every 5 s) while the

animal remained in the light-paired chamber. Entry into the other chamber ended the photostimulation. The following day GABAzine (10 μM, 0.5 μL total volume, Tocris) was wirelessly administered through replaceable drug cartridges 10 minutes prior to the testing. Mice were counterbalanced so that ~50 % received the GABAzine on day 2, there was no difference between animals that received the drug on day 2 or day 3. The side paired with photostimulation was counterbalanced across mice and across sessions. Time spent in each chamber and total distance traveled for the entire 20-minute trial was measured using Ethovision 10.5 (Noldus Information Technologies, Leesburg, VA). The triggered wireless photostimulation was elicited using a Noldus I/O Box coupled to a GPIO pin on the SimbleeCOM transmitter that wirelessly controlled the photostimulation output of the of the Lego optofluidic device.

4.14 Data Analysis

Data are expressed as means ± SEM. Data were normally distributed, and differences between the groups were determined using independent t-tests or one-way ANOVA followed by post hoc Bonferroni comparisons if the main effect was significant at $p < 0.05$. Paired t-tests were used in within-subject design experiments. Statistical analyses were conducted using Prism 7.0 (GraphPad).

4.15 Device and Smartphone App Availability

Please contact any of the corresponding authors for inquiring about the availability of the chronic Lego wireless devices and the iPhone version of the smartphone app. The smartphone app code will be made available upon request.

4.16 Additional Steps for Fabrication of Fully Implantable Optofluidic Device

4.16.1 Fabrication of Soft, Stretchable RF Energy Harvester

The RF harvester (Figure S3, Supporting Information) consists of a stretchable antenna, an impedance matching circuit, and a Villard cascade voltage tripler. Inductors (2.7 and 5 nH; 0.6 mm × 0.3 mm × 0.26 mm) and capacitors (1 pF; 0.6 mm × 0.3 mm × 0.26 mm) are used to match the antenna impedance to the input impedance for maximum power transfer. The signal is rectified and amplified as it passes through the voltage-tripler constructed with Schottky diodes (1PS66SB82, Nexperia; 2 mm × 2.1 mm × 0.9 mm) and capacitors (22 pF; 0.6 mm × 0.3 mm × 0.26 mm). The output DC voltage is stabilized using a decoupling capacitor (0.1 μF; 0.6 mm × 0.3 mm × 0.26 mm) to drive μ-ILEDs or actuate the fluid delivery.

4.16.2 Fabrication of the Battery-Free, Wireless Optofluidic Devices: Construction

of the device involves fabrication and integration of an RF harvester and an optofluidic device. The fabrication of an RF harvester starts with spincasting polymethyl methacrylate (PMMA, 200 nm thick; 495 PMMA A6, Microchem) on a glass substrate followed by curing at 180 °C for 1 h. A PDMS layer (500 μm thick, Sylgard 184, Dow Corning) is prepared by spin-coating and curing on the substrate, and a copper sheet (18 μm thick, DBT-III, Oak-Mitsui) is attached on top. Photolithographic patterning of the copper layer defines the layout of the RF harvester. Attachment of electronic components on the copper layer uses a solder paste (SMD290SNL250T5, Chipquik; curing at 220 °C for 2 min in a reflow oven) for robust bonding.

Encapsulation of the entire circuit with another PDMS layer (500 μm thick), followed by releasing by dissolution of the PMMA sacrificial layer in acetone, completes the fabrication. The fabrication protocols for an optofluidic device can be found in refs. [2,38]. The harvester and the optofluidic device are integrated together by connecting the output channels of the harvester to the electrodes of the optofluidic device using a silver epoxy (H2OE EPO-TEK, Ted Pella Inc.). The two components are sealed and further secured by adding PDMS encapsulation for protection and thermal insulation.

4.16.3 Experimental Subjects

Adult (25–35 g, 8–10 week old) male mice were group-housed, given access to food pellets and water ad libitum, and maintained on a 12:12 h light/dark cycle (lights on at 7:00 AM). All procedures were approved by the Animal Care and Use Committee of Washington University and conformed to US National Institutes of Health (NIH) guidelines.

4.16.4 Implantation of the Device

The optofluidic devices were implanted into the brain of adult mice following a similar method used for our previous soft neural implants.[25] Animals were mounted into a stereotaxic apparatus and anesthetized using isoflurane, while they rested on a heating pad for the duration of the procedure. After securing its head onto the apparatus, the mouse’s skull was exposed via a superficial midline incision performed under aseptic conditions. Following the identification of the desired stereotaxic coordinates for the implantation of the device, it was proceeded to drill a small opening for placement of the optofluidic probe. The soft RF harvester was implanted under the skin, caudal to the injection site. Placement of the optofluidic probe into the brain cortex was performed using a stereotaxic holder adapted for these devices, following temporary stiffening of

the implant with a biodegradable polymer (poly(lactic-co-glycolic acid); Sigma-Aldrich Inc.). After the implant was secured, the mouse's skin was sutured, and the animal was set aside for recovery. Nonetheless, additional care and appropriate surgical efforts need to be taken to avoid possible chances of an infection. The step-by-step process of the surgery can be found in **Fig. 3.16** in the Supporting Information.

4.17 References

[1] J.-W. Jeong *et al.*, "Wireless Optofluidic Systems for Programmable In Vivo Pharmacology and Optogenetics," *Cell*, vol. 162, no. 3, pp. 662–674, Jul. 2015.

[2] J. G. McCall *et al.*, "Preparation and implementation of optofluidic neural probes for in vivo wireless pharmacology and optogenetics," *Nat. Protocols*, vol. 12, no. 2, pp. 219–237, Feb. 2017.

[3] K. N. Noh *et al.*, "Miniaturized, Battery-Free Optofluidic Systems with Potential for Wireless Pharmacology and Optogenetics," *Small*, vol. 14, no. 4, p. 1702479, Jan. 2018.

[4] J. G. McCall *et al.*, "Fabrication and application of flexible, multimodal light-emitting devices for wireless optogenetics," *Nature Protocols*, vol. 8, no. 12, pp. 2413–2428, Nov. 2013.

[5] T. Kim *et al.*, "Injectable, cellular-scale optoelectronics with applications for wireless optogenetics," *Science*, vol. 340, no. 6129, pp. 211–216, Apr. 2013.

[6] R. Al-Hasani *et al.*, "Distinct Subpopulations of Nucleus Accumbens Dynorphin Neurons Drive Aversion and Reward," *Neuron*, vol. 87, no. 5, pp. 1063–1077, Sep. 2015.

[7] M. R. Bruchas, B. B. Land, J. C. Lemos, and C. Chavkin, "CRF1-R Activation of the Dynorphin/Kappa Opioid System in the Mouse Basolateral Amygdala Mediates Anxiety-Like Behavior," *PLOS ONE*, vol. 4, no. 12, p. e8528, Dec. 2009.

[8] J. G. McCall *et al.*, "CRH Engagement of the Locus Coeruleus Noradrenergic System Mediates Stress-Induced Anxiety," *Neuron*, vol. 87, no. 3, pp. 605–620, Aug. 2015.

[9] E. R. Siuda *et al.*, "Spatiotemporal Control of Opioid Signaling and Behavior," *Neuron*, vol. 86, no. 4, pp. 923–935, May 2015.

5 Conclusion

This thesis focused on presenting two new classes of wireless optofluidic devices (wOF), each of which solves a unique set of problems and offers advanced improvements that previous tools and technologies lacked. Here we will summarize briefly some of the important features of both devices what type of challenges they helped solve for the neuroscientific community.

5.1 Key Summary

5.1.1 Chronic Head mounted wOF Device

First was the chronic Lego wOF device introduced in Chapter 2 which could deliver optofluidic stimulation wirelessly for prolonged periods. It signifies the first-ever demonstration of a neural device capable of unlimited long-term delivery of both lights and drugs wirelessly as a standalone system. This was enabled by using μ-ILEDs for chronic optogenetics and replaceable Lego cartridges for chronic drug supply. The systematically engineered Lego interface requires optimal force for assembling the device such that the force is not too low to allow leakage from the Lego interface but at the same time not too high to create issues while assembling it on the head of live mice. Its wireless ability to be controlled from any commercial and readily available smartphone without any line of sight or directional handicaps greatly increased its viability to be used for *in vivo* studies. Moreover, its wirelessly selective nature, closed loop features and wireless reprogrammable abilities truly leverage its powerful capabilities for use in neural device research. At the same time, the Lego device offers its unique ability to sequence multiple wavelengths of light simultaneously with multiple doses of a drug such that scientists could pre-program a specific set of stimulation sequences involving frequency and intensity of lights as well as sequencing of drugs with a specific pre-set delay in between. The delay could be wirelessly re-programmed from

sub-second resolution to several hours as we did in the *in vivo* study, thus allowing researchers to conduct pre-set experiments even when they are not physically present in the laboratory. This can further offer unique opportunities in providing very powerful ability in combinatorial brain stimulations involving both light and drugs over long periods of time such as chronic optopharmacology or unique set of multiple drug doses in a specific sequence for development of drugs. Its uniquely miniaturized footprint help conduct *in vivo* studies in small animals, as small as mice without affecting their natural behavior. Lastly, we compare the device with the best commercial drug pump available out there (with no optogenetic ability) and show how the Lego device offers a unique advantage over commercially available alternatives. Below are brief highlights of the device:

1. The Lego optofluidic devices possess the ability **to repeatedly deliver pharmacological agents and/or viral vectors wirelessly in freely moving animals** through its unique replaceable “Lego” drug cartridges. This feature allows the wireless standalone device to achieve chronic wireless *in vivo* pharmacology with potential for chronic wireless optopharmacology.
2. It furthermore allows **highly precise and customizable temporal control** for simultaneous or pre-programmed (and wirelessly re-programmable) delayed the release of multiple, distinct drugs, thus enabling versatile, combinatorial chronic pharmacology in freely behaving animals. This was demonstrated through two unique experiments, one table top (to highlight precise temporal resolution) and another *in vivo* (to demonstrate wirelessly reprogrammable delay for multiple drug deliveries over several days in multiple animals):
3. Integration of **independently controlled, multi-wavelength μ-ILEDs** at the tip of microfluidic channels allows programmable and multi-modal photo-switching of distinct opsins or chemical compounds within the same local region of tissue, thus opening up

opportunities for advanced *in vivo* optogenetics, pharmacology as well as optopharmacology in a chronic yet stable manner.

4. **Uniqueness with Bluetooth:** Bluetooth allowed us to conduct studies that are inefficient and hard to be achieved through tethered and other wireless approaches:
    a. Integration of a Bluetooth wireless module enables **user-friendly smartphone control**, eliminating complex, bulky and expensive tools that are hard to be controlled by non-engineers, and easy to use in typical animal testing environments.
    b. Bluetooth facilitates **scalable, dynamic selective control** that allows to efficiently run multiple behavioral experiments with same or distinct stimulation profiles within a limited laboratory space, thus improving data throughput and efficiency over time.
    c. Bluetooth **allows an omnidirectional and long range of operation** (up to 100 m), which also enables wireless control from outside the behavioral room, thus completely removing the potential for observational effects on the experimental session.
    d. Moreover, **easy-to-set-up wireless closed loop** controls further widen opportunities for complex behavior experiments such as social interaction studies.
    e. The **wirelessly re-programmable nature** allows neuroscientists to reprogram multimodal stimulation profiles on-the-fly, including timed delays and sequencing for combinatorial multidrug deliveries and/or multiwavelength photostimulation patterns, thus significantly improving flexibility and versatility of experiments.
5. **Advantages over a state-of-the-art commercial pump** (more detailed review in the next section): The Lego optofluidic device provides a significant advance over the state-of-the-art commercially available wireless pumps (SMP-300, iPrecio) by allowing multidrug release without affecting animal's natural behavior within a single behavior session and

easy switching of drugs through replaceable Lego cartridges for versatile chronic studies, unlike the commercial pump, which can deliver only a single drug within a behavioral session and requires cumbersome process of cleaning a reservoir before replacing an original drug with a different type. Furthermore, the Lego device is smaller and lighter (Lego device: 1260 mm^3; 2 g vs SMP-300: 2678 mm^3; 3.3 g), thus allowing implantation in freely moving animals as small as mice. Even with a smaller form factor compared to the smallest commercial alternative, the device also allows simultaneous and independent neural manipulation with four distinct drugs and photostimulation with two unique wavelengths, providing an ultra-compact multimodal, multifunctional solution. Thus, by integrating rechargeable batteries and replaceable cartridges, the Lego device enables truly chronic optofluidic studies, unlike disposable commercial alternative which cannot be used once the battery is exhausted (1-6 weeks depending on usage).

5.1.2 Battery-free Fully Implantable wOF Device

All previous head-mounted optofluidic devices including the Lego device were limited to be used in the brain only. That is primarily due to their bulky size and head-mounted setup which limits their use in peripheral parts of the body. In Chapter 3, we present an entirely implantable, battery-free soft wireless optofluidic system with stretchable radiofrequency (RF) antenna for wireless power transfer. This design not only eliminates the need for large batteries, making the device tiny (125 mm^3) and light (220 mg) but also allows the device to be implanted in various space-critical locations of the body.

The fully wireless, battery-free optofluidic device enabled selective control of fluid pump and μ-ILEDs operation at 1.8 GHz (channel 1) and 2.9 GHz (channel 2) with 2 W and 0.2 W of average transmitted power, respectively. Systematic electromechanical studies show that the optimized stretchable antenna design allows minimal degradation in wireless power transmission

efficiency and sufficient channel isolation even under 20% stretching of the antenna structure, verifying its reliability in dynamic motion within the tissue. Moreover, the antenna featured an omnidirectional radiation pattern, which offered stable operation of the device irrespective of its angular variations. The proof-of-concept implantation and experiment in live mice showed its potential for wireless pharmacology and optogenetics.

Though the battery-free, fully implantable wOF implemented a battery-free and fully implantable design, it should be noted that at the same time it couldn't solve the features the Lego wOF device offered like for chronic drug delivery and powerful smartphone-controlled platform. But at the same time, this miniaturized, battery-free optofluidic device possesses the potential for fully implantable and completely wireless operation for *in vivo* pharmacology and optogenetics in freely moving animal. The number of antenna channels is also scalable; thus it can enable more complex operation for various neuroscience experiments.

5.2 Key findings

Some other key findings mentioned throughout the thesis regarding an ideal optofluidic neural device are as follow:

1. For optogenetic stimulation, microscale sized LEDs offer better chronic integration with biological tissues when compared to optical fiber methods, both due to their miniaturized sizes which reduce tissue inflammation and response as well as to their low power operation helping integrate wireless power harvesters and low power electronics to power them[1]. This was demonstrated in devices showcased in Chapter 2 and 3.
2. Parylene C is among the best available materials to coat neural fibers both to encapsulate electrodes to insulate them from surrounding biological fluids as well as to improve biocompatibility with the tissue as is shown in many previous studies[2]–[4] as shown in Chapter 2.

3. Mechanically soft neural probe implants reduce tissue damage and inflammation[5]–[8] when compared to rigid probes like conventional metal cannulas for drug delivery and silica fibers for optogenetic stimulation as highlighted in Chapter 2 and 3.
4. Neural probes with small cross-sectional areas reduce tissue displacement, damage and subsequent immune response as shown in both Chapter 2 and 3 as well as consistently mentioned in several previous studies as well[6]–[8].
5. Replaceable cartridges can be used for chronic drug delivery in wireless standalone drug delivery devices (as shown in Chapter 2). However, the reservoirs and the microfluidic channel dimensions need to be adjusted accordingly to precisely engineering the volume delivered and the flow rate.
6. The device footprint can be significantly reduced by replacing bulky rigid batteries with soft and stretchable power harvesting circuits which can enable to implant the device completely inside the body (as shown in Chapter 3)

5.3 Future Directions

5.3.1 Possible Improvements in presented technologies

Integration of advanced materials and efforts for optimized engineering design can help unleash the full potential of these devices by further improvements. Currently, the inability to easily modify the volume of fluid delivery as well as the speed of the infusion rate hinders the real-time customization of fluid control. Though these can be controlled by modifying drug reservoirs and microfluidic channel dimensions. This can be overcome by integrating micro-stepper motors or micromachined linear actuators for refined fluid control. Also, wireless neural recording capabilities can enhance the utility of these devices by allowing real-time closed-loop control for

tissue stimulation. The current thermal actuation technique also requires the drugs to be thermally stable and compatible with the reservoir temperatures (~60°C) during heater activation. The concern associated with high-temperature actuation can be dramatically mitigated by replacing the current expandable polymer composite with thermally responsive hydrogel, which can be engineered to have its activation temperature as low as 32 °C. The use of hydrogels in drug reservoirs also facilitates loading drugs into cartridge reservoirs without oxygen plasma treatment due to its hydrophilic characteristic (**Fig. 5.1**).

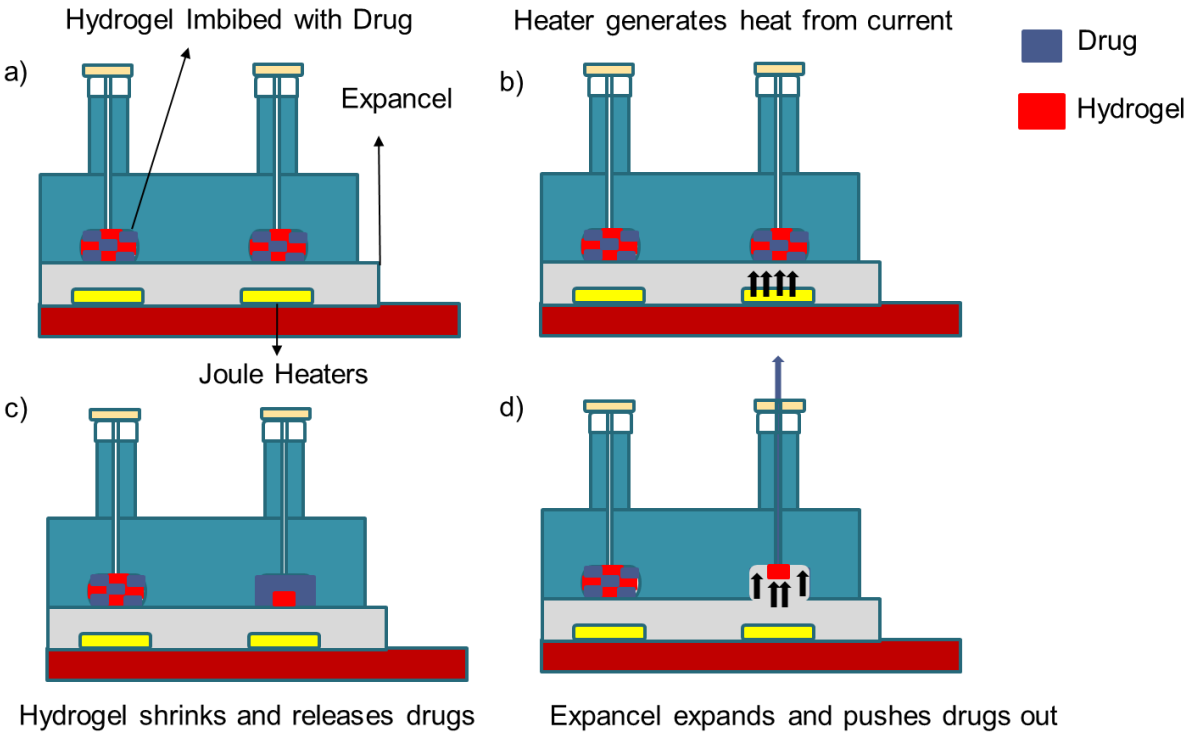

Figure 5.1 – Concept of use of hydrogel to enhance drug loading.

5.3.2 Piconet and Internet of Things (IoT) Wireless Ecosystem

The choice of implementing Bluetooth technology over other wireless techniques in the Lego wOF device has three main reasons:

a) Ability to connect and send different data to multiple chips at the same time,

b) High accuracy, decent range, more speed, no LOS, less energy and

c) Easy integration with smartphones for IoT (Internet of Things).

The abridged idea is "*to be able to send different messages to each individual LED or drug output of each probe and to each probe in the network independently or simultaneously through your smartphone*". However, we can further extend this Bluetooth technology to create a very powerful wireless ecosystem by allowing simultaneous control of 7 or more devices using a smartphone (Piconet) or from anywhere in the world by connecting to the internet (Internet of Neuroscience).

I) **Piconet Networks in Neuroscience:** The ability to control multiple circuits simultaneously can offer powerful tools to neuroscientists to conduct very complex social experiments in freely moving animals. The working principle of this concept follows this sequence: a) First, you can connect your smartphone to all the probes you want, using the smartphone app. A piconet network can connect up to 7-14 active slave devices at the same time. b) Then select same/different frequencies for LEDs (or drug reservoirs) of same/different probes and then click "Send". The smartphone will send messages quickly to each LED (or drug output). Through this method, we can control each individual LED (or drug release) on each probe at any one of the many frequencies it was programmed for. Also, if we are sending data to multiple probes in the piconet network at the same time, we still can make any group of LEDs simultaneously blink, with each LED blinking at same or different frequencies, irrespective of their probe. Thus, we will have simultaneous control of many LED's in the network, at the same or different combination of frequencies, irrespective of other LED's in the same network. This feature was tested as shown in **Figure 5.2 - 5.3**.

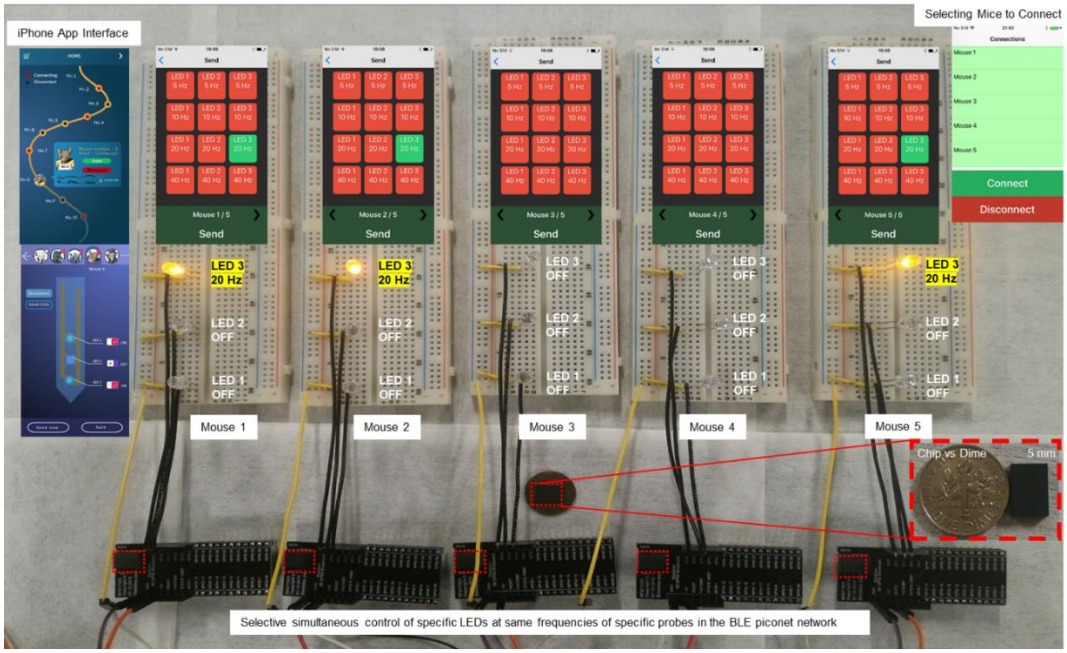

Figure 5.2 – Piconet concept for simultaneous same LED control in multiple circuits selectively.

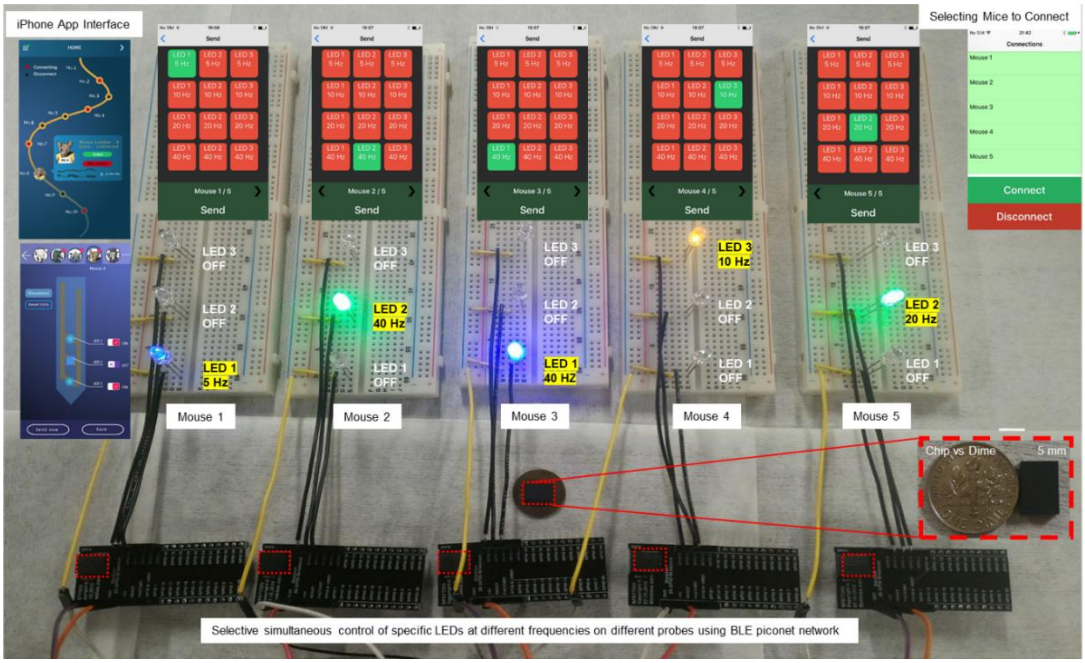

Figure 5.3 – Piconet concept for simultaneous different LED control in multiple circuits.

II) **Internet of Things in Neuroscience (IoN) Networks:** To further advance our knowledge regarding the functional aspects of the complex neural circuitry, we plan to implement an 'IoT (Internet of Things) in Neuroscience' (IoN) which will empower

neuroscientists with the novel tools and techniques to remotely control and study a huge network of interconnected neural devices (**Fig. 5.4**). To realize the full potential of applications involving 'IoN', we will be exploiting the advantages of both BLE (Bluetooth Low Energy) and the Wi-Fi (Wireless Fidelity) protocols. The BLE protocol will enable us to implement a very low-energy scatternet (an ad hoc computer network consisting of 2 or more piconets) which will also give our network the power to control 'simultaneous' stimulations while as the Wi-Fi capability will allow us to control this network from any remote part of the world (long distance wireless control) with an internet connection through PC or smartphone (device independent).

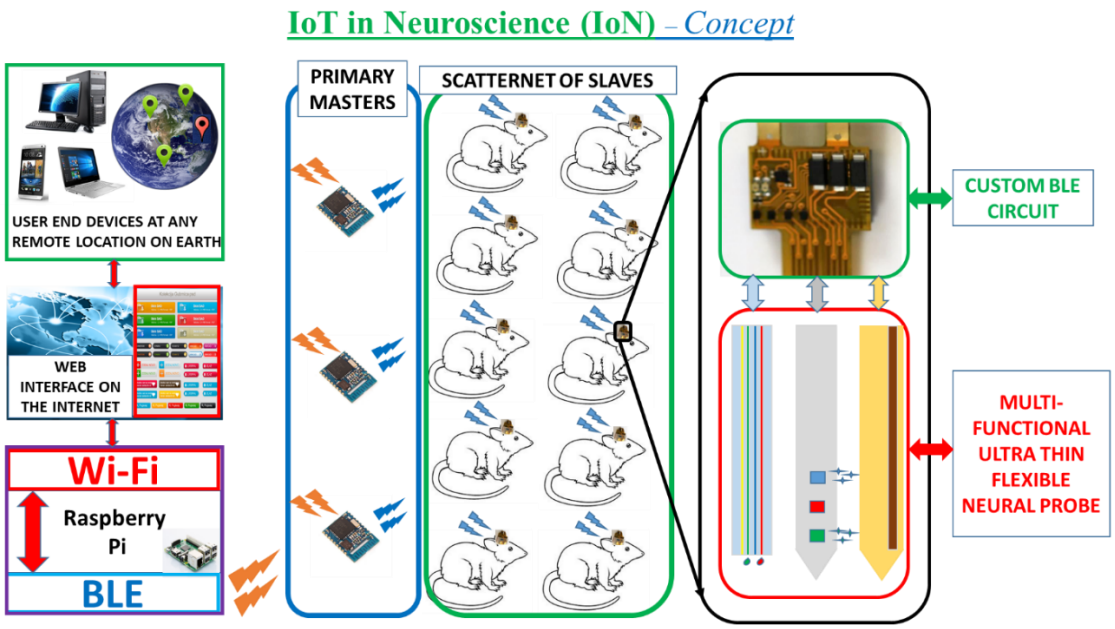

Figure 5.4 – Internet of Things concept for applications in neuroscience

Moreover, such remote location access to behavioral sessions from around the world can raise questions on the wireless signal integrity and security within such large connected networks. The reliability to remotely control these wireless networks can be improved by enabling password protection that can help limit accessibility to specific groups of people as well as other techniques like enabling cryptic software keys to

scrutinize and filter only secure stimulation commands. This can be further bolstered by sending email and text confirmation directly to the smartphone or computer that the researcher will be using in any part of the world.

5.3.3 Alternate Micropumps for Thermally Sensitive Drugs

We can further implement novel micropump actuators that can possibly replace a current thermally actuated pump that restricts the use of thermally sensitive drugs. Two alternate approaches that can conduct a bidirectional movement to both deliver drugs and sample tissues are shown below:

I) Electromagnetic Drug Actuator or Tissue Sampler (**Fig. 5.5**): A thin metal plate can be controlled by an electromagnetic induction coil to move up and down inside a fixed reservoir, thus enabling release of stored drugs or suction of tissue samples.

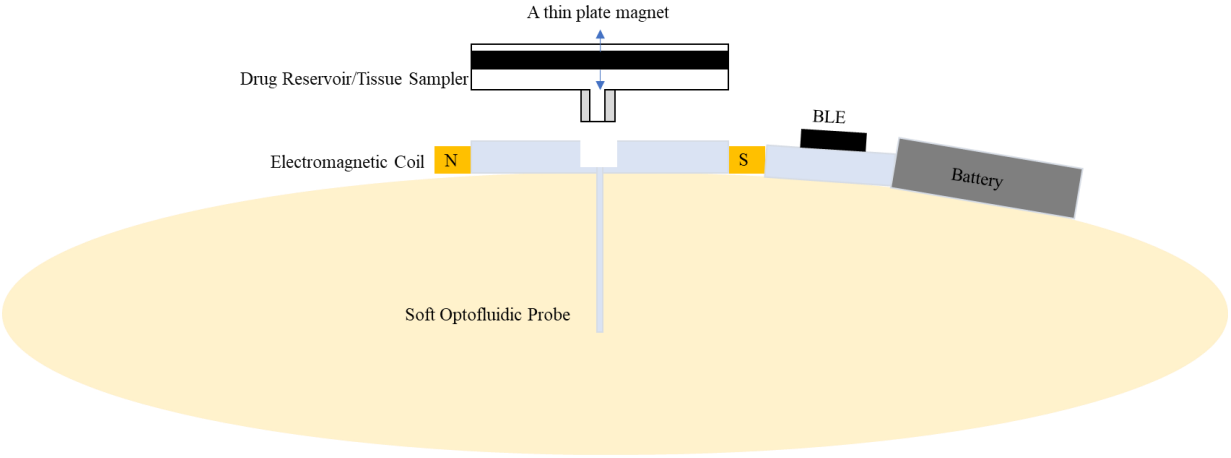

Figure 5.5 – An electromagnetic drug actuator and tissue sampler concept.

II) Stepper Motor Drug Actuator or Tissue Sampler (**Fig. 5.6**): A bidirectional stepper motor integrated with a linear coupler can allow drug actuation and tissue sampling through a small orifice which can be connected to a microfluidic probe. The step

resolution is important as it can determine the smallest amount of linear motion it can achieve which in turn will control the smallest amount of drug it can release.

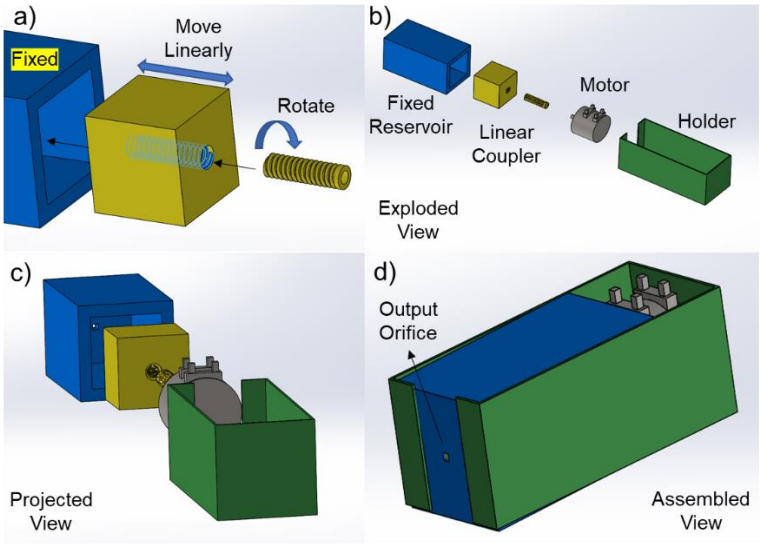

Figure 5.6 – A bidirectional stepper motor drug actuator and tissue sampler concept.

5.3.4 Fully Implantable wOF device with replaceable Lego cartridges

To combine the best advantages of both Lego wOF devices and fully implantable wOF devices into a single platform will enable a very powerful neural device that can allow chronic drug and light delivery wirelessly to any part of the central or peripheral nervous systems. Combinatorial integration of custom-fabricated or unpackaged Bluetooth and IC chips, wireless energy harvester, and refillable cartridges refilled with a syringe needle through the skin has the potential to create such miniaturized, wireless neural systems that could be chronically embedded in tissue. Specifically, this miniaturized, fully implantable device could be achieved by encapsulating the entire system built with unpackaged small and thin IC components and refillable reservoirs with soft, biocompatible waterproof structures (**Fig. 5.7**), thus garnering applications for incorporation into other areas of the body.

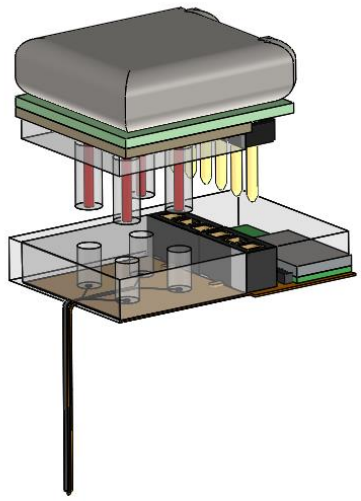

Figure 5.7 – A fully implantable wOF device with replaceable cartridge concept.

5.4 Final Remarks

We have presented two standalone wOF devices that can offer uninterrupted multimodal access the deep brain regions of freely behaving animals as small as mice. The Lego wOF device (Chapter 2) can offer chronic drug delivery and smartphone control while as the fully implantable wOF device (Chapter 3) is battery-free and can be implanted anywhere inside the body. Additionally, all fabrication steps and codes for reproducibility of these devices have been appropriately detailed (Chapter 4). Moreover, we have discussed (Chapter 5) other alternate wireless configurations (for complex neuroscience experiments) and drug micropumps (for thermally sensitive drug compounds) which can be further improved on in the near future.

5.5 References

[1] R. Qazi, C. Y. Kim, S.-H. Byun, and J.-W. Jeong, “Microscale Inorganic LED-Based Wireless Neural Systems for Chronic in vivo Optogenetics,” *Front. Neurosci.*, vol. 12, 2018.

[2] C. Hassler, R. P. von Metzen, P. Ruther, and T. Stieglitz, “Characterization of parylene C as an encapsulation material for implanted neural prostheses,” *Journal of Biomedical Materials Research Part B: Applied Biomaterials*, vol. 93B, no. 1, pp. 266–274, Apr. 2010.

[3] B. J. Kim *et al.*, “3D Parylene sheath neural probe for chronic recordings,” *J. Neural Eng.*, vol. 10, no. 4, p. 045002, 2013.

[4] S. A. Hara, B. J. Kim, J. T. W. Kuo, C. D. Lee, E. Meng, and V. Pikov, “Long-term stability of intracortical recordings using perforated and arrayed Parylene sheath electrodes,” *J. Neural Eng.*, vol. 13, no. 6, p. 066020, 2016.
[5] J. Y. Sim, M. P. Haney, S. I. Park, J. G. McCall, and J.-W. Jeong, “Microfluidic neural probes: in vivo tools for advancing neuroscience,” *Lab Chip*, vol. 17, no. 8, pp. 1406–1435, Apr. 2017.
[6] J.-W. Jeong *et al.*, “Wireless Optofluidic Systems for Programmable In Vivo Pharmacology and Optogenetics,” *Cell*, vol. 162, no. 3, pp. 662–674, Jul. 2015.
[7] T. Kim *et al.*, “Injectable, Cellular-Scale Optoelectronics with Applications for Wireless Optogenetics,” *Science*, vol. 340, no. 6129, pp. 211–216, Apr. 2013.
[8] J.-W. Jeong, G. Shin, S. I. Park, K. J. Yu, L. Xu, and J. A. Rogers, “Soft Materials in Neuroengineering for Hard Problems in Neuroscience,” *Neuron*, vol. 86, no. 1, pp. 175–186, Apr. 2015.

Bibliography

Chapter 1:

[1] E. R. Kandel *et al.*, *Principles of neural science*, vol. 4. McGraw-hill New York, 2000.

[2] G. J. Morton, D. E. Cummings, D. G. Baskin, G. S. Barsh, and M. W. Schwartz, “Central nervous system control of food intake and body weight,” *Nature*, vol. 443, no. 7109, pp. 289–295, Sep. 2006.

[3] J. C. Brüning *et al.*, “Role of Brain Insulin Receptor in Control of Body Weight and Reproduction,” *Science*, vol. 289, no. 5487, pp. 2122–2125, Sep. 2000.

[4] M. A. Goodale and A. D. Milner, “Separate visual pathways for perception and action,” *Trends in Neurosciences*, vol. 15, no. 1, pp. 20–25, Jan. 1992.

[5] J. A. Neubauer, A. Simone, and N. H. Edelman, “Role of brain lactic acidosis in hypoxic depression of respiration,” *Journal of Applied Physiology*, vol. 65, no. 3, pp. 1324–1331, Sep. 1988.

[6] H. D. Critchley, P. Rotshtein, Y. Nagai, J. O’Doherty, C. J. Mathias, and R. J. Dolan, “Activity in the human brain predicting differential heart rate responses to emotional facial expressions,” *NeuroImage*, vol. 24, no. 3, pp. 751–762, Feb. 2005.

[7] E. A. Mayer, “Gut feelings: the emerging biology of gut–brain communication,” *Nature Reviews Neuroscience*, vol. 12, no. 8, pp. 453–466, Aug. 2011.

[8] R. Bastos, W. Abra˜o Saad, J. Vanderlei Menani, A. Renzi, J. Nogueira Silveira, and L. A. de Arruda Camargo, “Role of adrenergic pathways of the medial preoptic area in ANGII-induced water intake and renal excretion in rats,” *Brain Research*, vol. 636, no. 1, pp. 81–86, Feb. 1994.

[9] L. M. Garcia-Segura, J. A. Chowen, and F. Naftolin, “Endocrine Glia: Roles of Glial Cells in the Brain Actions of Steroid and Thyroid Hormones and in the Regulation of Hormone Secretion,” *Frontiers in Neuroendocrinology*, vol. 17, no. 2, pp. 180–211, Apr. 1996.

[10] R. I. Weiner and W. F. Ganong, “Role of brain monoamines and histamine in regulation of anterior pituitary secretion.,” *Physiological Reviews*, vol. 58, no. 4, pp. 905–976, Oct. 1978.

[11] B. D. Martino, D. Kumaran, B. Seymour, and R. J. Dolan, “Frames, Biases, and Rational Decision-Making in the Human Brain,” *Science*, vol. 313, no. 5787, pp. 684–687, Aug. 2006.

[12] G. Bush *et al.*, “Dorsal anterior cingulate cortex: A role in reward-based decision making,” *PNAS*, vol. 99, no. 1, pp. 523–528, Jan. 2002.

[13] K. Yamada, M. Mizuno, and T. Nabeshima, “Role for brain-derived neurotrophic factor in learning and memory,” *Life Sciences*, vol. 70, no. 7, pp. 735–744, Jan. 2002.

[14] T. Allison, A. Puce, and G. McCarthy, “Social perception from visual cues: role of the STS region,” *Trends in Cognitive Sciences*, vol. 4, no. 7, pp. 267–278, Jul. 2000.

[15] R. E. Clark and L. R. Squire, “Classical Conditioning and Brain Systems: The Role of Awareness,” *Science*, vol. 280, no. 5360, pp. 77–81, Apr. 1998.

[16] R. Adolphs, “Social cognition and the human brain,” *Trends in Cognitive Sciences*, vol. 3, no. 12, pp. 469–479, Dec. 1999.

[17] K. Hashimoto, E. Shimizu, and M. Iyo, “Critical role of brain-derived neurotrophic factor in mood disorders,” *Brain Research Reviews*, vol. 45, no. 2, pp. 104–114, May 2004.

[18] I. Liberzon *et al.*, “Brain activation in PTSD in response to trauma-related stimuli,” *Biological Psychiatry*, vol. 45, no. 7, pp. 817–826, Apr. 1999.

[19] S. Feldman, N. Conforti, and J. Weidenfeld, “Limbic pathways and hypothalamic neurotransmitters mediating adrenocortical responses to neural stimuli,” *Neuroscience & Biobehavioral Reviews*, vol. 19, no. 2, pp. 235–240, Jun. 1995.

[20] B. S. McEwen and P. J. Gianaros, “Central role of the brain in stress and adaptation: Links to socioeconomic status, health, and disease,” *Annals of the New York Academy of Sciences*, vol. 1186, no. 1, pp. 190–222, 2010.

[21] C. Zuccato and E. Cattaneo, “Role of brain-derived neurotrophic factor in Huntington’s disease,” *Progress in Neurobiology*, vol. 81, no. 5, pp. 294–330, Apr. 2007.

[22] Pei Chin Tang, “Brain stem control of respiratory depth and rate in the cat ,2,” *Respiration Physiology*, vol. 3, no. 3, pp. 349–366, Dec. 1967.

[23] D. P. Brooks, L. Share, and J. T. Crofton, “Role of Brain Prostaglandins in the Control of Vasopressin Secretion in the Conscious Rat,” *Endocrinology*, vol. 118, no. 4, pp. 1716–1722, Apr. 1986.

[24] R. Chen, A. Canales, and P. Anikeeva, “Neural recording and modulation technologies,” *Nature Reviews Materials*, vol. 2, no. 2, p. 16093, Feb. 2017.

[25] J. M. Kerns, A. J. Fakhouri, H. P. Weinrib, and J. A. Freeman, “Electrical stimulation of nerve regeneration in the rat: The early effects evaluated by a vibrating probe and electron microscopy,” *Neuroscience*, vol. 40, no. 1, pp. 93–107, Jan. 1991.

[26] M. S. Humayun, E. de Juan, G. Dagnelie, R. J. Greenberg, R. H. Propst, and D. H. Phillips, “Visual Perception Elicited by Electrical Stimulation of Retina in Blind Humans,” *Arch Ophthalmol*, vol. 114, no. 1, pp. 40–46, Jan. 1996.

[27] S. C. Núñez, A. S. Garcez, S. S. Suzuki, and M. S. Ribeiro, “Management of Mouth Opening in Patients with Temporomandibular Disorders through Low-Level Laser Therapy and Transcutaneous Electrical Neural Stimulation,” *Photomedicine and Laser Surgery*, vol. 24, no. 1, pp. 45–49, Feb. 2006.

[28] P. D. MacLean and J. R. Delgado, “Electrical and chemical stimulation of frontotemporal portion of limbic system in the waking animal,” *Electroencephalography and Clinical Neurophysiology*, vol. 5, no. 1, pp. 91–100, Feb. 1953.

[29] T. L. Rose and L. S. Robblee, “Electrical stimulation with Pt electrodes. VIII. Electrochemically safe charge injection limits with 0.2 ms pulses (neuronal application),” *IEEE Transactions on Biomedical Engineering*, vol. 37, no. 11, pp. 1118–1120, Nov. 1990.

[30] E. S. Boyden, F. Zhang, E. Bamberg, G. Nagel, and K. Deisseroth, “Millisecond-timescale, genetically targeted optical control of neural activity,” *Nature Neuroscience*, vol. 8, no. 9, p. nn1525, Aug. 2005.

[31] R. Guduru *et al.*, “Magnetoelectric ‘spin’ on stimulating the brain,” *Nanomedicine*, vol. 10, no. 13, pp. 2051–2061, May 2015.

[32] R. Chen, G. Romero, M. G. Christiansen, A. Mohr, and P. Anikeeva, “Wireless magnetothermal deep brain stimulation,” *Science*, vol. 347, no. 6229, pp. 1477–1480, Mar. 2015.

[33] K. Eom *et al.*, “Enhanced Infrared Neural Stimulation using Localized Surface Plasmon Resonance of Gold Nanorods,” *Small*, vol. 10, no. 19, pp. 3853–3857, 2014.

[34] J. D. Wells, C. Kao, E. D. Jansen, P. E. Konrad, and A. Mahadevan-Jansen, “Application of infrared light for in vivo neural stimulation,” *JBO*, vol. 10, no. 6, p. 064003, Nov. 2005.

[35] M. Chernov and A. W. Roe, “Infrared neural stimulation: a new stimulation tool for central nervous system applications,” *NPh*, vol. 1, no. 1, p. 011011, Aug. 2014.

[36] “Transcranial focused ultrasound modulates the activity of primary somatosensory cortex in humans | Nature Neuroscience.” [Online]. Available: https://www.nature.com/articles/nn.3620. [Accessed: 13-Apr-2018].

[37] L. R. Gavrilov, E. M. Tsirulnikov, and I. ab I. Davies, “Application of focused ultrasound for the stimulation of neural structures,” *Ultrasound in Medicine and Biology*, vol. 22, no. 2, pp. 179–192, Jan. 1996.

[38] M. D. Menz, Ö. Oralkan, P. T. Khuri-Yakub, and S. A. Baccus, “Precise Neural Stimulation in the Retina Using Focused Ultrasound,” *J. Neurosci.*, vol. 33, no. 10, pp. 4550–4560, Mar. 2013.

[39] B. Franklin, “An Account of the Effects of Electricity in Paralytic Cases. In a Letter to John Pringle, M. D. F. R. S. from Benjamin Franklin, Esq; F. R. S.,” *Philosophical Transactions (1683-1775)*, vol. 50, pp. 481–483, 1757.

[40] B. L. Roth, “DREADDs for Neuroscientists,” *Neuron*, vol. 89, no. 4, pp. 683–694, Feb. 2016.

[41] J. G. Bernstein and E. S. Boyden, “Optogenetic tools for analyzing the neural circuits of behavior,” *Trends in Cognitive Sciences*, vol. 15, no. 12, pp. 592–600, Dec. 2011.

[42] J. G. Bernstein, P. A. Garrity, and E. S. Boyden, “Optogenetics and thermogenetics: technologies for controlling the activity of targeted cells within intact neural circuits,” *Current Opinion in Neurobiology*, vol. 22, no. 1, pp. 61–71, Feb. 2012.

[43] A. Guru, R. J. Post, Y.-Y. Ho, and M. R. Warden, “Making Sense of Optogenetics,” *Int J Neuropsychopharmacol*, vol. 18, no. 11, Oct. 2015.

[44] L. Grosenick, J. H. Marshel, and K. Deisseroth, “Closed-Loop and Activity-Guided Optogenetic Control,” *Neuron*, vol. 86, no. 1, pp. 106–139, Apr. 2015.

[45] T. Kim *et al.*, “Injectable, Cellular-Scale Optoelectronics with Applications for Wireless Optogenetics,” *Science*, vol. 340, no. 6129, pp. 211–216, Apr. 2013.

[46] G. Shin *et al.*, “Flexible Near-Field Wireless Optoelectronics as Subdermal Implants for Broad Applications in Optogenetics,” *Neuron*, vol. 93, no. 3, pp. 509-521.e3, Feb. 2017.

[47] R. Qazi, C. Y. Kim, S.-H. Byun, and J.-W. Jeong, “Microscale Inorganic LED Based Wireless Neural Systems for Chronic in vivo Optogenetics,” *Front. Neurosci.*, vol. 12, 2018.

[48] S. I. Park *et al.*, “Stretchable multichannel antennas in soft wireless optoelectronic implants for optogenetics,” *Proceedings of the National Academy of Sciences*, p. 201611769, 2016.

[49] J. G. McCall *et al.*, “Fabrication and application of flexible, multimodal light-emitting devices for wireless optogenetics,” *Nature Protocols*, vol. 8, no. 12, pp. 2413–2428, Nov. 2013.

[50] R. Delmdahl, R. Pätzel, and J. Brune, “Large-Area Laser-Lift-Off Processing in Microelectronics,” *Physics Procedia*, vol. 41, pp. 241–248, Jan. 2013.

[51] M. Schwaerzle, O. Paul, and P. Ruther, “Compact silicon-based optrode with integrated laser diode chips, SU-8 waveguides and platinum electrodes for optogenetic applications,” *J. Micromech. Microeng.*, vol. 27, no. 6, p. 065004, 2017.

[52] J.-W. Jeong *et al.*, “Wireless Optofluidic Systems for Programmable In Vivo Pharmacology and Optogenetics,” *Cell*, vol. 162, no. 3, pp. 662–674, Jul. 2015.

[53] F. Zhang, A. M. Aravanis, A. Adamantidis, L. de Lecea, and K. Deisseroth, “Circuit-breakers: optical technologies for probing neural signals and systems,” *Nature Reviews Neuroscience*, vol. 8, no. 8, p. nrn2192, Aug. 2007.

[54] K. M. Tye and K. Deisseroth, “Optogenetic investigation of neural circuits underlying brain disease in animal models,” *Nature Reviews Neuroscience*, vol. 13, no. 4, p. nrn3171, Mar. 2012.

[55] M. A. Parada, M. Puig de Parada, and B. G. Hoebel, “A new triple-channel swivel for fluid delivery in the range of intracranial (10 nl) and intravenous (100 µl) self-administration volumes and also suitable for microdialysis,” *Journal of Neuroscience Methods*, vol. 54, no. 1, pp. 1–8, Sep. 1994.

[56] H. J. Lee *et al.*, “A new thin silicon microneedle with an embedded microchannel for deep brain drug infusion,” *Sensors and Actuators B: Chemical*, vol. 209, pp. 413–422, Mar. 2015.

[57] Zhang Wenguang, Ma Yakun, and Li Zhengwei, “Experimental evaluation of neural probe’s insertion induced injury based on digital image correlation method,” *Medical Physics*, vol. 43, no. 1, pp. 505–512, Jan. 2016.

[58] T. D. Y. Kozai *et al.*, “Ultrasmall implantable composite microelectrodes with bioactive surfaces for chronic neural interfaces,” *Nat Mater*, vol. 11, no. 12, pp. 1065–1073, Dec. 2012.

[59] A. Sridharan, J. K. Nguyen, J. R. Capadona, and J. Muthuswamy, “Compliant intracortical implants reduce strains and strain rates in brain tissue in vivo,” *J. Neural Eng.*, vol. 12, no. 3, p. 036002, 2015.

[60] J. K. Nguyen *et al.*, “Mechanically-compliant intracortical implants reduce the neuroinflammatory response,” *J. Neural Eng.*, vol. 11, no. 5, p. 056014, 2014.

[61] G. Lind, C. E. Linsmeier, and J. Schouenborg, “The density difference between tissue and neural probes is a key factor for glial scarring,” *Scientific Reports*, vol. 3, p. 2942, Oct. 2013.

[62] J.-W. Jeong, G. Shin, S. I. Park, K. J. Yu, L. Xu, and J. A. Rogers, “Soft Materials in Neuroengineering for Hard Problems in Neuroscience,” *Neuron*, vol. 86, no. 1, pp. 175–186, Apr. 2015.

[63] A. Canales *et al.*, “Multifunctional fibers for simultaneous optical, electrical and chemical interrogation of neural circuits *in vivo*,” *Nature Biotechnology*, vol. 33, no. 3, pp. 277–284, Mar. 2015.

[64] S. Park *et al.*, “One-step optogenetics with multifunctional flexible polymer fibers,” *Nature Neuroscience*, vol. 20, no. 4, pp. 612–619, Apr. 2017.

[65] C. Dagdeviren *et al.*, “Miniaturized neural system for chronic, local intracerebral drug delivery,” *Science Translational Medicine*, vol. 10, no. 425, p. eaan2742, Jan. 2018.

[66] J. G. McCall *et al.*, “Preparation and implementation of optofluidic neural probes for in vivo wireless pharmacology and optogenetics,” *Nat. Protocols*, vol. 12, no. 2, pp. 219–237, Feb. 2017.

[67] K. N. Noh *et al.*, “Miniaturized, Battery-Free Optofluidic Systems with Potential for Wireless Pharmacology and Optogenetics,” *Small*, vol. 14, no. 4, p. 1702479, Jan. 2018.

[68] B. A. Copits, M. Y. Pullen, and R. W. Gereau, “Spotlight on pain: optogenetic approaches for interrogating somatosensory circuits,” *Pain*, vol. 157, no. 11, pp. 2424–2433, Nov. 2016.

[69] T. Kim *et al.*, “Injectable, cellular-scale optoelectronics with applications for wireless optogenetics,” *Science*, vol. 340, no. 6129, pp. 211–216, Apr. 2013.

[70] S. I. Park *et al.*, “Soft, stretchable, fully implantable miniaturized optoelectronic systems for wireless optogenetics,” *Nature Biotechnology*, vol. 33, no. 12, pp. 1280–1286, Nov. 2015.

[71] K. L. Montgomery *et al.*, “Wirelessly powered, fully internal optogenetics for brain, spinal and peripheral circuits in mice,” *Nature Methods*, vol. 12, no. 10, pp. 969–974, Aug. 2015.

[72] G. Shin *et al.*, “Flexible Near-Field Wireless Optoelectronics as Subdermal Implants for Broad Applications in Optogenetics,” *Neuron*, vol. 93, no. 3, pp. 509-521.e3, Feb. 2017.

Chapter 2:

[1] A. C. Felix-Ortiz, A. Beyeler, C. Seo, C. A. Leppla, C. P. Wildes, and K. M. Tye, “BLA to vHPC Inputs Modulate Anxiety-Related Behaviors,” *Neuron*, vol. 79, no. 4, pp. 658–664, Aug. 2013.

[2] J. H. Jennings *et al.*, “Distinct extended amygdala circuits for divergent motivational states,” *Nature*, vol. 496, no. 7444, pp. 224–228, Apr. 2013.

[3] R. H. Kramer, A. Mourot, and H. Adesnik, “Optogenetic pharmacology for control of native neuronal signaling proteins,” *Nat Neurosci*, vol. 16, no. 7, pp. 816–823, Jul. 2013.

[4] J. G. McCall and J.-W. Jeong, “Minimally invasive probes for programmed microfluidic delivery of molecules in vivo,” *Current Opinion in Pharmacology*, vol. 36, pp. 78–85, Oct. 2017.

[5] J. Y. Sim, M. P. Haney, S. I. Park, J. G. McCall, and J.-W. Jeong, “Microfluidic neural probes: in vivo tools for advancing neuroscience,” *Lab Chip*, vol. 17, no. 8, pp. 1406–1435, Apr. 2017.

[6] S. Park *et al.*, “One-step optogenetics with multifunctional flexible polymer fibers,” *Nature Neuroscience*, vol. 20, no. 4, pp. 612–619, Apr. 2017.

[7] A. Canales *et al.*, “Multifunctional fibers for simultaneous optical, electrical and chemical interrogation of neural circuits *in vivo*,” *Nature Biotechnology*, vol. 33, no. 3, pp. 277–284, Mar. 2015.

[8] J.-W. Jeong *et al.*, “Wireless Optofluidic Systems for Programmable In Vivo Pharmacology and Optogenetics,” *Cell*, vol. 162, no. 3, pp. 662–674, Jul. 2015.

[9] J. G. McCall *et al.*, “Preparation and implementation of optofluidic neural probes for in vivo wireless pharmacology and optogenetics,” *Nat. Protocols*, vol. 12, no. 2, pp. 219–237, Feb. 2017.

[10] M. Hashimoto, A. Hata, T. Miyata, and H. Hirase, “Programmable wireless light-emitting diode stimulator for chronic stimulation of optogenetic molecules in freely moving mice,” *NPh, NEUROW*, vol. 1, no. 1, p. 011002, May 2014.

[11] Y. Iwai, S. Honda, H. Ozeki, M. Hashimoto, and H. Hirase, “A simple head-mountable LED device for chronic stimulation of optogenetic molecules in freely moving mice,” *Neuroscience Research*, vol. 70, no. 1, pp. 124–127, May 2011.

[12] T. Kim *et al.*, “Injectable, cellular-scale optoelectronics with applications for wireless optogenetics,” *Science*, vol. 340, no. 6129, pp. 211–216, Apr. 2013.

[13] J. G. McCall *et al.*, “Fabrication and application of flexible, multimodal light-emitting devices for wireless optogenetics,” *Nature Protocols*, vol. 8, no. 12, pp. 2413–2428, Nov. 2013.

[14] K. N. Noh *et al.*, “Miniaturized, Battery-Free Optofluidic Systems with Potential for Wireless Pharmacology and Optogenetics,” *Small*, vol. 14, no. 4, p. 1702479, Jan. 2018.

[15] S. I. Park *et al.*, “Soft, stretchable, fully implantable miniaturized optoelectronic systems for wireless optogenetics,” *Nature Biotechnology*, vol. 33, no. 12, pp. 1280–1286, Nov. 2015.

[16] G. Shin *et al.*, “Flexible Near-Field Wireless Optoelectronics as Subdermal Implants for Broad Applications in Optogenetics,” *Neuron*, vol. 93, no. 3, pp. 509-521.e3, Feb. 2017.

[17] K. L. Montgomery *et al.*, “Wirelessly powered, fully internal optogenetics for brain, spinal and peripheral circuits in mice,” *Nature Methods*, vol. 12, no. 10, pp. 969–974, Aug. 2015.

[18] M. Alam, X. Chen, and E. Fernandez, “A low-cost multichannel wireless neural stimulation system for freely roaming animals,” *J. Neural Eng.*, vol. 10, no. 6, p. 066010, 2013.

[19] T. Ativanichayaphong, J. W. He, C. E. Hagains, Y. B. Peng, and J.-C. Chiao, “A combined wireless neural stimulating and recording system for study of pain processing,” *Journal of Neuroscience Methods*, vol. 170, no. 1, pp. 25–34, May 2008.

[20] C.-W. Chang and J.-C. Chiou, “A Wireless and Batteryless Microsystem with Implantable Grid Electrode/3-Dimensional Probe Array for ECoG and Extracellular Neural Recording in Rats,” *Sensors*, vol. 13, no. 4, pp. 4624–4639, Apr. 2013.

[21] S. I. Park *et al.*, “Ultraminiaturized photovoltaic and radio frequency powered optoelectronic systems for wireless optogenetics,” *Journal of Neural Engineering*, vol. 12, no. 5, p. 056002, Oct. 2015.

[22] R. C. Pinnell, J. Dempster, and J. Pratt, “Miniature wireless recording and stimulation system for rodent behavioural testing,” *Journal of Neural Engineering*, vol. 12, no. 6, p. 066015, Dec. 2015.

[23] C. T. Wentz, J. G. Bernstein, P. Monahan, A. Guerra, A. Rodriguez, and E. S. Boyden, “A wirelessly powered and controlled device for optical neural control of freely-behaving animals,” *Journal of Neural Engineering*, vol. 8, no. 4, p. 046021, Aug. 2011.

[24] A. J. Yeh, J. S. Ho, Y. Tanabe, E. Neofytou, R. E. Beygui, and A. S. Y. Poon, “Wirelessly powering miniature implants for optogenetic stimulation,” *Applied Physics Letters*, vol. 103, no. 16, p. 163701, 2013.

[25] L. K. Massey, *Permeability Properties of Plastics and Elastomers, 2nd Ed.: A Guide to Packaging and Barrier Materials*. William Andrew, 2003.

[26] R. Qazi, C. Y. Kim, S.-H. Byun, and J.-W. Jeong, “Microscale Inorganic LED Based Wireless Neural Systems for Chronic in vivo Optogenetics,” *Front. Neurosci.*, vol. 12, 2018.

[27] A. Mehrabian and Y. Abousleiman, “General solutions to poroviscoelastic model of hydrocephalic human brain tissue,” *Journal of Theoretical Biology*, vol. 291, pp. 105–118, Dec. 2011.

[28] Q. Liu, Z. Wang, Y. Lou, and Z. Suo, “Elastic leak of a seal,” *Extreme Mechanics Letters*, vol. 1, pp. 54–61, Dec. 2014.

[29] R. Frank, W. Bronzi, G. Castignani, and T. Engel, “Bluetooth Low Energy: An alternative technology for VANET applications,” in *2014 11th Annual Conference on Wireless On-demand Network Systems and Services (WONS)*, 2014, pp. 104–107.

[30] RF Digital Corp., “Getting Started with SimbleeCOM v1.0.” Simblee Corporation, 2015.

[31] T. Kessler, “How to check Bluetooth connection strength in OS X,” *CNET*, 2013.

[32] F. Jenck, M. Bozarth, and R. A. Wise, “Contraversive circling induced by ventral tegmental microinjections of moderate doses of morphine and [D-Pen2, D-Pen5]enkephalin.,” *Brain Res*, vol. 450, no. 1–2, pp. 382–386, May 1988.

[33] D. P. Devine and R. A. Wise, “Self-administration of morphine, DAMGO, and DPDPE into the ventral tegmental area of rats,” *J. Neurosci.*, vol. 14, no. 4, pp. 1978–1984, Apr. 1994.

[34] P. Namburi, R. Al-Hasani, G. G. Calhoon, M. R. Bruchas, and K. M. Tye, “Architectural Representation of Valence in the Limbic System,” *Neuropsychopharmacology*, vol. 41, no. 7, pp. 1697–1715, Jun. 2016.

[35] J. H. Jennings, G. Rizzi, A. M. Stamatakis, R. L. Ung, and G. D. Stuber, “The Inhibitory Circuit Architecture of the Lateral Hypothalamus Orchestrates Feeding,” *Science*, vol. 341, no. 6153, pp. 1517–1521, Sep. 2013.

[36] R. Al-Hasani *et al.*, “Distinct Subpopulations of Nucleus Accumbens Dynorphin Neurons Drive Aversion and Reward,” *Neuron*, vol. 87, no. 5, pp. 1063–1077, Sep. 2015.

[37] J. G. McCall *et al.*, “CRH Engagement of the Locus Coeruleus Noradrenergic System Mediates Stress-Induced Anxiety,” *Neuron*, vol. 87, no. 3, pp. 605–620, Aug. 2015.

[38] C. Dagdeviren *et al.*, “Miniaturized neural system for chronic, local intracerebral drug delivery,” *Science Translational Medicine*, vol. 10, no. 425, p. eaan2742, Jan. 2018.

[39] S. Spieth, A. Schumacher, C. Kallenbach, S. Messner, and R. Zengerle, “The NeuroMedicator—a micropump integrated with silicon microprobes for drug delivery in neural research,” *J. Micromech. Microeng.*, vol. 22, no. 6, p. 065020, 2012.

[40] I. R. Minev *et al.*, “Electronic dura mater for long-term multimodal neural interfaces,” *Science*, vol. 347, no. 6218, pp. 159–163, Jan. 2015.

[41] C. Dagdeviren *et al.*, “Miniaturized neural system for chronic, local intracerebral drug delivery,” *Science Translational Medicine*, vol. 10, no. 425, p. eaan2742, Jan. 2018.

[42] Y. Qiu and K. Park, “Environment-sensitive hydrogels for drug delivery,” *Advanced Drug Delivery Reviews*, vol. 53, no. 3, pp. 321–339, Dec. 2001.

[43] K.-I. Jang *et al.*, “Soft network composite materials with deterministic and bio-inspired designs,” *Nature Communications*, vol. 6, p. 6566, Mar. 2015.

[44] Y. Liu *et al.*, “Epidermal mechano-acoustic sensing electronics for cardiovascular diagnostics and human-machine interfaces,” *Science Advances*, vol. 2, no. 11, p. e1601185, Nov. 2016.

[45] M. R. Banghart and B. L. Sabatini, “Photoactivatable Neuropeptides for Spatiotemporally Precise Delivery of Opioids in Neural Tissue,” *Neuron*, vol. 73, no. 2, pp. 249–259, Jan. 2012.

[46] I. Tochitsky *et al.*, “Restoring visual function to blind mice with a photoswitch that exploits electrophysiological remodeling of retinal ganglion cells,” *Neuron*, vol. 81, no. 4, pp. 800–813, Feb. 2014.

[47] S. Banala *et al.*, “Photoactivatable drugs for nicotinic optopharmacology,” *Nature Methods*, vol. 15, no. 5, pp. 347–350, May 2018.

Chapter 3:

[1] E. S. Boyden, F. Zhang, E. Bamberg, G. Nagel, and K. Deisseroth, “Millisecond-timescale, genetically targeted optical control of neural activity,” *Nature Neuroscience*, vol. 8, no. 9, p. nn1525, Aug. 2005.

[2] O. Yizhar, L. E. Fenno, T. J. Davidson, M. Mogri, and K. Deisseroth, “Optogenetics in Neural Systems,” *Neuron*, vol. 71, no. 1, pp. 9–34, Jul. 2011.

[3] R. H. Kramer, A. Mourot, and H. Adesnik, “Optogenetic pharmacology for control of native neuronal signaling proteins,” *Nature Neuroscience*, vol. 16, no. 7, pp. 816–823, Jul. 2013.

[4] J. G. Bernstein and E. S. Boyden, “Optogenetic tools for analyzing the neural circuits of behavior,” *Trends in Cognitive Sciences*, vol. 15, no. 12, pp. 592–600, Dec. 2011.

[5] J. G. Bernstein, P. A. Garrity, and E. S. Boyden, “Optogenetics and thermogenetics: technologies for controlling the activity of targeted cells within intact neural circuits,” *Current Opinion in Neurobiology*, vol. 22, no. 1, pp. 61–71, Feb. 2012.

[6] K. A. Zalocusky, C. Ramakrishnan, T. N. Lerner, T. J. Davidson, B. Knutson, and K. Deisseroth, “Nucleus accumbens D2R cells signal prior outcomes and control risky decision-making,” *Nature*, vol. 531, no. 7596, pp. 642–646, Mar. 2016.

[7] V. Gradinaru, M. Mogri, K. R. Thompson, J. M. Henderson, and K. Deisseroth, “Optical Deconstruction of Parkinsonian Neural Circuitry,” *Science*, vol. 324, no. 5925, pp. 354–359, Apr. 2009.

[8] T. Bruegmann *et al.*, “Optogenetic control of heart muscle in vitro and in vivo,” *Nat Meth*, vol. 7, no. 11, pp. 897–900, Nov. 2010.

[9] V. Busskamp, S. Picaud, J. A. Sahel, and B. Roska, “Optogenetic therapy for retinitis pigmentosa,” *Gene Ther*, vol. 19, no. 2, pp. 169–175, Feb. 2012.

[10] A. C. Felix-Ortiz, A. Burgos-Robles, N. D. Bhagat, C. A. Leppla, and K. M. Tye, “Bidirectional modulation of anxiety-related and social behaviors by amygdala projections to the medial prefrontal cortex,” *Neuroscience*, vol. 321, pp. 197–209, May 2016.

[11] J.-W. Jeong *et al.*, “Wireless Optofluidic Systems for Programmable In Vivo Pharmacology and Optogenetics,” *Cell*, vol. 162, no. 3, pp. 662–674, Jul. 2015.

[12] K. N. Noh *et al.*, “Miniaturized, Battery-Free Optofluidic Systems with Potential for Wireless Pharmacology and Optogenetics,” *Small*, vol. 14, no. 4, p. 1702479, Jan. 2018.

Chapter 4:

[1] J.-W. Jeong *et al.*, “Wireless Optofluidic Systems for Programmable In Vivo Pharmacology and Optogenetics,” *Cell*, vol. 162, no. 3, pp. 662–674, Jul. 2015.

[2] J. G. McCall *et al.*, “Preparation and implementation of optofluidic neural probes for in vivo wireless pharmacology and optogenetics,” *Nat. Protocols*, vol. 12, no. 2, pp. 219–237, Feb. 2017.

[3] K. N. Noh *et al.*, “Miniaturized, Battery-Free Optofluidic Systems with Potential for Wireless Pharmacology and Optogenetics,” *Small*, vol. 14, no. 4, p. 1702479, Jan. 2018.

[4] J. G. McCall *et al.*, “Fabrication and application of flexible, multimodal light-emitting devices for wireless optogenetics,” *Nature Protocols*, vol. 8, no. 12, pp. 2413–2428, Nov. 2013.

[5] T. Kim *et al.*, “Injectable, cellular-scale optoelectronics with applications for wireless optogenetics,” *Science*, vol. 340, no. 6129, pp. 211–216, Apr. 2013.

[6] R. Al-Hasani *et al.*, “Distinct Subpopulations of Nucleus Accumbens Dynorphin Neurons Drive Aversion and Reward,” *Neuron*, vol. 87, no. 5, pp. 1063–1077, Sep. 2015.

[7] M. R. Bruchas, B. B. Land, J. C. Lemos, and C. Chavkin, “CRF1-R Activation of the Dynorphin/Kappa Opioid System in the Mouse Basolateral Amygdala Mediates Anxiety-Like Behavior,” *PLOS ONE*, vol. 4, no. 12, p. e8528, Dec. 2009.

[8] J. G. McCall *et al.*, “CRH Engagement of the Locus Coeruleus Noradrenergic System Mediates Stress-Induced Anxiety,” *Neuron*, vol. 87, no. 3, pp. 605–620, Aug. 2015.

[9] E. R. Siuda *et al.*, “Spatiotemporal Control of Opioid Signaling and Behavior,” *Neuron*, vol. 86, no. 4, pp. 923–935, May 2015.

Chapter 5:

[1] R. Qazi, C. Y. Kim, S.-H. Byun, and J.-W. Jeong, “Microscale Inorganic LED-Based Wireless Neural Systems for Chronic in vivo Optogenetics,” *Front. Neurosci.*, vol. 12, 2018.

[2] C. Hassler, R. P. von Metzen, P. Ruther, and T. Stieglitz, “Characterization of parylene C as an encapsulation material for implanted neural prostheses,” *Journal of Biomedical Materials Research Part B: Applied Biomaterials*, vol. 93B, no. 1, pp. 266–274, Apr. 2010.

[3] B. J. Kim *et al.*, “3D Parylene sheath neural probe for chronic recordings,” *J. Neural Eng.*, vol. 10, no. 4, p. 045002, 2013.

[4] S. A. Hara, B. J. Kim, J. T. W. Kuo, C. D. Lee, E. Meng, and V. Pikov, “Long-term stability of intracortical recordings using perforated and arrayed Parylene sheath electrodes,” *J. Neural Eng.*, vol. 13, no. 6, p. 066020, 2016.

[5] J. Y. Sim, M. P. Haney, S. I. Park, J. G. McCall, and J.-W. Jeong, “Microfluidic neural probes: in vivo tools for advancing neuroscience,” *Lab Chip*, vol. 17, no. 8, pp. 1406–1435, Apr. 2017.

[6] J.-W. Jeong *et al.*, “Wireless Optofluidic Systems for Programmable In Vivo Pharmacology and Optogenetics,” *Cell*, vol. 162, no. 3, pp. 662–674, Jul. 2015.

[7] T. Kim *et al.*, “Injectable, Cellular-Scale Optoelectronics with Applications for Wireless Optogenetics,” *Science*, vol. 340, no. 6129, pp. 211–216, Apr. 2013.

[8] J.-W. Jeong, G. Shin, S. I. Park, K. J. Yu, L. Xu, and J. A. Rogers, “Soft Materials in Neuroengineering for Hard Problems in Neuroscience,” *Neuron*, vol. 86, no. 1, pp. 175–186, Apr. 2015.

Appendix

Wireless BLE Firmware Codes

A. Wireless Receiver Circuit Code

```
//Simblee chip with this code can be controlled with our iPhone app as well as any third party
//BLE app
//We have used limited number of commands as an example but more customizable commands
can be quickly added and
//easily scaled for multitude of output modalities and stimulation profiles.
//This uses both BLE and COM receive functions to control the device in
//a) BLE or USER mode (Graphical User Interface in Smartphone) or b) COM mode (Closed
Loop/Automatic)
//This code starts in BLE mode but can be made to go in COM mode easily by sending
appropriate command through smartphone

#include <SimbleeBLE.h>
#include "OTA_Bootloader.h"

//Assign names to LED port numbers
#define portLed1 9
#define portLed2 11
#define portLed3 12
#define portHeat1 15
#define portHeat2 16
#define portHeat3 18
#define portHeat4 17
#define redLed 29
#define greenLed 30

//Unique key for each message
const char msg1_Led1 = 'a';//LED1
const char msg2_Led1 = 'b';//LED1
const char msg3_Led1 = 'c';//LED1
const char msg4_Led1 = 'd';//LED1
const char msg1_Led2 = 'e';//LED2
const char msg2_Led2 = 'f';//LED2
const char msg3_Led2 = 'g';//LED2
const char msg4_Led2 = 'h';//LED2
const char msg1_Led3 = 'i';//LED3
const char msg2_Led3 = 'j';//LED3
const char msg3_Led3 = 'k';//LED3
```

```
const char msg4_Led3 = 'l'; //LED3
const char msg_Heat1 = 'm'; //Heater1
const char msg_Heat2 = 'n'; //Heater2
const char msg_Heat3 = 'o'; //Heater3
const char msg_Heat4 = 'p'; //Heater4
const char msg_LedOff = 'q'; // Turn all LED states off
const char msg_reset = 'r'; //Reset Chip
const char msg_Sleep = 's'; //ULP Mode
const char msg_WakeUp = 't'; // Wake Up
const char boot = 'z'; //OTA Bootloader Mode
const char done[4] = {'D', 'o', 'n', 'e'}; //For sending back receive confirmation

//These commands allow the receiver to change from COM mode (Inter-Simblee Network) to
//BLE mode (Smartphone Control)
const char COM_to_BLE = 'B'; //COM to User mode
const char BLE_to_COM = 'C'; //User to COM mode

//The Simblee shouldn't be free to take commands from any transmitter for security and
//reliability in COM mode.  For this reason, it
//will only listen to transmissions that have been sent from a machine that sent it a secret key
//"U" in the past.  The last machine to
// send it a "U" has its serial number stored in the variable called transmitter.
const char master = 'U';
unsigned int transmitter;

//These booleans are used to control the current Bluetooth states.
bool btoc = false; //btoc indicates the transition from BLE to COM
bool isBLE = true; //isBLE is a boolean variable that is true when in BLE mode, and false when
//in COM mode.

//Predefined off time for 4 different led operations, change these numbers for off time for each
//led program
const unsigned long led5 = 188500; // 5Hz
const unsigned long led10 = 89300; // 10Hz
const unsigned long led20 = 39700; // 20Hz
const unsigned long led40 = 14800; // 40Hz

//Heater Variables Initialization
unsigned long heatTimer = 0;
const unsigned long heatTime = 20000; //20000ms for each heater
boolean heatFlag = LOW;  //For heater state
boolean heatMem1 = LOW; //To store heater activation memory, so it is activated only once
boolean heatMem2 = LOW;
boolean heatMem3 = LOW;
boolean heatMem4 = LOW;

//LED variables for blinking
boolean ledState1 = LOW;
unsigned long ledTimer1 = 0; //Used for blinking LED 1
```

```
boolean led_On_Off1 = LOW; //LED1 Flag
unsigned long ledSwitchTimer1 = 0; //LED1 Timer
unsigned long ledOff1 = 0; //LED1 off duration

boolean ledState2 = LOW;
unsigned long ledTimer2 = 0;
boolean led_On_Off2 = LOW;
unsigned long ledSwitchTimer2 = 0;
unsigned long ledOff2 = 0;

boolean ledState3 = LOW;
unsigned long ledTimer3 = 0;
boolean led_On_Off3 = LOW;
unsigned long ledSwitchTimer3 = 0;
unsigned long ledOff3 = 0;

//Sleep and Reset flag
boolean Sleep = LOW;

////////////////////////////////////// INITIALIZATIONS ////////////////////////////////////////////////

void setup() {

  //Set Up UART features for debugging purposes
  Serial.begin(9600);

  //Set Up SimbleeBLE parameters
  SimbleeBLE.deviceName = "Mouse 1";
  SimbleeBLE.advertisementData = "Simblee";
  SimbleeBLE.advertisementInterval = MILLISECONDS(300);
  SimbleeBLE.txPowerLevel = +4;  // (-20dbM to +4 dBm)
//Reduce value to consume less power (decreases range as well)

  //Configure Simblee ports
  pinMode(portLed1, OUTPUT);
  pinMode(portLed2, OUTPUT);
  pinMode(portLed3, OUTPUT);
  pinMode(portHeat1, OUTPUT);
  pinMode(portHeat2, OUTPUT);
  pinMode(portHeat3, OUTPUT);
  pinMode(portHeat4, OUTPUT);
  pinMode(redLed, OUTPUT);
  pinMode(greenLed, OUTPUT);

  //Initial start up sequence, blinks each led 3 times
  blinkGreenLed();
  blinkRedLed();

  // Start the SIMBLEE BLE mode (Smartphone mode)
```

```
  SimbleeBLE.begin(); //Start BLE protocol
  isBLE = true; //Begin in BLE mode
}

//////////////////////////////// FUNCTION DECLARATIONS ////////////////////////////////

// If in BLE mode and receives information
void SimbleeBLE_onReceive(char *data, int len)
{
  SimbleeBLE.send(done, 4); //Send back a confirmation that Simblee has received the command

//The BtoC function crashes if called here.  So set a flag to make the transition as soon as we
//exit the function in the main loop
//If user sends command to go into COM mode
  if(data[0] == BLE_to_COM){
    btoc = true;
  }
  //If user sends any other command except for COM mode
  else
    action(data[0]); //In Simblee data[0] stores the received character by default and send it to
//action function to execute proper codes
}

//When we receive data while in the COM mode.  This comes from the SimbleeCOM transmitter
void SimbleeCOM_onReceive(unsigned int esn, const char *payload, int len, int rssi)
{
  printf("%c", payload[0]); //Can be used for debugging

 //If the message is a "U", that means the data is secure and we should listen to future
//transmissions from this source
  if(payload[0] == master){
    transmitter = esn;
  }

//If there is a GPIO pin voltage change for COM to BLE (B), call the function that does this
//transition
  else if(payload[0] == COM_to_BLE){
    COMtoBLE();
  }

//Otherwise check if we trust this transmitter by comparing its serial number to the one we
//have stored
//If it matches, then we can call the action using the first letter of the transmission.
  else if(esn == transmitter){
     action(payload[0]);
  }
 printf("\n"); //Organizes debugging Data by pushing a new line between prints
}
```

```
//Turn off BLE mode and begin COM mode
void BLEtoCOM()
{
  SimbleeBLE.end(); //Stop BLE mode
  SimbleeCOM.begin(); //Start COM Mode
  isBLE = false; //Reset BLE mode variable
}

//Turn off COM mode and begin BLE mode
void COMtoBLE()
{
  SimbleeCOM.end(); //Stop COM Mode
  SimbleeBLE.begin(); //Start BLE mode
  isBLE = true; //Set BLE mode variable
}

//Heater OFF function since it actually gets turned ON in action loop unlike LEDs
// As a safety feature it turns everything off, just to make sure more than one heater isn't
//accidentally turned on.
//This function is executed when the preset time for the heater is reached, 20 or 30 sec
//depending on the button pressed
void HeatersOff(void)
{
  digitalWrite(portHeat1, LOW);
  digitalWrite(portHeat2, LOW);
  digitalWrite(portHeat3, LOW);
  digitalWrite(portHeat4, LOW);
  digitalWrite(redLed, LOW);
  heatFlag = LOW;
}

//This function just blinks the indicator LED(Green)thrice before it goes into sleep and to
//indicate initialization process.
void blinkGreenLed (void)
{
  for (int i = 0; i < 3; i++)
  {
    digitalWrite(greenLed, HIGH);
    delay(100);
    digitalWrite(greenLed, LOW);
    delay(100);
  }
  return;
}

//This function blinks heater LED (Red)thrice after indicator LED (Green) blinking to indicate
//initialization process.
void blinkRedLed (void)
{
```

```
  for (int i = 0; i < 3; i++)
  {
    digitalWrite(redLed, HIGH);
    delay(100);
    digitalWrite(redLed, LOW);
    delay(100);
  }
  return;
}

//This is the decoder function that depending on the message decoded, carries out the necessary
//operation.
void action (int now)
{
  if (now == -1) //If nothing is received
  {
    return; //Do nothing
  }

  /*|||||||||||||||||||||||||||||| Bootme mode ||||||||||||||||||||||||||||||*/

  else if (now == boot)
  {
    if(isBLE)
      SimbleeBLE.end(); //Turn off BLE mode
    else
      SimbleeCOM.end(); //Turn off COM mode
    digitalWrite(redLed, HIGH); //Visual indication
    digitalWrite(greenLed, HIGH);
    ota_bootloader_start(); //begins OTA enabled state
  }


  /*|||||||||||||||||||||||||||||| Heater 1 ||||||||||||||||||||||||||||||||||*/

  if ((now == msg_Heat1) && (heatFlag == LOW))
//Case checks the received controller message and if any other heater is ON
  {
    if (heatMem1 == LOW) //if this heater has not been turned ON before this
    {
      heatFlag = HIGH; // Now other heaters cannot be turned ON during this loop
      heatMem1 = HIGH;
//Sets the channel memory HIGH so same heater cannot be activated again in the future
      heatTimer = millis(); //Stores clock counter value
      digitalWrite(portHeat1, HIGH); //Turns the heater ON
      digitalWrite(redLed, HIGH);
      return;
    }
    else
```

```
    {
      blinkRedLed();  //if the case is that it is the right controller message but this heater has
//been activated before, it flashes heater
      return;          //indicator (red) LED to let user know that it cannot be turned on unless reset.
    }
  }

  /*|||||||||||||||||||||||||||||||| Heater 2 ||||||||||||||||||||||||||||||||*/

  if ((now == msg_Heat2) && (heatFlag == LOW))
  {
    if (heatMem2 == LOW)
    {
      heatFlag = HIGH;
      heatMem2 = HIGH;
      heatTimer = millis();
      digitalWrite(portHeat2, HIGH);
      digitalWrite(redLed, HIGH);
      return;
    }
    else
    {
      blinkRedLed();
      return;
    }
  }

  /*|||||||||||||||||||||||||||||||| Heater 3 ||||||||||||||||||||||||||||||||*/

  else if ((now == msg_Heat3) && (heatFlag == LOW))
  {
    if (heatMem3 == LOW)
    {
      heatFlag = HIGH;
      heatMem3 = HIGH;
      heatTimer = millis();
      digitalWrite(portHeat3, HIGH);
      digitalWrite(redLed, HIGH);
      return;
    }
    else
    {
      blinkRedLed();
      return;
    }
  }
  /*|||||||||||||||||||||||||||||||| Heater 4 ||||||||||||||||||||||||||||||||*/

  if ((now == msg_Heat4) && (heatFlag == LOW))
```

```
{
  if (heatMem4 == LOW)
  {
    heatFlag = HIGH;
    heatMem4 = HIGH;
    heatTimer = millis();
    digitalWrite(portHeat4, HIGH);
    digitalWrite(redLed, HIGH);
    return;
  }
  else
  {
    blinkRedLed();
    return;
  }
}

// In this function, led cases only initiates the LED sequence by setting the state of the LED
//variables whether it is activated or not and the actual turning on and off is handled in the main
//loop.
//The case matching for received message is that LEDs turn on and off with single button
//press.
//To debounce the circuit on the receiving side also, time between previous button press and
//current button press must be greater than 50 ms.

  /*|||||||||||||||||||||||||||||||| LED 1 ||||||||||||||||||||||||||||||||*/

  if ((now == msg1_Led1) && (millis() - ledSwitchTimer1 >= 50))
//checks the controller message, and whether it has been more than 50ms since last press
  {
    ledState1 = ! ledState1;
//Flips back and forth, this does not handle the physical turning ON and OFF of the LED
    ledOff1 = led5;   //Loads the timing variable used by the actual LED loop
    ledSwitchTimer1 = millis();
//Stores the current counter timer for the comparison in the if statement condition
    return;
  }

  if ((now == msg2_Led1) && (millis() - ledSwitchTimer1 >= 50))
  {
    ledState1 = ! ledState1;
    ledOff1 = led10;
    ledSwitchTimer1 = millis();
    return;
  }
  else if ((now == msg3_Led1) && (millis() - ledSwitchTimer1 >= 50))
  {
    ledState1 = ! ledState1;
    ledOff1 = led20;
```

```
  ledSwitchTimer1 = millis();
  return;
}
if ((now == msg4_Led1) && (millis() - ledSwitchTimer1 >= 50))
{
  ledState1 = ! ledState1;
  ledOff1 = led40;
  ledSwitchTimer1 = millis();
  return;
}

/*|||||||||||||||||||||||||||||||| LED 2 ||||||||||||||||||||||||||||||||*/

if ((now == msg1_Led2) && (millis() - ledSwitchTimer2 >= 50))
{
  ledState2 = ! ledState2;
  ledOff2 = led5;
  ledSwitchTimer2 = millis();
  return;
}

else if ((now == msg2_Led2) && (millis() - ledSwitchTimer2 >= 50))
{
  ledState2 = ! ledState2;
  ledOff2 = led10;
  ledSwitchTimer2 = millis();
  return;
}
if ((now == msg3_Led2) && (millis() - ledSwitchTimer2 >= 50))
{
  ledState2 = ! ledState2;
  ledOff2 = led20;
  ledSwitchTimer2 = millis();
  return;
}
if ((now == msg4_Led2) && (millis() - ledSwitchTimer2 >= 50))
{
  ledState2 = ! ledState2;
  ledOff2 = led40;
  ledSwitchTimer2 = millis();
  return;
}

/*|||||||||||||||||||||||||||||||| LED 3 ||||||||||||||||||||||||||||||||*/

if ((now == msg1_Led3) && (millis() - ledSwitchTimer3 >= 50))
{
  ledState3 = ! ledState3;
  ledOff3 = led5;
```

```
    ledSwitchTimer3 = millis();
    return;
  }

  if ((now == msg2_Led3) && (millis() - ledSwitchTimer3 >= 50))
  {
    ledState3 = ! ledState3;
    ledOff3 = led10;
    ledSwitchTimer3 = millis();
    return;
  }
  if ((now == msg3_Led3) && (millis() - ledSwitchTimer3 >= 50))
  {
    ledState3 = ! ledState3;
    ledOff3 = led20;
    ledSwitchTimer3 = millis();
    return;
  }
  if ((now == msg4_Led3) && (millis() - ledSwitchTimer3 >= 50))
  {
    ledState3 = ! ledState3;
    ledOff3 = led40;
    ledSwitchTimer3 = millis();
    return;
  }

  // Turn Off all LED States

  if (now == msg_LedOff)
  {
    ledState1 = LOW;
    ledState2 = LOW;
    ledState3 = LOW;
  }

  //Reset and Wake Up Simblee wirelessly
  if (now == msg_reset)
  {
    Simblee_systemReset(); // This allows waking a Simblee from its sleep mode wirelessly
    return;
  }

  //Simblee ULP(Ultra Low Power)
  if (now == msg_Sleep && (heatFlag == LOW) && (ledState1 == LOW) && (ledState2 == LOW)
&& (ledState3 == LOW))
 //If sleep button is pressed, and Sleep flag is LOW and heater is OFF and LED is in OFF state,
//execute the sleep function.
  {
    Sleep = HIGH; //Setting sleep variable. The actual process happens in the loop
```

```
  }
}


void loop()
{
//As the BLEtoCOM function in the receive interrupt function couldn't be called, use the flag
//btoc, check to see if that flag has been set, and if it has been, call its function.
  if(btoc){
    BLEtoCOM();
    btoc = false;
  }

  if (Sleep == HIGH)
  {
    blinkRedLed();
    Simblee_ULPDelay(INFINITE); //Go to Ultra Low Power Mode
    Sleep = LOW; //Reset Sleep Flag
    blinkGreenLed(); //Indication for the user
  }
/*|||||||||||||||||||||||||||||||| Heaters OFF ||||||||||||||||||||||||||||||||*/
  if ((heatFlag == HIGH) && (millis() - heatTimer >= heatTime))
//Counts the timer and turns off the heaters when the time is reached
  {
    HeatersOff(); //Turn off each heater after 20 s
  }

  //LED Indicator = Green LED continuously ON

  boolean ledFlag = ledState1 || ledState2 || ledState3; //If any of the LEDs is ON
//This code can control 3 independent LEDs simultaneously although we used only two in our
//optofluidic probe
  digitalWrite (greenLed, ledFlag); // then Green LED remains ON


/*|||||||||||||||||||||||||||||||| LED 1 ||||||||||||||||||||||||||||||||*/

  if (ledState1 == HIGH)   //This is the loop that handles the timing of turning the LED on and off
  { //Runs only when the led state is HIGH
    if (led_On_Off1 == LOW)   //if the LED is physically off,
    {
      digitalWrite(portLed1, HIGH);    //turns it on and waits for 10ms and turns it off.
      delayMicroseconds(9850);    //delay is adjusted to precisely turn the LED on for 10ms,
//compensating for few clock cycles of error
      digitalWrite(portLed1, LOW);
      ledTimer1 = micros();        //stores the time when it was turned off
      led_On_Off1 = HIGH;          //sets the state high, meaning that it has been turned on and it
//must wait for exact amount of time before it can be turned back on again
    }
```

```
    else if (micros() - ledTimer1 >= ledOff1)    //This handles how much it stays off
    { //used the ledTimer and ledOff, which was defined when it was initiated in the action
      //function
      led_On_Off1 = LOW;
//waits until the time passes since LED has been turned off. Reset the led_On_Off to zero
    }
  }

/*|||||||||||||||||||||||||||||||| LED 2 ||||||||||||||||||||||||||||||||*/

  if (ledState2 == HIGH)
  {
    if (led_On_Off2 == LOW)
    {
      digitalWrite(portLed2, HIGH);
      delayMicroseconds(9850);
      digitalWrite(portLed2, LOW);
      ledTimer2 = micros();
      led_On_Off2 = HIGH;
    }
    else if (micros() - ledTimer2 >= ledOff2)
    {
      led_On_Off2 = LOW;
    }
  }

/*|||||||||||||||||||||||||||||||| LED 3 ||||||||||||||||||||||||||||||||*/

if (ledState3 == HIGH)
  {
    if (led_On_Off3 == LOW)
    {
      digitalWrite(portLed3, HIGH);
      delayMicroseconds(9850);
      digitalWrite(portLed3, LOW);
      ledTimer3 = micros();
      led_On_Off3 = HIGH;
    }
    else if (micros() - ledTimer3 >= ledOff3)
    {
      led_On_Off3 = LOW;
    }
  }
}
```

B. SimbleeCOM transmitter code for Closed Loop Control Experiment

```
/*
* This code is only needed for COM mode operation since in BLE mode, smartphone is the transmitter
* This folder allows for GPIO changes to broadcast signals in the SimbleeCOM mode.
* Pin 7 must be powered LOW in order to enable COM Mode, only then the pins control the output signals to be sent
* There is no BLE pairing or smartphone control involved. This is a broadcasting technique where SimbleeCOM
* Transmitter broadcasts signals and all SimbleeCOM Receivers receive it.
*/

#include <SimbleeBLE.h>
#include "OTA_Bootloader.h"

//Boolean indicating the current state of the system
bool isCOM;

//Characters that save the commands that are to be transmitted
char * send1;
char * send2;
char * send3;
char * send4;

//The lengths of the transmitted commands
int len1 = 1;
int len2 = 1;
int len3 = 1;
int len4 = 1;

//We send commands on low to high transitions.  In order to do this
//We need the current and previous state of each pin. These hold the
//previous state of the pins
int lastLoop2 = 0; //Store previous state of Pin 2
int lastLoop3 = 0; //Store previous state of Pin 3
int lastLoop4 = 0; //Store previous state of Pin 4
int lastLoop5 = 0; //Store previous state of Pin 5

void setup() {
  //Set Up SimbleeBLE parameters
  SimbleeBLE.deviceName = "COM_TX_1";
  SimbleeBLE.advertisementData = "Simblee";
  SimbleeBLE.advertisementInterval = MILLISECONDS(300);
  SimbleeBLE.txPowerLevel = +4;  // (-20dbM to +4 dBm)
```

```
  //This is the only digital input pin.
  pinMode(2, INPUT);
  pinMode(3, INPUT);
  pinMode(4, INPUT);
  pinMode(5, INPUT);
  pinMode(6, INPUT);
  pinMode(8, INPUT);
//It determines the Bluetooth protocol (BLE(1) or COM(0)) for SimbleeCOM Trasmitter

//This is an indicator LED to show the system is running.  It is not necessary.
  pinMode(7, OUTPUT);

//Create strings on the heap in order to permanently store the message data (large malloc for
//longer strings)
  send1 = (char*)malloc(20*sizeof(char));
  send2 = (char*)malloc(20*sizeof(char));
  send3 = (char*)malloc(20*sizeof(char));
  send4 = (char*)malloc(20*sizeof(char));

//Set the default transmissions to be a,b,c and d. More commands can be added based on
//number of available pins
//More commands can be easily added and appended to more GPIO pins as necessary
//As an example we are used only 4 out of all example commands that Simblee chips were
//programmed for
  stringCopy(send1,"r",len1);
// To reset all SimbleeCOM chips (makes them enter default BLE mode wirelessly)
  stringCopy(send2,"b",len2); // For 10Hz blinking of LED1
  stringCopy(send3,"c",len3); // For 20Hz blinking of LED1
  stringCopy(send4,"d",len4); // For 40Hz blinking of LED1

  //Start the transmitter in the COM state and set the state indicator
  SimbleeCOM.begin();
  isCOM = true;
}


//If the transmitter is in BLE mode and receives information, it is likely a new message
//that needs to be transmitted.  If the first letter of the message is a 'z', the transmitter
//enters ota mode to be reprogrammed.  Otherwise the first char should correspond to the pin
//number we want to overwrite for example the message "2a" would store the message 'a' in pin
//2.
void SimbleeBLE_onReceive(char *data, int len)
{
  //If my first letter is a z, enter OTA mode to be reprogrammed
  if (data[0] == 'z')
  {
    if(isCOM)
      SimbleeCOM.end();
    else
```

```
    SimbleeBLE.end();
   ota_bootloader_start(); //begins OTA enabled state
  }

  //Store the first letter of the string and remove it from the array.
  int pin = data[0]-'0';
  data++;
  len--;

  //If the first letter of the string matched one of our pins, store the information in the
  //corresponding array.  Else exit the function having done nothing.
  if(pin == 2){
    stringCopy(send1,data,len);
    len1 = len;
  }
  else if(pin == 3){
    stringCopy(send2,data,len);
    len2 = len;
  }
  else if(pin == 4){
    stringCopy(send3,data,len);
    len3 = len;
  }
  else if(pin == 5){
    stringCopy(send4,data,len);
    len4 = len;
  }
}

//Turn off BLE, and turn on COM.  Toggle the isCOM Boolean. This is for SimbleeCOM
//transmitter itself
void BLEtoCOM()
{
  SimbleeBLE.end();
  SimbleeCOM.begin();
  isCOM = true;
}

//Turn off COM, and turn on BLE.  Toggle the isCOM Boolean. This is for SimbleeCOM
//transmitter itself
void COMtoBLE()
{
  SimbleeCOM.end();
  SimbleeBLE.begin();
  isCOM = false;
}

//Copy the string
void stringCopy(char *output, char *input, int length){
```

```
  for(int i =0; i< length; i++){
    output[i] = input[i];
  }
}

void loop()
{
//Constantly write pin seven high.  This lets us see whether or not the system has reset
  digitalWrite(7,HIGH);

//Pin 8 defines the mode of the Bluetooth in SimbleeCOM transmitter.  When it is grounded
//(LOW) the transmitter
//should be in COM mode.   If the pin is HIGH, call the function to change the state.
  if(digitalRead(8)&&isCOM)
  {
    COMtoBLE();
  }
  else if (!digitalRead(8) && !isCOM)
  {
    BLEtoCOM();
  }

  //We only want to transmit when in the COM state
  if(isCOM)
  {
//The reciever's will only listen to the last machine that sent it a U.
//So send a U whenever we transmit.
// This can avoid interference and crosstalk when implementing multiple closed loops
// Longer security keys can also be enabled to ensure reliable and secure broadcasting control
    SimbleeCOM.send("U",1);

      //Store the previous loops analog information.
      lastLoop2 = analogRead(2);
      lastLoop3 = analogRead(3);
      lastLoop4 = analogRead(4);
      lastLoop5 = analogRead(5);


    //Wait a semi-significant amount of time
    delay(100);

//If the voltage on any of the pins has changed send the appropriate change method to the
//other Simblees

//The first four messages are configurable which were created and initialized earlier
      if((lastLoop2<600 && analogRead(2)>600) || (lastLoop2>600) && (analogRead(2)<600))
SimbleeCOM.send(send1, len1);
      if((lastLoop3<600 && analogRead(3)>600) || (lastLoop3>600) && (analogRead(3)<600))
SimbleeCOM.send(send2, len2);
```

```
    if((lastLoop4<600 && analogRead(4)>600) || (lastLoop4>600) && (analogRead(4)<600))
SimbleeCOM.send(send3, len3);
    if((lastLoop5<600 && analogRead(5)>600) || (lastLoop5>600) && (analogRead(5)<600))
SimbleeCOM.send(send4, len4);

//To make SimbleeCOM receivers go into enter BLE mode (B)
    if(analogRead(6)>900)SimbleeCOM.send("B", 1);
//Sends all Simblee receivers from COM mode into BLE mode
  }
```